University of Southampton

Faculty of Engineering and Physical Sciences

School of Chemistry

Molecular Dynamics or: How I Learned to Stop Worrying and Love the Membrane

Graham Michael Saunders MBioSci
Thesis for the degree of Doctor of Philosophy
September 2019

UNIVERSITY OF SOUTHAMPTON

ABSTRACT

Faculty of Engineering and Physical Sciences

Computational Chemistry

Thesis for the degree of Doctor of Philosophy

Molecular Dynamics or: How I Learned to Stop Worrying and Love the Membrane

Graham Michael Saunders

The rise of antibiotic resistant bacterial species is an international problem. The structure, function and dynamic behaviour of the bacterial cell envelope must be thoroughly understood in order to design novel antimicrobial molecules. This thesis presents the use of molecular dynamics techniques to investigate the function of the Gram-negative outer membrane enzyme LpxR, as well as the subsequent effect of the protein on the dynamics of the outer membrane. LpxR covalently modifies a constituent of the outer membrane, lipopolysaccharide, which can modulate the immune response of the host. Simulations enabled the identification of a putative closed conformation for the protein, as well as a secondary ion binding site. These observations led to the proposition of an evaluated catalytic mechanism for the membrane enzyme.

The effect of lipopolysaccharide deacylation on wider membrane properties and dynamics was also investigated. Deacylated lipopolysaccharide induced positive curvature on the membrane when in distinct patches; cardiolipin phospholipids also clustered in areas of the inner leaflet corresponding with the patches of deacylated lipopolysaccharide in the outer leaflet. The application of an electric field to these modified membranes identified structural weaknesses at the interface between deacylated and wildtype lipopolysaccharide. Electroporation of the outer membrane model with OmpA embedded was also performed, and these simulations indicated that the presence of integral proteins may cause localised weakness in the membrane.

Finally, the interactions between polymyxin B1, an antimicrobial peptide, and the outer membrane were examined, to gain a further understanding of how the molecule infiltrates the Gram-negative cell envelope. The peptides were observed to permeate through both the outer and inner membrane models, resulting in phospholipid flip-flopping, thereby degrading the lipid asymmetry of the outer membrane. Data presented here provide the basis for an updated self-promoted uptake mechanism of cellular infiltration for polymyxin B1.

Table of Contents

List of Tables

Table 1. *All coarse-grained simulations performed in this chapter. All LPS-containing simulations performed at 310 K (x2) and 323 K (x1), and DPPC containing simulations at 323 K (x3).*

Table 2. *All united-atom simulations performed in this chapter. All protein simulations, unless otherwise stated, were performed using an Ra LPS asymmetric membrane with 64 lipids in the outer leaflet.*

Table 3. *All equilibrium molecular dynamics simulations performed in this chapter. Each asymmetric membrane had an inner leaflet composed of 90% PE, 5% PG and 5% cardiolipin. All simulations performed at 310 K (x2) and 323 K (x1)*

Table 4. *All simulations performed in this chapter with an electric field applied. Inner leaflet, unless specified otherwise, is as previously described. All simulations performed at 310 K.*

Table 5. *Solvent accessible surface area of the lipid A segment of LPS per molecule for asymmetric membrane systems solvated with SPC, NW or PW models.*

Table 6. *Time taken for pore formation in each membrane system with an external electric field applied.*

Table 7. *All single membrane or solution simulations performed in this chapter under equilibrium molecular dynamics. Inner leaflet of all membrane systems consists of 90% PE, 5% PG and 5% cardiolipin mixture. All simulations performed at 310 K (x2) and 323 K (x1).*

Table 8. *All simulations performed in this chapter with an electric field applied. Inner leaflet of membranes is as previously described. All simulations performed at 310 K.*

List of Figures

united-atom resolution. ***15c)*** *the same tetra-acylated Re LPS species at coarse-grained resolution.*

Figure 16a) *The X-ray structure of LpxR (PDB 3FID), with visible extracellular loops and periplasmic turns labelled.* ***16b)*** *LpxR backbone with Re LPS bound within active site..* ***16c)*** *Re LPS in LpxR binding site, as modelled by Rutten et al., with scissile bond labelled with an asterisk* (129)*.* ***16d)*** *Key residues of binding site labelled with water molecule and* Ca^{2+} *ion (yellow) from Rutten et al. model shown. Interatomic distances H122 and water ~0.2 nm, T34 and* Ca^{2+} *ion ~0.19 nm, D10 and* Ca^{2+} *ion ~0.18 nm and N9 and* Ca^{2+} *ion ~0.36 nm.*

Figure 17*. The catalytic mechanism of LpxR, as proposed and published by Rutten et al. along with the X-ray structure of the OMP* (129)*. A hydrogen bond between the carbonyl oxygen of E128 and the protonated* $N\delta$ *of H122 stabilises the imidazole ring in position, allowing a hydrogen bond to activate a mechanistic water molecule, which hydrolyses the scissile bond of LPS and leads to the removal of two of its six acyl tails.*

Figure 18. *Initial starting conformation for the atomistic dimer investigation simulations with the protein backbones coloured in green and purple, with side (****18a)****) and top-down (****18b)****) views of the proteins. Key extracellular loops (Lx) and periplasmic turns (Tx) are noted, and LPS binding site is marked with an asterisk.*

Figure 19. *Membrane thickness heat map, as described by the intermolecular distances between phosphates of opposing bilayer leaflets.* ***19a)*** *Showing thickness of smaller LpxR-in-Ra LPS membrane system.* ***19b)*** *Showing thickness of larger LpxR-in-Ra LPS membrane system.*

Figure 20a) *Deuterium order parameters for the six tails of LPS in the bulk lipid region of the membrane, greater than 2 nm from LpxR.* ***20b)*** *Order parameters for LPS tails within 0.5 nm of LpxR.* ***20c)*** *Order parameters for LPS tails of molecules within 0.5 nm of the binding site.* ***20d)*** *Acts as a graphical legend for* ***20a)*** *to* ***20c)****.*

Figure 21. *Mass densities of leaflet phosphate headgroups for Ra LPS-containing systems. Solid line denotes protein-embedded system and dashed line the membrane-only snapshot. Black line denotes Re LPS, red PE, green PG and blue cardiolipin.*

Figure 22a) *Protein-Ra LPS contacts as defined as an intermolecular distance of* $\leq$*0.4 nm, represented in a BWR scale heat-map. Top-down view with extracellular loops annotated and binding site marked with an asterisk.* ***22b)*** *As* **a** *but directly focusing on the LPS binding site.* ***22c)*** *Intermolecular hydrogen bond between I125 and a sugar moiety of a nearby Ra LPS molecule. Also visible are intramolecular hydrogen bonds of the Ra LPS molecule, which stabilise the conformation of the molecule.* ***22d)*** *Electrostatic interactions between R120, R123 and nearby Ra LPS sugar moieties, with Ra LPS carbon atoms shown in cyan and protein carbon atoms in yellow. All other atoms are coloured as the literature standard. Ionic interactions such as these stabilise the L3* α*-helix of LpxR.*

Figures 23a) *to* ***23c)*** *Calculations of the RMSD of different backbone regions of apo LpxR when embedded in Ra LPS (black), Re LPS (red) or DPPC (green).* ***23a)*** *Total backbone RMSD.* ***23b)*** *RMSD of the backbone of beta barrel residues.* ***23c)*** *RMSD of the backbone of residues in loops L1 and L3.* ***23d)*** *Rolling average (red) of apo protein backbone RMSD (black).*

Figure 24*. RMSF of whole apo protein backbone when embedded in Ra LPS (black), Re LPS (red) or DPPC (green). Extracellular loops and periplasmic turns are annotated as* L_x *and* T_x *respectively.*

Figure 25a) *2d projection of the first two principal components of protein backbone movement for each lipid or detergent environment, from Ra LPS (black) to Re LPS (red), DPPC (green) and DPC (blue).* ***25b)*** *Extreme projections of LpxR backbone movement, with protein conformations overlaid every 20 ps with BWR colour scale, corresponding to the first principal component in the Ra LPS membrane.* ***25c)*** *As previous but in Re LPS membrane.* ***25d)*** *As previous but in DPPC membrane.* ***25e)*** *As previous but in DPC micelle.*

Figure 26a) *Secondary structure analysis of LpxR residues across 1 μs simulation of protein in Ra LPS membrane at 323 K, with yellow denoting β-sheet, pink α-helix, green turn, blue 3_{10}-helix, white coil, red π-helix and brown an isolated bridge.* ***26b)*** *As* ***a.*** *but analysis of LpxR residues in a representative 500 ns simulation of protein in DPC micelle at 323 K, with colours the same.*

Figure 27. *Showing the mean barrel tilt angle with respect to the bilayer normal in coarse-grained (**27a)**) and united atom (**27b)**) simulation systems.*

Figure 28. *Density of backbone atoms of amino acid residues across the z axis for LpxR, with bilayer interfaces marked as thick black lines. On plots, black lines denote His, Tyr and Trp residues, red Phe residues.* ***28a)*** *LpxR in Ra LPS.* ***28b)*** *LpxR in DPPC.*

Figure 29a) *The initial configuration of LpxR, position restrained, with 100 DPC molecules surrounding. Water and ions removed for clarity.* ***29b)*** *Protein-micelle configurations, with four DPC molecules, water and ions removed for clarity.* ***29c)*** *Solvent accessible surface area of LpxR as shown by water molecules within 0.3 nm of the protein after 500 ns in DPC micelle environment.* ***29d)*** *As* ***c.*** *but after 500 ns in DPPC bilayer environment.*

Figure 30. *The minimum distance between H122 and E128 over the course of a representative 1 μs simulation of ligand-bound LpxR in Ra LPS at 323 K.*

Figure 31. *Specific residue movement and molecular coordination. In all images, the protein backbone is in yellow, protein residues have carbon in cyan, Re LPS has carbon in grey and cations are in purple.* ***31a)*** *and 3**1b)*** *Showing the snorkelling movement of K67 towards the 4’ phosphate moiety of the Re LPS substrate over the course of 1 μs simulation at 323 K, with distance between K67 amine moiety and 4’ phosphate moiety labelled. 3**1c)*** *The coordination of Ca^{2+} by LpxR residues D10 and T34, as well as water molecules and the Re LPS substrate. 3**1d)*** *Cation coordination in the LPS binding site by residues N9, D10, D11 and T34.*

Figure 32a) *A representation of the frequency of protein residue contacts with Ca*$^{2+}$ *over the course of a 1* μ*s ligand-bound LpxR simulation in Ra LPS at 323 K. Contact defined as an interatomic distance of* $\leq$*0.4 nm and colour scheme is BWR, with residues in red denoting those in most frequent contact with Ca*$^{2+}$*. Protein backbone is in blue and residues in contact with Ca*$^{2+}$ *are shown explicitly.* ***32b)*** *As* ***a*** *but calculating contacts between protein residues and the Mg*$^{2+}$ *counterions present in the system. Only residues in the protein binding site are shown explicitly and labelled.*

Figure 33. *The effect of point mutation of secondary conformation or cation coordination in ligand-bound LpxR systems after 1* μ*s in an Ra LPS membrane at 323 K.* ***33a)*** *The conformation of the* α *helix of loop L3, with residue A12 labelled.* ***33b)*** *Cation coordination in the LPS binding site after D10A mutation, with Ca*$^{2+}$ *in green and Mg*$^{2+}$ *in purple.* ***33c)*** *Cation coordination in the LPS binding site after D11A mutation, with Ca*$^{2+}$ *in green and Mg*$^{2+}$ *in purple.* ***33d)*** *Cation coordination in the LPS binding site after T34A mutation, with Ca*$^{2+}$ *in green and Mg*$^{2+}$ *in purple.*

Figure 34. *The catalytic hydrolysis of LPS by LpxR, as presented by Saunders et al. Reversed protonation of His122 is highlighted by red characters.*

Figure 35. *Showing the diffusion of the cleaved acyl tails of LPS from the binding site of LpxR to the inner leaflet over the course of 500 ns. Protein backbone is shown in blue, Ra LPS and inner leaflet phosphates in green and purple respectively, cleaved tail in yellow and Re LPS carbons in cyan. Ra LPS phosphates occluding view of the protein-lipid complex have been removed for clarity.*

Figure 36. *A comparison of the X-ray crystal symmetric dimers of LpxR and OmpLA, with protein backbones in purple and green, divalent cations in grey and other co-crystallised ligands coloured as the literature standard.* ***36a)*** *the LpxR X-ray structure (3FID), co-crystallised with Zn*$^{2+}$ *ions, glycerol and pentaethylene-glycol-monodecyl-ether.* ***36b)*** *the OmpLA X-ray structure (1QD6), co-crystallised with Ca2+ and 1-hexadecanosulfonic acid.*

***Figure 37a)** The minimum intermolecular distance between LpxR molecules in an Ra LPS membrane in coarse-grain simulations with two protein molecules present. **37b)** The distance between protein molecules when three copies were present. Black line shows distance between molecules a – b, red b – c, and green a – c.*

***Figure 38a)** The minimum intermolecular distance between LpxR molecules in DPPC membrane in coarse-grain simulations with two protein molecules present. **38b)** The distance between protein molecules when three copies were present. Black line shows distance between molecules a – b, red b – c, and green a – c.*

***Figure 39a)** Potential LpxR dimer conformation embedded in DPPC after 2 μs at 323 K. Protein backbones shown in purple and green, and DPPC coloured as literature standard. **39b)** as **a** but viewing the transmembrane segments of the two protein molecules, with DPPC molecules obstructing the view removed for clarity.*

***Figure 40a)** RMSD of two LpxR molecules embedded in DPPC over 2 μs at 323 K. Protein A (purple in **40c)**) barrel and loop L3 backbone are shown in black and green respectively, and protein B (green in **40d)**) barrel and loop L3 backbone are shown in red and blue respectively. **40b)** RMSF of two LpxR molecules embedded in DPPC over 2 μs at 323 K. Protein A (purple in **40c)**) backbone shown in black and protein B (green in **40c)**) backbone in red. **40c)** Showing the conformational arrangement of the binding site of protein A, with backbone in purple and key residues labelled. Residues 123-130 of loop L3 have been removed for clarity. **40d)** The conformational arrangement of the binding site of protein B, with backbone in green and key residues labelled. Again, residues 123-130 of loop L3 have been removed for clarity.*

***Figure 41.** Showing a potential dimer interface of two LpxR molecules after 2 μs at 323 K embedded in a DPPC membrane. **41a)** All residues of protein A (purple) within 0.35 nm of protein B (green) have carbons coloured in grey and residues for protein B have carbons coloured in cyan. All other elements are coloured at the literature standard. **41b)** Colouring as **a.** but showing electrostatic interactions between residues of loop L3 of the two LpxR molecules. **41c)** Colouring as previous, but showing*

*(**46b)**) and OANT (**46c)**) LPS-containing, asymmetric membrane systems. Inner and outer leaflet phosphates are annotated with IL and OL respectively.*

***Figure 47.** Interaction of MARTINI polarisable water with Re (**47a**), Ra (**47b**) and O-antigen (**47c**) type LPS chemotypes.*

***Figure 48.** Area per lipid (APL) profiles for LPS molecules in LPS-containing asymmetric membrane systems, with rolling average and standard error fitted **48a)**. APL for Re LPS in united-atom systems solvated with SPC water **48b).** APL for Re LPS in systems solvated with polarisable MARTINI water (red) and normal MARTINI water (green) **48c).** APL for Ra LPS in united-atom systems solvated with SPC water **48d).** APL for Ra LPS in systems solvated with polarisable MARTINI water (red) and normal MARTINI water (green).*

***Figure 49.** Effect of lipopolysaccharide deacylation on membrane topology and system density. Images i and ii show lipid phosphate beads at 0 μs and 20 μs respectively, with wildtype LPS phosphates blue, deacylated LPS phosphates red and inner leaflet phosphates grey, and iii shows the density of system components over 20 μs, averaged between three independent simulations. Here polarisable water is shown in black, and the phosphates of wildtype LPS, deacylated LPS and inner leaflet lipids are shown in blue, red and grey respectively. **49a)** shows the results of the REMP membrane condition. **49b)** the qDEMP membrane condition. **49c)** the hDEMPc membrane condition. **49d)** the tqDEMP membrane condition. **49e)** the DEMP membrane condition.*

***Figure 50.** The effect of Re LPS deacylation on wider membrane properties over entire 20 μs simulation timeframe. All plots show rolling average with standard error for block averages. Plots **a, b** and **c** coloured as REMP membrane black, qDEMP membrane red, hDEMPc membrane green, tqDEMP blue and DEMP membrane yellow. **50a)** membrane thickness. **50b)** average APL for LPS molecules in upper leaflet. **50c)** whole membrane area. **50d)** APL for inner leaflet phospholipids of REMP (black), hDEMPc (red) and hDEMPc* (green).*

Figure 51. Mean squared displacement for upper and lower leaflets over 20 μs simulations for each membrane condition. Wildtype Re LPS shown in black, deacylated Re LPS in red and inner leaflet phospholipids in green. **51a)** REMP membrane condition. **51b)** qDEMP membrane condition. **51c)** hDEMPc membrane condition. **51d)** tqDEMP membrane condition. **51e)** DEMP membrane condition. **51f)** tqDEMP membrane condition, showing MSD of just wildtype and deacylated LPS.

***Figure 52**. Effect of lipopolysaccharide deacylation on membrane curvature and system density. Images i and ii show lipid phosphate beads at 0 μs and 20 μs respectively. Image colouring is the same as **Figure 49**. **52a)** shows the results of the hDEMPa membrane condition and **52b)** the hDEMPb condition.*

***Figure 53.** Distribution of different lipid types in the xy plane from the hDEMPa membrane condition. **53a)** 2D heat-map representation mass density of deacylated Re LPS, **53b)** mass density of cardiolipin, **53c)** mass density of wildtype Re LPS and **53d)** showing the clustering of cardiolipin in the inner leaflet corresponding to patches of deacylated Re LPS in the outer leaflet, with wildtype LPS, deacylated LPS and cardiolipin coloured blue, red and green respectively. Image generated from system coordinates resulting after 20 μs simulation at 310 K.*

***Figure 54.** Distribution of different lipid types in the xy plane from the hDEMPb membrane condition. **54a)** 2D heat-map representation mass density of deacylated Re LPS, **54b)** mass density of cardiolipin, **54c)** mass density of wildtype Re LPS and **54d)** showing the clustering of cardiolipin in the inner leaflet corresponding to patches of deacylated Re LPS in the outer leaflet, with colours as in **Figure 53**. Image generated from system coordinates resulting after 20 μs simulation at 310 K.*

***Figure 55.** Correlation of mass density of deacylated Re LPS and cardiolipin in the xy plane in the hDEMPa* system with inner leaflet modified. **55a)** 2D heat-map representation mass density of deacylated Re LPS, **55b)** mass density of cardiolipin, **55c)** mass density of wildtype Re LPS. **55d)** periplasmic view of the membrane, showing cardiolipin clustering, with colours as in **Figure 53**. Image generated from system coordinates resulting after 5 μs simulation at 310 K.*

*channel opens up and membrane lipids rearrange to line the pore, with greater movement seen from inner leaflet phosphates **59d)** & **59h)** image of headgroups lining the newly formed pore. Carbon atoms of LPS molecules coloured cyan and phospholipids grey. Water omitted for clarity.*

Figure 60. *Electroporation of the Re LPS membrane with an OmpA monomer embedded with a 0.15 V/nm external electric field applied.* ***60a)*** *System at equilibrium. OmpA is coloured green; Re LPS coloured with sugars yellow, phosphates tan and acyl tails cyan; phospholipids coloured with amines blue, phosphates tan, glycerols silver, acyl tails grey and unsaturated segments purple.* ***60b)*** *Inner leaflet annular phospholipids rearrange such that headgroups are in the membrane core.* ***60c)*** *water (red) is able to flow freely through the phospholipid-lined membrane pore.*

Figure 61. *The location of pore formation relative to patches of deacylated Re LPS lipids in membranes with an external electric field of 0.3 V/nm applied. Location of pore formation in each of three repeats denoted by a black circle.* ***61a)*** *Pore location in hDEMPa* membrane condition.* ***61b)*** *Pore location in hDEMPb* membrane condition.*

Figure 62. *Electroporation of the Ra LPS asymmetric membrane at united-atom resolution (**a, b, c**) and coarse-grained resolution (**d, e, f**).* ***62a)*** *&* ***62d)*** *membrane at equilibrium, with water and phosphate beads shown. Inner and outer core LPS phosphates are shown in blue and green respectively, and inner leaflet phosphates in grey* ***62b)*** *&* ***62e)*** *movement of water into the hydrophobic core leads to a membrane defect* ***62c)*** *&* ***62f)*** *a water channel opens up and membrane lipids rearrange to line the pore, with greater movement seen from inner leaflet phosphates**.***

Figure 63. *Electroporation of the Ra LPS membrane with an OmpA monomer embedded with a 0.15 V/nm external electric field applied.* ***63a)*** *System at equilibrium. OmpA is coloured green; Ra LPS coloured with sugars yellow, phosphates tan and acyl tails cyan; phospholipids coloured with amines blue, phosphates tan, glycerols silver, acyl tails grey and unsaturated segments purple.* ***63b)*** *Inner leaflet annular phospholipids rearrange such that headgroups are in the membrane core.* ***63c)*** *water (red) is able to flow freely through the phospholipid-lined membrane pore.*

united-atom PMB1 molecule into the Ra LPS membrane. ***80b)*** *extent of penetration by a coarse-grained PMB1 molecule into the Ra LPS membrane.*

Figure 81. *Number of contacts between PMB1 and LPS segments at coarse-grained resolution. Contact is defined here as an intermolecular distance of ≤0.6 nm. Segments are coloured as follows: acyl tails black, lipid A red, inner core sugars green, outer core sugars blue, O-antigen sugars yellow. Contacts with LPS phosphates are on separate plots and coloured as follows: 1 and 4' phosphates of lipid A coloured black and red, and the 4 and 4' phosphates the outer core coloured green and blue.* ***81a)*** *PMB1 contacts with Re LPS segments.* ***81b)*** *PMB1 contacts with Re LPS phosphates.* ***81c)*** *PMB1 with Ra LPS segments membrane.* ***81d)*** *PMB1 contacts with Ra LPS phosphates.* ***81e)*** *PMB1 contacts with O-antigen LPS segments.* ***81f)*** *PMB1 contacts with O-antigen phosphates.*

Figure 82. *Penetration of PMB1 through LPS core and O-antigen sugars.* ***82a)*** *PMB1 penetration through Re LPS inner core sugars.* ***82b)*** *PMB1 penetration through Ra LPS core sugars.* ***82c)*** *PMB1 penetration through LPS O-antigen sugars.*

Figure 83. *Rolling average area per lipid with standard error fitted for coarse-grained resolution LPS membranes in the presence of PMB1, and z axis system densities showing membrane localisation of PMB1, with phosphates in black, PMB1 red and polarisable water green.* ***83a)*** *APL of Re (black), Ra (red) and O-antigen (green) LPS lipids in membrane. Data from systems with PMB1 present shown with solid lines and error bars, and data from membrane-only systems with dashed lines.* ***83b)*** *Re LPS with PMB1 system density.* ***83c)*** *Ra LPS with PMB1 system density.* ***83d)*** *O-antigen LPS with PMB1 system density.*

Figure 84. *The interaction of PMB1 with Re LPS.* ***84a)*** *number of contacts between PMB1 and Re LPS segments at coarse-grained resolution. Contact is defined here as an intermolecular distance of ≤0.6 nm. Segments are coloured as follows: acyl tails black, lipid A sugars red, inner core sugars green, 1 phosphate of primary GlcNAc blue and 4' of secondary GlcNAc yellow****. 84b)*** *image of PMB1 penetration through*

inner core sugars of annular LPS lipids. PMB1 in green, OmpA in blue and Re LPS in yellow (core sugars), tan (phosphates) and cyan (acyl tails).

Figure 85. *The interaction of PMB1 and the Re LPS membrane under an external electric field.* ***85a) & 85b)*** *Re LPS membrane electroporating in the presence of PMB1 under and electric field of strength 0.2 V/nm. System coloured as follows: PMB1 in green, POPE in grey, POPG in blue, cardiolipin in red, and Re LPS core sugars, acyl tails and phosphates in yellow, cyan and tan respectively.* ***85c)*** *number of contacts between PMB1 and Re LPS segments with a -0.1 V/nm electric field applied.* ***85d)*** *contacts between PMB1 and Re LPS segments with a -0.15 V/nm electric field applied.*

Figure 86. *System starting configuration before external electric field removed and subsequent number of contacts between PMB1 and Re LPS segments.* ***86a)*** *PMB1 in in the lumen of a Re LPS membrane pore. System coloured as follows: PMB1 in green, POPE in grey, POPG in blue, cardiolipin in red, phospholipid phosphates in purple and Re LPS core sugars, acyl tails and phosphates in yellow, cyan and tan respectively.* ***86b)*** *Contacts between PMB1 and Re LPS segments. Contact is defined as an intermolecular distance of ≤0.6 nm. Segments are coloured as in* ***Figure 85****.*

Figure 87a) *Number of contacts between PMB1 and Re LPS segments in system with OmpA embedded and external electric field applied. Contact is defined as an intermolecular distance of ≤0.6 nm. Segments are coloured as in* ***Figure 84****.* ***87b)*** *Two PMB1 molecules pass through a membrane pore formed by annular lipids. Image coloured as follows: OmpA in blue, PMB1 in green, POPE in grey, POPG in purple, cardiolipin in red and Re LPS core sugars, acyl tails and phosphates in yellow, cyan and tan respectively.*

Figure 88. *Ionic permeation of PMB1 through the Re LPS membrane model compartment. System colours as follows: POPE grey, POPG blue, cardiolipin red, PMB1 green, all phosphates purple, chloride ion orange, and Re LPS sugars and acyl tails yellow and cyan.* ***88a)*** *PMB1 in a transmembrane conformation, interacting with lipids of both bilayer leaflets.* ***88b)*** *a chloride ion passing through a transient membrane pore into the central compartment.* ***88c)*** *view of outer leaflet after pore*

interacting with LPS lipids lining the pore. ***92b)*** *two PMB1 molecules interacting with lipids of opposing leaflets after degradation of membrane pore.* ***92c)*** *view of inner leaflet of one membrane with four PMB1 molecules located in the area corresponding to deacylated Re LPS lipids in the opposing leaflet.* ***92d)*** *Representative system configuration after 5 μs.*

Figure 93. *Ionic permeation of PMB1 through the inner membrane model compartment. System colours as follows: PMB1 green, POPE grey, POPG blue, cardiolipin red.* ***93a)*** *open membrane pore.* ***93b)*** *PMB1 permeating membrane.* ***93c)*** *PMB1 molecules embedded in inner leaflet after pore degradation, showing transient association with PG and cardiolipin.* ***93d)*** *representative system configuration after 5 μs.*

Declaration of Authorship

I, Graham Michael Saunders, declare that this thesis and the work presented in it are my own and has been generated by me as the result of my own original research.

I confirm that:

1. This work was done wholly or mainly while in the candidature for a research degree at this University;
2. Where any part of this thesis has previously been submitted for a degree or any qualification at this University or any other institution, this has been clearly stated;
3. Where I have consulted the published work of others, this is always clearly attributed;
4. Where I have quoted work of others, the source is always given. With the exception of such quotations, this thesis is entirely my own work;
5. I have acknowledged all main sources of help;
6. Where the thesis is based on work done by myself jointly with others, I have made clear exactly what was done by others and what I have contributed myself;
7. Part of this work have been published as:

Saunders, G.M., Bruce Macdonald, H.E., Essex, J.W., Khalid, S. (2018). Prediction of the Closed Conformation and Insights into the Mechanism of Membrane Enzyme LpxR. *Biophys J*. 115 (8): 1445-1456.

Signed: ………………………………………………………………………………

Date: ………………………………………………………………………………

Acknowledgements

Firstly I would like to thank Prof. Syma Khalid for the insightful discussions, along with excellent subject knowledge and advice whenever needed. Your guidance has been invaluable throughout my PhD study, across all projects.

I would also like to recognise past and present members of the Khalid group, particularly Jon, Alister, Taylor, Firdaus and James, whose humorous and intellectual discussions helped support me during my studies. Discussions with Tom Piggot also proved incredibly useful in the understanding of key lipopolysaccharide behaviours.

I would like to thank my family for their incredible encouragement. I cannot express the extent of my gratitude, but your pride in my work frequently provided a source of motivation to continue. Daisy, your unwavering, unconditional support made this achievement possible.

Abbreviations

APL	area per lipid
CG	coarse-grained
COL	colistin
DAG	diacylglycerol
DPPC	dipalmitoylphosphatidylcholine
EM	energy minimisation
IM	inner membrane
LPS	lipopolysaccharide
LpxR	lipid A 3’ O-deacylase
LJ	Lennard-Jones
PBP1	penicillin binding protein 1
PE	phosphatidylethanolamine
PG	phosphatidylglycerol
PMB1	polymyxin B1
PME	particle mesh Ewald
POPE	palmitoyloleoylphosphatidylethanolamine
POPG	palmitoyloleoylphosphatidylglycerol
PS	phosphatidylserine
PVPE	palmitoylvaccenylphosphatidylethanolamine
PVPG	palmitoylvaccenylphosphatidylglycerol
MD	molecular dynamics
NAG	N-acetylglucosamine
NAM	N-acetylmuramic acid
OM	outer membrane
OMP	outer membrane protein
OmpA	outer membrane protein A
OmpLA	outer membrane phospholipase A
SASA	solvent accessible solvent area
UA	united-atom
VMD	visual molecular dynamics

Chapter 1: Introduction

In recent times, resistance to antibiotics and other antimicrobial treatments has become increasingly prevalent (1,2). It is imperative that the mechanisms via which resistance develops are understood if they are to be overcome by novel, more effective therapeutics. The more that is understood about bacteria, including their chemical makeup and behaviour in response to certain environments and stimuli, the easier it becomes to identify particular processes to target in order to stem bacterial proliferation.

1.1 The Bacterial Cell Envelope

One of the defining characteristics of nearly all classes of bacteria, is the presence of a layered cell wall, enveloping the cell, for the purpose of structural integrity(3). The cell wall in an additional barrier for these organisms, sequestering vital metabolites and excluding cytotoxic molecules, and is composed of a peptide and saccharide mesh as well as at least one lipid membrane. Due to its structural rigidity, the cell wall will even resist cellular lysis due to osmotic pressure (4). The cell wall is essential for cellular survival, and is not present in human or other animal cells; this makes it an excellent target for treatments in terms of selective toxicity. Indeed, many classes of antibiotics function through the disruption of cell wall synthesis but are harmless to human cells. For example, penicillins irreversibly inhibit penicillin binding protein 1 (PBP1), a transpeptidase responsible for cross-linking the sugar strands of peptidoglycan which has no homologue in human cells (5,6).

Bacteria are classified by the composition of their cell walls. Through the stepwise application of crystal violet dye, ethanol solution and safranin dye, bacteria within the culture with high and low concentrations of peptidoglycan will be stained purple and pink respectively (7). This is known as the Gram method and as such bacterial species with higher (50-90% of cell envelope) or lower (10% of cell envelope) concentrations of peptidoglycan are classified as Gram positive or Gram negative respectively. It is thought that Gram-negative bacteria do not retain the crystal violet dye due to the nature of their outer membrane and the relatively smaller concentration of peptidoglycan. The Gram method is not definitive for all bacterial species, as some classes fit into the Gram-variable or Gram-indeterminate groups due to their unpredictable response to the dyes (8).

1.2 Gram Positive and Gram Negative Bacteria

As mentioned, the major architectural difference between Gram-positive and Gram-negative bacterial cell wall lies in the prevalence of peptidoglycan. The Gram positive class of bacteria are enveloped by a cellular membrane and a ~25 nm coating of peptidoglycan; the peptidoglycan is associated to the cellular membrane through interactions with lipidated and non-lipidated teichoic acid molecules (9,10). The lipidated teichoic acid (lipoteichoic acid) residues sit within the cellular membrane, whereas teichoic acid residues may be covalently bound to the peptidoglycan. The teichoic acid molecules are a copolymer consisting of carbohydrate and glycerol phosphate residues and contribute up to 50% of the charged bulky mass of the Gram positive cell wall. Peptidoglycan, in both Gram positive and Gram negative, is a repeating polymer of N-acetylglucosamine (NAG) and N-acetylmuramic (NAM) acid sugars, crosslinked by a polypeptide (11).

Gram-negative bacteria have a much smaller (2-3 nm) volume of peptidoglycan between two membranes in an area termed the periplasmic space (3,12). The inner, cytoplasmic membrane is comprised of many of the same phospholipids (PLs) found in Gram-positive cytoplasmic membranes, whereas the outer membrane (OM) contains perhaps one of the most naturally complex lipids, lipopolysaccharide (LPS) (13,14). The distance between the peptidoglycan layer and both membranes is maintained by a series of covalent and non-covalent interactions, which will be discussed further in a subsequent section. The composition of “wildtype” LPS, which is found in the outer leaflet of the OM, varies between Gram-negative bacterial species. The formal charge of LPS molecules can be modified through the addition or removal of moieties to sugar groups, in response to perceived environmental dangers or other stimuli (15,16). LPS molecules often contain an O-antigen, consisting of repeating sugar residues; this segment is the antigenic determinant of the bacterium, and there are more than 20 known saccharide units which may appear within it in various arrangements. An illustration of the differences between the Gram-negative and Gram-positive cell envelopes can be seen in **Figure 1a** and **1b**.

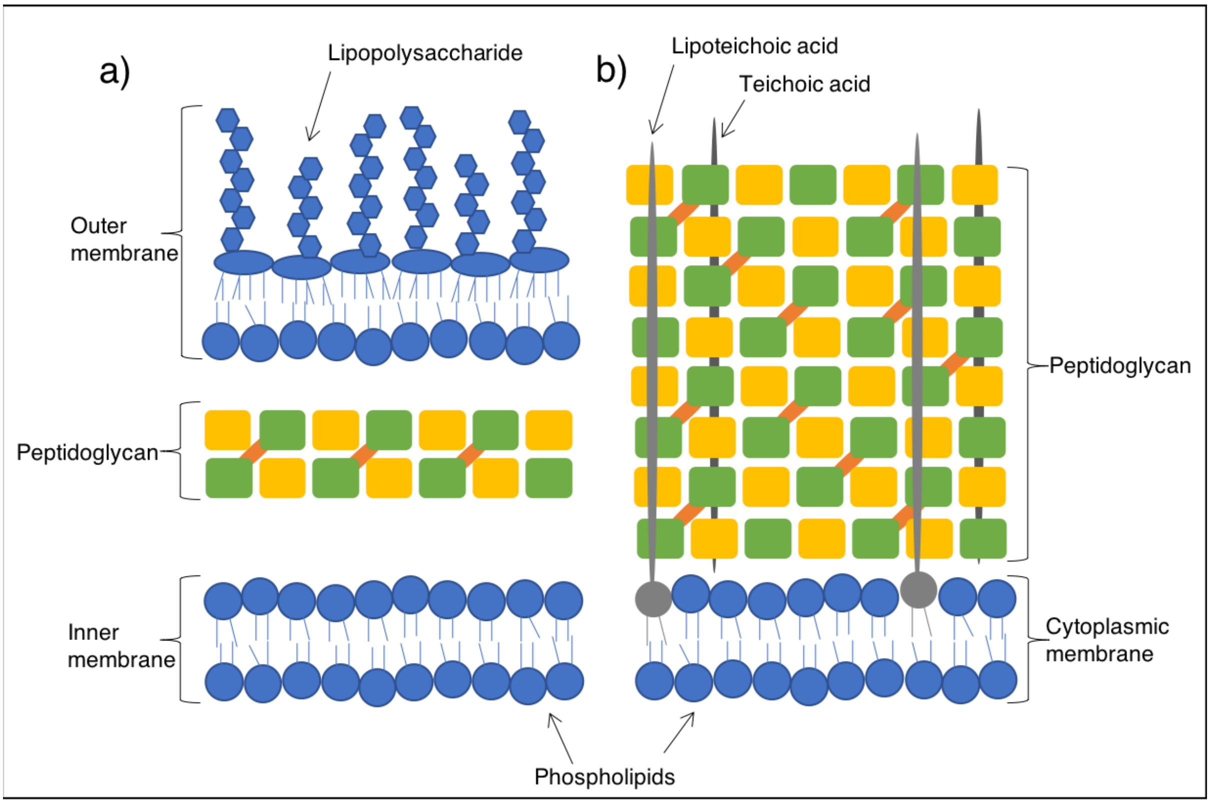

Figure 1. *The Gram-negative (**1a)**) and Gram-positive (**1b)**) cell envelopes, with molecule types annotated.*

This thesis endeavours to further understand the workings of the Gram-negative cell envelope, specifically focusing on the behaviour of certain outer membrane proteins (OMPs), as well as the dynamics of the OM itself.

1.3 The Inner Membrane

The defining feature of prokaryotic cells is the lack of nucleus (17). However, research in recent years has disputed the lack of compartmentalisation within bacteria; while no organelles as such have been identified, it is clear that some bacterial species possess the ability to sequester nutrients into distinct sections of the cell (18,19). Although prokaryotic cells may lack the specific organelles which provide the location of lipid biosynthesis, protein modification and energy production in eukaryotes, these functions are conserved in bacteria.

In Gram-negative bacterial species, proteins involved in energetic functions can often be found associated in or near the inner membrane (IM) (20–22). Transmembrane proteins typically have a hydrophobic section which interacts with the acyl tails of PLs, and charged or polar amino acid residues which sit outside of the hydrophobic membrane core and interact with PL headgroups; amino acid residues with aromatic side groups are often found in proteins such that they are able to interact with phosphate residues of neighbouring lipids. PLs directly interacting with membrane proteins are termed annular lipids.

The Gram-negative IM is similar to the majority of cytoplasmic membranes found in the cells of eukaryotic and prokaryotic species in its broad composition of PLs, transmembrane proteins and detergent molecules. The PLs in the IM of *Escherichia coli*, often the laboratory standard model, are typically phosphatidylethanolamine (PE), phosphatidylglycerol (PG), cardiolipin and phosphatidylserine (PS). Examples of these PLs can be seen in **Figures 2a** to **2d**. Cardiolipin, as shown in **Figure 2d** consists of two covalently linked PG lipids. Both the length of the PL acyl tails, as well as the saturation of these tails, can vary (23,24); the length of these tails is typically between 12 – 18 carbons, with palmitic (16:0), palmitoleic (16:1), heptadecanoic (17:0) and oleic (18:1) acids being the most common (13,25,26).

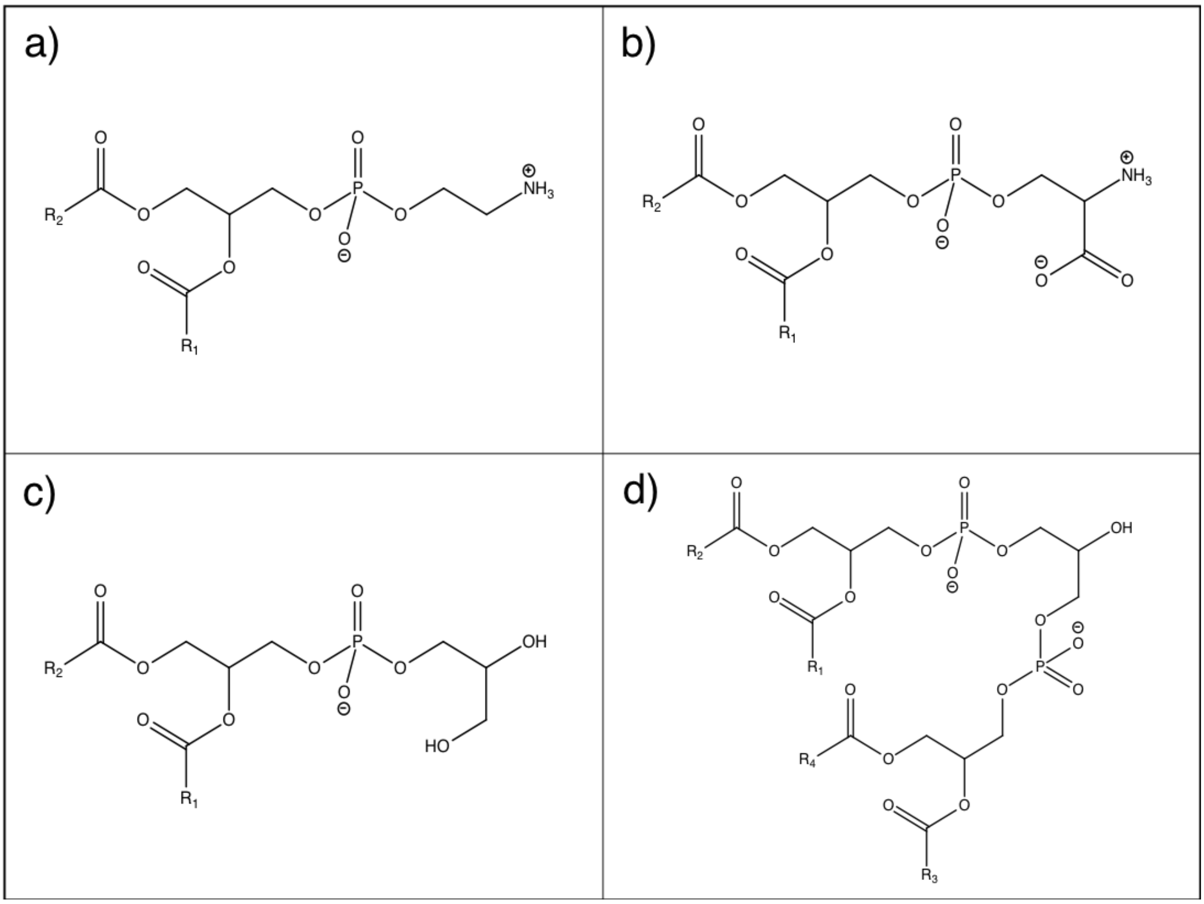

Figure 2. *The chemical composition of major phospholipid headgroup types of the Gram-negative inner membrane.* ***2a)*** *PE.* ***2b)*** *PS.* ***2c)*** *PG.* ***2d)*** *cardiolipin.* R_x *groups denote fatty acid chains conjugated to headgroups.*

PLs consist of hydrophobic fatty acid chains attached to polar, hydrophilic headgroups. The amphipathic nature of PLs produces the selective permeability of a membrane, which acts as a barrier to larger molecules but may allow certain smaller molecules and water through. To aid this function, a significant number of IM transmembrane proteins are pores or ion channels, assisting in the movement of small organic molecules and ions between the cytoplasm and the periplasmic space (27–29). The IM can contain sections of protein complexes which span the entire cell envelope, which may be involved in molecular secretion; for example, the AcrBZ subunit of the AcrABZ-TolC secretion complex is found in the IM. This complex is a multidrug efflux pump, implicated in both intrinsic and acquired drug resistance (30–32).

In Gram-negative bacteria, energy production is performed at the IM due to the lack of specific intracellular organelles. Similarly to the mitochondria of eukaryotic cells, the IM is used to maintain a proton gradient, or protonmotive force. This gradient is used to drive the ATP synthase, which produces adenosine triphosphate (ATP) (33). Any disruption to the IM can lead to the deterioration of vital proton and other ionic gradients, and can lead to cellular death. Antimicrobials such as the polymyxins disrupt the IM of Gram-negative bacteria, causing cell death. These molecules are the subject of further investigation in this thesis (34).

1.4 Peptidoglycan and the Periplasm

As mentioned, a peptidoglycan mesh lies between the IM and OM, and consists of a polysaccharide glycan strand cross-linked with a polypeptide chain (11,35). The repeating NAG and NAM sugars are linked by a β-1,4-glycosidic bond. Attached to the NAM sugar is a pentapeptide constructed of L-alanine, D-isoglutamate, meso-diaminopimelic acid and two D-alanine residues. A transpeptidase enzyme catalyses the cross-link between the penultimate residue, D-alanine, of one pentapeptide chain and the third residue, meso-diaminopimelic acid, of another; during this transpeptidation, the terminal D-alanine residue is cleaved from both pentapeptides (5).

It is currently thought that the frequency of cross-linking between glycan strands varies at ~50%, which suggests that there are pores in the peptidoglycan of variable sizes (36,37). As there are protein complexes known to span the entire cell envelope, it seems feasible that any pores or free space between glycan strands might be allocated to these trans-envelope proteins to facilitate their functions. Peptidoglycan is a bulky structure which envelopes the cytoplasm and IM, but cannot determine the overall structure of the organism without precise direction. This direction comes from MreB, a functional homologue of the eukaryotic protein actin. MreB is a scaffold protein, assisting in the width and shape determination of the rod-shaped *E. coli* (38,39). As such, strains with a defective or deleted *mreB* gene lose their rod shape and take on a spherical shape (40,41).

The periplasmic space is maintained through a series of both covalent and non-covalent interactions between the peptidoglycan and proteins associated with the inner or outer membranes. Braun’s lipoprotein (BLP) facilitates the attachment of peptidoglycan to the OM through a covalent bond at its C-terminal lysine residue to a meso-diaminopimelic acid residues in the peptide cross-link region of peptidoglycan (20,42). While one third of these lipoproteins are covalently linked to the peptidoglycan, two thirds also exist in a free form. BLP is transcribed from the *lpp* gene and is modified post-translation with the addition of a lipid moieties at its N-terminus. As well as this, the lipoprotein is able to trimerize. The lipid moieties of both monomer and trimer units are able to interact with the hydrophobic regions of lipids in the OM (43). It has been suggested that the free form of BLP may be surface-exposed, but this has not been proven conclusively (44). In Δ*lpp,* or in mutants without the ability to covalently link BLP to the peptidoglycan, the OM blebs and may dissociate from the cell envelope, making the organism hypersensitive to antimicrobial molecules .

As well as BLP, the outer membrane protein A (OmpA) has the ability to associate to the peptidoglycan (45). OmpA consists of an N-terminal transmembrane domain, with extracellular loops, and a flexible C-terminal linker region which contains a peptidoglycan-binding domain. OmpA is able to dimerize in the OM, and both monomeric and dimeric forms of the protein have been observed to associate with peptidoglycan in molecular dynamics simulations (43,46,47).

Recent molecular dynamics studies have shown that IM protein TolR interacts with the peptidoglycan via a periplasmic linker region, which extends through the periplasmic space (48). As well as the interaction between TolR and peptidoglycan, the periplasmic space by cell envelope-spanning complexes such as AcrABZ-TolC. Protein complexes such as AcrABZ-TolC act as efflux pumps, and are one of several mechanisms of antimicrobial resistance developed by certain prokaryotic organisms. **Figure 3** shows the covalent and non-covalent interactions between proteins in the OM and IM, necessary for maintaining the width of the periplasmic space.

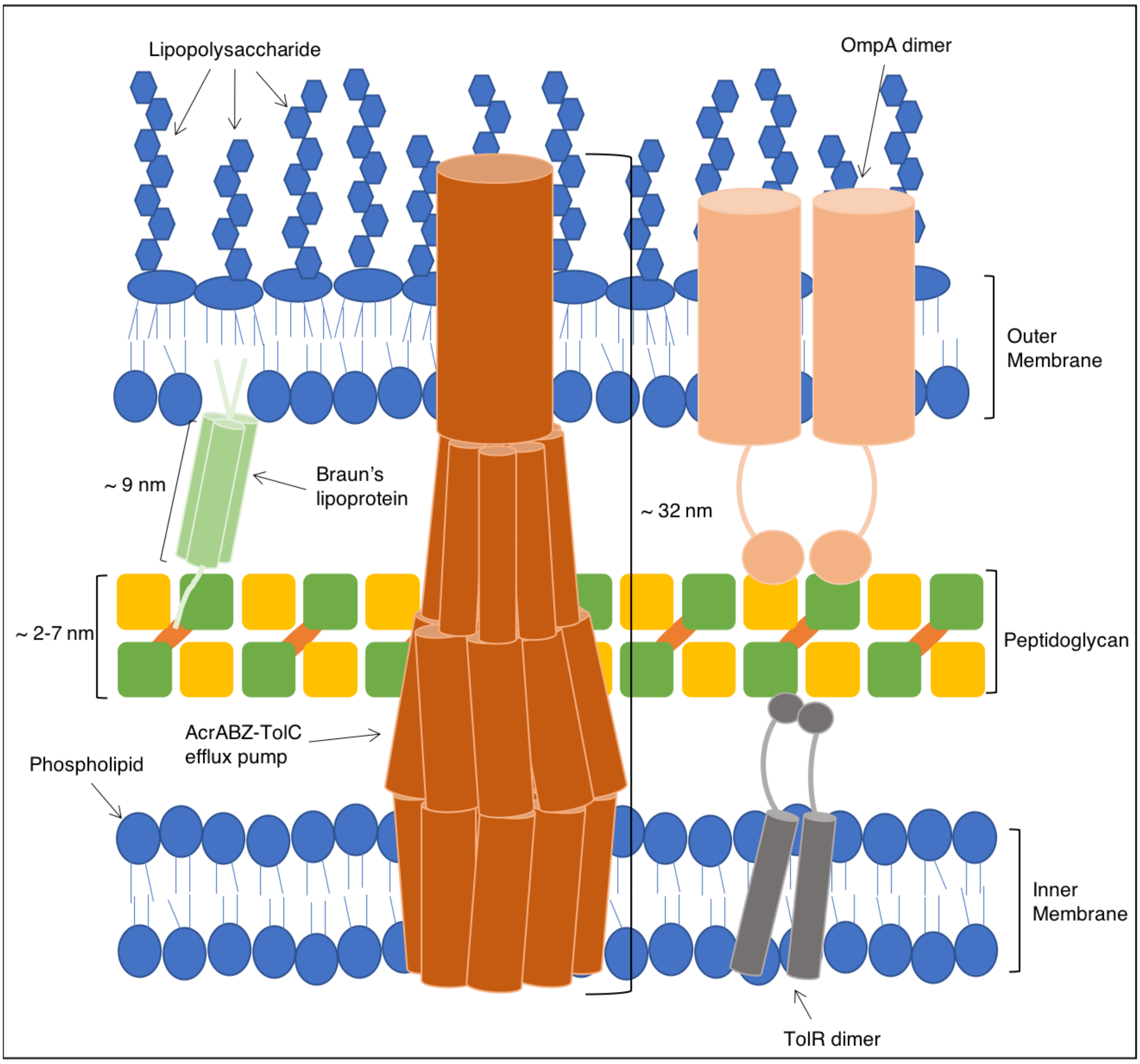

Figure 3. *The role of covalent and non-covalent interactions between membrane proteins and the peptidoglycan in maintaining the periplasmic space in the cell envelope.*

1.4 The Outer Membrane

The OM is asymmetric and each leaflet is composed of vastly different lipids. The composition of the inner leaflet is largely similar to that of the IM, a mixture of PLs. The outer leaflet, as previously mentioned, contains the most complex naturally occurring lipid, LPS. LPS is often discussed in terms of its constituent parts, namely the lipid A segment, the core sugar region and the O-antigen. In the literature, the terms smooth, rough and deep-rough are used to describe LPS. These refer to the complement of sugar residues attached the lipid A segment of the molecule. Each of the smooth, rough and deep-rough chemotypes of LPS can be found in vivo, at different points in an organism's lifecycle. The smooth LPS chemotype is a complete structure, with the O-antigen attached, whereas the rough chemotype is without the O-antigen, and the deep-rough chemotype without the O-antigen and outer core sugars. In this thesis, and often in the literature, *rough* and *deep-rough* LPS are referred to as Ra LPS and Re LPS. A representation of LPS, as well as further clarification of the nomenclature used in this thesis to discuss specific chemotypes of the molecule, can be seen in **Figures 4a** and **4b**.

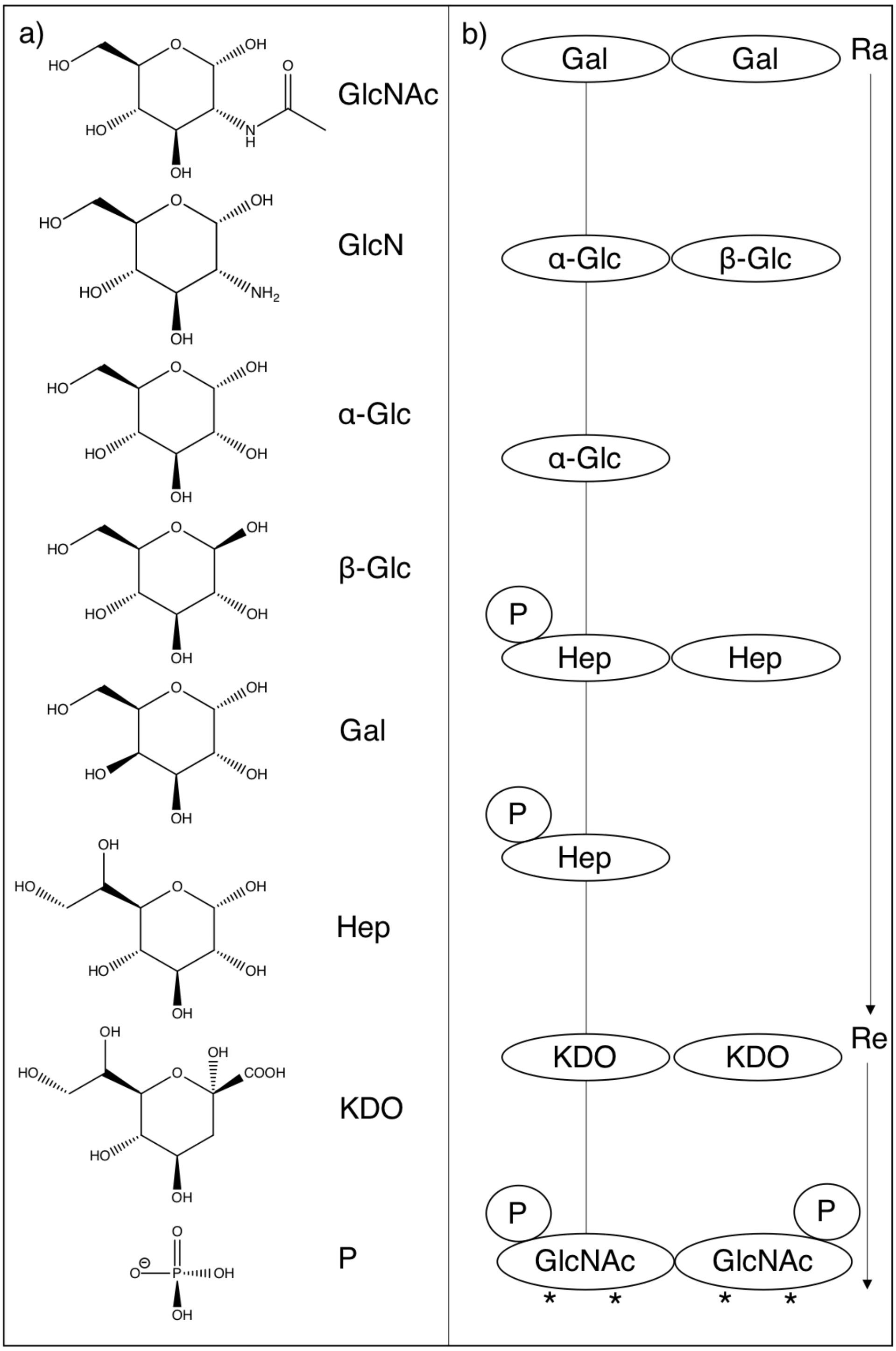

Figure 4. *The chemotypes of LPS.* ***4a)*** *Chemical formulae of sugar and phosphate moieties incorporated into E. coli LPS molecules. From top to bottom, sugar names are N-acetylglucosamine, glucosamine, α-glucose, β-glucose, galactose, heptose and 3-deoxy-D-manno-oct-2-ulosonic acid.* ***4b)*** *Sugar molecules in the lipid A and core segments of LPS molecules, with Ra and Re level annotated. Asterisks denote position of acyl tails on lipid A segment.*

The most common chemotype of in *E. coli* is a hexa-acylated molecule. The saccharide moieties of the lipid A and inner core segments are NAG and keto-deoxyoctulosonate (KDO) residues respectively, but the outer core sugars can vary between strains.

LPS molecules stabilise the structure of the OM through a network of electrostatic attractions between saccharide moieties. Further to this, cross-linking of neighbouring phosphate moieties by divalent cations allows LPS molecules to form a rigid mesh-like structure in the outer leaflet, denying or perturbing entry to the cell for larger molecules (49). While monovalent cations can replace divalent cations to neutralise the charges of LPS molecules, experimental evidence shows that this leads to greater permeability in the OM. Indeed, molecular dynamics simulations show that divalent cations induce closer and relatively more rigid packing of LPS core sugars compared with monovalent cations (50). An example of cross-linking of neighbouring LPS molecules by divalent cations can be seen in **Figure 5**.

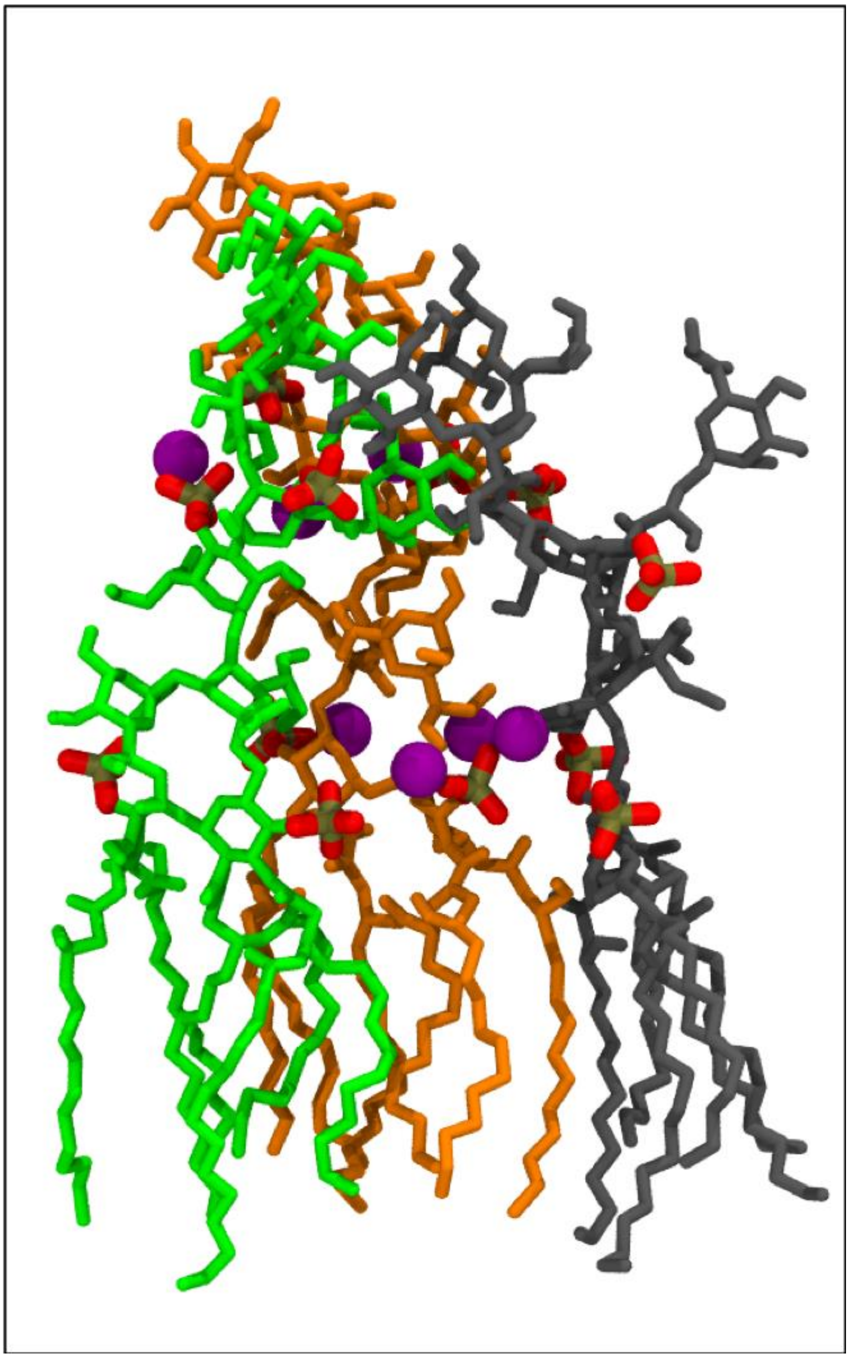

Figure 5. *Charged phosphate moieties sequester divalent cations for the purpose of cross-linking with neighbouring LPS molecules. LPS molecules in grey, orange and green, with phosphorous and oxygen atoms of phosphate moieties in tan and red respectively.* Mg^{2+} *ions in purple.*

The thick, negatively charged OM of Gram-negative bacteria affords the organism a great deal of protection from its local environment, it also provides a considerable challenge in terms of treating bacterial infections. With the prevalence of antibiotic bacterial strains known to be on the rise, the structure, dynamics and behaviour of the OM must be fully understood if we are to regain the upper hand which is being lost through the irresponsible application of antibiotics. Antimicrobial peptides such as the polymyxins target the OM and destroy Gram-negative bacteria through membrane disruption, entering cells through a self-promoted uptake mechanism (51). Further to this, a molecular dynamics study suggested that polymyxin B1 induces glass phase characteristics in LPS molecules in the OM and in fact has a localised ordering effect on the membrane (52). The mechanism of action of polymyxin antimicrobial peptides will be discussed further in a subsequent section of this introduction.

LPS is also known as the bacterial endotoxin, and it is the lipid A portion of the molecule which triggers an immune response in the host. Human leukocytes express the toll-like receptor 4 (TLR-4) on their cell surface along with MD-2, and it is the interaction between lipid A, TLR-4 and MD-2 which leads to the activation and subsequent propagation of an immune response (53). Aside from immune activation via TLR-4, LPS is also implicated in the activation of the complement system through both classical and alternative pathways (54). The end result of complement activation is the formation of the membrane attack complex (MAC), which penetrates the OM and leads to cellular opsonisation. With regard to the susceptibility of a bacterium to complement-mediated opsonisation, it appears that different chemotypes of LPS confer different levels of resistance to complement attack; in *Salmonella* species, a complete lack of O-antigen may result in total susceptibility to opsonisation, but an uncontrolled or bimodal O-antigen length may confer even greater resistance than uniform length (55,56).

LPS is biosynthesised in a multi-step process whilst being translocated to the outer leaflet of the OM. The lipid A and core saccharides are constructed and combined at the IM, and the O-antigen is attached in the periplasmic space between the two membranes. Finally, LPS is transferred to the outer leaflet of the OM by the Lpt complex; LPS insertion into the OM is carried out by the LptDE sub-complex (57). Further modifications to LPS in the OM may occur *in situ*, and these will be discussed further in a subsequent section.

1.5 Outer Membrane Proteins

Gram-negative OMPs are a major relay point of information between the bacterial interior and the extracellular environment. They are instrumental in cell-cell and cell-surface adhesion, as well communication between organisms within a bacterial colony (58–62). While the information relayed by OMPs may take the form of quorum sensing molecules, it can also be as simple as ion transfer across the membrane. Ultimately, the goal of many OMPs is to aid the OM in its function of selective ion and substrate uptake, as well as the efflux of cellular waste and other cytotoxic substances. OMPs are also the target of synthetic attack, as research concluded that membrane proteins make up the majority of all drug targets (63–65).

There are strong parallels between the OMPs of Gram-negative bacteria and those of the mitochondria found in eukaryotic cells, in that the vast majority take on the tertiary structure of a β barrel. In fact, Gram-negative OMPs are almost exclusively β barrels, bar a few α helical proteins involved in secretion; examples of these can be found in the Wza translocon, as well as a subsection of the type IV secretion complex (66–69). Membrane proteins broadly fall into one of two categories: integral and peripheral. Peripheral membrane proteins are found entirely outside of a membrane and interact with membrane lipids through van der Waals, ionic or hydrogen bonding interactions. In the case of peptidoglycan-bound BLP, it is the lipid tails of the protein which interact with membrane lipids, leaving the protein body outside of the membrane core and the C-terminal lysine covalently bound to peptidoglycan. In Gram-negative bacteria, peripheral membrane proteins may be required to interact with integral membrane proteins, as well as periplasmic proteins and those associated with the peptidoglycan, to participate in signal transduction. For example, autoinducer molecules activate the LuxPQ receptor, which transduces the signal by phosphorylating the downstream LuxU in the quorum sensing bacterium *Vibrio harveyi* (70).

Integral membrane proteins interact with both the headgroups and the acyl tails of membrane lipids and may have multiple transmembrane sections which contribute to the tertiary structure of the protein. OmpA, for example, is an eight-stranded integral protein with β barrel structure and interacts with the lipid headgroups of both leaflets of the OM, as well as the hydrophobic membrane core (46). Transmembrane β barrel proteins characteristically have outward-facing hydrophobic residues on the barrel segment which interact with the fatty acid tails of the surrounding annular lipids. Similarly, these proteins will have polar or charged residues at their water or phosphate headgroup interface. Another example of a transmembrane protein found in the OM is OmpLA, a phospholipase A1 enzyme with broad substrate specificity (71). OmpLA degrades PLs in the OM by Ca^{2+}-dependent hydrolysis, and this behaviour has been implicated in assisting bacteriocin release. The degradation of PLs by OmpLA results in a build-up of lysophospholipids and free fatty acids in the OM, which increases its permeability. This increased permeability aids bacteriocin secretion (72).

Typically, β barrel OMPs exhibit bands of aromatic amino acid residues corresponding with the positions of phosphate moieties of neighbouring membrane lipids (73,74). This is useful when predicting protein orientation and location from an X-ray structure. The distance between the two bands of aromatic residues often matches with the hydrophobic width of the β barrel of the protein, and it is the mismatch between the hydrophobic widths of the protein and the membrane which can lead to localised membrane disruption. An example of the bands of aromatic residues exhibited in OmpA can be seen in **Figure 6**; due to the thickness of the LPS leaflet of the OM, interactions are also observed between OMPs and LPS core sugars. Aromatic residues may also be in contact with LPS core sugars, some of which may be phosphorylated.

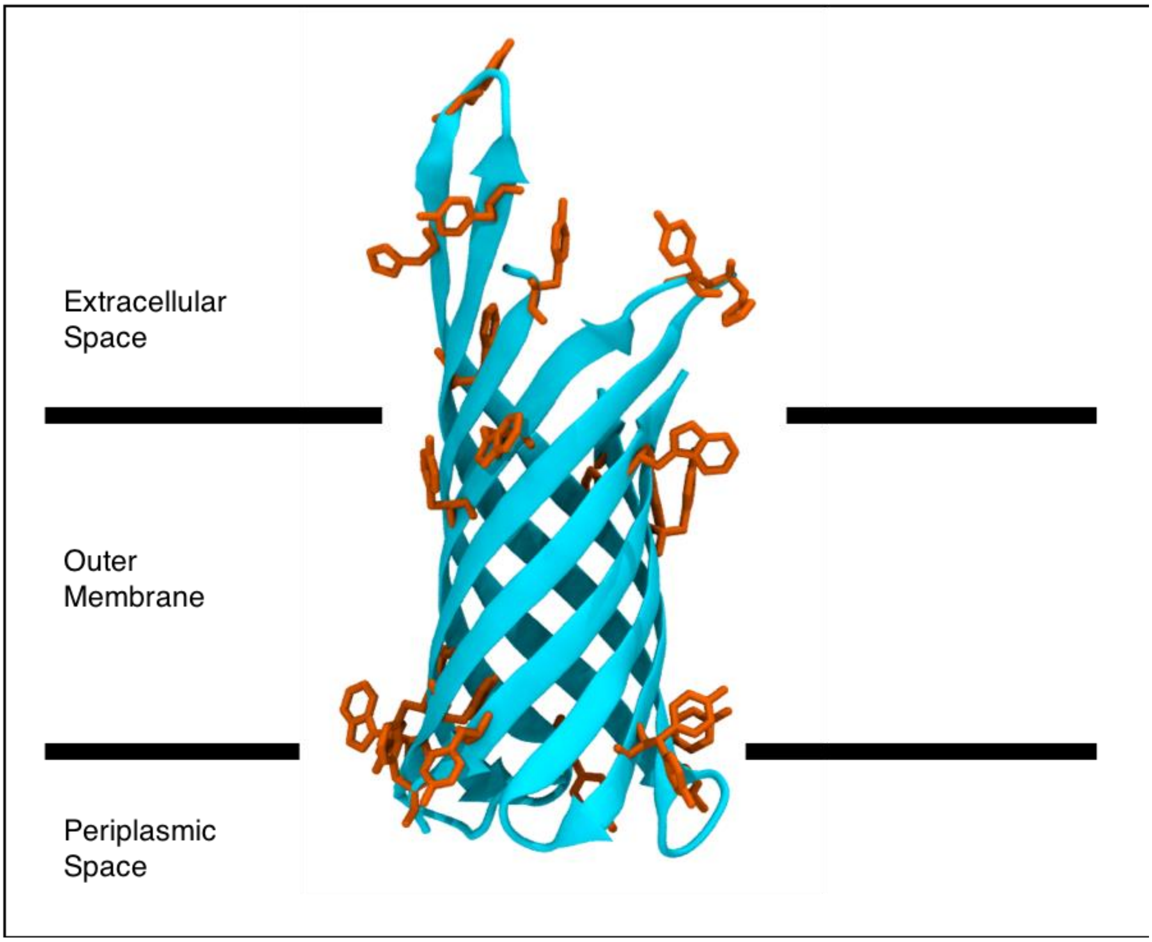

Figure 6. *Two bands of aromatic amino acid residues in OmpA correspond to membrane lipid phosphates in each leaflet of the OM. The positions of membrane phosphate headgroups are denoted by black lines.*

The ability of β barrel OMPs to occupy the transmembrane region of the OM is due to their tertiary structure. These proteins are translated in the cytoplasm and subsequently translocated to the OM. Insertion of these OMPs into the OM is thought to be assisted by the β-barrel assembly machinery (BAM) complex, one monomer of which is a β barrel protein itself (75). The BAM complex consists of five different proteins (BamA, -B, -C, -D and -E) and the subunits together exhibit scaffold and chaperone behaviour for other proteins. Protein precursors are delivered to the periplasmic side of the OM through the Sec translocon, which subsequently modifies the proteins to their active forms. The Bam complex is then thought to insert the protein into the OM, providing the scaffold for the protein to fold correctly. The proteins are then laterally ejected by the Bam complex into the OM and diffuse away.

1.6 Modifications to Lipopolysaccharide

Modifications to LPS can affect the capacity of the host immune system to identify a bacterium. Particularly with the lipid A portion of LPS, which is recognised by the TLR4-MD2 complex as a pathogen-associated molecular pattern, alterations such as the removal of acyl tails can significantly decrease the inflammatory response (53).

While LPS modifications do not appear necessary for cell growth, they do appear to be involved with the modulations of organism virulence. Additions of phosphate moieties, phosphoethanolamine (PEtN), 4-amino-4-deoxy-L-arabinose (Ara4N), or the hydroxylation, addition or removal of saturated or unsaturated acyl tails are all examples of LPS modifications exhibited in the OM of Gram-negative bacteria such as *E. coli* and *Salmonella typhimurium*. An illustration of the modifications made to LPS can be seen in **Figure 7**.

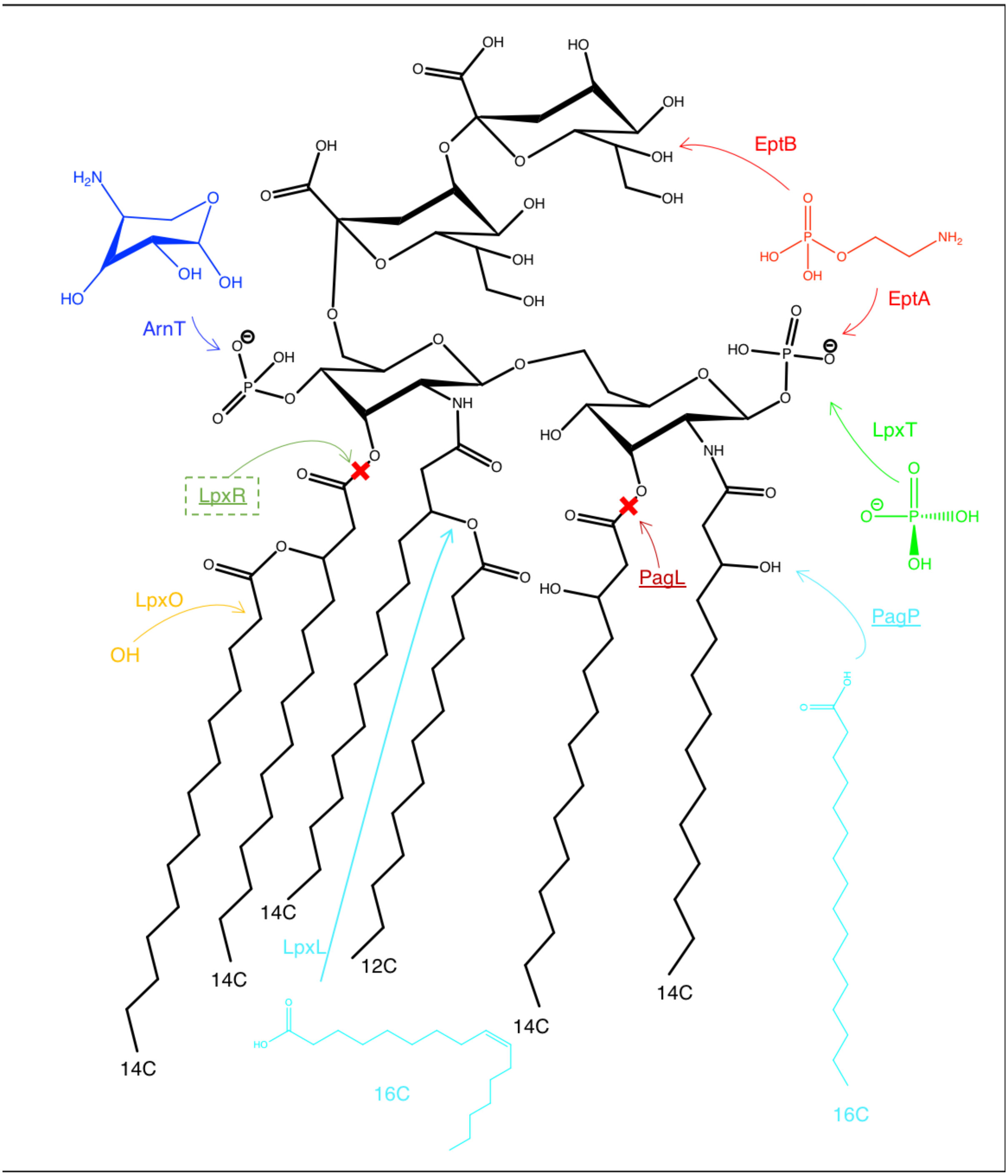

Figure 7. *Molecular modifications made to LPS in response to environmental stimuli. Moieties added or removed are highlighted and annotated with the relevant enzymatic machinery and colour-coded accordingly. Enzymes which modify LPS* *<u>in situ</u>*, *in the OM, are underlined.*

In *E. coli*, around one third of the LPS molecules have an additional phosphate added at the 1-phosphate position by LpxT in the IM. Here the phosphate group is transferred from an undecaprenyl diphosphate lipid. *E. coli* strains with 1-diphosphate moieties on the LPS show great susceptibility to polymyxins, it is logical that LpxT activity is typically observed to be downregulated, or even inhibited in polymyxin-resistant strains (76).

PEtN may be added to one or both phosphate moieties on the lipid A segment of LPS by IM protein EptA (77). While the primary target of EptA is the 1-phosphate of lipid A, PEtN can be added to the 4'-phosphate in the absence of Ara4N. Alternatively, PEtN may be attached to the KDO sugars of the inner core by IM protein EptB (78). The PEtN molecules used for LPS modification are donated by the surrounding PE PLs in the IM. In prokaryotes, PE lipids are synthesised through the decarboxylation of PS lipids.

Ara4N is added to the 4'-phosphate moiety of lipid A by IM protein ArnT (77). Unlike PEtN, which is present in PE lipids in the IM, Ara4N is synthesised in the cytoplasm and transferred to the IM but a number of Arn proteins. Ara4N is conjugated to undecaprenyl-phosphate before its transfer to Re LPS at the outer leaflet of the IM.

The fluidity of the hydrophobic membrane core affects membrane integrity, so modifications to this region are certain to influence membrane dynamics. A good example of this is observed with the addition of cholesterol or hopanoids to a membrane, which leads to decreased membrane fluidity and localised ordering of lipid acyl tails (79–82). Similarly, direct modifications to lipid acyl tails influence membrane properties. Modifications may be made in response to environmental stimuli; LpxO, for example, hydroxylates the secondary myristate tail attached via the 3' oxygen atom of lipid A in LPS in response to the presence of O_2 (83).

The addition of the monounsaturated palmitoleate to lipid IV_A by LpxP instead of the usual laurate by LpxL during LPS synthesis is observed in *E. coli* as a cold-shock response when the temperature of the organism drops below 12 °C (84). After this addition, LPS synthesis concludes with the addition of myristate, forming a final hexa-acylated LPS species with one unsaturated acyl tail, rather than the usual fully saturated species. The inclusion of this monounsaturated palmitoleate introduces greater steric hindrance between acyl tails in the membrane core, decreasing the ability of LPS to pack close together and decreasing the ordering of lipid acyl tails. This in turn assists the OM in remaining out of the gel or even solid phase at temperatures below 12 °C.

The LPS modification machinery mentioned in this subsection so far are all present and active at the IM, and act during LPS biosynthesis. However, there are membrane proteins which modify LPS once it has been translocated to the OM. These proteins are found as β barrel proteins situated in the OM.

PagP adds a secondary palmitoyl moiety to the 2-C myristate chain of lipid A, modifying the structure to a hepta-acylated LPS species (85). PagP activity confers resistance to β defensins, a class of antimicrobials produces by the human immune system, as well as antagonising the TLR4 pathway of pathogen detection. Conversely, PagL removes an acyl tail from the 3-O position of lipid A, leaving a penta-acylated LPS species (86). Decreased PagL activity is observed at temperatures below 15 °C, suggesting that removal of the 3-O acyl chain is not conducive to membrane fluidity in the same way as the incorporation of the unsaturated palmitoleate chain by LpxP. PagL activity is often observed in tandem with PagP, resulting in an isomeric hexa-acylated LPS species.

The lipid A 3’O-deacylase, LpxR, also removes an acyl moiety from lipid A, leaving a tetra-acylated LPS species (87). Similarly to PagP and PagL, LpxR is found in the OM as a β barrel protein and modifies the number of acyl tails attached to the glucosamine sugars. LpxR is the subject of further investigation in this thesis, and as such will be further described in the subsequent chapter: *Investigating the structure, function and interactions of the outer membrane protein lipid A 3’O-deacylase (LpxR) from Salmonella typhimurium, and the prediction of its closed conformation.*

1.7 Antimicrobial Peptides

Antimicrobial peptides (AMPs) are cytotoxic molecules consisting mostly of amino acid residues. The Gram-positive bacterial species *Paenibacillus polymyxa* produce polymyxins to destroy local Gram-negative bacterial communities which may be competing for resources. Polymyxins are cytotoxic due to the membrane permeablisation that the lipopeptides induce; they are also polycationic, which is thought to aid adsorption onto the predominantly negatively charged OM. The membrane permeablisation can lead to OM disintegration, which may in turn lead to the leakage of cellular contents (88). Once through the OM, polymyxins also cause the dissipation of any ionic and osmotic gradients across the inner membrane, thereby disrupting a number of vital cellular processes (89,90). In the literature, polymyxins are hypothesised to act through a self-promoted uptake mechanism (91), whereby the disruption of the OM by initial polymyxin molecules facilitates permeation of further polymyxin molecules. This mechanism will be discussed in greater detail in the relevant chapter.

Polymyxin B1 (PMB1) and polymyxin E1 (COL), also known as colistin, are highly similar polymyxin chemotypes. The only difference between the two is the inclusion of a leucine residue in COL rather than the phenylalanine in PMB1. The chemical structures of PMB1 and COL can be seen in **Figures 8a** and **8b**. Both PMB1 and COL consist of the same basic structure, with six L-α-γ-diaminobutyric acid (DAB) residues, along with two threonine and one leucine residues. One of the six DAB residues is cyclised, but the other five are all protonated, giving both PMB1 and COL a formal charge of +5 at physiological pH. Further to this, the seven carbonyl oxygen atoms present in the cyclic component of these lipopeptides will promote interaction with the divalent cations present at the OM (92).

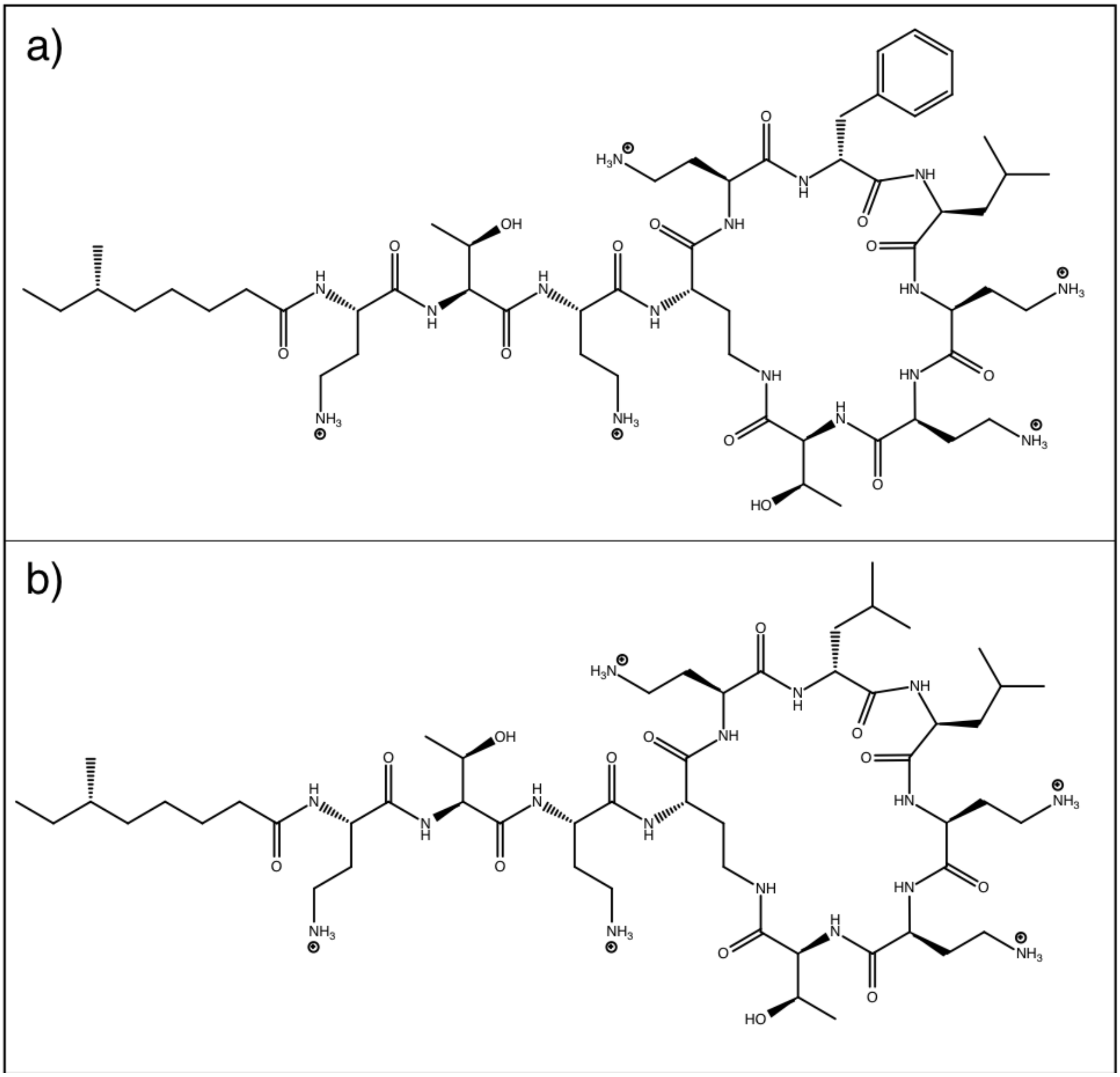

Figure 8. _Chemical structure of polymyxin B1 (**8a)**) and colistin (**8b)**)._

Polymyxins are in the class of non-ribosomal peptides as they are synthesized by non-ribosomal peptide synthetases, rather than ribosomes, in a process independent of messenger RNA. The process is highly specific, with each synthetase producing one chemotype of polymyxin. Polymyxins are used as a treatment of last resort in multidrug-resistant chronic bacterial infections in humans (34,93). Due to their cytotoxicity, polymyxins must be applied with care in order to minimise damage to host cells.

Gram-negative bacteria are able to resist the membrane permeabilising effects of the polymyxins through modifications to LPS, as mentioned previously in this chapter. Modification to LPS through the addition of PetN and Ara4N moieties to LPS is strongly linked to polymyxin resistance, as it is the introduction of amines in these moieties which is responsible for the disruption of polymyxin interactions with LPS. The presence of these groups also increases steric hindrance, physically obstructing polymyxin molecules from reaching the target phosphate moieties on the LPS. As the polymyxins are no longer able to interact with LPS phosphates, the AMPs cannot insert themselves into the OM in order to disrupt it (94). The specific interactions of PMB1 with the OM, as well as investigations into the permeation of the AMP through the cellular envelope will be discussed in greater depth in the subsequent chapter: *Investigating the permeation of polymyxin B1 through the inner and outer membranes of Escherichia coli.*

The research presented in this thesis begins with the investigation of the behaviour, structure and function of the OMP LpxR; the effect of the LPS modification by LpxR on the structure and dynamic properties of the OM are examined subsequently. Finally, the interactions between PMB1 and the OM are analysed, as well as the permeation of the AMP through two Gram-negative membranes.

Chapter 2: Methodology

2.1 Molecular Simulations

Molecular simulations are an application of theoretical chemistry. By categorising the behaviours of atoms and molecules with empirical and semi-empirical evidence, these behaviours can be reproduced *in silico* and the molecules can be observed in native, and perhaps novel environment models. This is particularly useful in the context of understanding biological environments, which are inherently dynamic. Molecular simulations can complement data gained through experimental techniques; for example, conformational flexibility is often a necessity in the cellular function of a protein, but an experimental technique such as X-ray crystallography may only provide evidence of one, static protein conformation. This could lead to inaccurate assumptions being made on the behaviour of the protein, but by employing molecular dynamics (MD) the researcher is able to gain a clearer picture of important conformational rearrangements. While certain nuclear magnetic resonance (NMR) techniques will also provide data on protein dynamics, the clear advantage of MD is that anyone with a desktop computer can perform basic simulations. The MD techniques employed in this thesis allow the observation of prokaryotic membrane systems on the microsecond timescale in order to ascertain both protein and lipid behaviours when placed in certain conditions. Molecular simulation techniques can also be applied in the design on novel drugs (95,96). By understanding the characteristics and dynamics of membrane proteins in particular, which make up the majority of all drug targets, researchers can tailor-make drug molecules and then test and refine their formulae *in silico* (63–65).

2.2 Classical Molecular Dynamics

In MD simulations, particle momenta and positions are solved using Newton's second law, shown in Equation 1, in which F is the force vector, m mass and a the acceleration vector.

$$\vec{F} = m\vec{a} \tag{1}$$

The selected force field contains descriptions of atomic interactions, which are used to calculate the negative gradient of the potential energy of the system. Calculated for every particle, this equates to the force exerted on the system (Equation 2).

$$\vec{F} = -\nabla E_{System} \tag{2}$$

The combination of Equations 1 and 2 with the acceleration of particles within the system shows how the change in particle position relates to its potential energy. This is shown in Equation 3, in which *a* is the acceleration vector, *v* is the velocity vector, *t* is the time interval for acceleration and *r* the particle position.

$$-\nabla E_{System} = m\vec{a} = m\frac{\delta \vec{v}}{\delta t} = m\frac{\delta^2 r}{\delta t^2} \tag{3}$$

Acceleration is applied to particles for a fixed time period, or timestep, by the selected integrator. This results in updated system coordinates, with updated potential energies. The repeated calculation of these equations enables the generation of a trajectory, which describes how the system changes over time.

2.3 Timestep

The timestep is the unit of time for which acceleration is applied to particles within the system. While a smaller timestep increases the computational cost of a simulation, a larger timestep introduces the risk of particles adopting energetically unfavourable configurations, resulting in an unstable system due to the high energies generated from Pauli repulsion. For the MD simulations presented in this thesis, timesteps of 2 fs, 10 fs or 20 fs were used; typically the highest timestep available for the chosen force field was used in order to maximise timescales. The timestep is chosen in order to observe the vibration within the system with the highest frequency. Covalent bonds involving hydrogen atoms have the highest vibrational frequency, and as such constraints such as the LINCS algorithm can be used to fix bond length to therefore increase the timestep (97).

2.4 Integrator

The force acting on a particle depends on the proximity and type of surrounding particles, as well as its own position. The consequence of this is a many-body problem due to the intricately coupled motions and complex dependencies of particles within the system. This issue is resolved through the estimation of particle position, velocity and acceleration in iterative steps based on a Taylor series expansion, which is used to solve the equations of motion for each timestep.

The Leap-frog integrator was used for all MD simulations within this thesis. This integrator uses Equations 4 and 5.

$$v\left(t+\frac{1}{2}\delta t\right)=v\left(t-\frac{1}{2}\delta t\right)+a(t)\delta t \tag{4}$$

$$r(t+\delta t)=r\ (t)+v\left(t+\frac{1}{2}\delta t\right)\delta t \tag{5}$$

The leap-frog integrator uses the position of a particle at time *t*, and its velocity at time $t-\frac{1}{2}\delta t$. Particle velocities and positions are calculated separately, at times *t* and $t+\frac{1}{2}\delta t$ respectively. Initial velocities are calculated using Equation 4, and initial positions with Equation 5. After initial calculations, the same timestep is used for subsequent calculation, which results in calculations with the timestep offset by $t+\frac{1}{2}\delta t$ between the two calculations.

2.5 Simulation Accuracy

The major limitation to MD methods is the trade-off between simulation accuracy and timescale. All-atom (AA) models provide details of interatomic interactions and can be considerably computationally expensive, which often results in reduced timescales. Conversely, coarse-grained (CG) models can facilitate longer timescales, but no longer show specific interatomic interactions. In AA models, each atom is a separate particle, whereas in CG models three or four atoms are grouped together into one particle or bead; the parameters of this bead represent its components in terms of mass, polarity and formal charge. There are four categories of bead in the MARTINI force field, including charged, polar, non-polar and apolar. These categories are further split into subtypes, giving a total of 20 different bead types (98). The united-atom (UA) model groups non-polar hydrogen atoms with their attached carbon, enabling a timestep of 2 fs to be used due to the removal of the rapid oscillations of C-H bonds. In the context of covalent bonds, oscillation refers to the rapid shortening and elongation of interatomic distance. Examples of Re LPS at different resolutions can be seen in **Figure 9**.

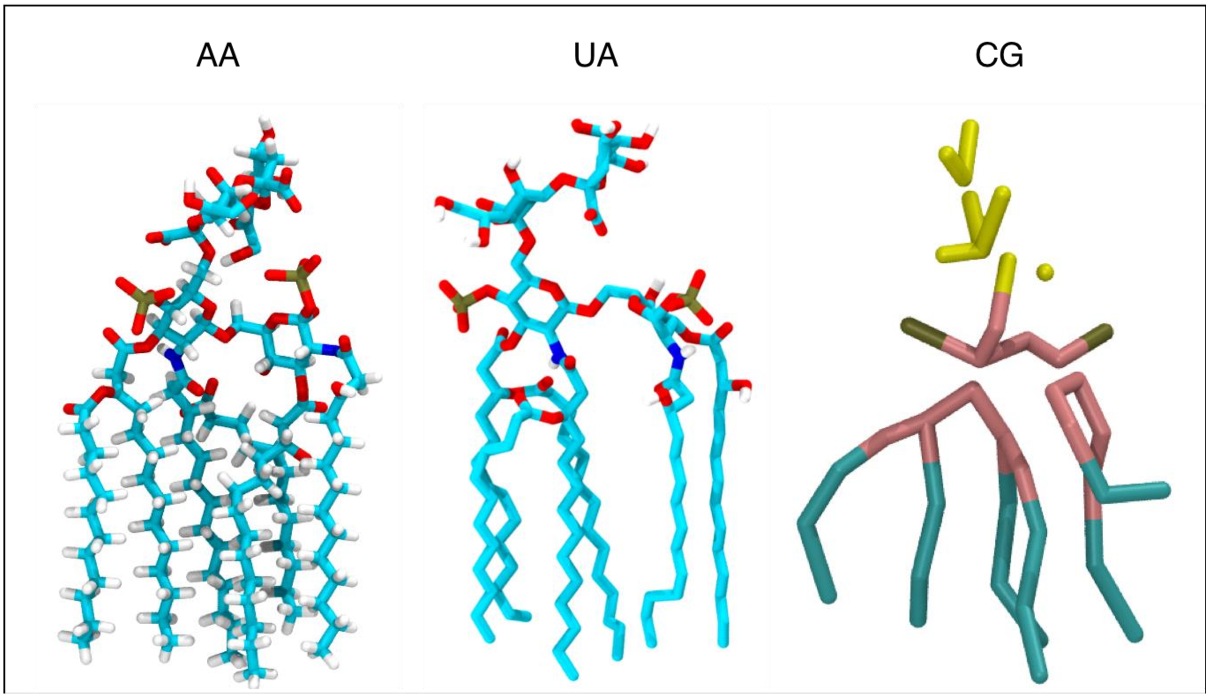

***Figure 9**. Re LPS at all-atom (AA), united-atom (UA) and coarse-grained (CG) resolutions.*

It is important to utilise each model in the most effective manner, even combining resolutions where necessary. For example, CG models can be implemented for unbiased orientation studies in the context of integral membrane proteins, or to observe protein or phospholipid clustering over longer time periods (99–101). These simulations can be followed up with UA or AA simulations to investigate specific protein-protein or protein-phospholipid interactions. Data at each resolution provide valuable clues to protein dynamics and behaviour.

2.6 Force Fields

The force field contains descriptions of how all bonded and non-bonded particles within a system interact with each other, and are used to calculate the potential energy of every particle within the system (Equation 6).

$$PE = \sum bonded + \sum non\text{-}bonded \tag{6}$$

Force fields are designed to be self-consistent, and as such parameters cannot be mixed and matched. One force field must be used in order to produce meaningful results. Some of the more popular force field sets are CHARMM, AMBER or, as employed in this thesis, GROMOS and MARTINI (98,102–104).

2.7 Bonded Interactions

The bonded term is the sum of all interactions between connected atoms within the system. This includes bond stretching and bond angle bending, as well as proper and improper dihedral potentials, as seen in Equation 7.

$$\sum bonded = \sum angles + \sum bonds + \sum proper\ dihedrals + \sum improper\ dihedrals \tag{7}$$

Bond angle bending represents the bending of a bond angle between three atoms and is represented by Equation 8, in which *k* is the spring constant, θ the displacement of the angle from equilibrium and θ_{eq} the bond angle at equilibrium.

$$PE = \frac{1}{2} k_{\theta} \left(\theta - \theta_{eq}\right)^2 \tag{8}$$

Bond stretching represents the oscillation of a bond and, similar to bond angle bending, is described by a harmonic potential (Equation 9), in which *b* is the displacement of bond length from equilibrium and b_{eq} is the bond length at equilibrium.

$$PE = \frac{1}{2}k_b\left(b - b_{eq}\right)^2 \tag{9}$$

Dihedral potentials concern groups of four atoms and are classed as either proper or improper. Proper dihedral potentials cover the rotation of atoms around a central bond, whereas improper dihedrals aim to prevent rotation around a central atom. Proper dihedrals allow for 360° rotation and are as such described using a cosine potential, as seen in Equation 10. The calculation of potential energy from proper dihedrals takes into account the number of minima and maxima, or periodicity, of the potential. Here *n* is the integer which determines the periodicity of the potential ϕ is the angle displacement from equilibrium and ϕ_{eq} the equilibrium angle.

$$PE = k(1 + \cos(n\phi - \phi_{eq})) \tag{10}$$

Improper dihedral potentials maintain the special configuration of a group of four bonded atoms. This is particularly useful with regards to planar aromatic rings, such as benzene, or chiral centres, as found in amino acids. These are described with a harmonic potential (Equation 11). Here ϕ is the displacement of angle from equilibrium and ϕ_{eq} the equilibrium angle.

$$PE = \frac{1}{2}k\left(\phi - \phi_{eq}\right)^2 \tag{11}$$

Representations of the discussed potentials, along with appropriate plots detailing potential energy with respect to the potentials can be seen in **Figures 10a** to **10d**.

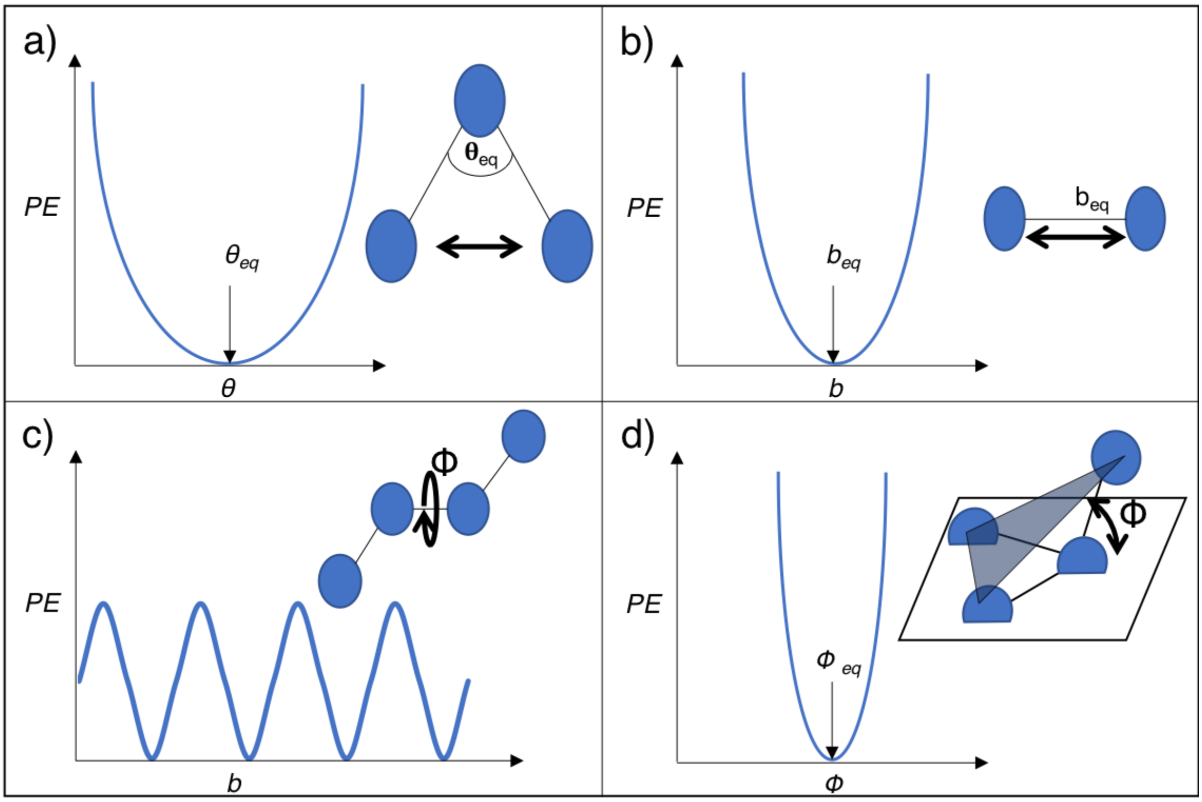

Figure 10. *Representations of the potentials employed in MD simulations to replicate observed properties, along with potential energy plots. Blue spheres represent atoms and black lines between them bonds.* ***10a)*** *bond angle bending.* ***10b)*** *bond stretching.* ***10c)*** *a proper dihedral. PE is zero at ϕ_{eq}.* ***10d)*** *an improper dihedral. Planes are represented here by a white parallelogram and transparent grey triangle.*

2.8 Non-Bonded Interactions

The non-bonded term is the sum of all interactions in the system which are not covalently linked, or described by the bonded term. As such, this term is more computationally expensive during calculations. The non-bonded term can be described as in Equation 12.

$$\sum non\text{-}bonded = \sum van\ der\ Waals + \sum electrostatic \tag{12}$$

All van der Waals interactions are calculated using the Lennard-Jones potential, which models short-range repulsion and longer-range attraction between particles as seen in Equation 13. Here V_{LJ} is the Lennard-Jones potential, σ_{ij} is the distance of zero potential between two particles, r_{ij} the distance between the two, and ε the minimum of interatomic potential energy.

$$V_{LJ} = 4\varepsilon\left(\left(\frac{\sigma_{ij}}{r_{ij}}\right)^{12} - \left(\frac{\sigma_{ij}}{r_{ij}}\right)^{6}\right) \tag{13}$$

In Equation 13, the interatomic potential energy approaches infinity as interatomic distance nears zero. This is due to Pauli repulsion preventing the overlap of electron dense regions surrounding the atoms. Due to the exclusion principle, more than one electron cannot occupy the same orbital, so atoms moving towards each other incur an energy penalty and are forced apart, as described in the 12th order term. The 6th order term describes the instantaneous dipole interactions. A graphic representation of the Lennard-Jones potential can be seen in **Figure 11**.

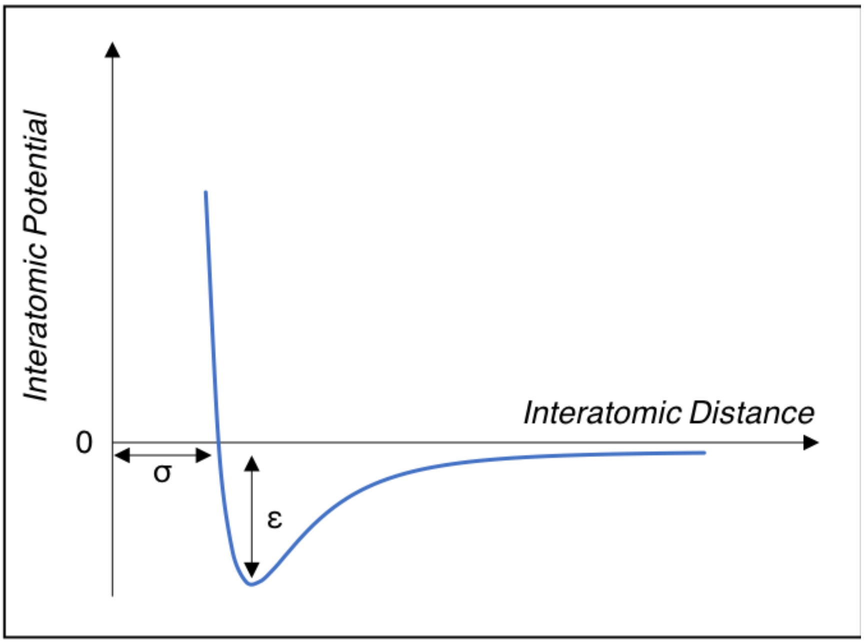

Figure 11. *The Lennard-Jones potential. A greater* ε *value indicates a greater strength of attraction between the two particles, and the* σ *indicates the minimum achievable interatomic distance between two particles.*

Both ε and σ are relative to the type of particle involved in the interaction. To calculate the $PE_{non\text{-}bonded}$ of two dissimilar atoms, the Lorentz-Berthelot mixing rules can be used. The Lorentz and Berthelot rules can be seen in Equations 14 and 15 respectively. The Lorentz mixing rule is used to find the distance of zero interatomic potential for particles *i* and *j*, and the Berthelot mixing rule is used to find the minimum value of interatomic potential energy between particles *i* and *j*.

$$\sigma_{ij} = \frac{\sigma_{ii}+\sigma_{jj}}{2} \tag{14}$$

$$\varepsilon_{ij} = \sqrt{\varepsilon_{ii}\varepsilon_{jj}} \tag{15}$$

Tabulated values for ε and σ are used to derive the appropriate values to calculate V_{LJ} for each van der Waals interaction .

Coulombic interactions are those observed between particles with non-zero charge and are calculated using Coulomb's law, Equation 16. Here $V_{electrostatic}$ is the electrostatic potential, q_i and q_j the charge of particles *i* and *j* respectively, ε_0 the permittivity of free space and r_{ij} the distance between the two particles.

$$V_{electrostatic} = \frac{q_i q_j}{4\pi\varepsilon_0 r_{ij}} \tag{16}$$

Particle interactions are selected from the neighbour list, which identifies all particles within a certain range, or cut-off. This neighbour list is updated every 5-10 timesteps. The cut-off used will depend on the selected force field. For example, the gromos54a7 force field, used for UA simulations in this thesis, requires a cut-off of 1.4 nm as the V_{LJ} and forces are almost zero beyond 1.4 nm (105,106). The use of cut-offs is a method of reducing the computational cost of simulations.

When calculating electrostatic interactions, there is typically a short-range cut-off, after which interactions are treated differently. In simulations presented in this thesis, long-range interactions are calculated using the particle-mesh Ewald (PME) summation method, which implements Fourier transforms of the potential and charge density(107); a fast Fourier transform is used to evaluate the Fourier transform of charge density on a discrete lattice in space. Using PME, the sum of interactions is split into two parts. The short-range term is calculated directly from the interactions between particles, whereas the long-range term is calculated using the Fourier transform method previously mentioned. This method enables rapid convergence of energies compared with the direct summation method.

2.9 Periodic Boundary Conditions

To prevent particles at the edge of a simulation box approaching vacuum conditions, periodic boundary conditions are used. Particles within the simulation box are surrounded by translated copies of themselves in each dimension in order to imitate an infinite system. However, the number of particles within the system remains constant, as if a particle travels across the periodic boundary in one dimension, it appears back in the box at the opposite side. Simulation boxes can take the form of any three dimensional shape, as long as it can be tessellated. An example of a system with periodic boundaries, along with a particle crossing a boundary, can be seen in **Figure 12**.

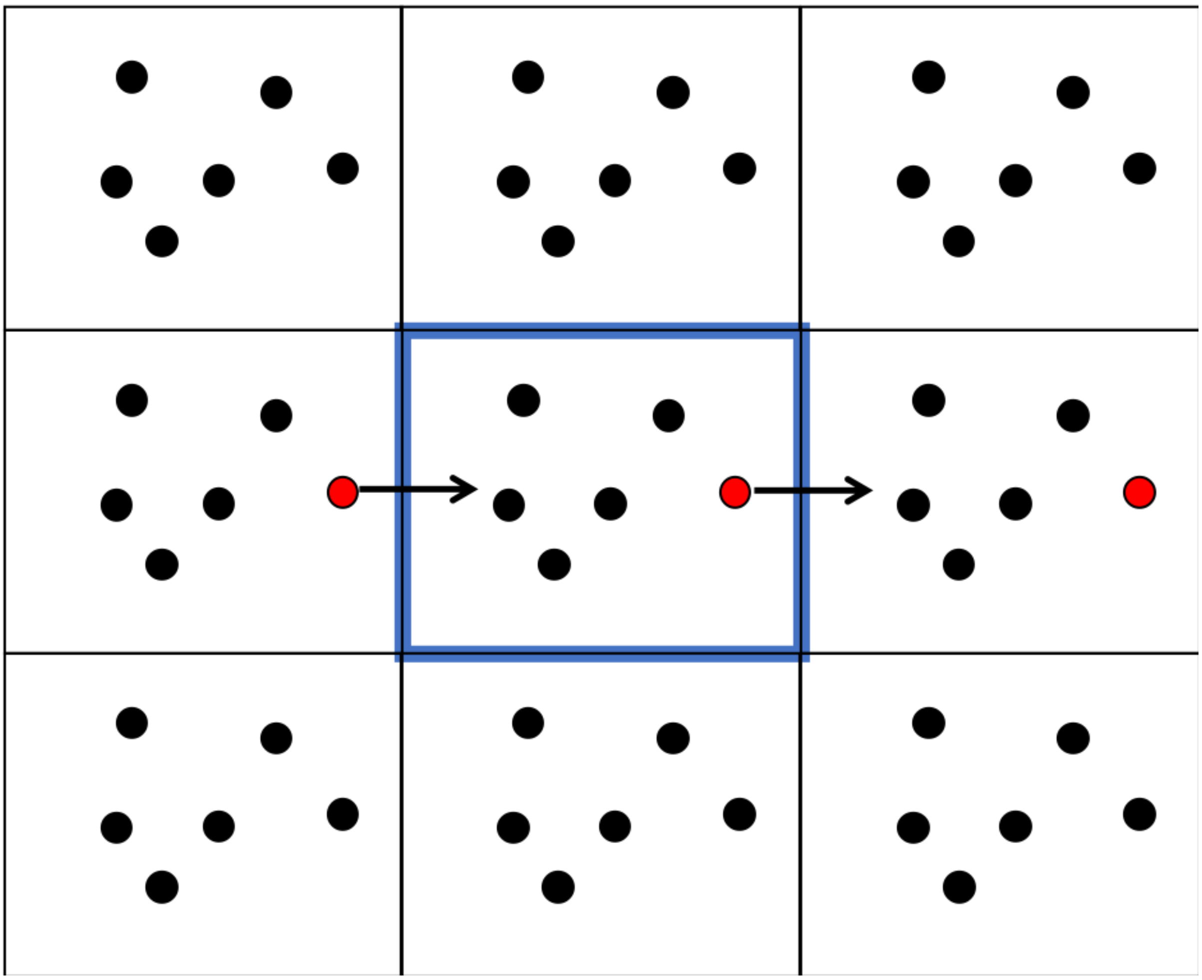

Figure 12. *Periodic boundary conditions prevent vacuum-like conditions. Arrows show movement of particle across periodic boundary causing it to appear on the other side of the simulation box (highlighted in blue).*

2.10 Energy Minimisation

Energy minimisation (EM) must be performed on system coordinates before simulations can be run. This is the process of moving particles within the system into a configuration with lower total potential energy. EM is performed in order to remove steric clashes between particles and bring the system to a local energy minimum. Systems presented in this thesis were minimised using the steepest descent gradient, which is a first derivative method which moves the system configuration orthogonally to the previous step.

2.11 Thermodynamic Ensembles

Simulations are performed in thermodynamic ensembles, the most common of which are microcanonical, canonical and isothermic-isobaric. The ensemble chosen denotes which variables within the simulation are kept constant; in NVE, NVT and NPT, which are microcanonical, canonical and isothermic-isobaric ensembles respectively, the variables are the number of particles (N), simulation box volume (V), total system energy (E), system temperature (T) and system pressure (P). In this thesis, the NVT and NPT ensembles were used to equilibrate simulation system properties, and the NPT ensemble was used to produce trajectories to analyse.

2.12 Temperature and Pressure

The temperature of simulation systems is controlled by a thermostat which modifies particle velocities. The relationship between system temperature and particle velocity is described in Equations 17 and 18. In Equation 17, E_k is kinetic energy, and in Equation 18, k_B and T are the Boltzmann constant and system temperature respectively.

$$E_k = \frac{1}{2}mv^2 \tag{17}$$

$$\bar{E}_k = \frac{3}{2}k_B T \tag{18}$$

For temperature control, a Boltzmann distribution is taken to assign velocities to individual atoms at the beginning of a simulation and the “temperature” is maintained by a thermostat such as the Nosé-Hoover, Berendsen or velocity-rescaling (V-rescale) thermostats (108–111). Thermostats scale the velocity of particles within the simulation system to keep them in line with the Boltzmann distribution. The barostat alters the simulation box vectors over the course of a simulation, and monitors system pressure by altering system volume.

The pressure of simulation systems is controlled by a barostat which modifies box size. The relationship between box size and system pressure is describe by Boyle’s law (Equation 19). Here *V* is system volume, k_{VT} is a constant value representative of the system temperature and volume, and *P* is the system pressure.

$$V = \frac{k_{VT}}{P} \tag{19}$$

2.13 Non-Equilibrium Molecular Dynamics

As simulations are often designed in order to observe a particular phenomenon, care must be taken to ensure that data gathered are accurate and not an artefact of a poorly equilibrated system. For example, if conformational stability of a membrane protein in a membrane environment is investigated, but membrane lipids are not given an opportunity to relax around the protein after its insertion, then any conformational flexibility observed may be a result of a poorly equilibrated system. To avoid this problem, position restraints may be placed on molecules within a system to allow other particles, such as water, ions or lipids, to relax into more favourable positions around the restrained molecule. Position restraints are potentials added to particles, so the particles incur an energy penalty if they move from their position. Alternatively, distance restraints may be used to tether molecules a certain distance from each other, but not necessarily in place. After appropriate equilibration, these restraints are typically removed. The timescale required for equilibration will depend on system constituents. For example, upwards of 10 μs equilibration time may be required for convergence of CG LPS membrane properties (31,112).

Another benefit of performing theoretical experiments such as those using MD is that creating unusual environments for molecules within a system becomes much easier. For example, to generate an electric field to study its effect on a cellular membrane *in vivo*, specialist equipment is required. This is made much easier in software such as GROMACS (113), which allows the application of an electric field across a simulation box with the addition of one line to the input parameters. An electric field of varying strength was applied to simulation systems in this thesis. In GROMACS version 2016.3, the version used to apply an electric field in this thesis, the electric field is applied uniformly across the simulation box at a set polarity and strength (114); the field acts as a vector force only upon charged particles, and causes acceleration of particles in a direction according to their charge and the polarity of the field in the dimension applied, as can be seen demonstrated in **Figure 13**.

Experimental electroporation protocols typically involve voltages in the kV range, over a distance of 1–2 mm, with the pulse lasting ~1 ms (115,116). In order to observe the electroporation mechanism in molecular dynamics, an increased electric field is employed.

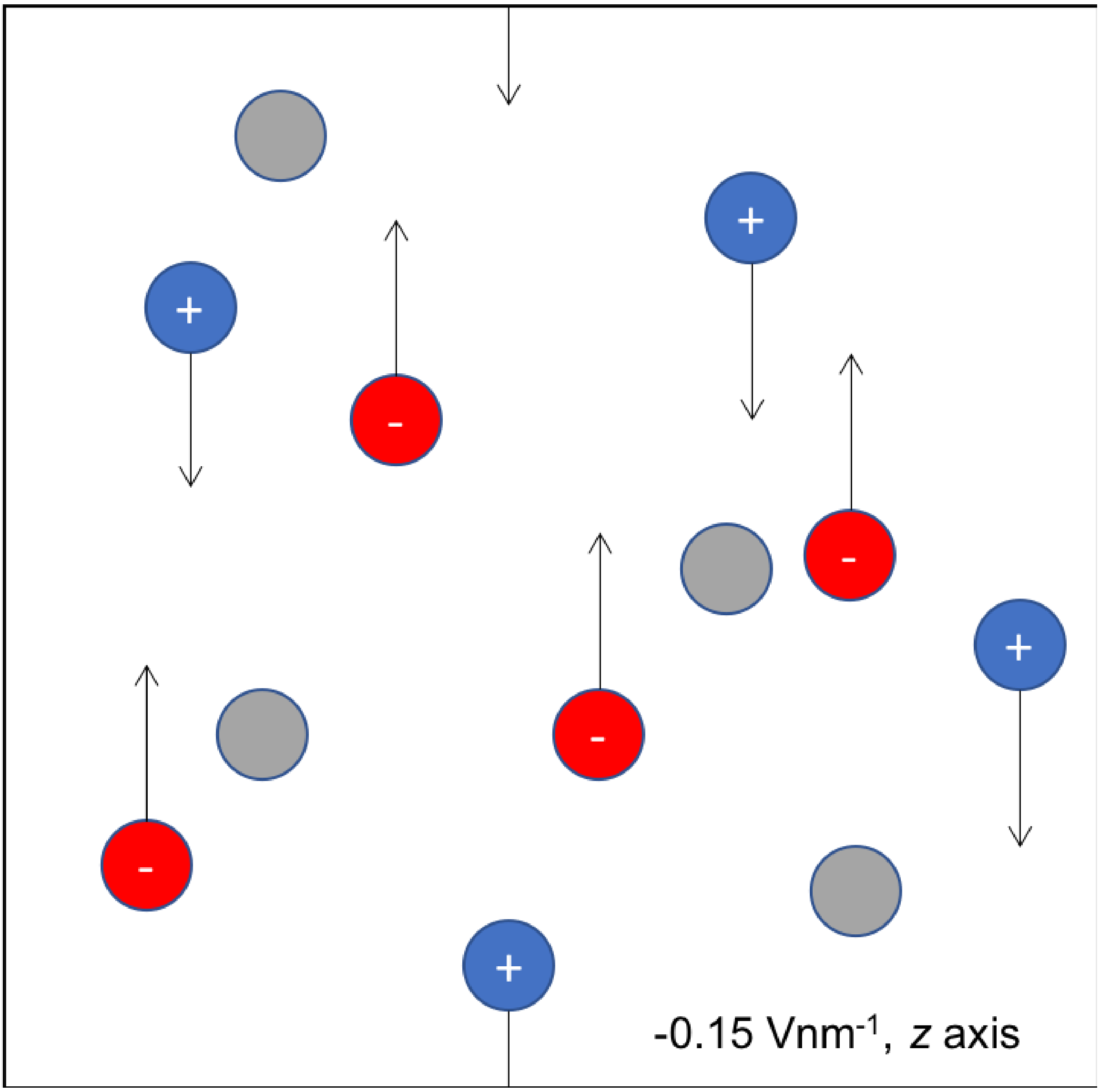

Figure 13. *The movement of charged particles in a simulation box with an electric field applied across the z axis. Acceleration of charged particles is proportional to the electric field strength applied. Positively charged, negatively charged and neutral particles are coloured blue, red and grey respectively.*

2.14 Water Models

Water is the most important solvent in terms of biology. Due to this, it is of vital importance that an appropriate model is used to represent water molecules in computational work. In this thesis, the atomistic simple point charge (SPC) model and the coarse-grained standard and polarisable MARTINI water models are used(117–119). The three water models can be seen in **Figures 14a** to **14c**.

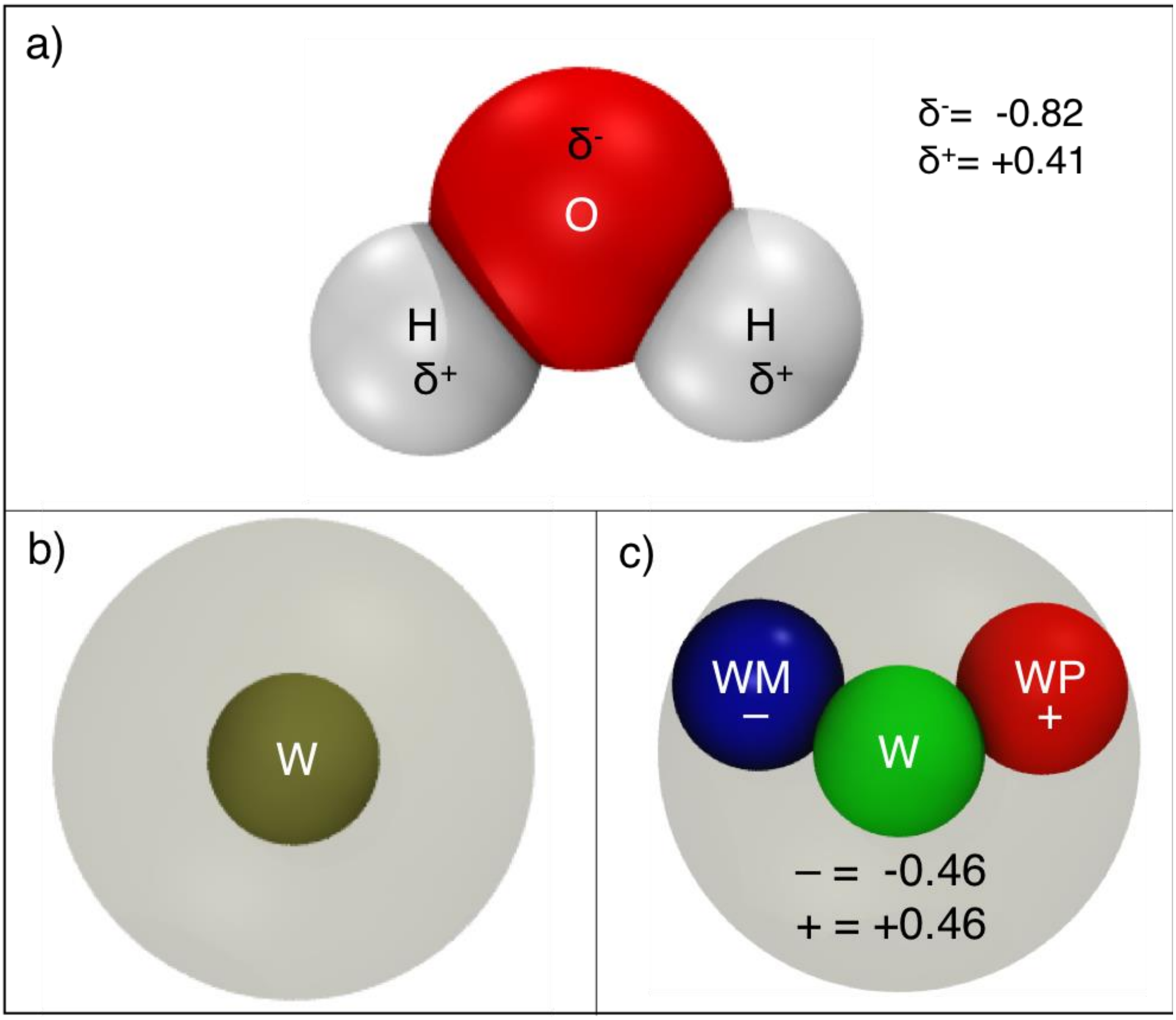

***Figure 14.** The water models employed in this thesis, with charges and partial charges annotated. The van der Waals radii of the coarse-grained water beads are also shown. **14a)** SPC water. **14b)** standard MARTINI water. **14c)** polarisable MARTINI water.*

The atomistic SPC model depicts water molecules as three particle sites, with a partially charged oxygen atom bonded to two partially charged hydrogen atoms. Lennard-Jones parameters are assigned to each atom and the structure is rigid. In the standard MARTINI water model, four individual water molecules are represented by one uncharged bead with the accumulative mass of the water molecules. Perhaps due to the loss of charge resolution, standard MARTINI water may be observed to undergo freezing at temperatures well above the freezing point of real water. This freezing is triggered by nucleation, however, and so is overcome with the introduction of “anti-freeze” particles into the system, which are described with increased size, thereby disrupting the intermolecular configuration of water particles. This decreases the likelihood of water particles settling, forming a point of nucleation and thus freezing.

The polarisable MARTINI water model builds on the premise of the standard model, in that it represents four individual water molecules. The polarisable model, however, consists of three sites with the combined mass of the represented water molecules. The central bead, W, is uncharged and interacts with other particles in the system in the same manner as the standard MARTINI water model. The other two beads, WP and WM, hold a positive and negative charge respectively and interact with other particles in the system by Coulombic function alone and without a Lennard-Jones potential. WP and WM beads within the same molecule have their interactions excluded from each other so, as the W-WP and W-WM distances are constrained, the charged beads can freely rotate around the central W bead. As such, the dipole moment about the molecule will vary from zero, when WP and WM overlap, to a maximum of $2ql$ (where q is particle charge and l is distance from central W bead), when the two beads are at the further distance from each other as allowed by their constraint to the central W bead.

2.15 Parameterisation of Novel Molecules

Every particle or molecule within a system must be described, or parameterised, before a simulation can begin. When using GROMACS, parameters for certain atoms and molecule types, such as basic ions and water, may be included in with the force field description (113). GROMACS also provides a tool for producing a topology for a given protein, through the selection of previously generated parameters, which also includes the interactive choice of protonation or oxidation states of various amino acids (113). Formulating parameters for a novel molecule, the mass, charge and polarity, along with values for its bonded and non-bonded interactions, must be described in a manner consistent with the chosen force field. While the mass and overall molecular charge may be obvious from the chemical formula, partial charges on each atom are more difficult to discern and may require the use of quantum mechanical calculations. Parameters for some molecules, such as lipids, may be found from online resources like Lipidbook (120), or be obtained from colleagues. Another option is to use online topology building tools such as PRODRG or the Automated Topology Builder (ATB) (121,122). While both PRODRG and ATB provide the user with the optimised, energy minimised structure of their input coordinates, ATB includes the use of semi-empirical calculations to refine bond lengths, angles and overall molecular geometry (121,122).

For the novel molecules simulated in this thesis, ATB was the online tool of choice. However, when constructing modified lipids, it was practical and sensible to modify the parameters of previously established and validated lipids. For example, when generating the parameters for a deacylated LPS species, the existing parameters of the wildtype LPS were modified to reflect the chemical differences between the modified and wildtype structures. Representations of the newly parameterised molecules employed in this thesis can be seen in **Figures 15a** to **15c**. Further details of these newly parameterised molecules will be discussed in the following chapter.

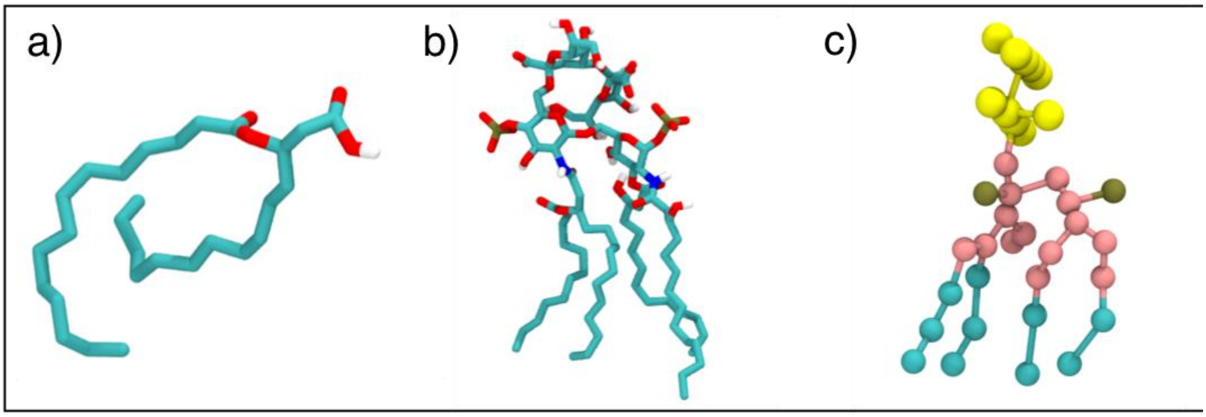

***Figure 15**. Novel molecules parameterised for the simulations discussed in this thesis. Coarse-grained structures are coloured consistently with the MARTINI force field* (98)*.* ***15a)** the acyl tail cleaved from LPS by LpxR.* ***15b)** a tetra-acylated Re LPS species at united-atom resolution.* ***15c)** the same tetra-acylated Re LPS species at coarse-grained resolution.*

2.16 Mutagenesis *in silico*

Mutagenesis is a technique often used *in vivo* to further understand protein behaviour, but it is also used in computational research (123). With the use of software such as PyMOL, amino acid residues within proteins can be mutated at the press of a button (124). The specific tautomer and rotamer of the mutated residue can also be selected, for further precision and specificity *in silico*.

To gather the data presented in this thesis, the OMP LpxR was mutated to further understand the importance of specific residues in the binding of both ions and its Re LPS substrate.

Chapter 3: Investigating the structure, function and interactions of the outer membrane protein lipid A 3'O-deacylase (LpxR) from Salmonella typhimurium, and the prediction of its closed conformation

3.1 Introduction

This chapter explores the outer membrane protein LpxR in both membrane and detergent environments, both with and without its substrate. Simulations employed here led to the prediction of a closed conformation for the protein, along with the identification of a secondary cation binding site and the evaluation of a previously published mechanism of action for the protein.

Modifications to LPS in the outer membrane of Gram-negative bacteria can both modulate the human immune response and limit the efficacy of antimicrobials (125,126). In particular, the lipid A 3'O-deacylase (LpxR) removes two of six acyl tails of LPS in *E. coli*, *S. typhimurium* and *Y. enterocolitica*, with homologues found in *V. cholerae* and *H. pylori* (127). Another OMP, PagL, is a functional analogue of LpxR and deacylates LPS at the 3 O position of its lipid A region (86). Conversely, PagP attaches a palmitoyl moiety to the existing amide-linked palmitoyl tail at the 2 C position of lipid A. Other LPS modifications, such as the addition of 4-amino-4-deoxy-L-arbinose (L-Ara4N) or phophoethanolamine (PetN) by ArnT and EptB respectively, modulate the charge of LPS and lead to the increased resistance of antimicrobial peptides such as polymyxin B1 (92,128).

When first characterising LpxR, Reynolds *et al.* noted hexa-acylated lipid A was the substrate for the enzyme, as long as the inner core keto-deoxyoctulosonate (KDO) sugars were present (87). Reynolds *et al.* performed activity assays and observed that LPS deacylation by LpxR is dependent on the presence of a divalent cation; Ca^{2+} yielded the greatest activity, followed by Sr^{2+} and then Cd^{2+}. Mg^{2+}, Ba^{2+} and Zn^{2+} led to catalytically inactive LpxR (87). Due to the relative abundance of Ca^{2+} compared with Sr^{2+} and Cd^{2+}, as well as the maximal activity observed, the mechanism of LpxR was labelled Ca^{2+}-dependent.

Like nearly all other outer membrane proteins (OMPs), LpxR adopts a beta barrel structure (85). The X-ray structure, which has a resolution of 1.9 Å (**Figure 16a**) shows the enzyme consists of twelve β-strands, five periplasmic turns and six extracellular loops (129). Of the periplasmic turns, T4 forms a plug inside the beta barrel and is stabilised in place by several salt bridges. Two of the extracellular loops (L1 and L3) form the sides of a cleft against the barrel wall, in which a number of highly conserved residues are located; after conducting activity assays on copies of the protein with conserved residues mutated to alanine residues, Rutten *et al.* concluded that this region must contain the active site of the enzyme (129). A representation of the protein-substrate complex, along with key residues in the binding cleft, can be seen in **Figures 16b** to **16d**.

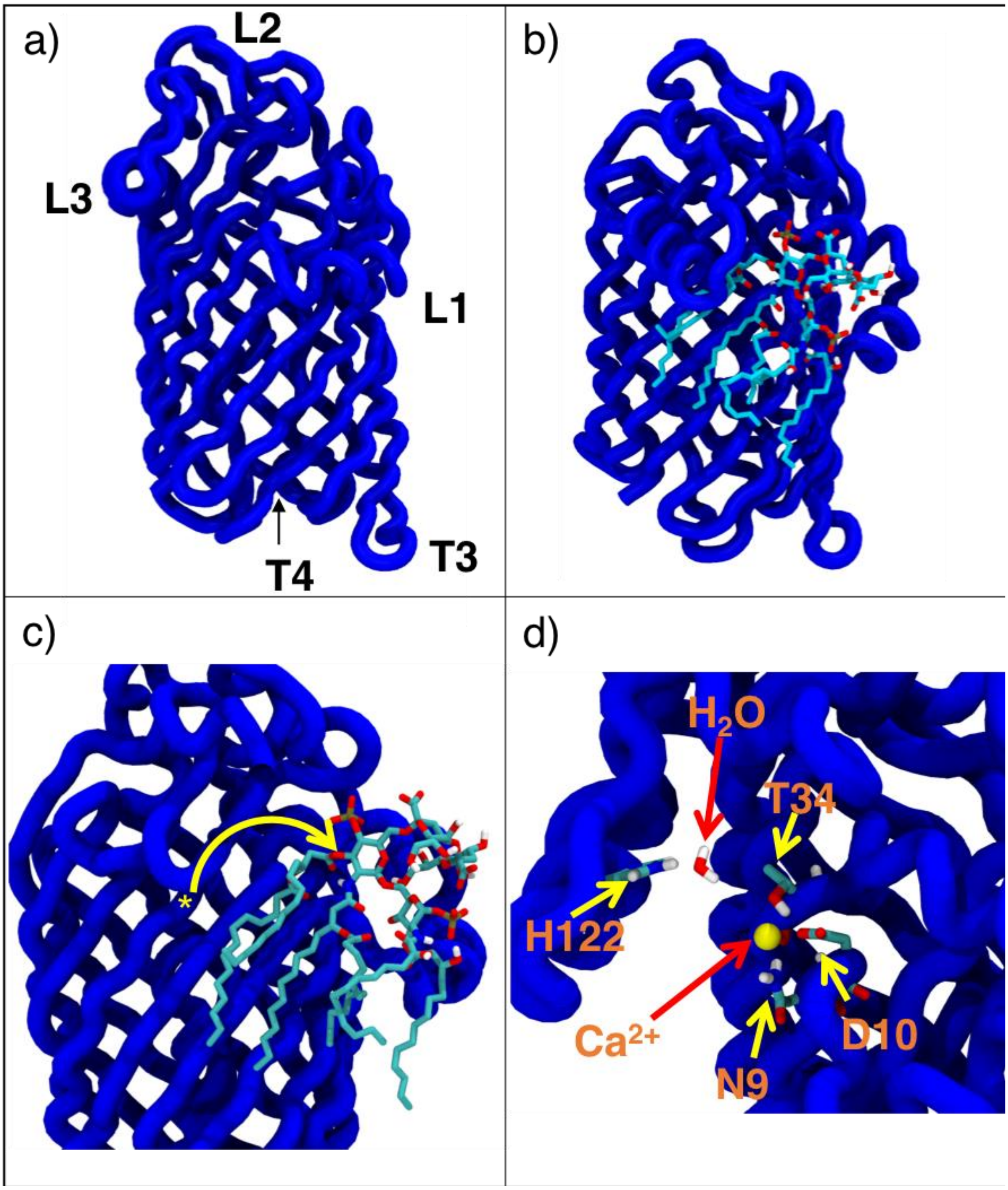

***Figure 16a)** The X-ray structure of LpxR (PDB 3FID), with visible extracellular loops and periplasmic turns labelled. **16b)** LpxR backbone with Re LPS bound within active site.. **16c)** Re LPS in LpxR binding site, as modelled by Rutten et al., with scissile bond labelled with an asterisk* (129). ***16d)** Key residues of binding site labelled with water molecule and Ca^{2+} ion (yellow) from Rutten et al. model shown. Interatomic distances H122 and water ~0.2 nm, T34 and Ca^{2+} ion ~0.19 nm, D10 and Ca^{2+} ion ~0.18 nm and N9 and Ca^{2+} ion ~0.36 nm.*

Parallels may be drawn between LpxR and the OM phospholipase A1 protein OmpLA, another twelve stranded OMP with a Ca^{2+}-dependent mechanism, which has a broad substrate specificity and removes the SN-1 acyl chain from various phospholipids in the inner leaflet of the outer membrane (72,85,130). OmpLA is activated through dimerisation and removes acyl tails from phospholipids by ester hydrolysis, and its structure is stabilised through specific interactions between extracellular loops and LPS (71,130). Simulation studies of OmpLA will be considered later, in the *Results and Discussion* section of this chapter.

Along with determining the crystal structure of LpxR, Rutten *et al.* used the online molecular docking tool HADDOCK2.0 to indicate a likely substrate binding site (129,131,132). The information from HADDOCK2.0, along with X-ray diffraction data the authors proposed a mechanism for the catalysis, in which a catalytic histidine, H122, activates a water molecule to hydrolyse the scissile bond of the substrate (**Figure 17**). While these data are invaluable for elucidating the catalytic processes of OMPs such as LpxR, they depend on static structures, given we know proteins are dynamic molecules, it seems likely that static structures cannot provide a thorough understanding of how protein conformational dynamics may impact upon the mechanism of action of LpxR. To understand the mechanism better molecular dynamics is an appropriate technique as it can use the existing structural data along with the docking information to add in the dynamics and also the biologically relevant environment, namely the outer membrane. In this chapter I aim to build a profile of LpxR by: 1) exploring the interplay between LpxR and its membrane, particularly the role of LPS core sugars in maintaining protein orientation, as well as any localised membrane distortion caused by the protein 2) identifying key interactions between protein and substrate in order to evaluate the catalytic mechanism proposed by Rutten *et al.* (129) 3) investigating potential mechanisms of activity regulation, such as dimerisation. Correspondingly, results of simulated conditions will be presented and discussed in three parts.

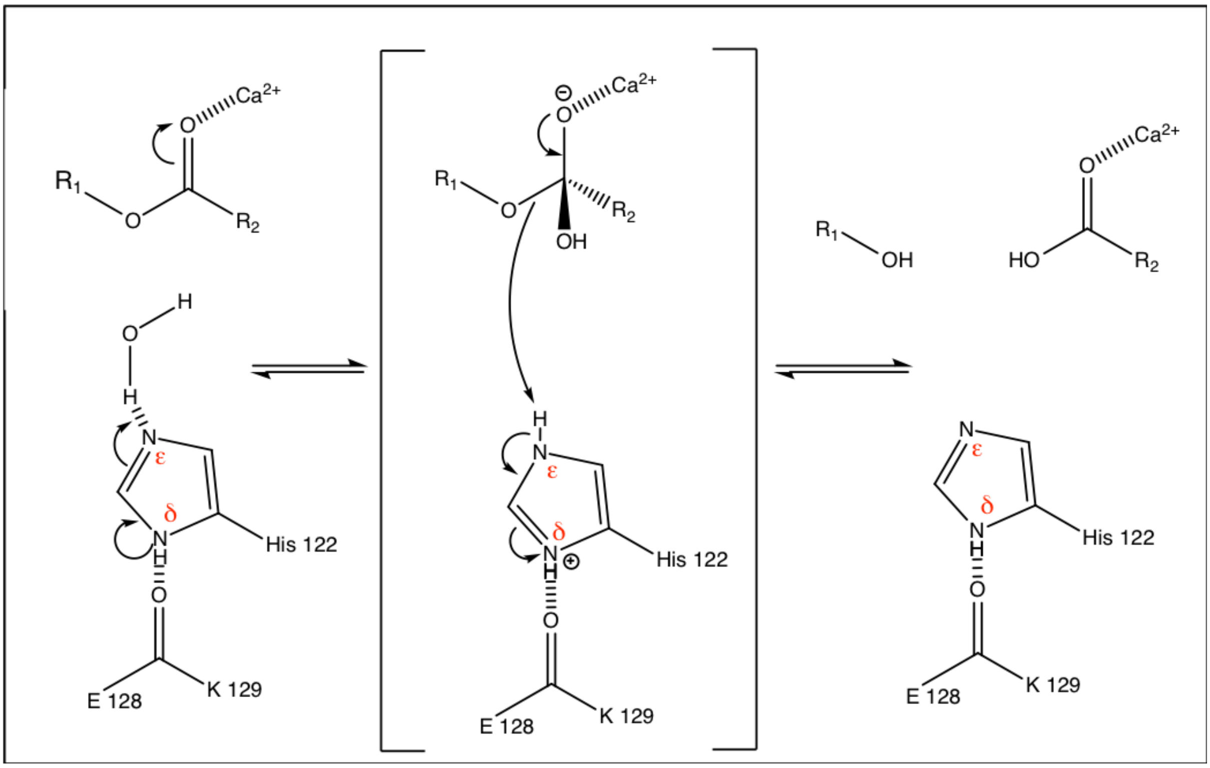

***Figure 17**. The catalytic mechanism of LpxR, as proposed and published by Rutten et al. along with the X-ray structure of the OMP* (129)*. A hydrogen bond between the carbonyl oxygen of E128 and the protonated Nδ of H122 stabilises the imidazole ring in position, allowing a hydrogen bond to activate a mechanistic water molecule, which hydrolyses the scissile bond of LPS and leads to the removal of two of its six acyl tails.*

3.2 Methods

3.2.1 Coarse-Grained Simulation Protocols

Membrane Simulations

Simulations at the coarse-grained resolution were performed to establish the favoured orientation of LpxR in a realistic asymmetric membrane consisting of Ra LPS in the outer leaflet, with PE (90%), PG (5%) and cardiolipin (5%) in the inner leaflet. Later, when investigating the potential for oligomerisation, multiple copies of LpxR were embedded into dipalmitoylphosphatidylcholine (DPPC) membranes; in membranes with 100% LPS in one leaflet, the lateral diffusion of embedded membrane proteins is typically highly or totally correlated with that of the LPS. Therefore, DPPC is a more appropriate membrane constituent as it allows for lateral diffusion of protein monomers relative to each other.

To set up these systems, LpxR was first converted from its X-ray structure (PDB 3FID) to coarse-grained resolution using the *martinize.py* script from the MARTINI website (http://cgmartini.nl/index.php/downloads) using MARTINI atom-to-bead mapping. The Ra LPS membrane was obtained pre-equilibrated from group member Pin-Chia Hsu, and had been validated previously (31,133). The DPPC membrane was obtained from the CHARMM-GUI website (134). Standard MARTINI water was used to solvate systems, and either Ca^{2+} or Na^{+} counterions were used to neutralise any residual system charge.

To embed LpxR into Ra LPS membrane systems, the protein(s) was superimposed onto the membrane, then LPS molecules within 1 nm of the protein centre-of-mass were removed. The system was then energy minimised using the steepest descent algorithm to a maximum of 50,000 steps then repeatedly simulated in the NPT ensemble with time steps of 1 fs, 2fs, 5 fs before finally 10 fs, each for 10,000 steps, to allow relaxation of any lipids in close proximity to the protein. For DPPC membrane systems, the GROMACS solvate tool was used to embed the protein(s). Positional restraints of 1000 kJ mol^{-1} nm^{2} stabilised the protein in place while any gaps in the membrane around the protein during simulation in NPT ensemble. After embedding, each system was subjected to 500 ns of simulation in the NPT ensemble, before production runs of either 2 μs or 10 μs and the resultant trajectories were analysed.

The MARTINI force field was used in all coarse-grained simulations with an integration time step of 10 fs. The Parrinello-Rahman barostat was used with a time constant of 1 ps for semi-isotropic pressure coupling (135,136). The system temperature was maintained using the velocity rescale thermostat with a time constant of 1 ps (137). Non-bonded interactions were calculated with Coulombic interactions cut-off at 1.4 nm and van der Waals reduced to zero between 0.9 – 1.4 nm. The GROMACS molecular dynamics software package (version 5.1.4) was used for all simulations in this chapter (113,138). Details of all coarse-grained resolution simulations are provided in **Table 1**.

Table 1. *All Coarse-Grained simulations performed in this chapter. All LPS-containing simulations performed at 310 K (x2) and 323 K (x1), and DPPC-containing simulations at 323 K (x3)*

System	**Outer Leaflet Composition**	**Inner Leaflet Composition**	**Ions Present**	**Timescale**
CG_LpxR x1	Ra LPS x63	PE x144, PG x8, cardiolipin x8	Ca^{2+} x334, Na^{+} x1	2 μs (x3)
	Ra LPS x240	PE x560, PG x30, cardiolipin x30	Ca^{2+} x1247, Na^{+} x1	2 μs (x3)
CG_LpxR x2	Ra LPS x229	PE x544, PG x32, cardiolipin x31	Ca^{2+} x1197	2 μs (x3)
	DPPC x215	DPPC x214	Na^{+} x10	10 μs (x3)
CG_LpxR x3	Ra LPS x216	PE x527, PG x31, cardiolipin x27	Ca^{2+} x1130	2 μs (x3)
	DPPC x188	DPPC x188	Na^{+} x15	10 μs (x3)

3.2.2 Atomistic Simulation Protocols

Membrane Simulations

The resultant trajectories from coarse-grained simulations were used to set up united atom resolution protein-in-membrane systems. The membranes used were either a simplistic, symmetric DPPC membrane, or more complex LPS-containing asymmetric membranes. Asymmetric LPS membranes containing either Ra or Re type LPS in the outer leaflet and PE (90%), PG (5%) and cardiolipin (5%) in the inner leaflet were obtained from group members Firdaus Samsudin and Tom Piggot and had been used and validated previously (46,47,139).

The GROMACS tool pdb2gmx was used to collate parameters consistent with the gromos54a7 force field for united atom simulations, and the protonation states of residues of interest were chosen. For simulations of the *apo* protein, the X-ray structure (PDB 3FID) was embedded by itself into a membrane using the GROMACS membed tool (113). For "*Model*" ligand-bound simulations, the modelled structure of Re LPS in the LpxR binding site (obtained from Piet Gros, as reported by Rutten *et al.* (129)) was embedded as into either an Ra or Re LPS-containing membrane. In "*Unbiased*" simulations, the water and Ca^{2+} modelled in by Rutten *et al.* were removed, to understand whether these sites would be re-occupied by the relevant particles and thus evaluate their importance. While the computational work of Rutten *et al.* was certainly decent, it remains that the divalent cation resolved in the X-ray structure, a Zn^{2+} ion, had a low electron density and thus may have been an artefact of the diffraction data (129). When investigating potential dimer interactions, two LpxR molecules were inserted into the DPPC membrane in the conformation present in the X-ray structure. This initial conformation can be seen in **Figures 18a** and **18b**.

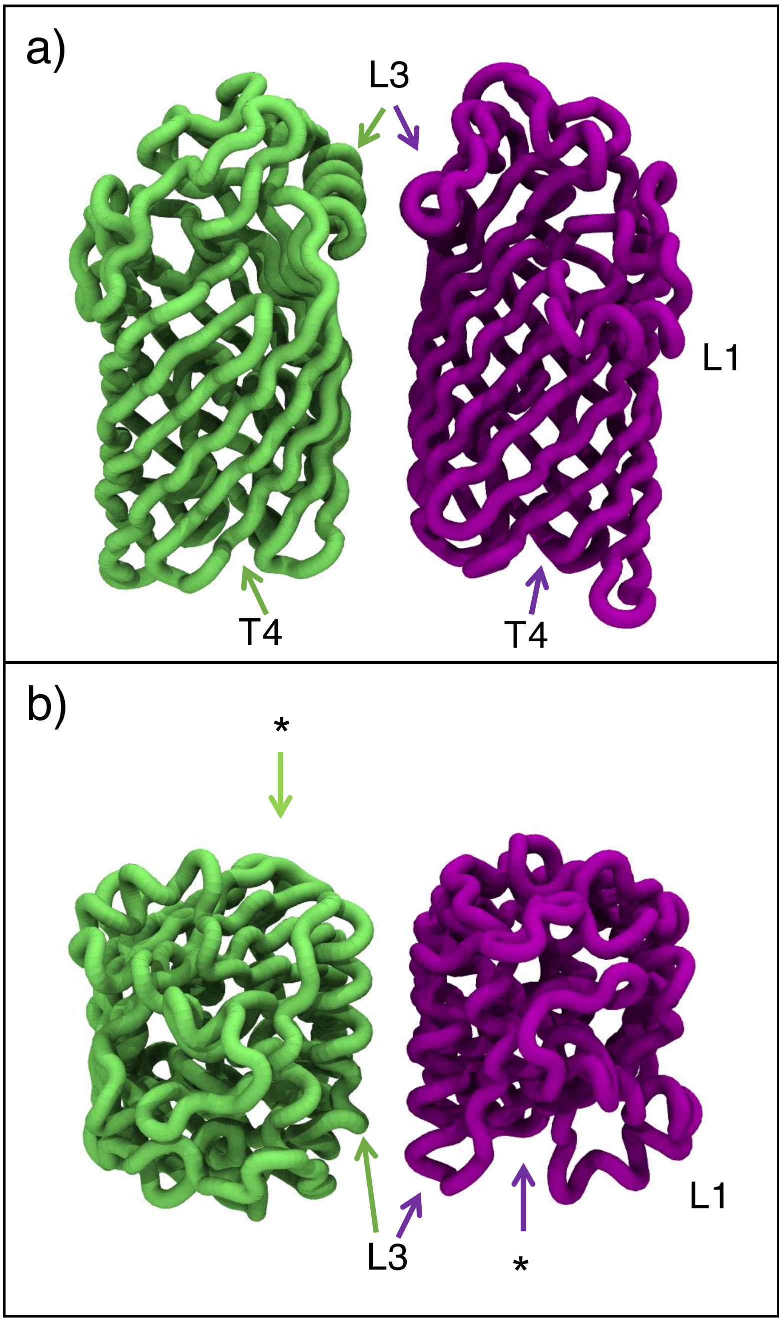

***Figure 18.** Initial starting conformation for the atomistic dimer investigation simulations with the protein backbones coloured in green and purple, with side (**18a)**) and top-down (**18b)**) views of the proteins. Key extracellular loops (Lx) and periplasmic turns (Tx) are noted, and LPS binding site is marked with an asterisk.*

The SPC water model was used for simulations at united-atom resolution, and counterions were added to each system to neutralise residual charge (117). For LPS membrane systems, Mg^{2+} ions were added, and for DPPC membrane systems, Na^{+}

ions. All systems were energy minimised after setup, using the steepest descent algorithm for a maximum of 50,000 steps. Systems were then subjected to 500 ps simulation in the NVT ensemble, then 20 ns in the NPT ensemble, both with 1000 kJ mol^{-1} nm^{2} positional restraints on protein Cα atoms, to allow membrane lipids to relax around the protein. After equilibration, production runs of from 300 ns up to 2 μs were performed and the resultant trajectories were analysed.

3.2.3 Micelle Simulations

Either one or two copies of the X-ray structure of LpxR (PDB 3FID) were placed in a box with 100 dodecylphosphocholine (DPC) molecules, then solvated with SPC water and neutralised with Na^{+} ions. Parameters for DPC were retrieved from http://wcm.ucalgary.ca/tieleman/downloads. DPC was chosen as the detergent for this condition due to its use in previous experimental and simulation studies investigating the behaviour of membrane proteins – this protocol emulates the procedures of those previous micellar simulation studies (140–143). The system was simulated in the NPT ensemble for 50 ns at 350 K, with 1000 kJ mol^{-1} nm^{2} positional restraints on protein Cα atoms, to allow for a DPC detergent micelle to form around the protein. After equilibration, production runs of 500 ns were performed at 323 K and the resultant trajectories analysed. For simulations in this condition, isotropic pressure coupling was used.

3.2.4 Mutated Protein Systems

For simulations of LpxR with mutated residues the X-ray structure (PDB 3FID) was modified using the PyMOL mutagenesis tool, and resultant structures were embedded into an Ra LPS membrane as previously described (124). As the purpose of these mutants was to aid the understanding of specific interactions between LpxR and either its substrate or coordinated cations, the Re LPS, Ca^{2+} and water molecules positioned by Rutten *et al.* was returned to the protein structure before the complex was embedded into the membrane. Details of all united atom resolution systems are provided in **Table 2**, and details of the parameterisation of novel molecules were described in the *Methodology* section of this thesis.

Table 2. *All atomistic simulations performed in this chapter. All protein simulations, unless otherwise stated, were performed using an Ra LPS asymmetric membrane with 64 lipids in the outer leaflet*

System	**Notes**	**Length of each simulation**	**Temperature and number of repeats**
Apo Model	X-ray structure with water and Ca^{2+} as reported by Rutten et al.	300 ns (x2)	310 K
		1 μs (x1)	323 K
Apo Model*	As above, but with positional restraints for first 100 ns	300 ns (x2)	310 K
		1 μs (x1)	323 K
Apo Unbiased	X-ray structure with key water and Ca^{2+} removed from starting structure	300 ns (x2)	310 K
		1 μs (x1)	323 K
Ligand-Bound Model	X-ray structure with water and Ca^{2+} and modelled in substrate as reported by Rutten et al.	300 ns (x2)	310 K
		1 μs (x1)	323 K
Ligand-Bound Model*	As above, but with positional restraints for first 100 ns	300 ns (x2)	310 K
		1 μs (x1)	323 K
Ligand-Bound Unbiased	X-ray structure with modelled in substrate, but without water and Ca^{2+}	300 ns (x2)	310 K
		1 μs (x1)	323 K
H122_p**	H122 is Nε-protonated	300 ns (x2)	310 K
		1 μs (x1)	323 K
D10A	Single point mutation in protein	300 ns (x2)	310 K
		1 μs (x1)	323 K

D11A	Single point mutation in protein	300 ns (x2)	310 K
		1 μs (x1)	323 K
T34A	Single point mutation in protein	300 ns (x2)	310 K
		1 μs (x1)	323 K
H122A	Single point mutation in protein	300 ns (x2)	310 K
		1 μs (x1)	323 K
Apo_Re LPS	X-ray structure inserted into Re LPS asymmetric membrane	2 μs (x3)	310 K (x2)
			323 K (x1)
Bond Break Model	Scissile bond removed in substrate	500 ns (x3)	310 K (x2)
			323 K (x1)
Bond Break Unbiased	As above but with key water and Ca^{2+} removed from starting structure	500 ns (x3)	310 K (x2)
			323 K (x1)
Micelle	Protein in self-assembled DPC micelle	500 ns (x3)	323 K (x3)
Micelle_Dimer	2× Protein in self-assembled DPC micelle	500 ns (x3)	323 K (x3)
Apo_DPPC	X-ray structure inserted into simple DPPC membrane	500 ns (x3)	310 K (x2)
			323 K (x1)
Apo_DPPC_Dimer	2× Protein inserted into simple DPPC membrane in varying starting conformations	2 μs (x3)	323 K (x9)

3.3 Results and Discussion

3.3.1 Interactions Between the Protein and Membrane Lipids

Integral membrane proteins contain hydrophobic regions, which occupy the transmembrane region, and hydrophilic regions, which interact with the charged or polar headgroups of phospholipids. It is also understood that aromatic amino acid residues have a role in anchoring these proteins to the membrane interface (73,74). Mismatch between the thickness of the hydrophobic section of membrane proteins and the bilayer can lead to localised thinning and disorder of acyl tails (144). This localised membrane disorder can be utilised to drive protein oligomerisation, or facilitate the assembly of further integral membrane proteins as in the case of the β-barrel assembly machinery (BAM) complex (145,146). This section of the *Results and Discussion* concerns specific interactions between LpxR and its local environment, and considers the influence of the protein on the surrounding OM.

In coarse-grained simulations of LpxR in Ra LPS, a consistent localised thinning of the membrane is observed, with membrane thickness being defined by the distance between phosphate moieties of opposing bilayer leaflets. In the smaller of the two coarse-grained system sizes, with 63 LPS molecules in the outer leaflet and one molecule of LpxR, the membrane is ~0.8 nm thinner within a radius of ~1.2 nm around the protein (**Figure 19a**). This is compared to the bulk lipid region (~4.0 nm), and echoes previous simulation studies, which also report membrane thinning as a response to hydrophobic mismatch between protein and membrane (75,144,147). In the larger coarse-grained system with 240 LPS molecules in the outer leaflet and one molecule of LpxR, similar behaviour is observed, with the membrane thinning ~1.2 nm to 3.2 nm in a radius of ~1.4 nm around the protein (**Figure 19b**). When studying two or three copies of LpxR in the Ra LPS membrane, distinct patches of localised membrane thinning are observed, corresponding to the locations of the proteins. Due to the nature of intermolecular cross-linking between LPS phosphate moieties via divalent cations(126,139,144), lateral movement of proteins is so slow that proteins are unable to move relative to each other in the timescales available (112).

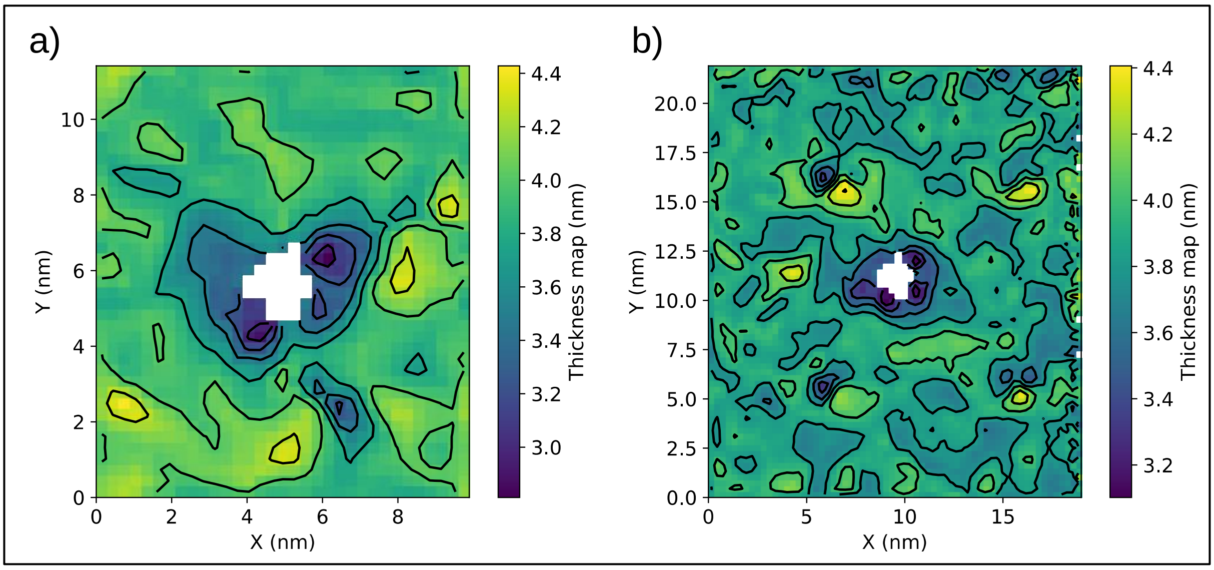

Figure 19. *Membrane thickness heat map, as described by the intermolecular distances between phosphates of opposing bilayer leaflets.* ***19a)*** *Showing thickness of smaller LpxR-in-Ra LPS membrane system.* ***19b)*** *Showing thickness of larger LpxR-in-Ra LPS membrane system.*

As localised membrane thinning has been observed in coarse-grained simulations, a great level of disorder in the acyl tails of the surrounding LPS molecules would also be expected; as the lipids are forced into unfavourable conformations by the previously mentioned hydrophobic mismatch, there is a decrease in space afforded to the tails in the *z* dimension. Therefore, the acyl tails become splayed and disordered. Indeed, the deuterium order parameters of LPS acyl tails in united atom *apo* protein systems are calculated as significantly lower within 1 nm of the protein, compared with further away, in the bulk lipid region (**Figures 20a** and **20b**). Furthermore, when calculating deuterium order parameters for LPS acyl tails directly adjacent to the binding site (**Figure 20c**), an even great level of disorder is observed. This lipid disordering may assist in the substrate-binding process; as the membrane region immediately surrounding LpxR is disrupted, particularly near the binding site, electrostatic interactions between LPS sugar moieties may also be perturbed. **Figure 20d** acts as a graphical legend for **Figures 20a** to **20c**.

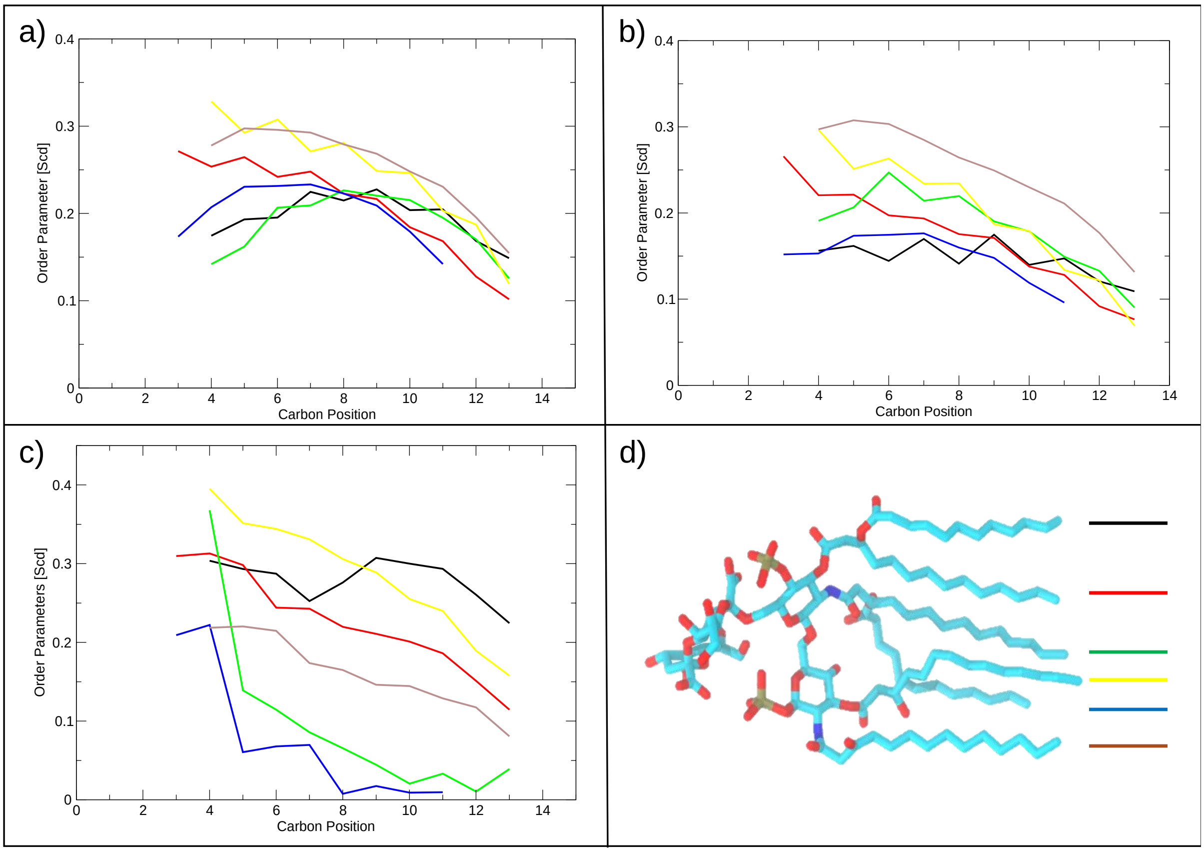

Figure 20a) *Deuterium order parameters for the six tails of LPS in the bulk lipid region of the membrane, greater than 2 nm from LpxR.* ***20b)*** *Order parameters for LPS tails within 0.5 nm of LpxR.* ***20c)*** *Order parameters for LPS tails of molecules within 0.5 nm of the binding site.* ***20d)*** *Acts as a graphical legend for* ***20a)*** *to* ***20c)****.*

To investigate whether any particular species between the PE, PG or cardiolipin phospholipids of the inner leaflet were involved in the thinning process, average density profiles were produced for systems with *apo* LpxR Re LPS-containing membranes.

As seen in **Figure 21**, phosphate headgroups of PE, PG and cardiolipin remained at a distance of 2 nm from the centre of the Re LPS-containing membrane, despite the presence of *apo* LpxR; no clear movement of any inner leaflet phosphate headgroup was seen to be implicated in the membrane thinning process. In one of three independent *apo* LpxR in Re LPS membrane simulations, cardiolipin was seen to cluster closer to the centre of the bilayer at a distance of 1.5 nm, but this was not a repeated occurrence.

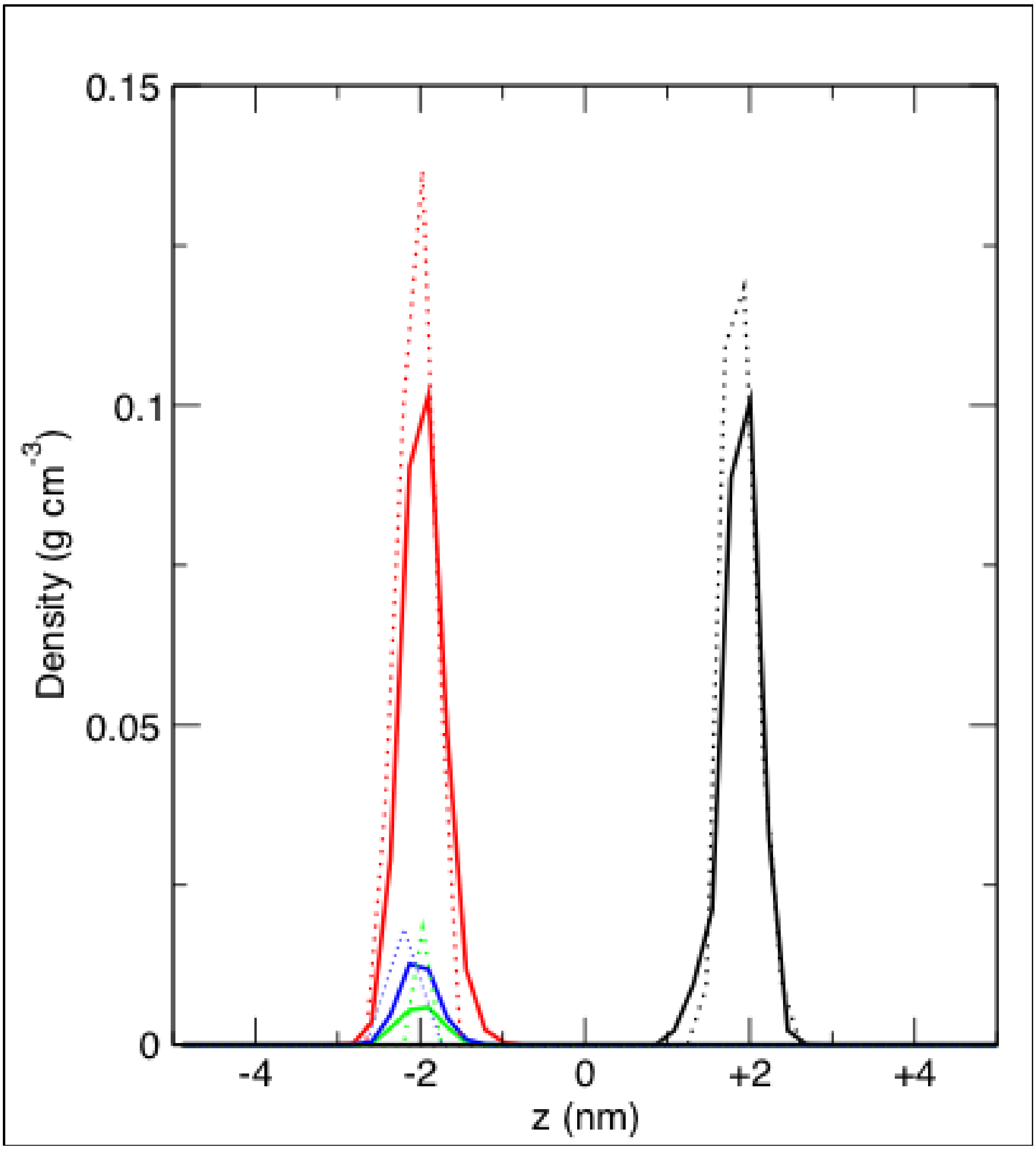

Figure 21. *Mass densities of leaflet phosphate headgroups for Re LPS-containing systems. Solid line denotes protein-embedded system and dashed line the membrane-only snapshot. Black line denotes Re LPS, red PE, green PG and blue cardiolipin.*

The area per lipid was calculated for Ra LPS lipids in an asymmetric membrane before protein insertion and averaged after two independent 1 μs simulations with embedded *apo* protein. An increase of 0.01 nm^2 to 0.28 nm^2 was noted, which is in very close agreement to the experimental value of 0.26 nm^2 for LPS lipid tails and suggests that these systems were equilibrated.

To fully understand the relationship between an integral membrane protein and the surrounding membrane, the specific interactions between protein and lipids must be considered. By calculating the frequency of interactions between *apo* LpxR and Ra LPS, a “heat-map” was produced (**Figure 22a** and **22b**). Here interactions are defined as the intermolecular distance being $\leq$0.4 nm, and “hotspots” are observed on extracellular loops L1 and L3, both of which contain residues thoughts to be essential in substrate binding and hydrolysis. In particular, R120, R123 and I125 of loop L3 and H25 of loop L1 were identified as residues consistently contacting Ra LPS molecules over the course of the 1 μs simulation at 323 K. Due to the configuration of the α-helix of loop L3, the backbone carbonyl oxygen of I125 points away from the barrel which may allow hydrogen bonds to form with sugar moieties of the LPS core region (**Figure 22c**). For LpxR *in vivo*, R120 and R123 are highly likely to be protonated and thus positively charged, enabling ionic interactions with phosphate moieties and electrostatic interactions with sugars of neighbouring LPS molecules. It is possible that R120 and R123 are involved in stabilising loop L3 during the binding and catalysis of LPS by LpxR (**Figure 22d**); however, R120 and R123 are not conserved between homologues, which may suggest that their importance here is circumstantial.

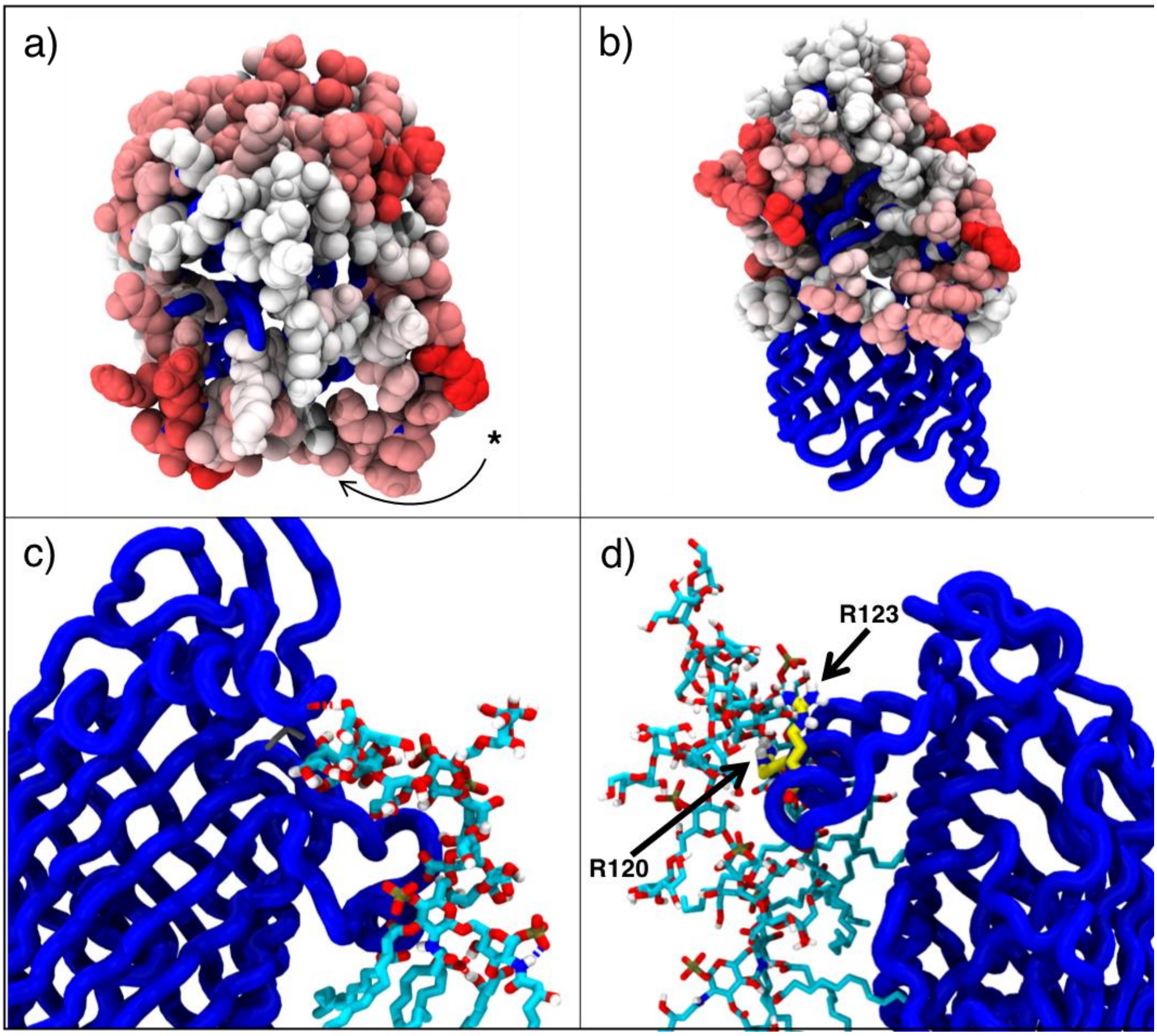

Figure 22a) *Protein-Ra LPS contacts as defined as an intermolecular distance of $\leq$0.4 nm, represented in a BWR scale heat-map. Top-down view with extracellular loops annotated and binding site marked with an asterisk.* ***22b)*** *As* **a** *but directly focusing on the LPS binding site.* ***22c)*** *Intermolecular hydrogen bond between I125 and a sugar moiety of a nearby Ra LPS molecule. Also visible are intramolecular hydrogen bonds of the Ra LPS molecule, which stabilise the conformation of the molecule.* ***22d)*** *Electrostatic interactions between R120, R123 and nearby Ra LPS sugar moieties, with Ra LPS carbon atoms shown in cyan and protein carbon atoms in yellow. All other atoms are coloured as the literature standard. Ionic interactions such as these stabilise the L3 α-helix of LpxR.*

3.3.2 Conformational Dynamics of the apo vs. ligand-bound Protein

Following the characterisation of the relationship between LpxR and its native membrane, the dynamics of the protein will now be considered, with particular focus on conformational rearrangement and substrate-binding. Results in this section are all produced from united-atom simulations.

Root mean square deviation (RMSD) and root mean square fluctuation (RMSF) calculations show the stability of LpxR in the outer membrane. For the beta barrel, the RMSD remains between 0.1-0.15 nm regardless of Re LPS bound to the protein; this is in agreement with many simulations of other OMPs (46,85,148,149). Further to this, the RMSD of the barrel remains low compared to that of the total backbone, regardless of bilayer composition. It is important to note that each RMSD calculated here is relative to the backbone of the X-ray structure of the protein (PDB 3FID). **Figures 23a** to **23c** show the RMSD of the protein backbone, barrel backbone and backbone of loops L1 and L3 respectively, with values from DPPC, Ra and Re LPS systems overlaid. In terms of RMSD, the Ra LPS membrane affords the total LpxR backbone the greatest structural stability, followed by the Re LPS and then the DPPC membranes. The RMSD of LpxR is expected to be lower in an Ra LPS membrane due to the increased number of scaffold-like interactions with the core sugar moieties of surrounding LPS molecules. In a DPPC membrane the extracellular loops are not supported by sugar moieties and so would be less structured. The membrane composition did not have an effect on the conformational stability of the β barrel region of LpxR, as shown by the negligible difference in backbone RMSD shown in **Figure 23b**.

In an effort to identify whether 300 ns simulations were an appropriate timescale for this system, the rolling average of RMSD of the *apo* protein backbone was calculated for an Ra LPS membrane system extended to 1 μs. If the fluctuation is the same at 300 ns as 1 μs, the system can be described as converged. This is shown in the form of mean square displacement over time, with an overlaid rolling average in **Figure 23d**.

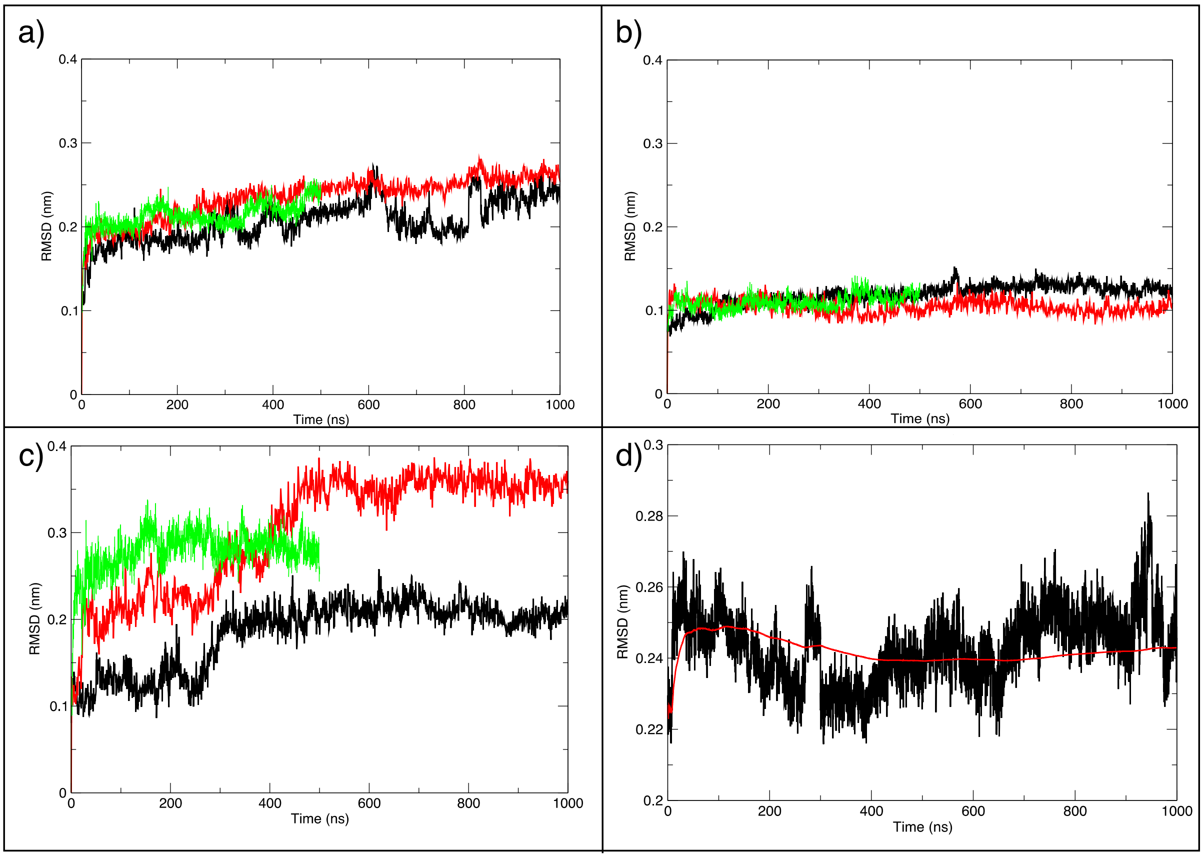

***Figures 23a)** to **23c)** Calculations of the RMSD of different backbone regions of apo LpxR when embedded in Ra LPS (black), Re LPS (red) or DPPC (green). **23a)** Total backbone RMSD. **23b)** RMSD of the backbone of beta barrel residues. **23c)** RMSD of the backbone of residues in loops L1 and L3. **23d)** Rolling average (red) of apo protein backbone RMSD (black).*

The backbone RMSF of *apo* LpxR in Ra LPS shows that the extracellular loops have greater flexibility compared to the barrel segment. This is logical, as the loops are not afforded the same scaffold-like support as the barrel by lipid acyl tails. When comparing *apo* LpxR to the ligand-bound protein, a decrease from between 0.3-0.35 nm to ~0.25 nm was noticed in the α-helical regions, suggesting that a bound substrate stabilises and reduces the flexibility of these regions.

When comparing the RMSF of the *apo* LpxR backbone between membranes, an interesting result is seen (**Figure 24**). A general increase in the RMSF of loops L3 and L6 is seen from Ra to Re LPS to DPPC membranes, with a general decrease of loops L1 and L2. The increased flexibility of L3 in the DPPC membrane is interesting as the loop contains the catalytic H122 residue. In DPPC membrane systems, as will be expanded upon when discussing protein-in-micelle simulations, H122 was seen to move closer to other binding site residues N9 and T34 due to conformational rearrangements in L3. It may be that the movement of L3 in DPPC membrane systems had a stabilising effect on loops L1 and L3 – as this movement was not seen in Ra and Re LPS membrane simulations, the stabilising effect was not present for the loops, so the calculated RMSF values for those regions were higher. Further to this, while the increased sugar packing around LpxR in the Ra LPS membrane should give greater stability to the extracellular regions, it may be that the introduction of extra negatively charged phosphate moieties in Ra LPS led to the disruption of secondary structure of loops L2 and L3. As expected, RMSF of backbone atoms of beta barrel residues remains low, regardless of membrane environment.

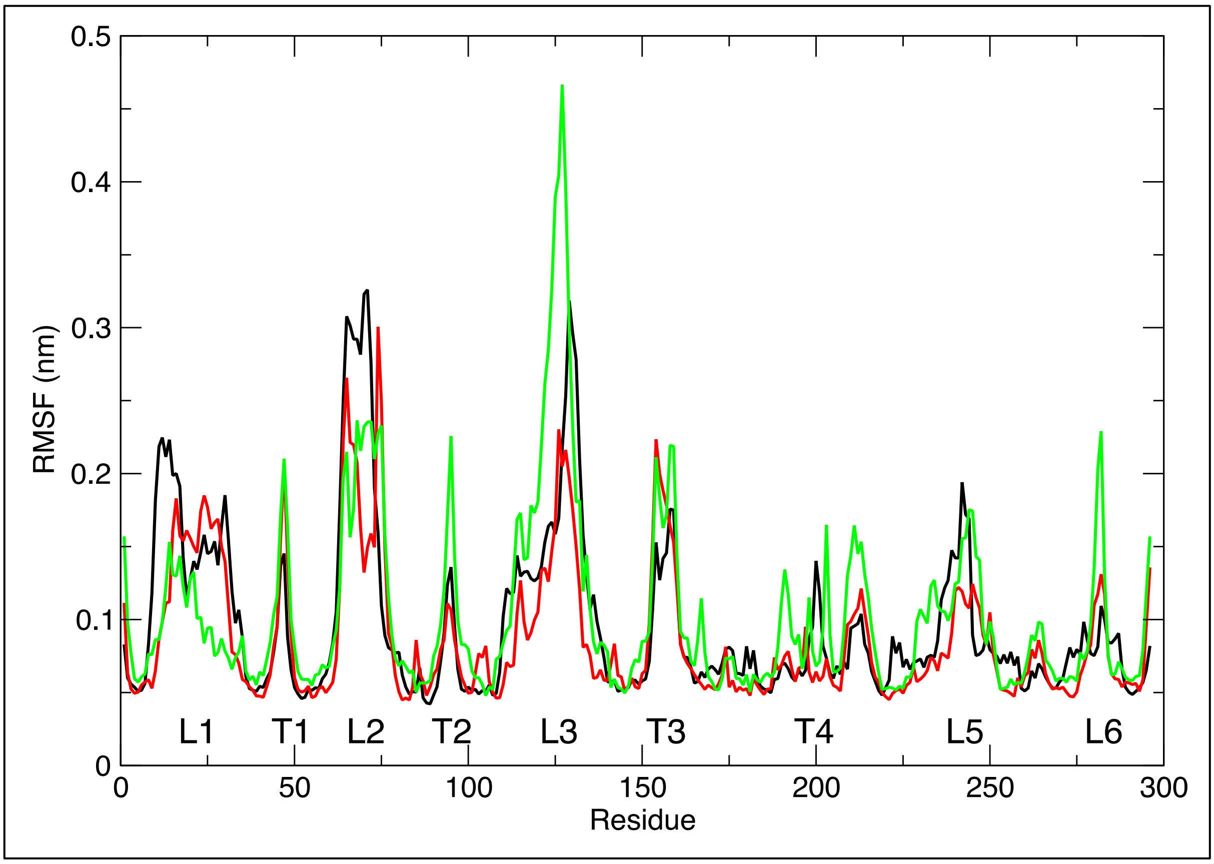

***Figure 24**. RMSF of whole apo protein backbone when embedded in Ra LPS (black), Re LPS (red) or DPPC (green). Extracellular loops and periplasmic turns are annotated as L_x and T_x respectively.*

While studying LpxR in a native membrane environment is vital for understanding its behaviour and function, there are limits imposed; due to slow diffusion rate of LPS, simulations require a much longer timescale if conformational changes are wished to be observed. Due to this, it becomes advisable to implement different environments, such as a more simplistic membrane or a detergent micelle. The use of detergent micelles for studying OMPs is well-documented experimentally due to the retention of barrel stability and increased conformational flexibility of extracellular loops due to the labile environment, and previous simulation studies corroborate, showing that faster conformational dynamics are enabled in detergent micelles (72,142,150,151).

During the three independent 500 ns micelle simulations at 323 K, occlusion of the LPS binding site of LpxR was observed due to the conformational rearrangements in extracellular loops L1 and L3. Additionally, intramolecular hydrogen bonds were observed between residues N9, T34 and H122; this is particularly significant as these residues were previously identified as vital for the enzyme's catalytic process (129).

Encouragingly, the same rearrangements were detected in the DPPC membrane systems; DPPC lipids are known to diffuse at a much faster rate than LPS (152), so greater conformational flexibility is to be expected than in Ra or Re LPS, but less than in the detergent micelle. This is reflected in the results of principal component analysis (PCA), which was conducted on *apo* protein in Ra and Re LPS-containing membranes, as well as *apo* protein in DPPC membrane and DPC micelle; **Figure 25a** shows the projection of the first two principal components of protein backbone movement from Ra and Re LPS, DPPC and DPC conditions – here tighter clusters of data points show reduced sampling of conformational space, or reduced conformational flexibility. **Figure 25a** quantitatively shows that a more densely packed membrane such as Ra or Re LPS restricts conformational change in a membrane protein such as LpxR. **Figures 25b** to **25e** show the motion of the LpxR backbone between the two extreme projections along the first principal component for each environmental condition; each of these figures show that the lipid environments sampled in this chapter have had no effect on the structural stability of the β barrel.

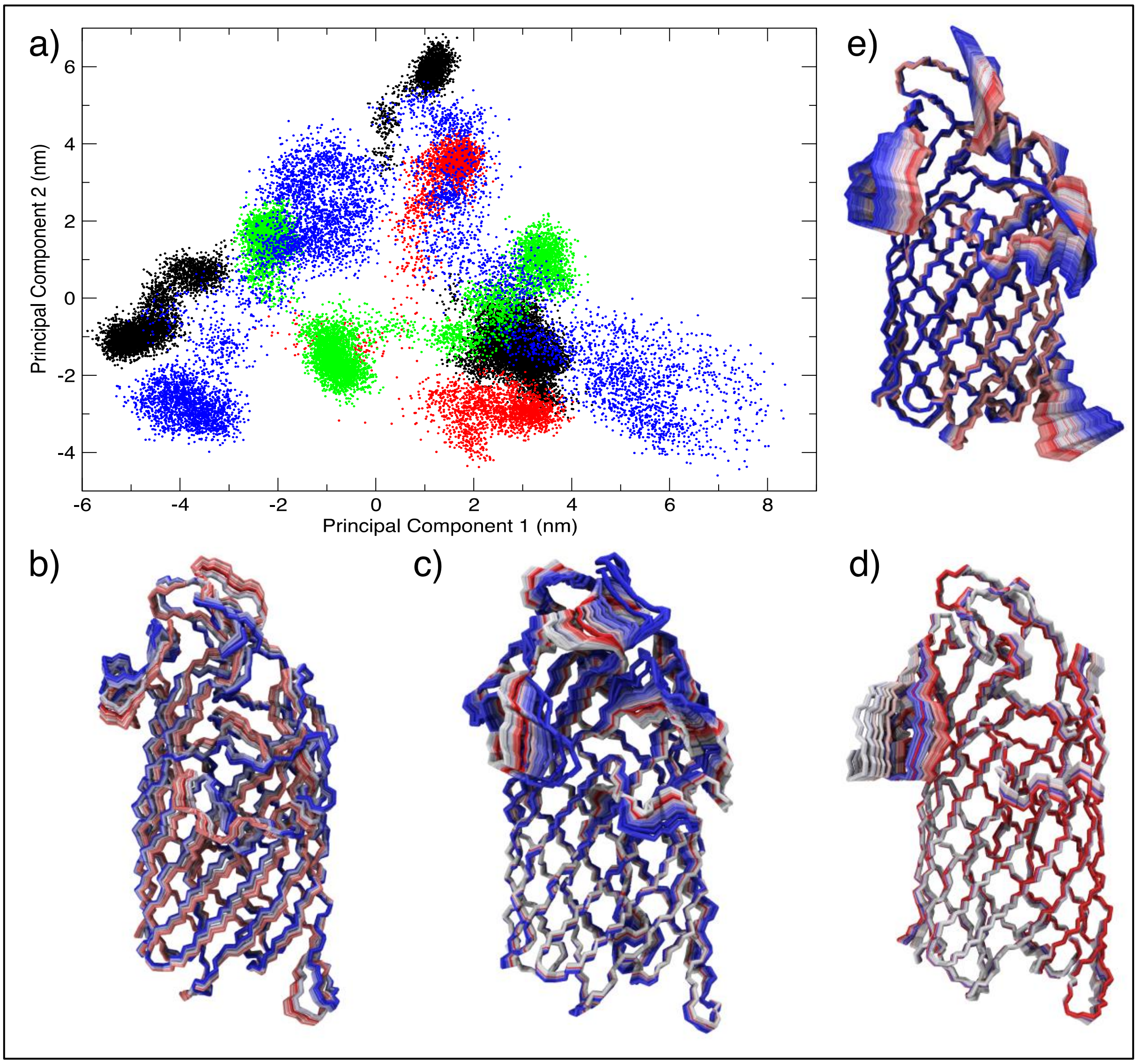

Figure 25a) *2d projection of the first two principal components of protein backbone movement for each lipid or detergent environment, from Ra LPS (black) to Re LPS (red), DPPC (green) and DPC (blue).* ***25b)*** *Extreme projections of LpxR backbone movement, with protein conformations overlaid every 20 ps with BWR colour scale, corresponding to the first principal component in the Ra LPS membrane.* ***25c)*** *As previous but in Re LPS membrane.* ***25d)*** *As previous but in DPPC membrane.* ***25e)*** *As previous but in DPC micelle.*

Further to the PCA exhibiting the enhanced structure that slow-diffusing and densely packed LPS molecules give to LpxR, secondary structure analysis confirms the conformational integrity of the beta barrel region of the protein, regardless of hydrophobic environment (**Figures 26a** and **26b)**. While the helical regions of the protein may be transient and occasionally buckle out of conformation, the combined strength of hydrogen bonds between neighbouring, antiparallel strands keeps the barrel in rigid conformation. The secondary structure of loop L3 remains constant regardless of lipid environment. In the DPC micelle, this may have been due to the conformational rearrangement of the protein into its closed conformation, involving additional hydrogen bonds with binding site residues N9 and T34 which supported L3 in its helical conformation.

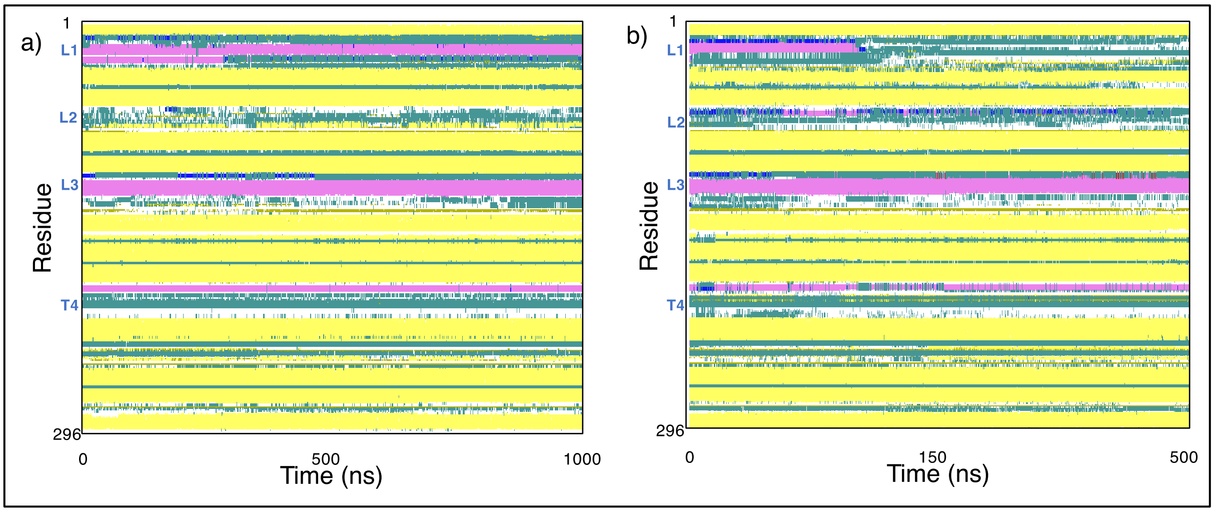

Figure 26a) *Secondary structure analysis of LpxR residues across 1 μs simulation of protein in Ra LPS membrane at 323 K, with yellow denoting β-sheet, pink α-helix, green turn, blue 3_{10}-helix, white coil, red π-helix and brown an isolated bridge.* ***26b)*** *As* ***a.*** *but analysis of LpxR residues in a representative 500 ns simulation of protein in DPC micelle at 323 K, with colours the same.*

For a membrane enzyme such as LpxR, the tilt of the barrel segment relative to the bilayer normal may influence catalytic activity. If the barrel tilts in an unfavourable direction, substrate may not be able to access the binding site and the LpxR cannot perform the deacylation. In both coarse-grained and united atom resolution simulations of LpxR in an Ra LPS membrane, the principal axis of the barrel remains tilted by ~13° relative to the bilayer normal. Comparison of tilt angles in coarse-grain and united atom systems can be seen in **Figure 27a** and **27b** respectively. MemProtMD, the online database which simulates membrane proteins in a symmetric phospholipid membrane, shows a snapshot tilt angle value of ~16° for LpxR (153) after

1μs coarse-grained simulation and subsequent back-mapping to atomistic resolution; LpxR-in-DPPC membrane simulations in this chapter contradict this value, showing the barrel to be tilt ~22° from the bilayer normal, much closer to the value given by the Orientations of Proteins in Membranes (OPM) database (154,155). The difference between the calculated values here and from MemProtMD certainly arises from sampling, as the barrel tilt angle calculated from simulations here ranged from ~7-28°. The disparities between barrel tilt angles from protein-in-Ra LPS and protein-in-DPPC membranes is due to the presence of LPS core sugars, which are densely packed around LpxR and true the principal barrel axis towards the bilayer normal. It is important to note here that membrane proteins are not static, but dynamic in nature – the tilt angle of any barrel protein is expected to vary *in vivo* due to lateral pressure from membrane lipids.

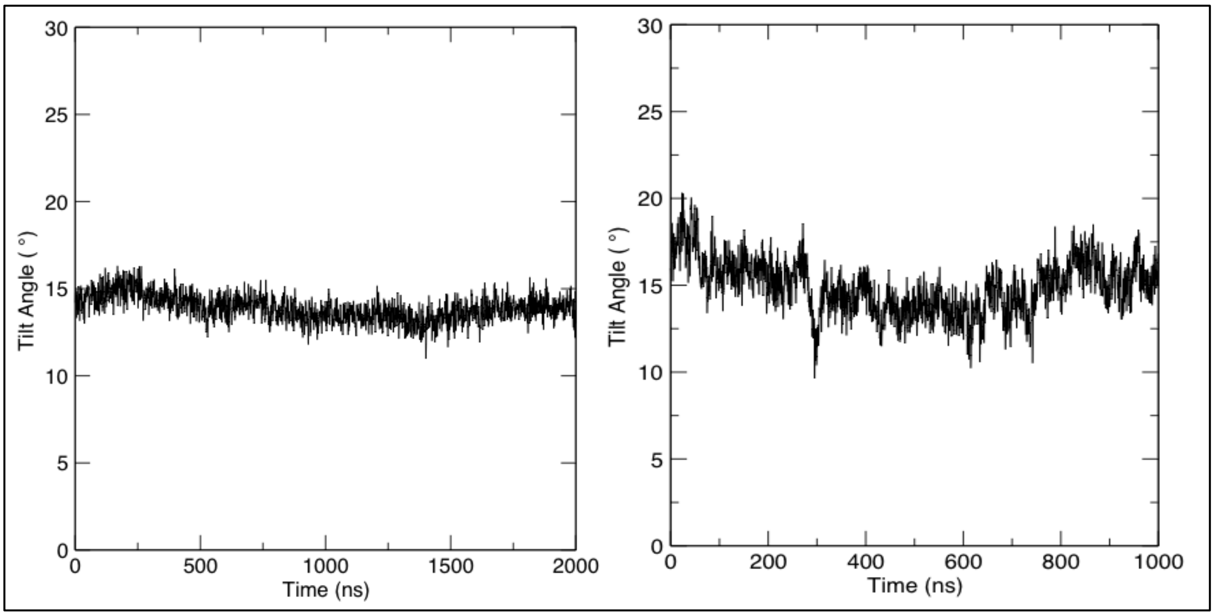

Figure 27. *Showing the mean barrel tilt angle with respect to the bilayer normal in coarse-grained (**27a)**) and united atom (**27b)**) simulation systems.*

It has been observed that aromatic amino acid residues anchor membrane proteins to the membrane interface, and hydrophobic residues are expected to occupy the membrane spanning region of a membrane protein. The densities of backbone atoms of all amino acid residues were calculated in the *z* dimension to investigate their distribution across the protein, and the densities of aromatic residues are shown in **Figure 28**. Densities were compared between Re LPS and DPPC membranes, and can be seen in **Figures 28a** and **28b** respectively. Aromatic residues were seen to be at a higher density at the membrane-water interface of both leaflets, for Re LPS and DPPC containing systems, and hydrophobic residues were at a higher density in the bilayer core. Bands of aromatic residues in membrane proteins corresponding with membrane lipid phosphates is well documented in the literature (156,157).

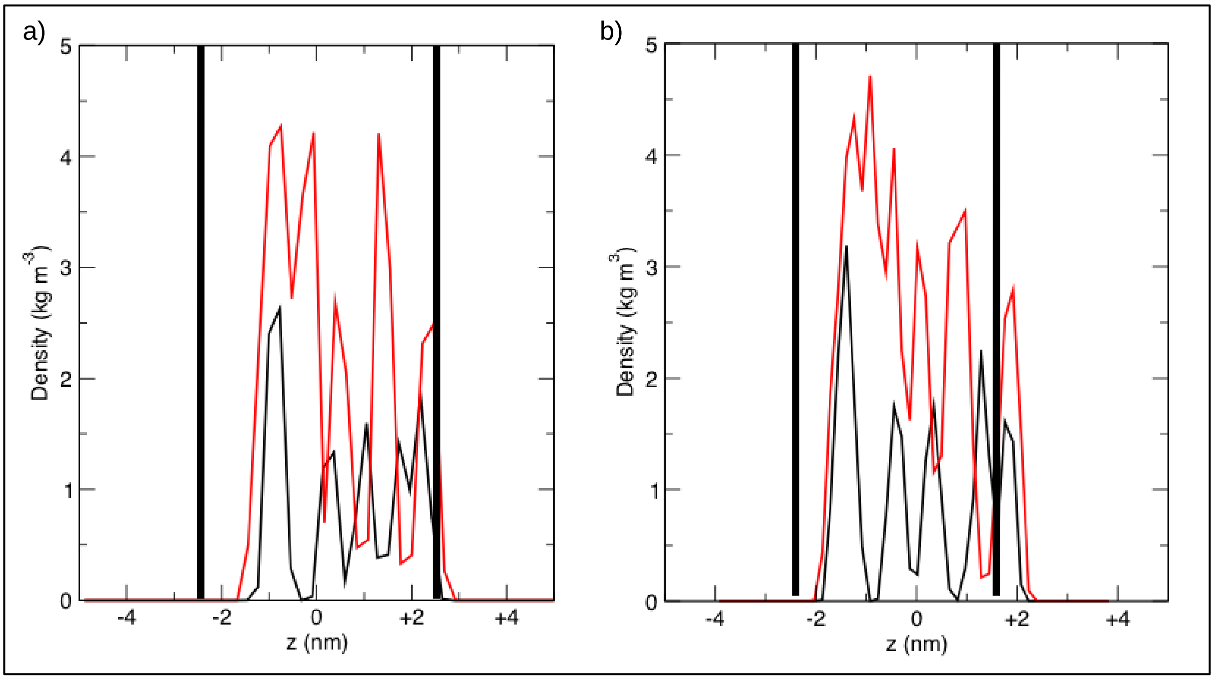

Figure 28. *Density of backbone atoms of amino acid residues across the z axis for LpxR, with bilayer interfaces marked as thick black lines. On plots, black lines denote His, Tyr and Trp residues, red* D*-Phe residues.* ***28a)*** *LpxR in Ra LPS.* ***28b)*** *LpxR in DPPC.*

Calculating the solvent accessible surface area (SASA) of lipid or detergent molecules around a protein in membrane or in a micelle gives a metric by which it can be understood just how tightly molecules have packed around the protein. It is known that lipids and detergent molecules behave differently on their own in water (141,150), compared with in the presence of a protein, and it is interesting to see the extent to which LpxR encourages the structuring and rearrangement of these molecules.

Furthermore, the packing of lipid or detergent molecules will also influence the number of water molecules able to interact directly with the protein. Tieleman *et al.* calculated the SASA values for pure DPC molecules in a micelle and DPPC in a membrane to be 1.80 nm^2 and 1.85 nm^2 respectively (158) and Bond *et al.* calculated a higher value for DPC molecules in a micelle surrounding OmpA at 1.92 nm^2 (150); a higher SASA value, when calculated for detergent or lipid molecules, indicates more diffuse packing and further signals how labile the environment is – highly relevant for the study the conformational dynamics of integral membrane proteins. Over the 1.5 μs total of micellar simulations, the mean SASA of DPC was 2.68 (±0.05) nm^2 per detergent monomer, compared with 1.78 nm^2 per detergent monomer when no protein was present. In DPPC membrane simulations, the SASA of DPPC was 2.33 (±0.05) nm^2 per lipid monomer with protein embedded, and 1.87 nm^2 per lipid monomer before protein was embedded. It seems that LpxR has stabilising effects on both detergent and lipid molecules in simulations presented here, and that the DPC detergent environment did indeed afford the protein a more labile environment. Representations of the formation of the DPC micelle around LpxR can be seen in **Figures 29a** and **29b**. Further to this, a graphical representation of the solvent accessible surface area of LpxR in both DPC micelle and DPPC bilayer can be seen in **Figures 29c** and **29d** respectively.

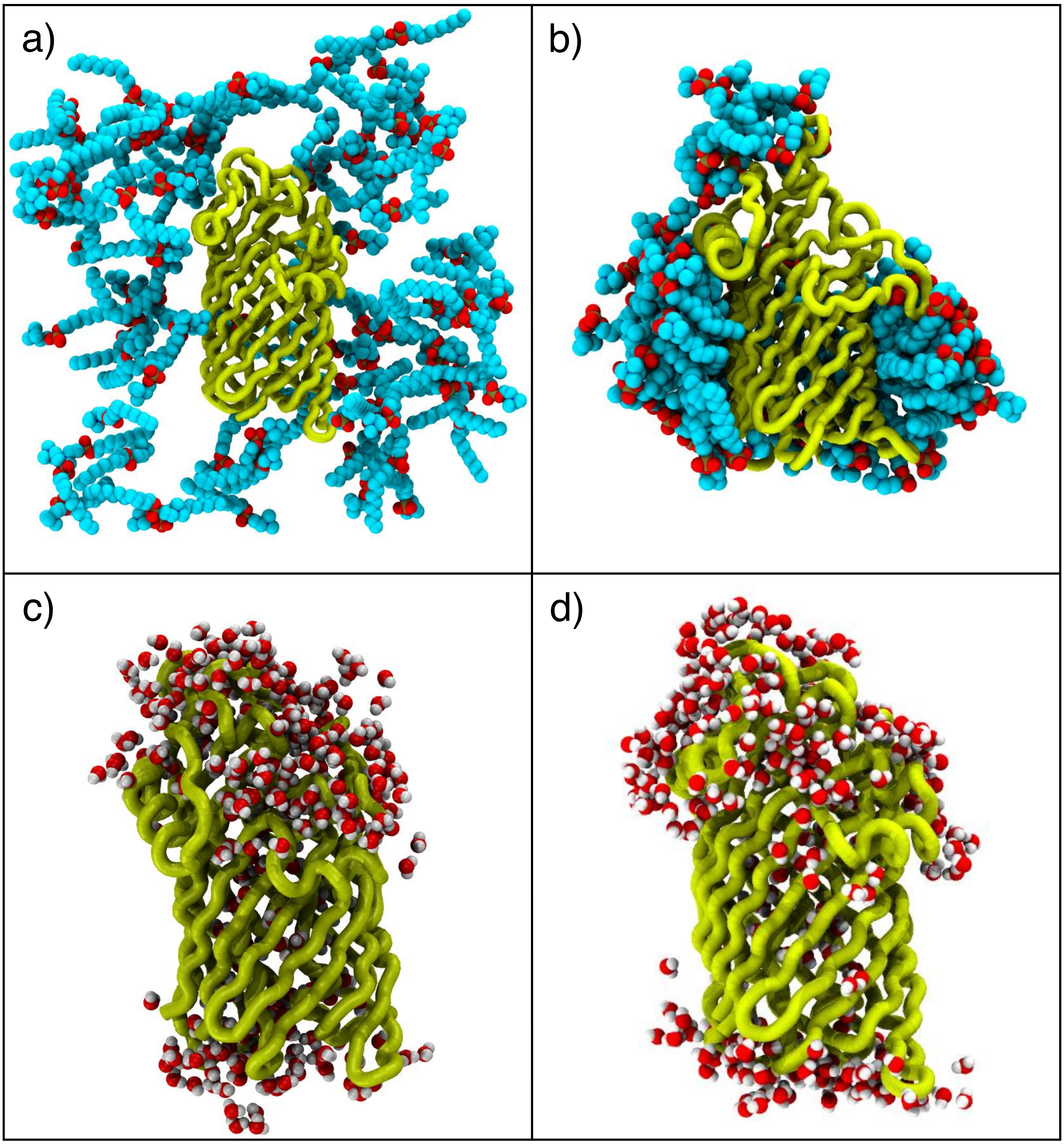

Figure 29a) *The initial configuration of LpxR, position restrained, with 100 DPC molecules surrounding. Water and ions removed for clarity.* ***29b)*** *Protein-micelle configurations, with four DPC molecules, water and ions removed for clarity.* ***29c)*** *Solvent accessible surface area of LpxR as shown by water molecules within 0.3 nm of the protein after 500 ns in DPC micelle environment.* ***29d)*** *As* ***c.*** *but after 500 ns in DPPC bilayer environment.*

In order to characterise the behaviour of both *apo* and ligand-bound LpxR with respect to cation and substrate binding sites, it seems logical to first review the catalytic mechanism proposed by Rutten *et al.* (**Figure 17**) (129); this mechanism crucially shows the imidazole of H122 to be Nδ protonated, enabling it to hydrogen bond with E128, and allowing the deprotonated Nε to increase the nucleophilicity of a mechanistic water and hydrolyse the scissile bond of the LPS substrate. Further to this, the mechanism highlights the importance of D10 and T34 in cation binding, in order for a Ca^{2+} ion to form the oxyanion hole required for catalysis.

Evidence of the hydrogen bond between H122 and E128 was sought. However, across the 4.8 μs of simulation of ligand-bound LpxR, or indeed across the 4.8 μs of *apo* LpxR (both in Ra LPS asymmetric membranes), no evidence of a stable hydrogen bond between these residues was found. The steric hindrance from backbone atoms of the α-helix of loop L3 does indeed make it easier for a hydrogen bond to form between the backbone carbonyl oxygen of E128 and the protonated nitrogen of H122, but this was seen to be a highly infrequent phenomenon, as evidenced in **Figure 30**, which shows that the minimum distance between the two residues only dropped below 0.3 nm fewer than ten times. Regardless of the protonation state of H122 in simulations performed in this chapter, a stable hydrogen bond was not seen between H122 and E128, leading to the presumption that another means in place to activate H122 for its catalytic purpose; it does remain possible the catalytic histidine does not require activation for LpxR to perform its hydrolysis – Rutten *et al.* showed that the addition of 100 mM imidazole to the catalytically inactive H122A mutant LpxR restored activity back to 30% of the wildtype activity by replacing the absent moiety (129).

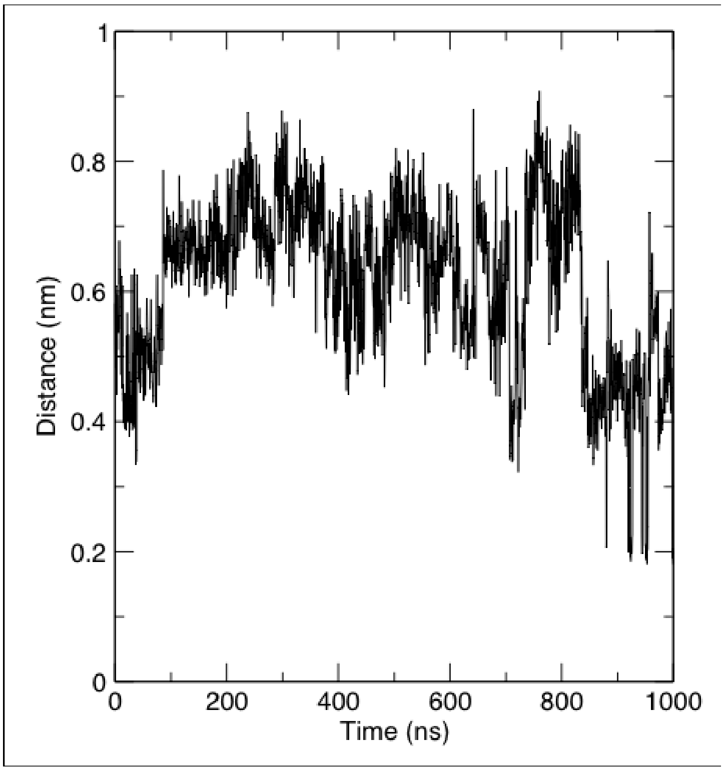

Figure 30. *The minimum distance between H122 and E128 over the course of a representative 1 μs simulation of ligand-bound LpxR in Ra LPS at 323 K.*

In all "*Model*" simulations of the *apo* protein, the Ca^{2+} ion positioned by Rutten *et al.* moved away from its initial binding site as soon as position restraints were removed, which suggests that a ligand must occupy the binding site for the cation to remain in place. When restrained, the ion remained ~0.25 nm from T34 in the enzyme's binding site, but moved away to ~1.2 nm when restraints were moved.

In ligand-bound LpxR in Ra LPS membrane simulations, the Re LPS lipid was non-covalently bound to the protein through a series of electrostatic interactions and hydrogen bonds. Residues Q16 and D29 form hydrogen bonds with the KDO sugar moieties, whereas K67 and Y130 interact with the 4' phosphate moiety; indeed, K67 is seen to snorkel towards this phosphate for this interaction to take place (**Figures 31a** and **31b**). Interactions between LpxR and the KDO sugars are of great significance, due to the evidence reported by Reynolds *et al.* that deep-rough LPS, in which the KDO sugars are absent, is not a good substrate for the enzyme(87). Simulation data here would suggest that this is in fact due to the lack of KDO sugars to stabilise the molecule in the LpxR binding site. Consistent Re LPS intramolecular interactions are also observed, with both phosphate moieties of Re LPS interacting with their nearest KDO sugar moiety. Further to this, electrostatic interactions are observed between the amide and hydroxyl moieties of the lipid tails.

In "*Model*" ligand-bound simulations, the positioned Ca^{2+} ion moves from ~0.27 nm from the side group carbonyl of N9 to ~1.0 nm away as the ions appears to favour coordination by D10, T34 and three water molecules, as well as the 4' phosphate of the Re LPS substrate (**Figure 31c**). Interestingly, these simulations show a second binding site for a cation, involving coordination by residues D10, D11 and localised water molecules. When the modelled Ca^{2+} ion was removed, in "*Unbiased*" systems, two Mg^{2+} ions do move into the substrate binding site during equilibration, but neither occupies the exact same position as the Ca^{2+} ion from the Rutten model(129). In these simulations, the two Mg^{2+} ions favour coordination by residues N9, D10 and carbonyl oxygens of ester bonds in the acyl tails of the Re LPS substrate (**Figure 31d**).

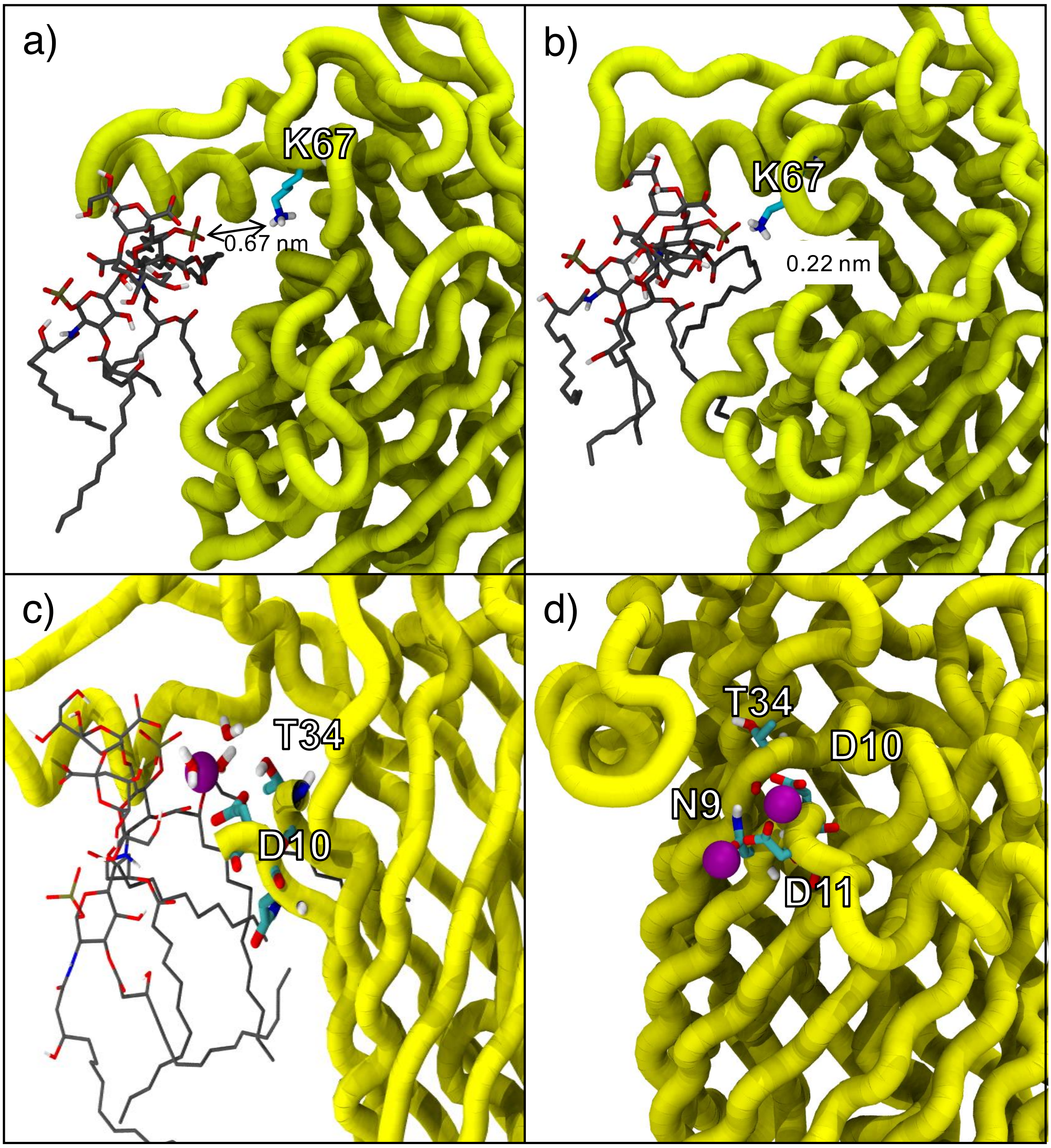

Figure 31. *Specific residue movement and molecular coordination. In all images, the protein backbone is in yellow, protein residues have carbon in cyan, Re LPS has carbon in grey and cations are in purple.* ***31a)*** *and 3**1b)** Showing the snorkelling movement of K67 towards the 4' phosphate moiety of the Re LPS substrate over the course of 1 μs simulation at 323 K, with distance between K67 amine moiety and 4' phosphate moiety labelled. 3**1c)** The coordination of Ca^{2+} by LpxR residues D10 and T34, as well as water molecules and the Re LPS substrate. 3**1d)** Cation coordination in the LPS binding site by residues N9, D10, D11 and T34.*

To quantify the interactions of protein residues with divalent cations across "*Model*" and "*Unbiased*" simulations of the ligand-bound protein, heat-maps similar to **Figures 22a** and **22b** were produced and can be seen in **Figure 32a** and **32b**, which count interaction as an interatomic distance of ≤0.4 nm.

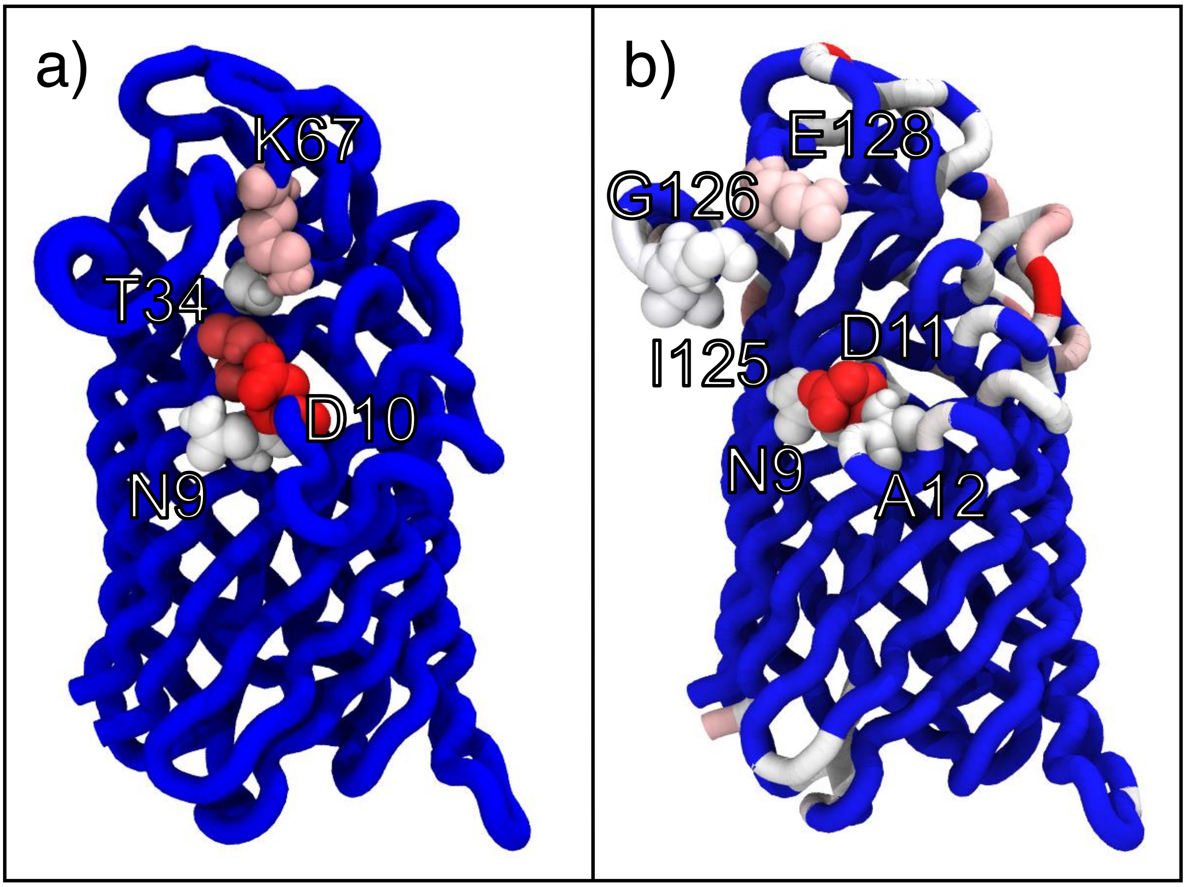

Figure 32a) *A representation of the frequency of protein residue contacts with Ca^{2+} over the course of a 1 μs ligand-bound LpxR simulation in Ra LPS at 323 K. Contact defined as an interatomic distance of ≤0.4 nm and colour scheme is BWR, with residues in red denoting those in most frequent contact with Ca^{2+}. Protein backbone is in blue and residues in contact with Ca^{2+} are shown explicitly.* ***32b)*** *As* ***a*** *but calculating contacts between protein residues and the Mg^{2+} counterions present in the system. Only residues in the protein binding site are shown explicitly and labelled.*

A series of point mutations were used to further investigate the importance of certain protein residues in cation and substrate coordination. The H122A mutation, as expected, did not affect protein interaction with either the Re LPS substrate or cations, nor did it change the α-helical conformation of the L3 loop (residues 110-126) and this is shown in **Figure 33a**. Conversely, the D10A mutant led to the Ca^{2+} ion moving out of the binding side to a distance at which it was no longer interacting with the protein; this provides further evidence with regards to the importance of D10 in Ca^{2+} coordination. The T34A mutant did not cause the same disturbance to the Ca^{2+} ion, suggesting that this residue, unlike D10, is not essential for Ca^{2+} coordination. All ligand-bound simulations thus far have indicated a role for D11 in cation binding, but there was no evidence of cation binding in this position in simulations of the D11A mutant. While D11 is not a conserved residue, it clearly has a role to play in cation binding in this species – it may be that D11 is involved in cation recruitment to the active site. The effect of point mutations on cation coordination can be seen in **Figures 33b** to **33d**.

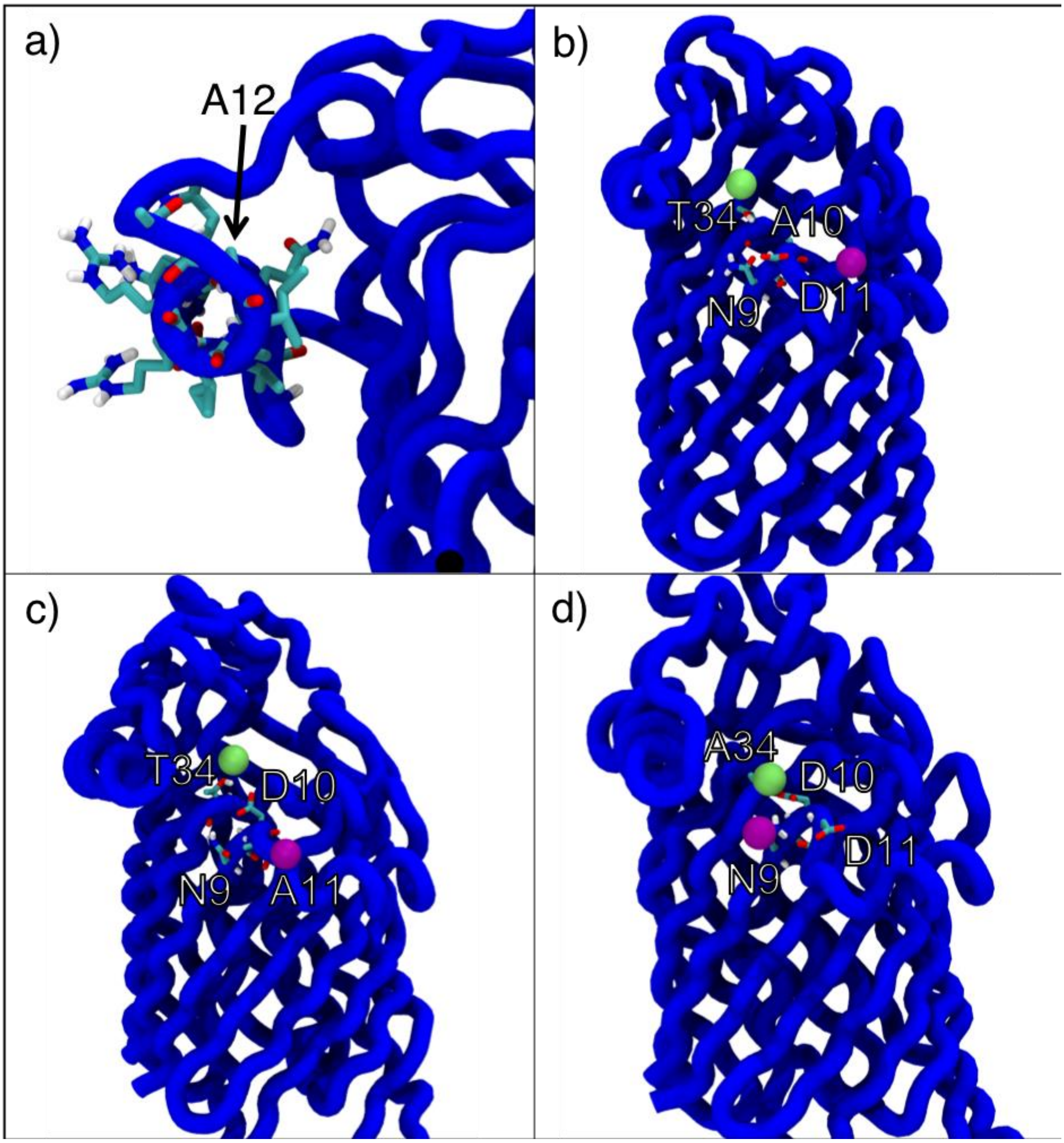

Figure 33. *The effect of point mutation of secondary conformation or cation coordination in ligand-bound LpxR systems after 1 μs in an Ra LPS membrane at 323 K.* ***33a)*** *The conformation of the α helix of loop L3, with residue A12 labelled.* ***33b)*** *Cation coordination in the LPS binding site after D10A mutation, with Ca^{2+} in green and Mg^{2+} in purple.* ***33c)*** *Cation coordination in the LPS binding site after D11A mutation, with Ca^{2+} in green and Mg^{2+} in purple.* ***33d)*** *Cation coordination in the LPS binding site after T34A mutation, with Ca^{2+} in green and Mg^{2+} in purple.*

The data presented so far in this chapter, along with the invaluable work by Hannah Bruce Macdonald with Grand Canonical Monte Carlo, led to the conclusion of a new, improved mechanism for the catalysis of LPS by LpxR; this mechanism is shown in **Figure 34** and further details can be found in the work published by Saunders *et al.* (159). The major differences in the new mechanism are the exclusion of the E128 – H122 hydrogen and the reversed protonation of H122.

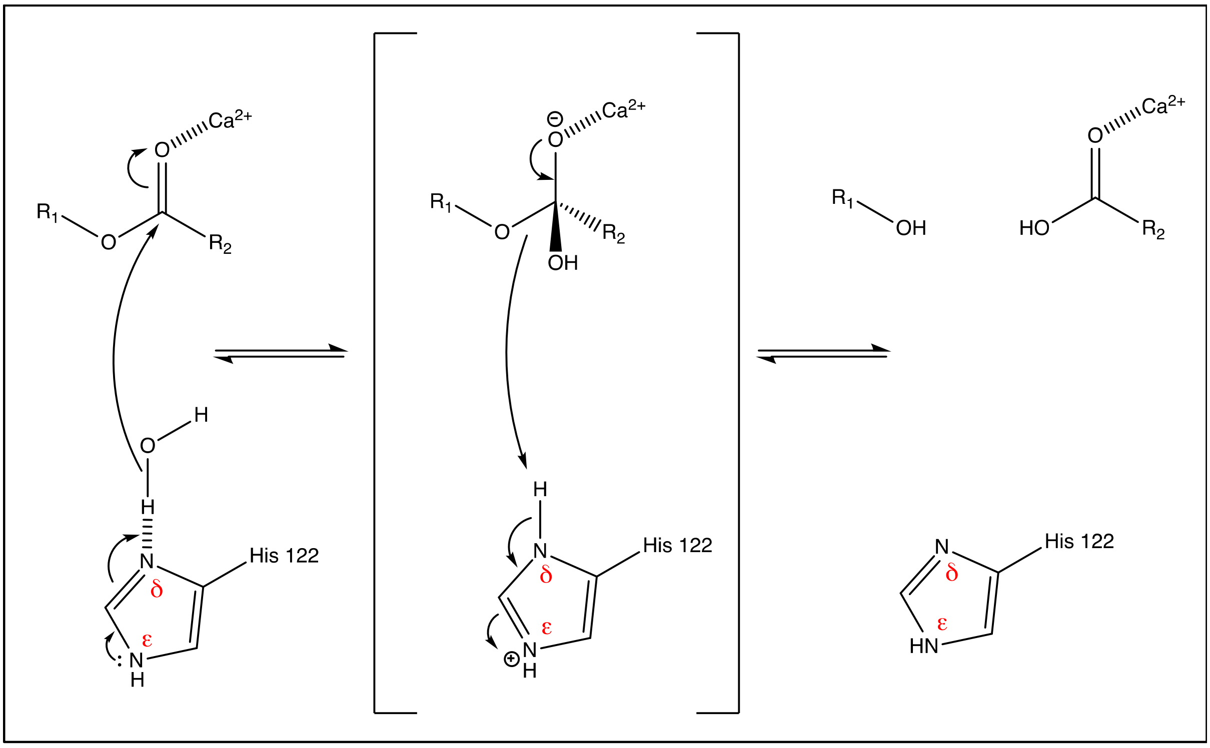

Figure 34. *The catalytic hydrolysis of LPS by LpxR, as presented by Saunders* *et al.* (159)*. Reversed protonation of His122 is highlighted by red characters.*

The application of molecular dynamics in this instance not only affords some insights into the catalytic mechanism, but also into the potential repercussions for the molecules involved after the deacylation event. To this end, the scissile bond of Re LPS was manually hydrolysed and independent "*Model*" and "*Unbiased*" simulations continued from this point. In six independent 500 ns simulations, the removed acyl tail of Re LPS rapidly move away from the now tetra-acylated Re LPS molecule towards the periplasmic leaflet of the OM (**Figure 35**). The tetra-acylated Re LPS molecule, however, remains in the LpxR binding site for the entire 500 ns; the slow-diffusing nature of LPS makes it unlikely for the full resetting process of this enzyme to be observed in the timescales available with the equilibrium molecular dynamics methods employed here.

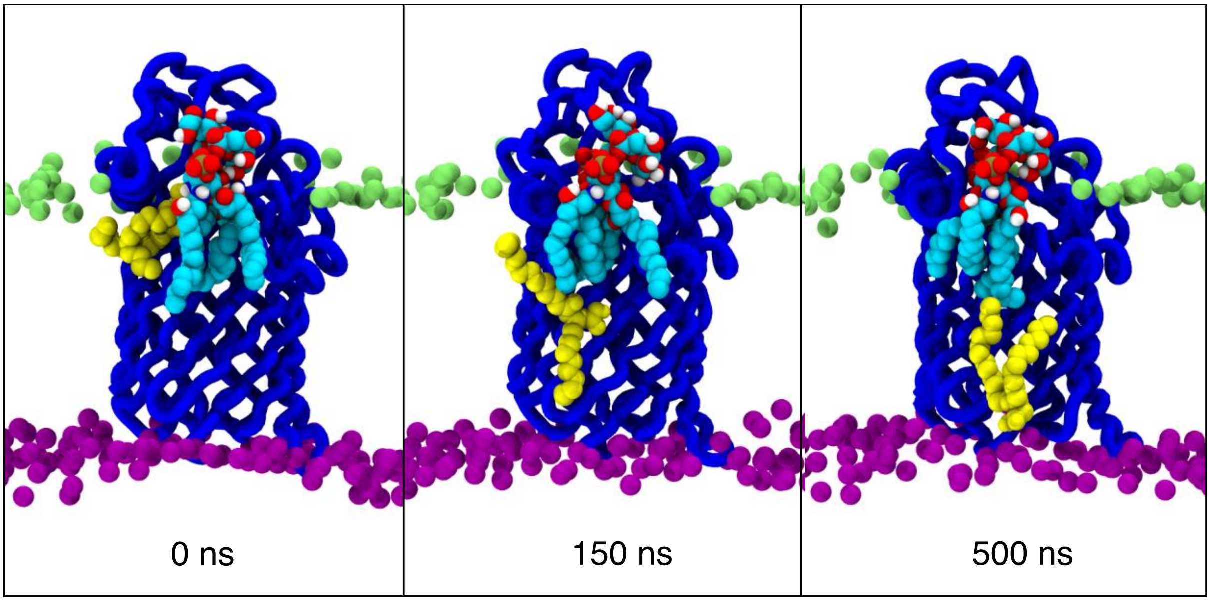

Figure 35. *Showing the diffusion of the cleaved acyl tails of LPS from the binding site of LpxR to the inner leaflet over the course of 500 ns. Protein backbone is shown in blue, Ra LPS and inner leaflet phosphates in green and purple respectively, cleaved tail in yellow and Re LPS carbons in cyan. Ra LPS phosphates occluding view of the protein-lipid complex have been removed for clarity.*

LPS modifications are known to impact both bacterial resistance to antibiotics and the immune response, but much less is known about how these modifications influence lipid behaviour and dynamics (125,126). The influence of LPS deacylation on the OM is investigated further in the following chapter of this thesis.

3.3.3 Interactions between Multiple Protein Monomers

Given the similarity in catalytic mechanisms between LpxR and OmpLA, it seems pertinent to examine for a similar mechanism of activity regulation. For activation, OmpLA requires two monomers to dimerise and the active site is formed at this dimer interface. The key dimer interactions are found within the hydrophobic part of the membrane and involve hydrogen bonds between polar residues. As the dimer forms, so too does an oxyanion hole, along with a functional binding pocket for the enzyme's substrate; these features are not observed in the monomeric protein and account for its lack of activity. A Ca^{2+} ion is required as a co-factor to stabilise the dimer and facilitate catalysis (72,130). Perhaps unusually, the enzyme is separated from its relatively non-specific substrate by having its active site situated in the outer leaflet of the OM – nearly all phospholipids of the OM are currently thought to be found in the inner leaflet(160–162). The X-ray structures of the LpxR and OmpLA crystal dimers can be seen in **Figures 36a** and **36b** respectively. LpxR is similar to OmpLA in that both are Ca^{2+}-dependent, twelve stranded OMPs responsible for lipid deacylation; however, evidence given by Reynolds *et al.*, Rutten *et al.* and Saunders *et al.* show that the LPS binding site of LpxR is present in the enzyme's monomeric form (87,129,159). Further to this, with the protein-substrate complex observed in molecular dynamics simulations presented here, it is very easy to envisage the deacylation event occurring without dimerisation. It therefore seems feasible that the protein could form a dimer to occlude its active site and inhibit deacylation. Consequently, a closer look at the experimental data is warranted.

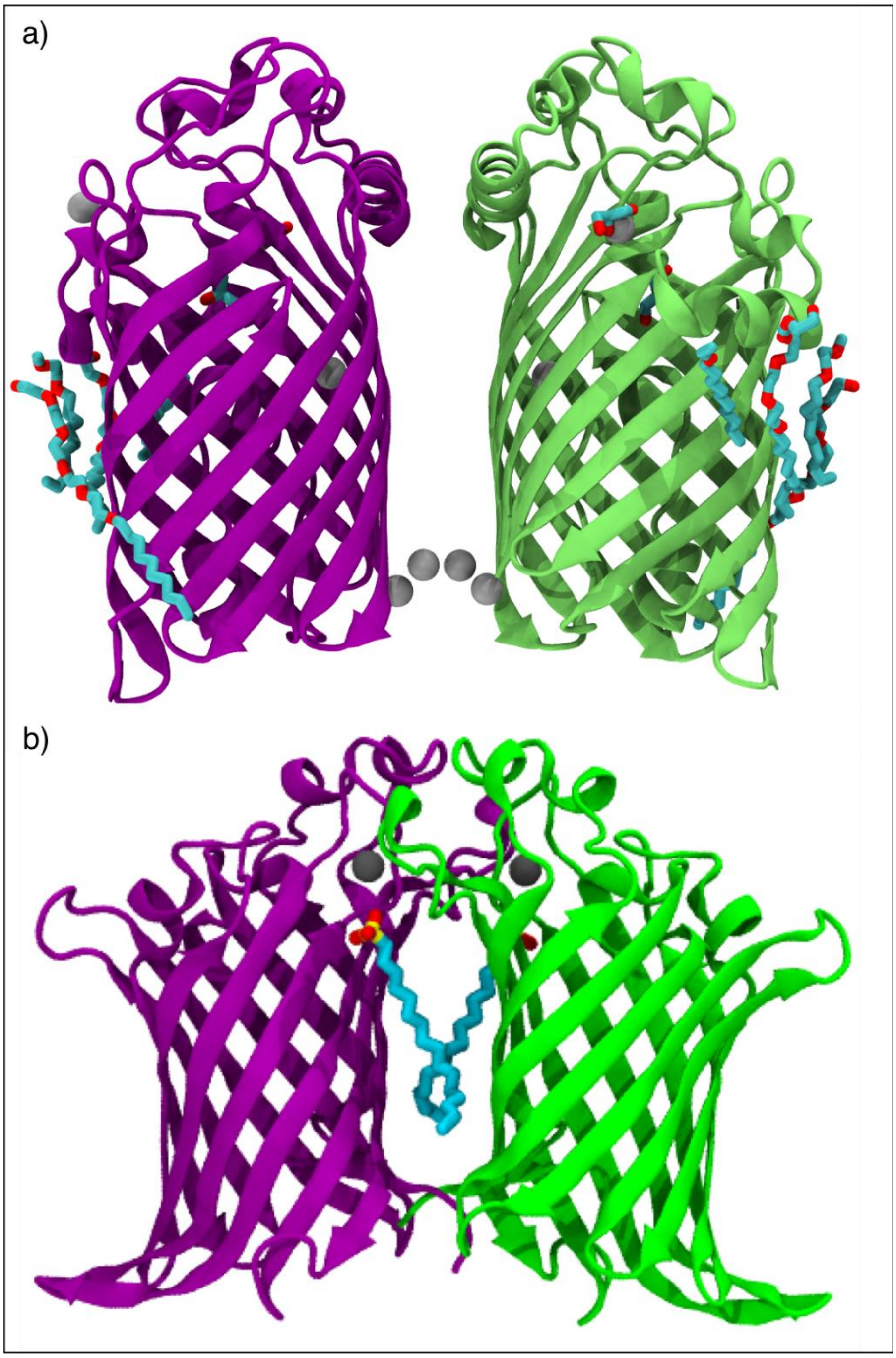

Figure 36. *A comparison of the X-ray crystal symmetric dimers of LpxR and OmpLA, with protein backbones in purple and green, divalent cations in grey and other co-crystallised ligands coloured as the literature standard.* ***36a)*** *the LpxR X-ray structure (3FID), co-crystallised with* Zn^{2+} *ions, glycerol and pentaethylene-glycol-monodecyl-ether.* ***36b)*** *the OmpLA X-ray structure (1QD6), co-crystallised with Ca2+ and 1-hexadecanosulfonic acid.*

When presenting the X-ray structure (PDB 3FID) of LpxR, Rutten *et al.* showed that the OMP formed a highly stable symmetric dimer with an RMSD for all protein atoms of only 0.015 nm. However, they also suggested that the results of their size exclusion chromatography, along with the online tool PISA from EMBL-EBI, negate the possibility of a dimer in solution (163). Despite this, the data they presented does not necessarily negate the existence of a dimer; given that the monomer of LpxR has an approximate mass of ~32 kDa, a dimer would be expected to have a mass of ~64 kDa. In the presented size exclusion chromatography, the recorded n-dodecyl-β-ᴅ-maltoside (DDM) micelle mass was between 39.8 kDa and 76 kDa. The online PISA tool from EMBL-EBI gives a complexation significance score of 0.037 which suggests that the dimer structure is a result of crystal packing. However, it is known that different lipids can encourage different behaviour in proteins (164–167), so although PISA suggests that the asymmetric crystal dimer in its current form is due to crystal packing, it remains to be seen whether a dimer geometry exists *in vivo*. The SDS-PAGE performed by Reynolds *et al.* only showed a protein band at ~32 kDa, consistent with monomeric LpxR without its signal peptide (87). Given that SDS-PAGE will not disrupt covalent bonds, it seems clear that any potential interaction between monomers is non-covalent. While Rutten *et al.* performed mass spectrometry on LPS lipids before and after deacylation, none was performed on LpxR itself. This would have given conclusive proof as to whether a dimer structure exists outside of a crystallised environment.

Due to the lack of availability of the appropriate experimental evidence, molecular dynamics was employed to investigate a potential dimer interface with the proteins in a range of environments. First, to gain the advantage of an extended timescale, coarse-grained systems with two or three copies of LpxR in an Ra LPS-containing membrane were produced. What were the initial orientations of the proteins with respect to each other. However, the thick, gel-like matrix of LPS core sugars, cross-linked via divalent cations proved too much of a barrier for any form of association between protein monomers. The distances between the centre-of-mass of protein copies did not tend to vary across 2 μs simulation at 323 K and this can be seen in **Figures 37a** and **37b**.

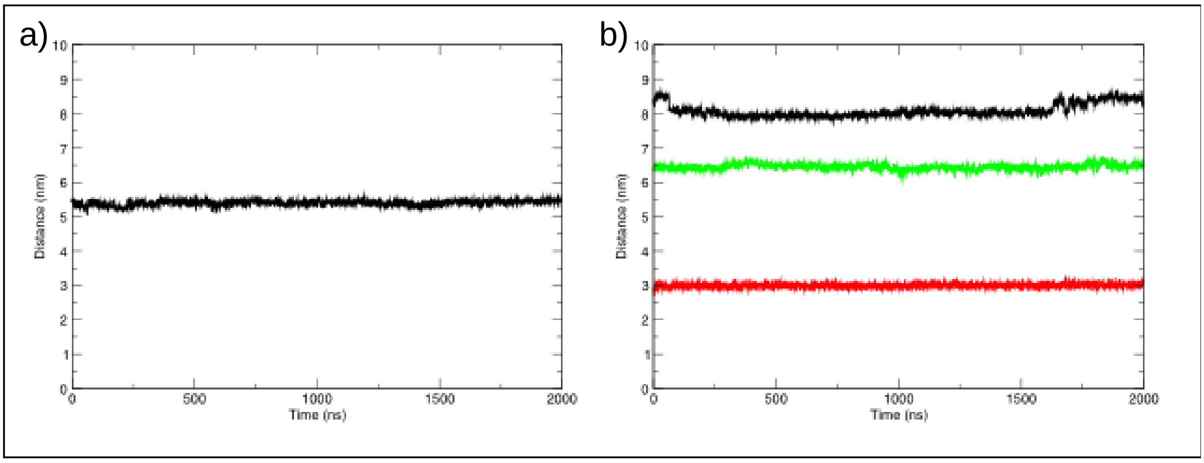

Figure 37a) *The minimum intermolecular distance between LpxR molecules in an Ra LPS membrane in coarse-grain simulations with two protein molecules present.* ***37b)*** *The distance between protein molecules when three copies were present. Black line shows distance between molecules a – b, red b – c, and green a – c.*

At this point, it was decided that a more labile environment must be used for studying potential dimerisation events of OMPs. Ideally, the environment will allow monomers to rotate relative to each other, enabling the identification of a possible dimer interface. Coarse-grained systems with two or three copies of LpxR in a DPPC membrane were produced and run for 10 μs in order to observe protein association. While protein association in "*CG_LpxR x2*" systems was observed within 100 ns, the individual proteins did not dissociate again, nor did they rotate relative to each other. Furthermore, in "*CG_LpxR x3*", two copies of LpxR associated within an average of ~100 ns and the third within an average of ~110 ns, but again dissociation of protein complexes was not observed. This was a repeated occurrence throughout the six independent 10 μs simulations (**Figures 38a** and **38b**). The issue of protein "stickiness" in the MARTINI force field has been investigated in the literature (168) and a potential solution has been advocated for the newest release of the force field, MARTINI 3. This does not mean that these MARTINI-based coarse-grained simulations are without worth, however, as they add further evidence of the phenomenon that membrane thinning can drive protein complexation, or indeed oligomerisation, given a labile enough membrane.

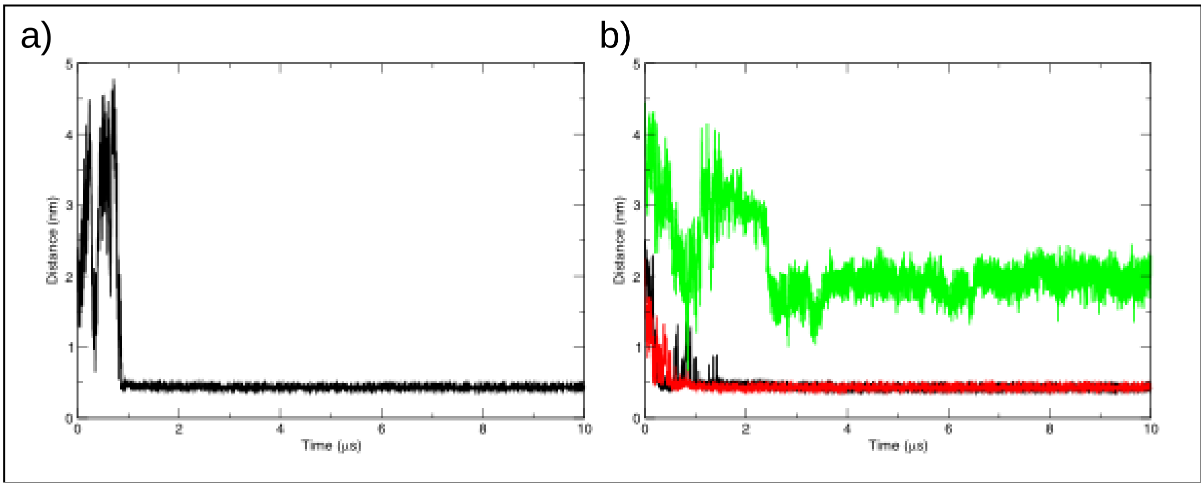

Figure 38a) *The minimum intermolecular distance between LpxR molecules in DPPC membrane in coarse-grain simulations with two protein molecules present.* ***38b)*** *The distance between protein molecules when three copies were present. Black line shows distance between molecules a – b, red b – c, and green a – c.*

The DPPC membrane was used to investigate potential protein oligomerisations due to its long-standing use as a model membrane for molecular dynamics studies of integral membrane proteins (145,146,152). The experimental value for DPPC membrane thickness, as defined by the distance between phosphate headgroups of opposing leaflets, is 3.9 nm. The bulk lipid membrane thickness in these coarse-grained systems was calculated to be ~4.0 nm, in excellent agreement with the experimental value. In systems with two protein molecules, localised membrane thinning was observed in a ~1.2nm radius around the protein complex. This was also seen systems with three protein molecules.

After investigating the diffusion of protein molecules relative to each other, as well as the compound effect exerted by two or three molecules on the coarse-grained DPPC membrane, the next step was to identify any structural rearrangements in the two protein molecules; for this, united-atom resolution simulations were used, with systems set up from scratch. **Figures 39a** and **39b** show the results of 2 μs united atom simulation of two LpxR molecules embedded in DPPC. Of particular note is the presence of DPPC tails between the two protein molecules, but the absence of phospholipid headgroup; this appears to be due to the bulky L3 loops favouring interaction with the neighbouring protein over that with local phospholipids.

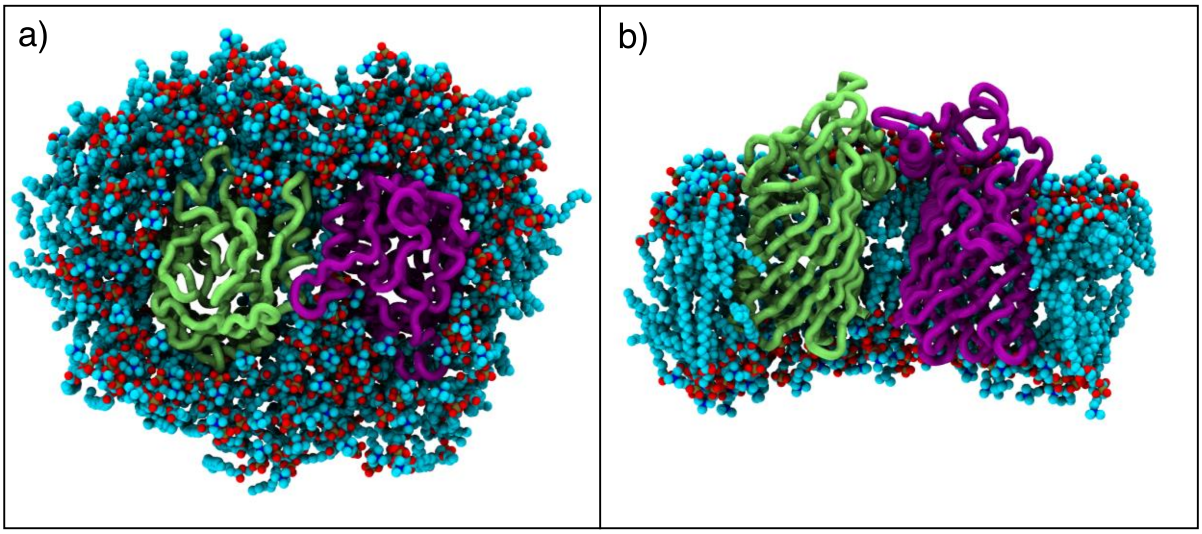

Figure 39a) *Potential LpxR dimer conformation embedded in DPPC after 2 μs at 323 K. Protein backbones shown in purple and green, and DPPC coloured as literature standard.* ***39b)*** *as* ***a*** *but viewing the transmembrane segments of the two protein molecules, with DPPC molecules obstructing the view removed for clarity.*

To assess potential conformational change induced in the protein molecules as a result of dimerisation, the RMSD and RMSF of the backbone of each protein molecule was calculated for united-atom resolution systems. As before, separate RMSD calculations were performed for the barrel and extracellular loops L1 and L3 of the molecules. Particular attention was paid to the conformational arrangement of loops L1 and L3 – if the LPS binding site remained in the "open" conformation, despite the lack of substrate, it may indicate that dimerisation assists in the activation, or at least binding process of the substrate. As in the monomer simulations, the backbone RMSD of the barrel regions of both protein molecules remained ~0.15 nm over the course of the three independent 2 μs simulations. The extracellular loops L1 and L3, which encompass the LPS binding site, exhibited an RMSD of ~0.4 nm, an increase of ~0.1 nm compared with monomer LpxR embedded in DPPC. The results of RMSD calculations are shown in **Figure 40a**. There were only minor discrepancies in the RMSF of the backbone residues of the two protein copies; loops L1, L5 and L6 all exhibited greater flexibility in protein A than in protein B when averaged across the three independent 2 μs simulations. The slight loss of helix-turn-helix conformation of loop L1 in protein A can be seen in **Figure 39b** (purple helix buried in hydrophobic region). There was no significant change in the flexibility of the barrel plug of either protein molecule, as evidenced in the T4 regions of **Figure 40b**. Compared with the protein monomer embedded in DPPC, there was an RMSF increase of ~0.25 nm and ~0.35 nm in the L2 loop of protein A and B respectively. Conversely, in the dimer simulations, an RMSF drop of ~0.12 nm was observed to ~0.3 nm in the L3 loop regions of both protein copies.

Upon visualisation of the united-atom dimer investigation simulations, it appeared that the two protein copies consistently occupied different conformations after 2 μs. In protein A (**Figure 40c**), the conformation of the binding site does not appear to rearrange such that binding of LPS could no longer be envisaged. Indeed, the interatomic distances between the Nε of H122 and the hydroxyl moiety of T34, and between the Nε of H122 and the amine of N9 were ~1.0 nm and ~1.5 nm respectively. Comparing this to the previously identified closed conformation, in which these distances were both <0.5 nm, it appears that protein A remained in its open conformation. However, the conformation of L3 loop of protein B did appear to rearrange such that the binding site was occluded. Here the interatomic distances between the same points of H122 and T34, and H122 and N9 dropped to ~0.3 nm and ~0.5 nm respectively. Crucially, hydrogen bonding was observed between residues D10 and T34, as in the closed monomer conformation; this is shown in **Figure 40d**.

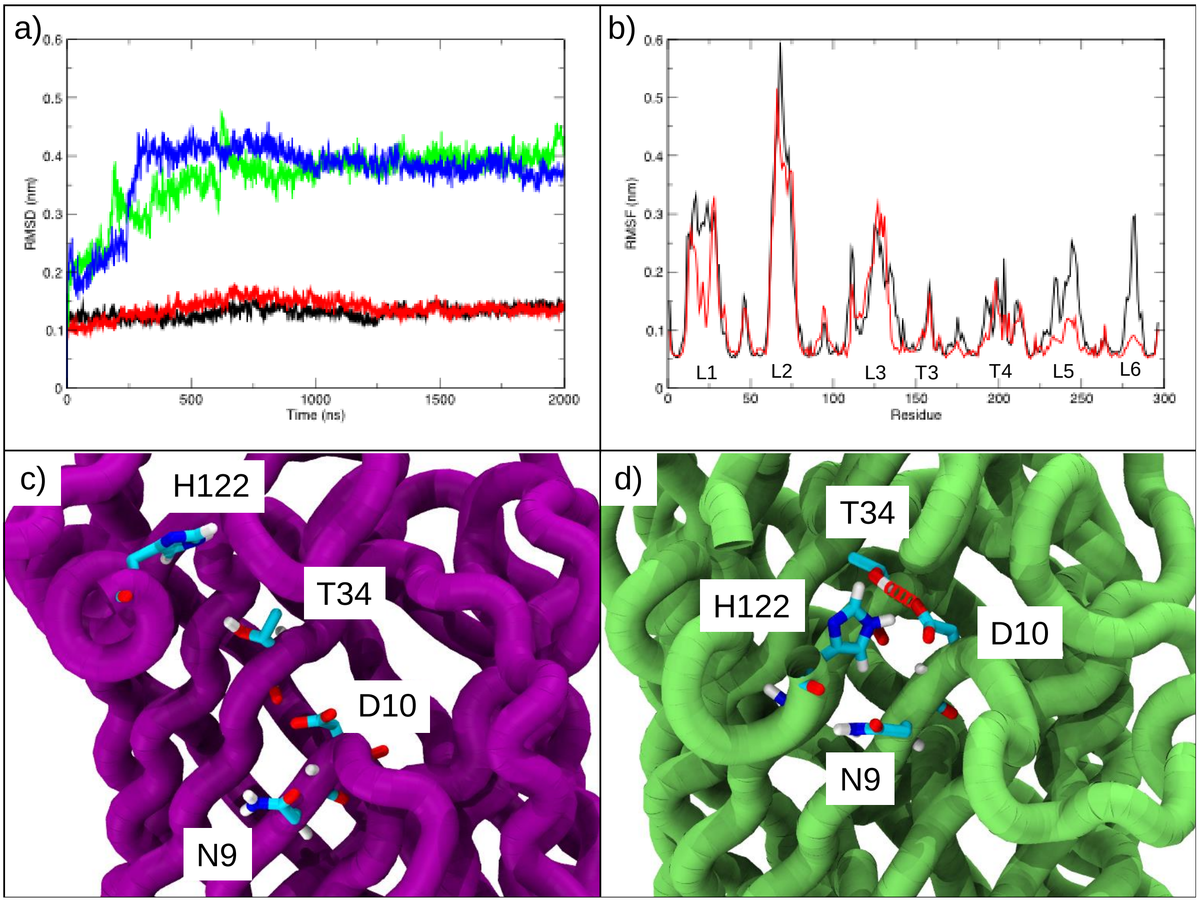

Figure 40a) *RMSD of two LpxR molecules embedded in DPPC over 2 μs at 323 K. Protein A (purple in* ***40c)****) barrel and loop L3 backbone are shown in black and green respectively, and protein B (green in* ***40d)****) barrel and loop L3 backbone are shown in red and blue respectively.* ***40b)*** *RMSF of two LpxR molecules embedded in DPPC over 2 μs at 323 K. Protein A (purple in* ***40c)****) backbone shown in black and protein B (green in* ***40c)****) backbone in red.* ***40c)*** *Showing the conformational arrangement of the binding site of protein A, with backbone in purple and key residues labelled. Residues 123-130 of loop L3 have been removed for clarity.* ***40d)*** *The conformational arrangement of the binding site of protein B, with backbone in green and key residues labelled. Again, residues 123-130 of loop L3 have been removed for clarity.*

After observing the independent conformational rearrangements, the potential causes of these structural effects were investigated, with particular attention paid to any key interactions between the two protein molecules which could mark the dimer interface.

Firstly, all residue contacts between the two protein molecules, as defined by an interatomic distance of ≤0.4 nm, were identified (**Figure 41a**). **Figure 41b** shows that there were a particularly high number of residues within this cut-off distance on the L3 loops of the two proteins, making any key residues in this region difficult to spot. At the base, or periplasmic side of the protein, three pairs of aromatic residues are seen to interact. These residues (Y41, F294 and F296 of protein A and H43, Y41 and F296 of protein B) are found specifically in the region of the protein termini and the observed conformations of the pairs, namely T-shaped and sandwich, may suggest the possibility of π-stacking interactions (169). While evidence of π-stacking interactions is difficult to prove from molecular dynamics calculations, given that electronic configurations are not accounted for, it is certainly not a leap to suggest that this type of interaction could be seen *in vivo*, if indeed a protein dimer exists. These interactions can be seen in **Figure 41c**. Returning to the L3 loops of both proteins, when the charged residues are selectively viewed (**Figure 41d**) another three pairs of residues are seen. These electrostatic interactions are observed consistently over the course of the three independent 2 μs simulations at 323 K.

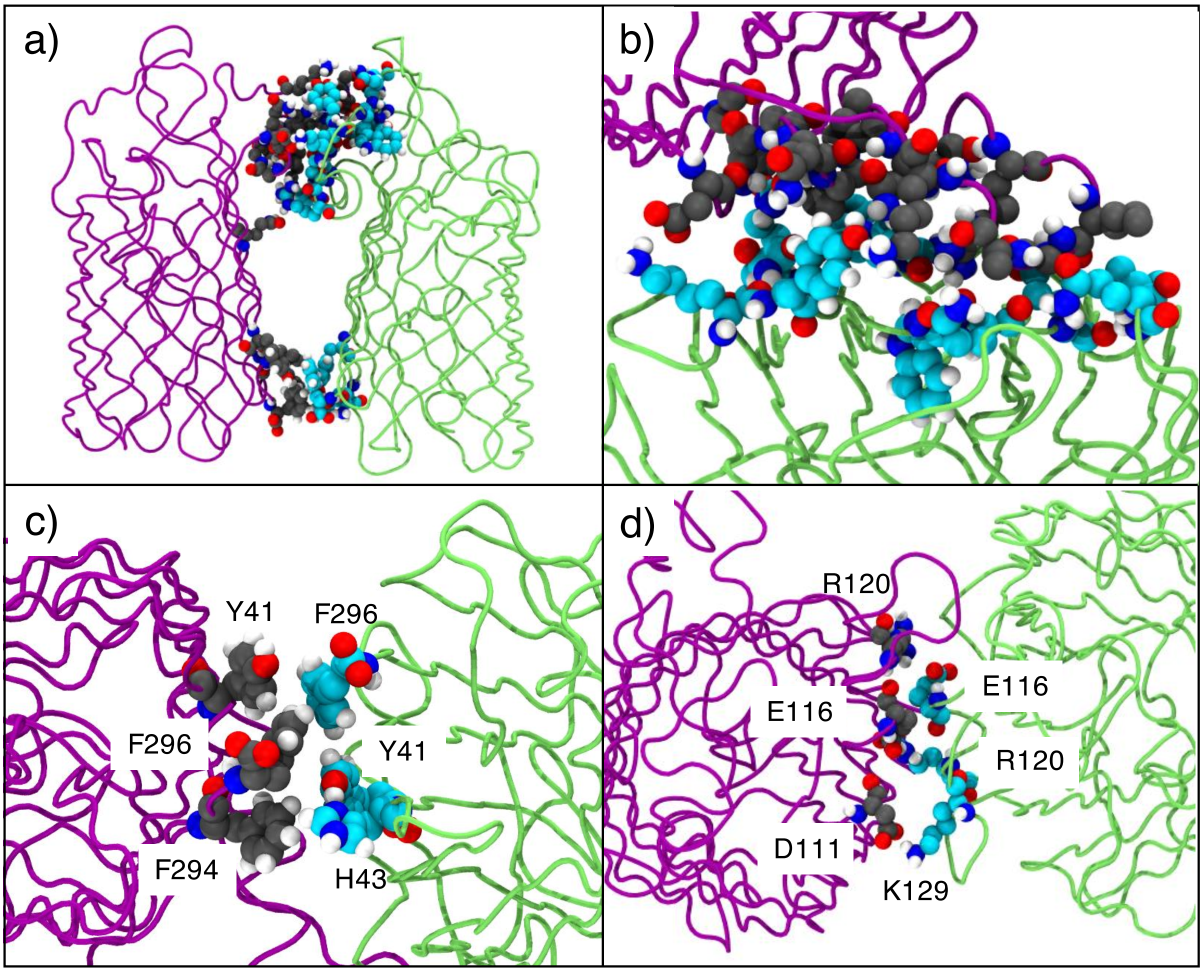

Figure 41. *Showing a potential dimer interface of two LpxR molecules after 2 μs at 323 K embedded in a DPPC membrane.* ***41a)*** *All residues of protein A (purple) within 0.35 nm of protein B (green) have carbons coloured in grey and residues for protein B have carbons coloured in cyan. All other elements are coloured at the literature standard.* ***41b)*** *Colouring as* ***a.*** *but showing electrostatic interactions between residues of loop L3 of the two LpxR molecules.* ***41c)*** *Colouring as previous, but showing interactions at the base, or periplasmic side of the protein.* ***41d)*** *Colouring as previous, showing all residues of loop L3 of each LpxR molecules within 0.35 nm of the other.*

While simulations here certainly show consistent interactions between two LpxR monomers, it remains uncertain as to whether the L3 loop and termini do indeed constitute a dimer interface. For conclusive evidence, an experimental technique such as mass spectrometry could be performed on a solution containing purified LpxR (170,171). For further evidence produced *in silico*, calculations on the free energy of association between LpxR monomers could be performed, provided a reliable force field was used which had replicated similar results (130).

The limitations of the methods employed in this chapter must be examined. Equilibrium molecular dynamics does not allow for the consideration of quantum effects such as polarisation; polarisation is important with regards to histidine-mediated catalysis as with LpxR it is hydrogen bond which activates a mechanistic water for the deacylation event to occur. However, the computational cost of quantum mechanical calculations on an integral membrane protein is enormous and the calculations have very little guidance in the current literature in terms of appropriate methodology. Indeed, this course would likely take the form of transition state searching, as implemented by Lever *et al.* (172). The development of such protocols in the future is an exciting prospect, and could lead to great advancements in the study of embedded membrane enzymes.

The gromos54A7 force field was applied in this chapter, and the ion parameters were unchanged from those in the previous 53A6 force field, which has been used effectively in several protein-ion-binding studies (104,173,174). The depiction of ionic behaviour in classical molecular mechanics is problematic due to the reliance on fixed charge and Lennard-Jones parameters, so are not necessarily a perfect representation of true ionic behaviour.

3.4 Conclusion

LPS modifications are of great importance with regards to microbiology and immunology, given that they can lead to antimicrobial resistance and modulate the host immune response (86,127). The use of equilibrium molecular dynamics in this instance have allowed the evaluation, and subsequent amendment, of a proposed catalytic mechanism for LpxR. Furthermore, a putative closed conformation for the membrane enzyme has been predicted, and the roles that residues in the binding site play in cation coordination have been ascertained. Simulations show that when the Re LPS substrate does not occupy the LpxR binding site, the same residues involved in deacylation form intramolecular hydrogen bonds to occlude the binding site; observed interactions between residues of loop L1 also help to explain the specificity of LpxR for its substrate. Simulations also show the prompt relocation of the removed acyl tail to the inner leaflet, where the molecule is presumably either extracted from the membrane, or metabolised for another purpose. Further to this, the association of LpxR monomers was observed when protein molecules were embedded in a simplistic membrane, most likely driven by the mismatch in hydrophobic area of membrane and protein. However, the same behaviour was not observed in the realistic, asymmetric membrane. While this could suggest that dimer association does not occur *in vivo*, it is also highly likely that the slow-moving nature of LPS molecules in the outer leaflet simply slows down the process, and that association may be observed over simulation timescales not feasible with current computational methods.

The modification of membrane constituents can be used by organisms in the process of homeoviscous adaptation. The deacylation of LPS is highly likely to impact wider membrane properties and dynamics, and is as such the next avenue of discussion in this thesis.

Chapter 4: Assessing the Change in Lipid Dynamics and Membrane Properties as a Result of Lipopolysaccharide Deacylation, and Exploring the Use of the Polarisable MARTINI Water Model in the Context of Electroporating Lipopolysaccharide-Containing Membranes

4.1 Introduction

This chapter investigates the effect of LPS deacylation on the properties of the *E. coli* outer membrane. Results here identify the triggering of membrane curvature and cardiolipin clustering when distinct patches of LPS are deacylated. Further to this, an electroporation protocol for complex LPS-containing membranes at the coarse-grained resolution was validated against a previously published atomistic resolution study.

Membrane integrity is fundamental for cellular survival. If the membrane around a cell deteriorates, the ability of the cell to sequester cellular processes such as respiration can fail, and the organism may die. The basis of this sequestration lies in the amphipathic nature of the membrane constituents, which are non-covalently linked together in the fluid phase through both electrostatic and hydrophobic interactions. These constituents are lipids and typically of three classes; phospholipids, glycolipids and sterols (26,175,176). In bacteria, the role of sterols is taken by the functional homologues hopanoids, which regulate membrane fluidity (81,82,177).

Perhaps the greatest consideration when discussing the properties of a given membrane is the particular species of lipid present, as this will determine the phase transition temperature of the membrane (178,179). Membranes typically consist of a mixture of phospholipid species *in vivo*, which can lead to the phenomenon of phase separation occurring, in which a confined region of lipids undergo phase transition (180,181); phase separation can be utilised for biochemical processes, as integral proteins may diffuse into the transitioned area, or even trigger the transition through the localised ordering of lipid acyl tails (182). In eukaryotes, phase separation can be observed around clusters of proteins in lipid rafts, which are thought to occur for the purpose of signal transduction (183,184). This phenomenon was shown to occur in bacteria as well, in the form of functional membrane microdomains (FMMs); FMMs develop in a similar process to eukaryotic lipid rafts, with their formation triggered by the clustering of macromolecules such as proteins, lipids or hopanoids. The formation of FMMs appears to be entropically driven, and a result of lipid sorting (185). As well as the formation of microdomains within a membrane, bacterial species may regulate their membranes through homeoviscous adaptation (24); in order to maintain fluidity, the proportion of unsaturated acyl tails, or concentration of lipid species with a lower liquid-gel phase transition temperature may be increased in the membrane, as evidenced in **Figure 42**.

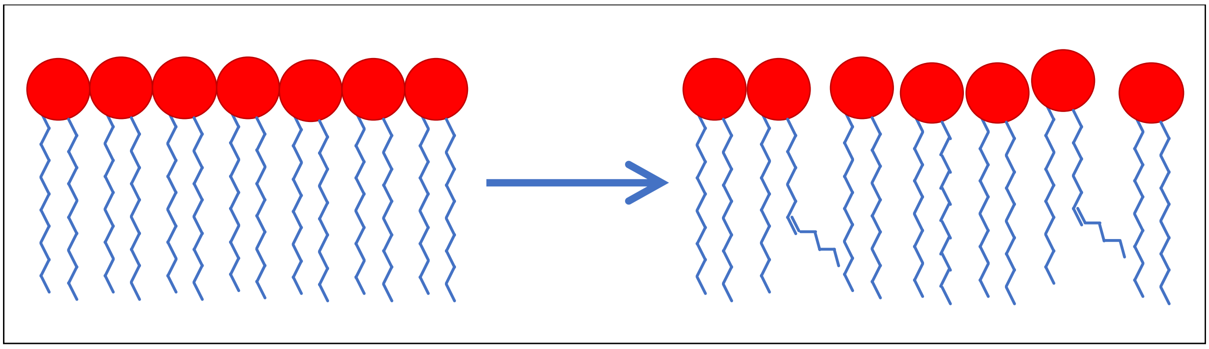

Figure 42. *An increase in unsaturated acyl tails leads to increased membrane fluidity due to steric hindrance. Ordered packing of neighbouring phospholipid acyl tails is also disrupted due to steric hindrance.*

Integral membrane proteins may exert a stabilising or disruptive effect on the lipid ordering in their local membrane environment; this was shown in the previous chapter concerning the OMP LpxR, which disrupts the ordering of surrounding lipids due to the hydrophobic mismatch between the protein barrel and adjacent acyl tails. Other OMPs may have specific phospholipid binding domains which can trigger the clustering of certain phospholipids in the inner leaflet around the protein (186). This in turn may be used for signal transduction. In eukaryotes, the clustering of phosphatidylinositol phospholipids can prompt the association of signalling proteins to the membrane, which can in turn propagate a signal further into the cytoplasm (187). In prokaryotes such as *E. coli*, the clustering of cardiolipin may play a similar role, stimulating the interaction of soluble periplasmic proteins with the inner leaflet of the OM.

In the context of the OM, membrane integrity is reinforced by the network of electrostatic interactions between sugar moieties of neighbouring LPS molecules in the outer leaflet (139); some of these sugars are phosphorylated and cross-linked together by divalent cations. In comparison, the inner leaflet is composed of a mixture of phospholipids which are not as chemically complex as LPS. Different types of LPS will confer different levels of membrane integrity; deep-rough, rough and smooth LPS have increasing numbers of sugar moieties and therefore increasing opportunities for electrostatic interactions. A size comparison of PE against some of the different wildtype LPS chemotypes can be seen in **Figures 43a** to **43d**. The increased complexity of the OM poses a problem for contemporary computational methods, as LPS is represented by sometimes frustratingly slow dynamics (188–190). Indeed, Shearer *et al.* showed that even coarse-grained resolution OM models required up to 20 μs to equilibrate (186). Given that simulating LPS is vital for understanding the function of integral OMPs, as well as understanding bacterial behaviour, researchers may attempt to overcome the problems through scaling the LPS intermolecular interactions or the ionic strength of divalent cations (191).

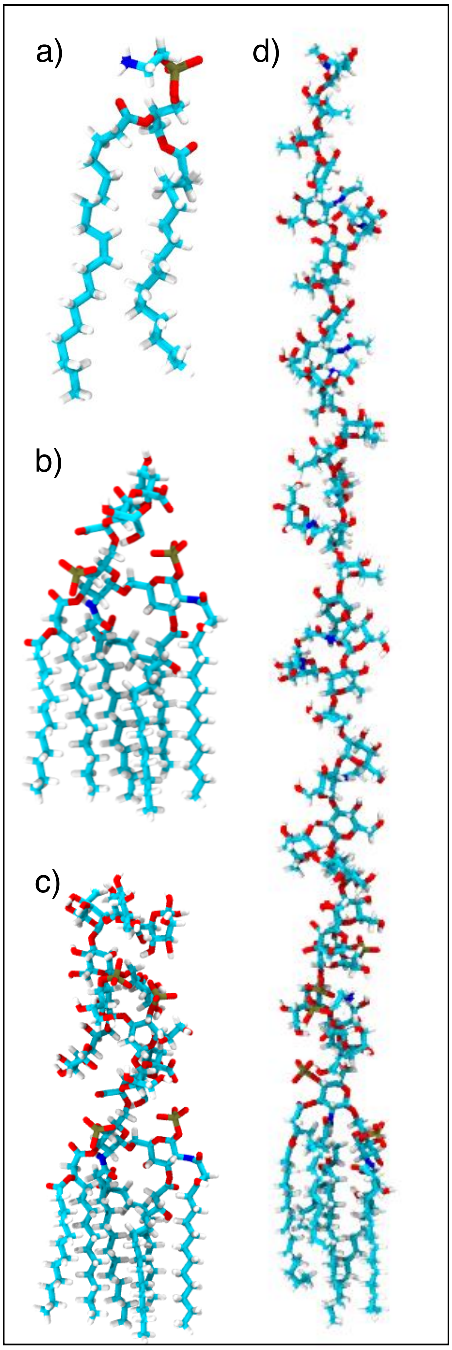

Figure 43. *Representations of the chemical structure of naturally occurring Gram Negative outer membrane lipids.* ***43a)*** *a phosphatidylethanolamine phospholipid.* ***43b)*** *deep rough LPS.* ***43c)*** *rough LPS.* ***43d)*** *smooth LPS.*

Due the complexity of the OM, Gram negative bacterial species have decreased permeability to larger charged molecules. This barrier can be overcome *in vivo* with the application of an external electric field, which causes the formation of a water channel across the membrane and can allow the larger molecules to traverse. This may be performed in the protocol of transfecting cell cultures in genetic studies (192). The process of electroporation has also been studied *in silico*, with an assortment of simplistic and complex membranes (139,193,194). Particularly of note here are the united-atom resolution simulations by Piggot *et al.* which involved electroporation of an asymmetric Rd_1 type LPS membrane (139). The literature shows that electroporation is preceded by the initial formation of a membrane defect by a single-file channel of water molecules attempting to cross the hydrophobic membrane core (195). This movement of water is stabilised through their interaction with hydrophilic lipid headgroups from the membrane leaflet containing the defect. The hydrophilic headgroups of opposing leaflets then interact with one another, leading to the membrane pinching and a pore forming. This allows water, ions and any other molecules to flow through. A representation of this process can be seen in **Figure 44**. Piggot *et al.* also observed that electroporation of Rd_1 LPS-containing membranes was consistently preceded by movement of inner leaflet phospholipids into the membrane core, rather than LPS (139).

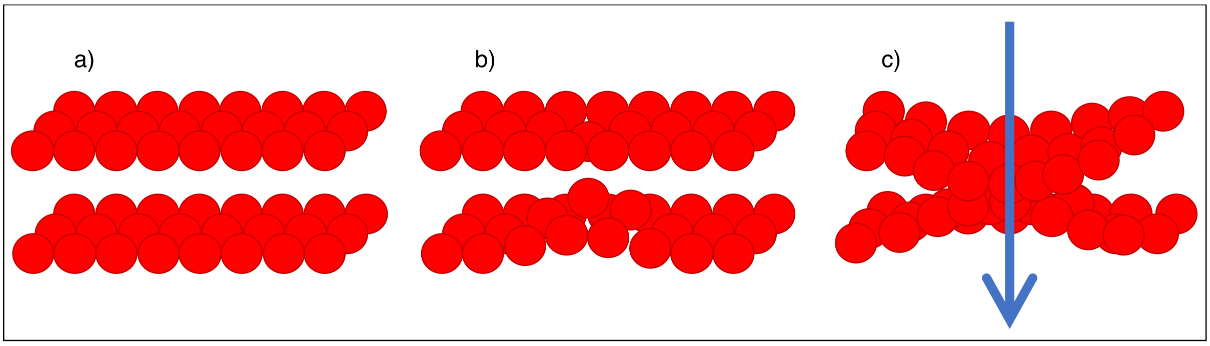

Figure 44. *An illustration of pore formation induced by electrical current in a simplistic, symmetric membrane, with phospholipid headgroups represented by red circles and acyl tails omitted for clarity.* ***44a)*** *membrane integrity is maintained, so large and charge molecules cannot diffuse through.* ***44b)*** *pore formation is preceded by a membrane defect. A phospholipid from either leaflet moves towards the bilayer core, and is accompanied by water molecules.* ***44c)*** *phospholipids rearrange such that headgroups of phospholipids from opposing leaflets are able to interact. Headgroups*

line the pore, enabling larger, charged molecules to cross the membrane. Arrow suggests molecular flow through membrane pore.

Electroporation has also been studied at the coarse-grained resolution. Yesylevskyy *et al.* developed the polarisable MARTINI water model (PW) which, when used in conjunction with an electric field, reproduces data from atomistic resolution simulation studies well for simplistic lipid bilayer systems (119). Another valuable property of PW is its resistance to the freezing problem exhibited with the standard MARTINI water model (NW) (98). A procedure not yet performed to date is the application of an electric field to a complex membrane such as the OM studied in this thesis, solvated with PW. This chapter has the following aims: 1) evaluate data produced from coarse-grained simulations of wildtype LPS membranes solvated with PW, compared with NW and atomistic simulations solvated with simple point-charge (SPC) water 2) assess the effect of LPS deacylation on lipid dynamics and on the OM bilayer as a whole and 3) attempt to reproduce data from an atomistic study of OM electroporation with coarse-grained PW simulations. Similarly, results of the simulations performed in this chapter will be presented in appropriate sections.

4.2 Methods

4.2.1 Coarse Grain Simulation Protocols

Membrane System Set-Up

In this chapter, a variety of asymmetric membranes were tested. For investigations into the wildtype membrane, LPS species with the full complement of O-antigen sugars (OANT), the full core segment (RAMP) or the only the inner core segment (REMP) were used for the outer leaflet of OM models. For investigations into the consequences of LPS deacylation, the deacylated Re LPS model (as described in the previous section) was used in the outer leaflet at a ratio of 1:3, 1:1 or 3:1 with wildtype Re LPS. In systems with a wildtype to deacylated Re LPS ratio of 1:1, three conditions were developed in order to compare lateral diffusion of the molecules. The deacylated LPS molecule, along with the starting configurations of the various mixed membranes can be seen in **Figures 45a** to **45f.** LPS membrane systems with OmpA embedded were obtained from Jon Shearer and further equilibrated for 5 μs (112). All simulations in this chapter were performed using the GROMACS molecular dynamics software package (version 2016.3) (114).

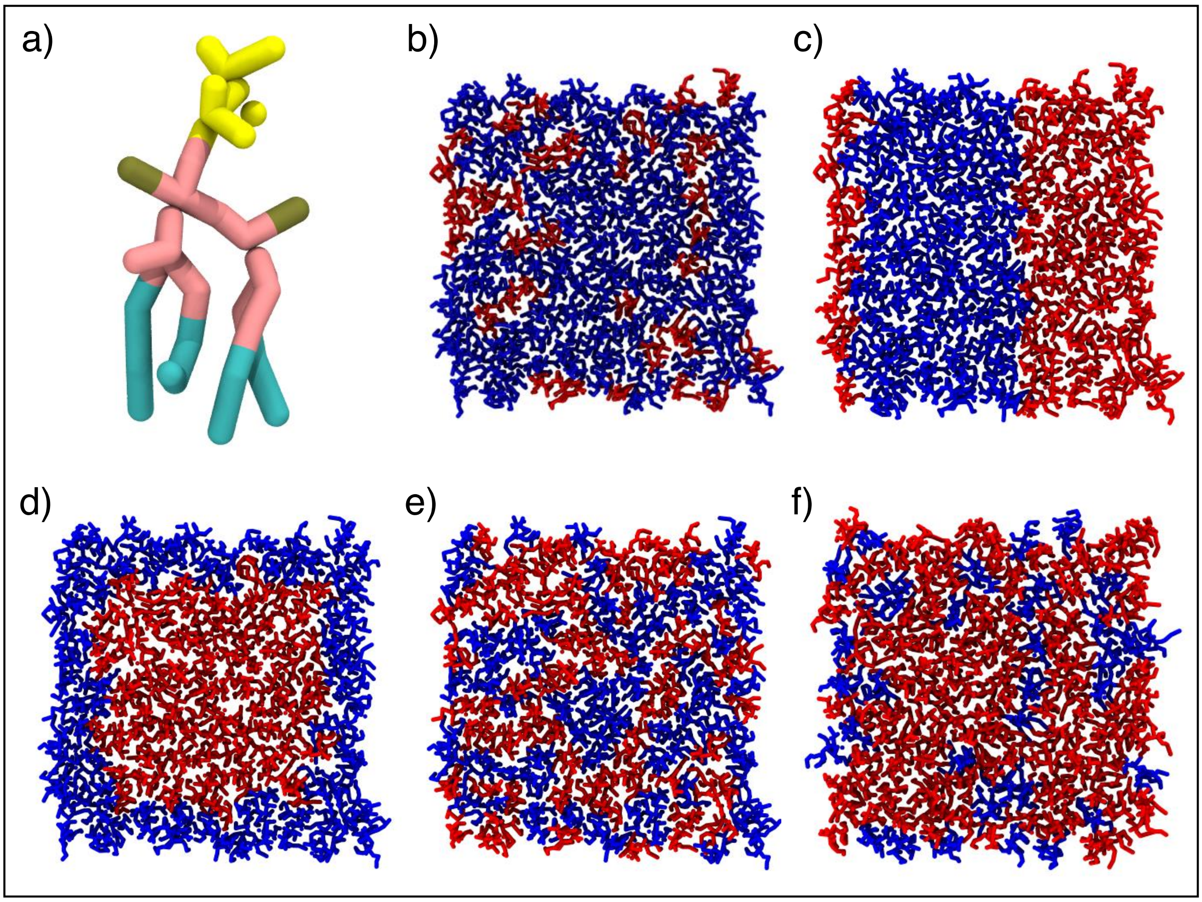

Figure 45. *The coarse-grained deacylated Re LPS model. 45**a)** a representative conformation of a deacylated Re LPS molecule parameterised for the MARTINI force field, coloured as follows: lipid A tails are cyan, lipid A sugars are pink, phosphate groups are tan and the inner core moieties are yellow.* ***45b)*** *an extracellular view of the starting configuration of the 25% deacylated Re LPS membrane* ***45c)*** *the starting configuration of the 50% deacylated Re LPS membrane, with modified lipids in a strip.* ***45d)*** *the starting configuration of the 50% deacylated Re LPS membrane, with modified lipids in a distinct patch.* ***45e)*** *the starting conformation of the 50% deacylated Re LPS membrane, with modified lipids randomly distributed throughout the* xy *plane.* ***45f)*** *the starting configuration of the 75% deacylated Re LPS membrane.*

Wildtype membrane systems were generated using the CHARMM-GUI online MARTINI Maker tool and solvated with either normal (NW) or polarisable (PW) MARTINI water (98,119,196). For membrane systems with deacylated Re LPS, molecules were selected from a wildtype Re LPS membrane and manually deacylated. Inner leaflet modifications were made over four separate steps, with a quarter of the required lipids being removed and the resultant membrane being equilibrated at each step.

All coarse-grained membrane systems were energy minimised using the steepest descent algorithm for a maximum of 50,000 steps. Systems were then subjected to three rounds of 100 ns in the NPT ensemble with a timestep of 5 fs, 10 fs and then 20 fs, before final equilibration in the NPT ensemble for 500 ns at 310 K. After equilibration, production runs of either 5, 10 or 20 μs were performed at 310 K and 323 K. During equilibration and production of PW systems, long-range electrostatic interactions were treated with the smooth particle mesh Ewald (PME) algorithm (197).

4.2.2 Atomistic Simulation protocols

Membrane System Set-Up

Re LPS and Ra LPS membrane systems obtained from Tom Piggot were pre-equilibrated, and had been previously simulated in the NPT ensemble for 2 μs at 310 K (198). These systems were then re-solvated with SPC water. Before further equilibration, all systems were subject to energy minimisation using the steepest decent algorithm to a maximum of 50,000 steps. After equilibration of all systems for 50 ns in the NPT ensemble, production runs of 500 ns were run. Details of the coarse-grained and united-atom simulations performed with equilibrium molecular dynamics can be found in **Table 3**.

Table 3. *All equilibrium molecular dynamics simulations performed in this chapter. Each asymmetric membrane has an inner leaflet composed of 90% PE, 5% PG and 5% cardiolipin. All simulations performed at 310 K (x2) and 323 K (x1)*

System	**Notes**	**Water Model**	**Length of Simulation**
AT_REMP	United-atom resolution asymmetric Re LPS membrane	SPC	500 ns (x3)
AT_RAMP	United-atom resolution asymmetric Ra LPS membrane	SPC	500 ns (x3)
CG_REMP	Coarse-grained resolution asymmetric Re LPS membrane	NW	20 µs (x3)
		PW	20 µs (x3)
CG_RAMP	Coarse-grained resolution asymmetric Ra LPS membrane	NW	20 µs (x3)
		PW	20 µs (x3)
CG_OANT	Coarse-grained resolution asymmetric LPS membrane with O-antigen	NW	10 µs (x3)
		PW	10 µs (x3)
CG_qDEMP	Coarse-grained resolution asymmetric Re LPS membrane, with 25% of Re LPS molecules deacyated at the 3' O position	PW	20 µs (x3)
			20 µs (x3)
CG_hDEMPa	Coarse-grained resolution asymmetric Re LPS membrane, with 50% of Re LPS molecules deacyated at the 3' O position in a distinct strip	PW	20 µs (x3)
			20 µs (x3)
CG_hDEMPb	Coarse-grained resolution asymmetric Re LPS membrane, with 50% of Re LPS molecules deacyated at the 3' O position in a distinct patch	PW	20 µs (x3)
			20 µs (x3)
CG_hDEMPc		PW	20 µs (x3)

	Coarse-grained resolution asymmetric Re LPS membrane, with a random 50% of Re LPS molecules deacyated at the 3' O position		20 μs (x3)
CG_tqDEMP	Coarse-grained resolution asymmetric Re LPS membrane, with 75% of Re LPS molecules deacyated at the 3' O position	PW	20 μs (x3)
			20 μs (x3)
CG_DEMP	Coarse-grained resolution asymmetric Re LPS membrane, with 100% of Re LPS molecules deacyated at the 3' O position	PW	20 μs (x3)
			20 μs (x3)

4.2.3 Electric Field System Set-Up

The coordinates of representative membrane systems after 10 or 20 μs simulation, solvated with PW, were used as a starting point for the application of electric fields of strength 0.2 – 0.5 V/nm. Systems were then simulated at 310 K for 200 ns, or until the periodic box became unstable due to membrane deterioration due to electroporation. If no electroporation was observed, the simulation was extended to 1 μs. An electric field was only applied to membrane systems solvated with PW as electroporation is initiated by water movement followed by phospholipid rearrangement. As NW does not contain partial charges, using it to solvate a system with an electric field applied is not expected to replicate atomistic resolution results, with poration being initiated by a membrane defect caused by water. Details of all simulations with an electric field applied can be found in **Table 4.**

Table 4. *All simulations performed in this chapter with an electric field applied. Inner leaflet unless specified is as previously described. All simulations performed at 310 K.*

System	**Notes**	**Field Strength (V/nm)**	**Length of Simulation**
AT_REMP	64x Re LPS lipids in outer leaflet. United-atom resolution.	0.2	1 µs (x1), 200 ns (x2)
		-0.2	1 µs (x1), 200 ns (x2)
		0.3	1 µs (x1), 200 ns (x2)
		-0.3	1 µs (x1), 200 ns (x2)
		0.4	1 µs (x1), 200 ns (x2)
		-0.4	1 µs (x1), 200 ns (x2)
		0.5	200 ns (x3)
		-0.5	200 ns (x3)
AT_RAMP	64x Ra LPS lipids in outer leaflet. United-atom resolution.	0.2	1 µs (x1), 200 ns (x2)
		-0.2	1 µs (x1), 200 ns (x2)
		0.3	1 µs (x1), 200 ns (x2)
		-0.3	1 µs (x1), 200 ns (x2)
		0.4	1 µs (x1), 200 ns (x2)
		-0.4	1 µs (x1), 200 ns (x2)
		0.5	200 ns (x3)
		-0.5	200 ns (x3)

CG_REMP	142x Re LPS lipids in outer leaflet. Coarse-grained resolution.	0.2	1 µs (x1), 200 ns (x2)
		-0.2	1 µs (x1), 200 ns (x2)
		0.3	200 ns (x3)
		-0.3	200 ns (x3)
		0.4	200 ns (x3)
		-0.4	200 ns (x3)
		0.5	200 ns (x3)
		-0.5	200 ns (x3)
CG_REMP_OmpA	Asymmetric Re LPS membrane with N-terminal domain of OmpA embedded. Coarse-grained resolution.	0.1	5 µs (x1)
		-0.1	5 µs (x1)
		0.15	1 µs (x1)
		-0.15	1 µs (x1)
CG_RAMP	112x Ra LPS lipids in outer leaflet. Coarse-grained resolution.	0.2	1 µs (x1), 200 ns (x2)
		-0.2	1 µs (x1), 200 ns (x2)
		0.3	200 ns (x3)
		-0.3	200 ns (x3)
		0.4	200 ns (x3)
		-0.4	200 ns (x3)
		0.5	200 ns (x3)
		-0.5	200 ns (x3)
CG_RAMP_OmpA	Asymmetric Ra LPS membrane with N-terminal domain of OmpA embedded. Coarse-grained resolution.	0.1	5 µs (x1)
		-0.1	5 µs (x1)
		0.15	1 µs (x1)
		-0.15	1 µs (x1)

CG_OANT	105x O-antigen LPS lipids in outer leaflet. Coarse-grained resolution.	0.2	1 μs (x1), 200 ns (x2)
		-0.2	1 μs (x1), 200 ns (x2)
		0.3	200 ns (x3)
		-0.3	200 ns (x3)
		0.4	200 ns (x3)
		-0.4	200 ns (x3)
		0.5	200 ns (x3)
		-0.5	200 ns (x3)
CG_hDEMPa	71x wildtype and 71x deacylated Re LPS lipids in outer leaflet. Deacylated LPS molecules in distinct strip. Coarse-grained resolution.	0.3	200 ns (x3)
		-0.3	200 ns (x3)
CG_hDEMPb	71x wildtype and 71x deacylated Re LPS lipids in outer leaflet. Deacylated LPS molecules in distinct patch. Coarse-grained resolution.	0.3	200 ns (x3)
		-0.3	200 ns (x3)
CG_Inner	75% POPE, 20% POPG and 5% cardiolipin even distributed between two leaflets. Coarse-grained resolution	0.3	200 ns (x3)
		-0.3	200 ns (x3)

4.2.4 Analytical Techniques

System densities, mean squared displacement (MSD) and solvent accessible surface area (SASA) were calculated using in-built GROMACS tools and systems were visualised using the Visual Molecular Dynamics software (114,199). In the electroporation protocol, voltages generated were calculated from the mean membrane thickness and the electric field strength applied.

The membrane thickness, as well as the area per lipid (APL) for membrane lipids, were calculated using the *fatslim* script (200). Membrane thickness is calculated using neighbourhood-averaged coordinates in order to account for fluctuations due to membrane curvature. The membrane thickness is still defined at the distance between upper and lower leaflet phosphates, but the local membrane normal is calculated for each lipid to limit anomalous results. APL is calculated starting with a neighbour search and gaging of the local membrane normal, before calculation of the Voronoi cell corresponding to the reference lipid. Phosphate beads are used as the point of reference for each lipid. This area is used as an accessible area approximation for the lipid. Membrane area can also be calculated using the length of the *xy* axes of the periodic box, although this method is not appropriate for curved membranes.

4.3 Results and Discussion

4.3.1 Evaluation of the Coarse-Grained Polarisable MARTINI Water Model with Respect to Complex Membranes

A strong, defined hydrophobic-hydrophilic interface is one of the key features of biological membranes which allow them to perform their cellular function. It is therefore vital that this behaviour is replicated in any theoretical models if the results are to be relied upon. As it is computationally inexpensive, the standard MARTINI water model is often chosen for coarse-grained studies. While the approximation of four water molecules as one van der Waals particle enables the user increased timescales in their simulations, it also leads to a number of physically unrealistic behaviours. For example, standard MARTINI water often freezes at temperature above 273.15 K, meaning that antifreeze particles must be added to simulation systems to prevent this.

The polarisable water (PW) model enables a much greater level of hydration of LPS core and O-antigen sugars than the standard coarse-grained MARTINI water (NW) model. This increased solvation is more apparent in the Ra and O-antigen type LPS membrane models, as seen in **Figures 46a** to **46c**. The Gram negative OM is often coated by further layers of sugars and peptides *in vivo*, and it is important that an accurate model for describing interactions between these materials and water is ascertained *in silico*. This outer coating is often referred to as the S-layer, and consists of proteins and glycoproteins (201).

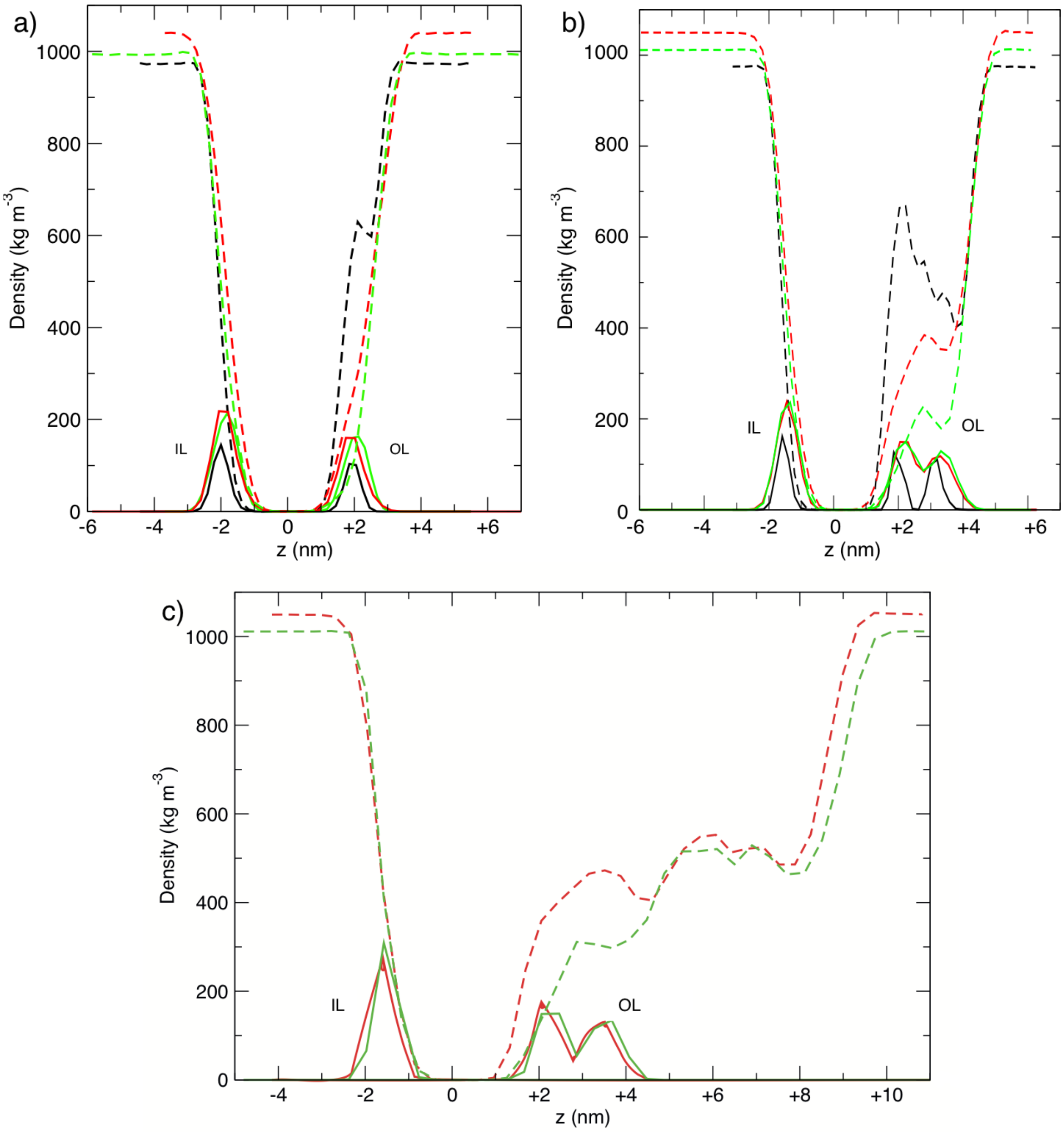

Figure 46. *Density profiles along system z axis for water (dashed line) and phosphate moieties (solid line) for SPC (black), PW (red) and NW (green) solvated Re (**46a)**), Ra (**46b)**) and OANT (**46c)**) LPS-containing, asymmetric membrane systems. Inner and outer leaflet phosphates are annotated with IL and OL respectively.*

The greatest differences in the level of solvation by each of the water models is seen at the core sugar region of the LPS molecules. The SPC and, to a lesser degree, PW models are able to hydrate the lipid A headgroup regions of the LPS lipids in the outer leaflet, whereas the NW model is mostly excluded from this region. There was no noticeable difference in the hydration of the inner leaflet phospholipid headgroups. Further to the evidence provided in the *z* axis density plots of **Figure 46** and **Figures 47a** to **47c** show the interactions between polarisable MARTINI water and the different LPS chemotypes studied here. United-atom and all-atom studies frequently report a network of hydrogen bonds between neighbouring LPS molecules and also with water (139,202,203). The improved ability of the polarisable MARTINI water to interact with the core and O-antigen sugars of LPS is encouraging for this reason, as it enables accurate solvation of these sugar regions.

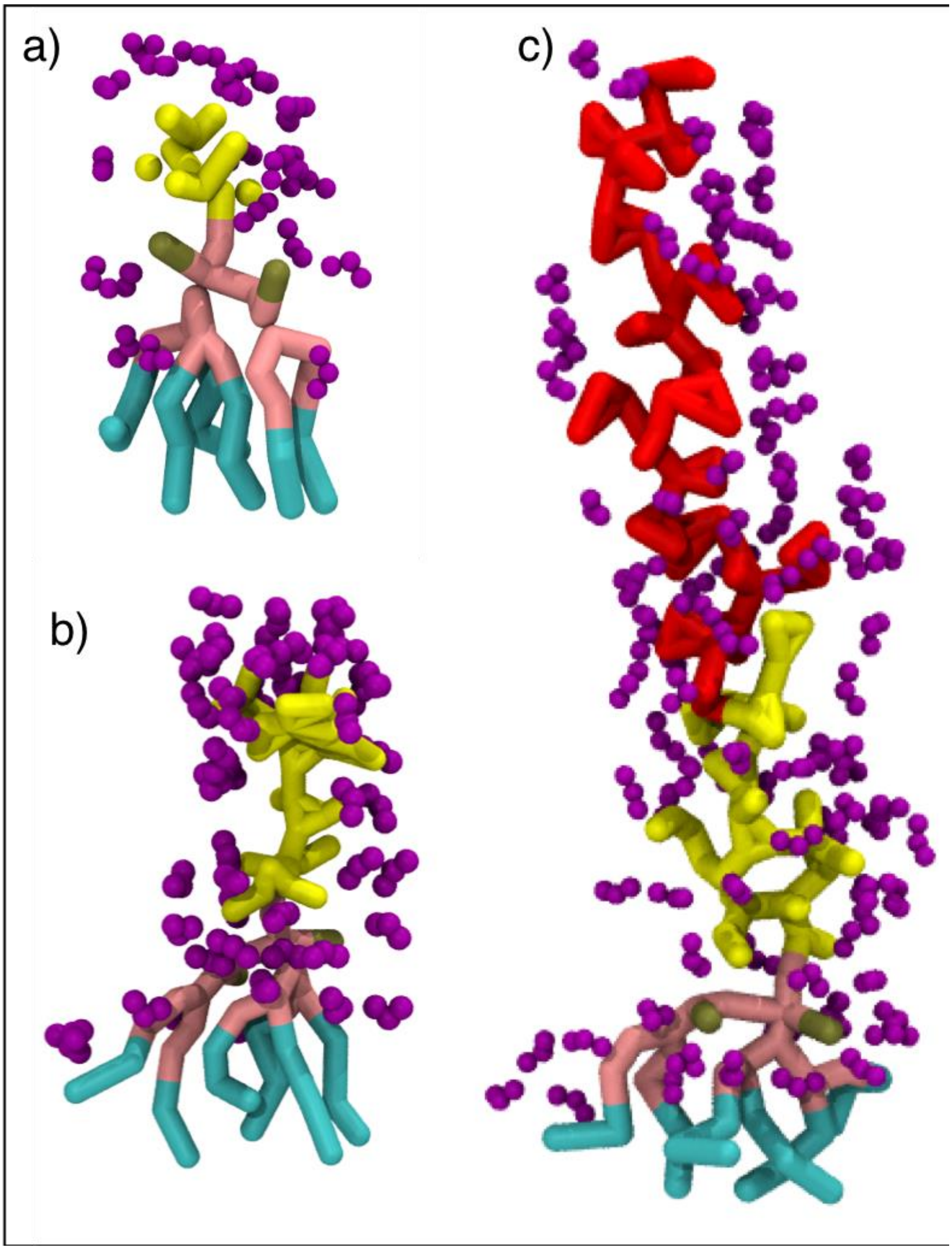

Figure 47. *Interaction of MARTINI polarisable water with Re (**47a**), Ra (**47b**) and O-antigen (**47c**) type LPS chemotypes.*

Wider membrane properties were tested as a further comparison between the united-atom SPC water model and the coarse-grained standard and polarisable MARTINI water models. The area per lipid (APL) is often used in the literature as a measure of system property convergence and, as such, is displayed here (112,204,205). Unfortunately there is a degree of disparity between each of the three models, with

APL values of 1.57 (±0.01) nm^2, 1.6 (±0.01) nm^2 and 1.76 (±0.02) nm^2 for the SPC, NW and PW solvated Re LPS membrane systems respectively. Closer values are seen for the NW and SPC water models, and this is further evidenced in **Figures 48a)** and **48b),** in which APL values are plotted against simulation time. In the Ra LPS membranes, APL values of 1.6 (±0.01) nm^2, 1.68 (±0.01) nm^2 and 1.78 (±0.01) nm^2 were observed for the SPC, NW and PW solvated membranes. APL values for Ra LPS lipids over the simulation time can be seen in **Figures 48c)** and **48d).** The APL values for the O-antigen LPS systems solvated with NW and PW were 1.75 (±0.02) nm^2 and 1.84 (±0.01) nm^2 respectively. Experimentally, the area per hydrocarbon tail has been given at approximately 0.26 nm^2 for LPS in liquid-crystalline bilayers (206). Here the systems solvated with SPC and NW models are in closest, with values of 0.26 nm^2 and 0.27 nm^2 respectively.

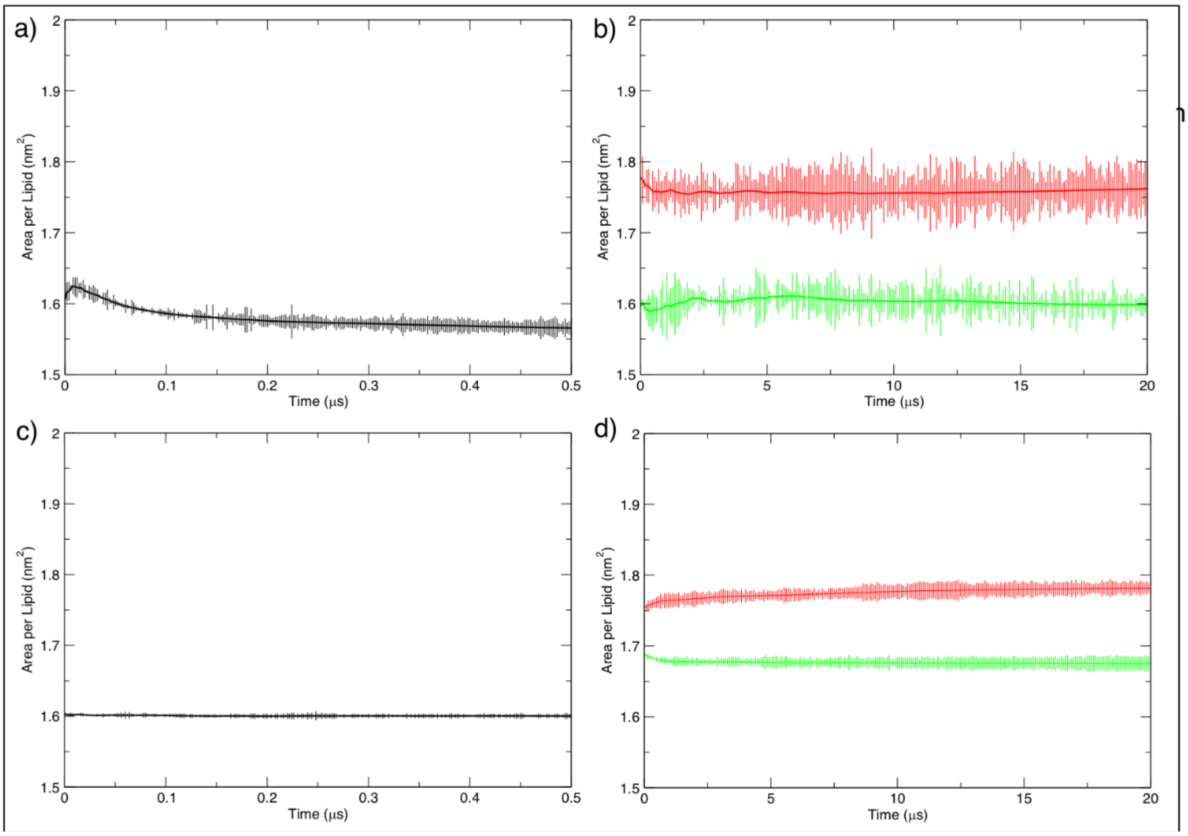

Figure 48. *Area per lipid (APL) profiles for LPS molecules in LPS-containing asymmetric membrane systems, with rolling average and standard error fitted* ***48a).*** *APL for Re LPS in united-atom systems solvated with SPC water* ***48b).*** *APL for Re LPS in systems solvated with polarisable MARTINI water (red) and normal MARTINI water (green)* ***48c).*** *APL for Ra LPS in united-atom systems solvated with SPC water* ***48d).*** *APL for Ra LPS in systems solvated with polarisable MARTINI water (red) and normal MARTINI water (green).*

Membrane thickness was also calculated for these membrane systems. Similar disparities were observed, with mean thickness values of 3.94 (±0.08) nm, 3.81 (±0.01) nm and 3.76 (±0.01) nm for the SPC, NW and PW solvated Re LPS membrane systems respectively over the last 10% of simulation time, averaged for repeats. In the Ra LPS membrane systems, the coarse-grained resolution membrane solvated with PW produced a closer membrane thickness value to that of the SPC-solvated united-atom system. Mean thickness values here were 3.83 (±0.01) nm, 4.63 (±0.43) nm and 3.84 (±0.08) nm for the SPC, NW and PW solvated systems respectively. Finally, in the O-antigen LPS membrane systems, mean thickness values were 3.65 (±0.04) nm and 4.03 (±0.02) nm for the NW and PW solvated systems. Membrane thickness is here defined as the distance between phosphate beads of opposing leaflets. To gain a more accurate description of the thickness Ra and O-antigen LPS membranes, the additional sugars should be taken into account.

As mentioned in the previous chapter of this thesis, the SASA for the acyl tails of membrane lipids can be used as metric for diffusivity. A greater value suggests a greater degree of diffusivity, and thus the lability of the local environment. The SASA values for Re, Ra and O-antigen type LPS solvated with the different water models can be seen in **Table 5**.

Table 5. *Solvent accessible solvent area of the lipid A segment of LPS per molecule for asymmetric membrane systems solvated with SPC, NW or PW models.*

	SPC	**NW**	**PW**
Re LPS	6.95 (± 0.53) nm^2	4.35 (± 0.07) nm^2	4.72 (± 0.08) nm^2
Ra LPS	7.39 (± 0.38) nm^2	4.79 (± 0.06) nm^2	5.31 (± 0.06) nm^2
OANT	N/A	5.89 (± 0.03) nm^2	5.63 (± 0.05) nm^2

SASA values for the lipid A segment of Re and Ra LPS lipids were significantly lower at the coarse-grained resolution compared with the united-atom resolution, suggesting restricted diffusivity. Re and Ra LPS lipids had greater SASA when the membrane was solvated with PW rather than NW. In contrast, the lipid A segment of the O-antigen LPS molecules exhibited a greater SASA when solvated with NW. Interestingly, an increase in the number of sugars correlated to an increase in lipid A SASA in systems solvated with each water model, which suggests that Ra and O-antigen type LPS-containing leaflets are somehow more labile than their Re LPS counterparts. This will be discussed further later in this chapter.

There are clear discrepancies between the observed membrane properties of systems solvated with NW or PW compared with the atomistic SPC water model used for the previous united-atom resolution simulations presented in this thesis. However, due to its ability to replicate physical behaviours such as electroporation, and as only a limited number of published LPS research involves the use of PW, it was selected as the water model of choice for the remainder of this chapter.

4.3.2 The Effect of Lipopolysaccharide Deacylation on Lipid Dynamics and Whole Membrane Properties

In order to assess how LPS deacylation by the OMP LpxR might influence the properties of the OM *in vivo*, a series of coarse-grained OM models were generated with an increasing percentage of LPS molecules deacylated. Initially, the inner leaflet was not modified. The dynamics and properties of these membranes were compared to those of the wildtype membrane. The 50:50 mixture of wildtype to deacylated LPS condition was split into three distinct configurations as previously described. To avoid overcomplication, the configurations with distinct patches of deacylated LPS (hDEMPa and hDEMPb) will be considered after the randomly mixed conditions.

A comparison of the membrane topology, shown in **Figure 49**, suggests that Re LPS deacylation does not have a significant effect on membrane curvature when the deacylated lipids are randomly mixed among wildtype lipids; while the increase in deacylated LPS is reflected in the system density plots, there is no clear movement of the density peaks either towards or away from the membrane core. Further to this, LPS deacylation does not appear to increase the penetration of solvent into the membrane core.

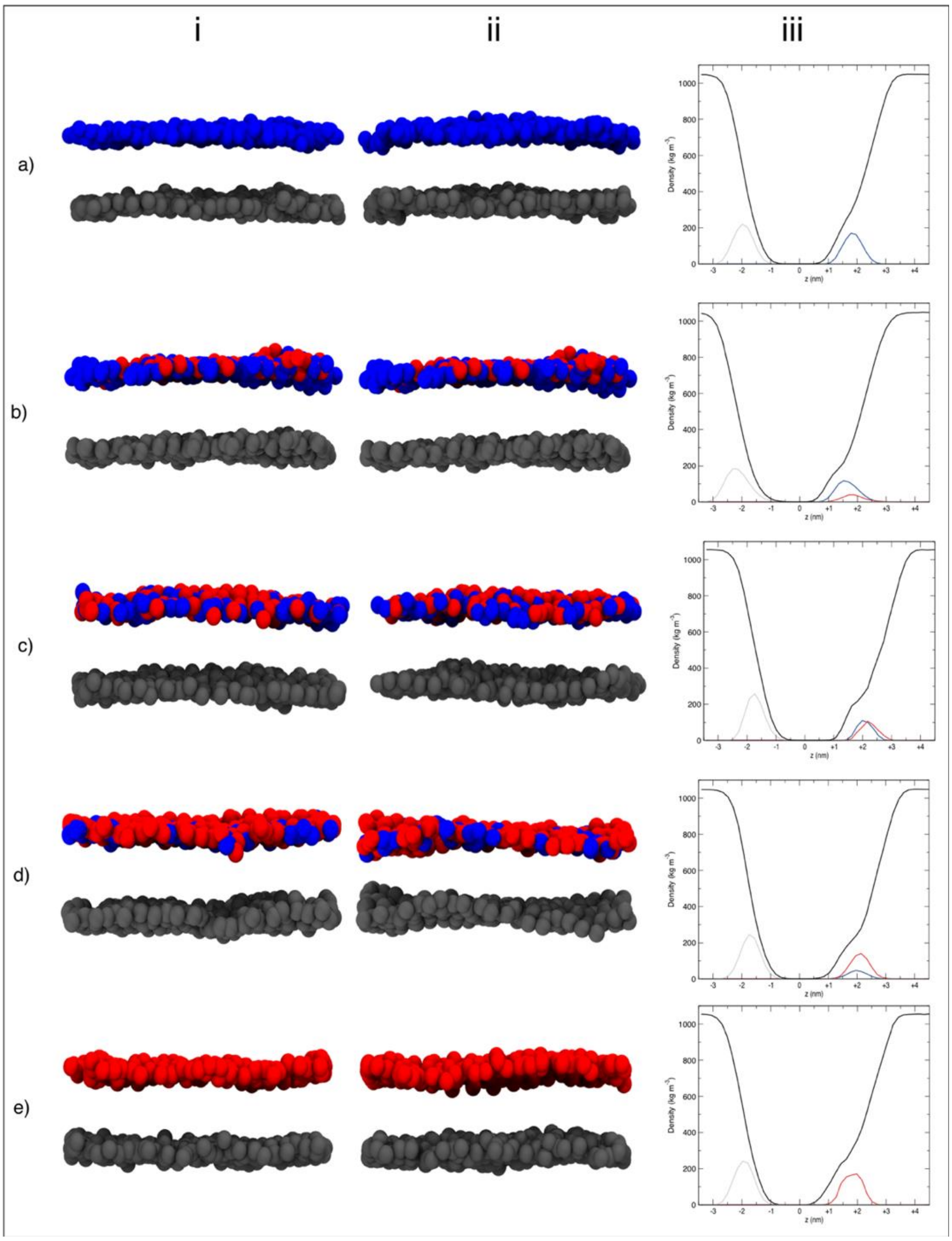

__Figure 49.__ Effect of lipopolysaccharide deacylation on membrane topology and system density. Images i and ii show lipid phosphate beads at 0 μs and 20 μs respectively, with wildtype LPS phosphates blue, deacylated LPS phosphates red and inner leaflet phosphates grey, and iii shows the density of system components over 20 μs, averaged between three independent simulations. Here polarisable water is shown in black, and the phosphates of wildtype LPS, deacylated LPS and inner leaflet lipids are shown in blue, red and grey respectively. __49a)__ shows the results of the REMP membrane condition. __49b)__ the qDEMP membrane condition. __49c)__ the hDEMPc membrane condition. __49d)__ the tqDEMP membrane condition. __49e)__ the DEMP membrane condition.

It is expected that LPS deacylation could lead to a decrease in membrane thickness, due to the removal of acyl tails from the membrane core. As the volume bulk water and pressure in the *z* axis remained unchanged in the setup of these systems, the pressure exerted on each membrane is constant. Interestingly, there was no significant decrease in membrane thickness until 50% of the membrane Re LPS lipids were deacylated. The mean membrane thickness (standard error in parentheses) for the REMP, qDEMP and hDEMPc conditions were 3.86 (±0.01) nm, 3.88 (±0.02) nm and 3.89 (±0.02) nm respectively, whereas the thickness drops to 3.80 (±0.01) nm and 3.77 (±0.02) nm for the tqDEMP and DEMP conditions respectively. As the thickness values of the REMP and qDEMP membranes are within error here, it can be concluded that the deacylation of 25% of the membrane here has not significantly influenced the overall membrane thickness. Membrane thickness over the 20 μs timescale, averaged for repeated simulations, can be seen in **Figure 50a**.

Conversely to membrane thickness, the area per lipid (APL) values for outer leaflet lipids show a significant decrease in the qDEMP membrane and hDEMPc membrane conditions compared with those from the wildtype REMP membrane. After the 50% of the LPS molecules have been deacylated, there were no further significant decreases in APL. The mean APL for lipids in the outer leaflet of the REMP, qDEMP and hDEMPc membrane conditions were 1.76 (±0.03) nm^2, 1.67 (±0.02) nm^2 and 1.59 (±0.02) nm^2 respectively, after which the values plateau at 1.60 (±0.02) nm^2 and 1.57 (±0.01) nm^2 for the tqDEMP and DEMP conditions respectively. The APL for inner leaflet lipids correspond with values for the outer lipid leaflets in that the largest decrease is seen between the REMP, qDEMP and hDEMPc conditions, with values of 0.66 (±0.01) nm^2, 0.63 (±0.01) nm^2 and 0.61 (±0.01) nm^2. The deacylation of every LPS lipid in the outer leaflet causes a decrease in APL of 0.06 nm^2 for the inner leaflet lipids. APL for the outer leaflet lipids over the 20 μs timescale, averaged for repeated simulations, can be seen in **Figure 50b.**

Similarly to the APL, there is a significant decrease in the whole membrane area of the wildtype REMP membrane compared with the qDEMP and hDEMPc membrane conditions. Again, after 50% of the LPS molecules have been deacylated, there were no further significant decreases in membrane area. The mean membrane area for the

REMP, qDEMP and hDEMPc membrane conditions were 243.03 (±2.74) nm^2, 232.40 (±2.37) nm^2 and 223.48 (±2.00) nm^2 respectively, compared with 222.72 (±1.52) nm^2 and 219.39 (±1.00) nm^2 for the tqDEMP and DEMP membrane conditions respectively. The whole membrane area is expected to decrease with the removal of lipid parts, simply because the mass of the membrane has decreased but the lateral pressure on the membrane remains constant. Membrane area over the 20 μs simulations can be seen in **Figure 50c.**

It is important to reiterate here that the inner leaflet of these membrane conditions had not been modified. In the interest of completeness, further modification was made to the hDEMPc membrane, such that the same total number of acyl tails had been removed from each leaflet, as described in the methodology section. Interestingly, this further modification led to an increase in APL for the inner leaflet phospholipids to 0.74 (±0.04) nm^2, compared with 0.66 (±0.01) nm^2 and 0.61 (±0.01) nm^2 for the REMP and hDEMPc conditions respectively, showing that the inner leaflet modification increases the area available to the phospholipids. In the upper leaflet, this further modification causes a decrease from 1.59 (±0.02) nm^2 to 1.54 (±0.02) nm^2 when comparing the hDEMPc and hDEMPc* conditions. There is also a decrease in whole membrane area observed from 223.48 (±2.00) nm^2 for the hDEMPc condition to 216.80 (±0.13) nm^2 for the hDEMPc* condition, compared with 243.03 (±2.74) nm^2 for the REMP condition. The APL for lower leaflet phosphates in the REMP, hDEMPc and hDEMPc* membrane conditions can be seen in **Figure 50d**.

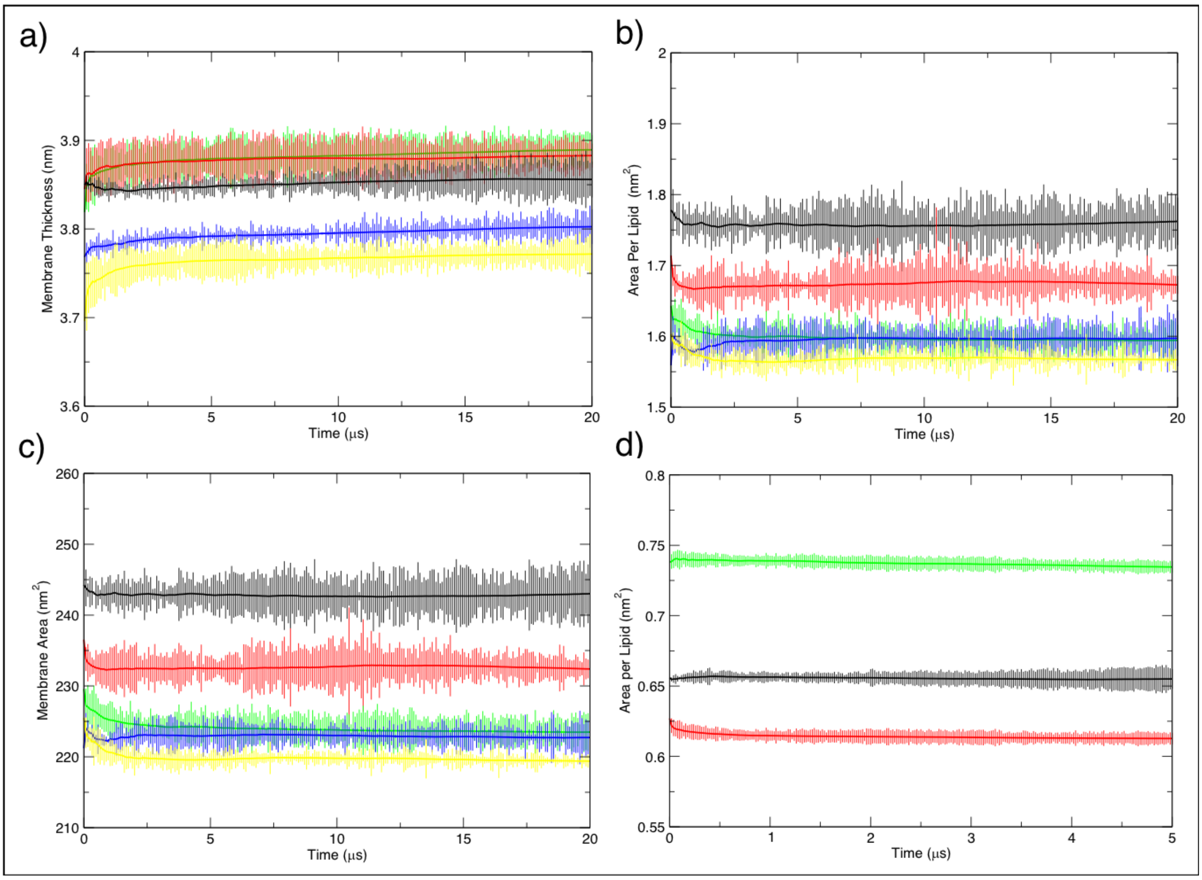

Figure 50. *The effect of Re LPS deacylation on wider membrane properties over entire 20 µs simulation timeframe. All plots show rolling average with standard error for block averages. Plots* ***a, b*** *and* ***c*** *coloured as REMP membrane black, qDEMP membrane red, hDEMPc membrane green, tqDEMP blue and DEMP membrane yellow.* ***50a)*** *membrane thickness.* ***50b)*** *average APL for LPS molecules in upper leaflet.* ***50c)*** *whole membrane area.* ***50d)*** *APL for inner leaflet phospholipids of REMP (black), hDEMPc (red) and hDEMPc* (green).*

The changes in whole membrane area of each condition, as well as the APL for inner and outer leaflet lipids, suggest that modifications to the outer leaflet have a greater effect on whole membrane properties than modifications to the inner leaflet. This is perhaps unsurprising, as the bulky inner core sugars of the LPS afford the outer leaflet greater structural integrity than the phosphatidylethanolamine or phosphatidylglycerol headgroups of the inner leaflet phospholipids due to the network of intermolecular electrostatic interactions (31,49,126).

The MSD was calculated for upper and lower leaflet lipids in order to ascertain whether deacylation would interfere with lateral diffusion. In each of the three mixed membrane conditions, the movement of deacylated and wildtype LPS lipids was completely correlated. Further to this, all membrane conditions showed both deacylated and wildtype LPS to move significantly slower than the inner leaflet phosphates. The deacylation of Re LPS did not alter the phosphate moiety and so did not affect the cross-linking by divalent cations; for this reason, the correlation of all LPS lipids in these conditions is still to be expected. MSD plots for each of the wildtype, mixed and fully deacylated membrane systems can be seen in **Figures 51a** to **51e**. Reduced lateral diffusion of LPS molecules compared with phospholipids, as well as complete correlation of LPS leaflet lipid movement has been reported previously (31). A comparison of the MSD of wildtype versus deacylated LPS in the qDEMP membrane condition can be seen in **Figure 51f**.

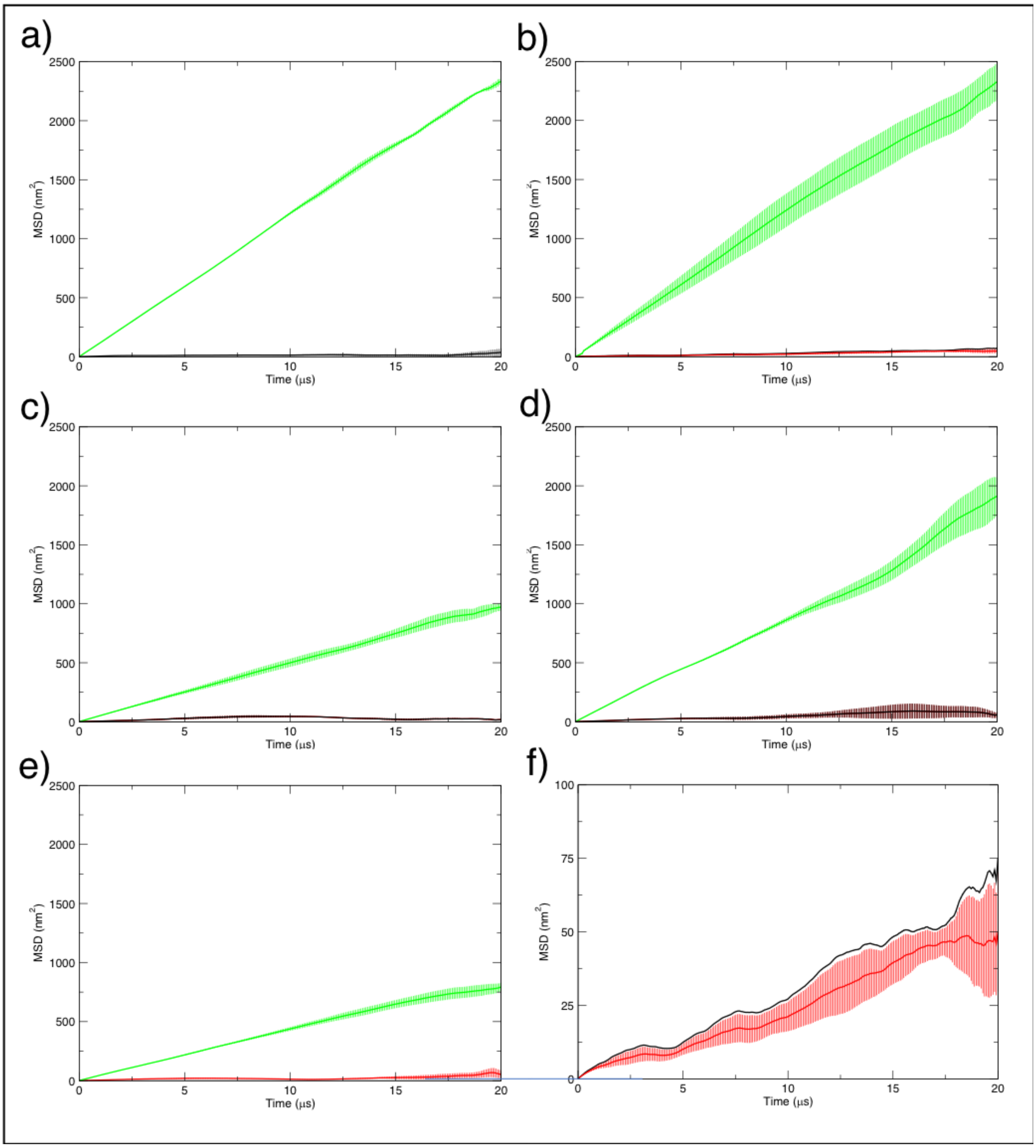

Figure 51. Mean squared displacement for upper and lower leaflets over 20 μs simulations for each membrane condition. Wildtype Re LPS shown in black, deacylated Re LPS in red and inner leaflet phospholipids in green. **51a)** REMP membrane condition. **51b)** qDEMP membrane condition. **51c)** hDEMPc membrane condition. **51d)** tqDEMP membrane condition. **51e)** DEMP membrane condition. **51f)** tqDEMP membrane condition, showing MSD of just wildtype and deacylated LPS.

4.3.3 Distinct patches of deacylated LPS lead to localised membrane curvature and clustering of cardiolipin phospholipids

The first striking observation of these membranes was the positive curvature of the membrane, seemingly caused by LPS deacylation, which occurred within the first 1μs of simulation for both the hDEMPa and hDEMPb conditions. As this curvature was not observed in the fully deacylated DEMP membrane condition, nor in the randomly mixed membranes, it leads to the suggestion that the distinct patches of LPS are responsible for the configurations of the membranes. In both hDEMPa and hDEMPb conditions, curvature is centred around the patch of deacylated LPS molecules. A sinusoidal, undulating topology was observed in the hDEMPa condition, due to the continuous strip of deacylated Re LPS in across the *y* plane. Similarly, in the hDEMPb condition an undulating topology is observed, with peaks forming at the centre of the square patch of deacylated lipid. Membrane topologies for the hDEMPa and hDEMPb membrane conditions can be seen in **Figure 52**. The undulations are further evidenced in the system density plots, which show clearly separated density peaks along the *z* axis for the wildtype and deacylated Re LPS species. Membrane curvature poses a difficulty in terms of analysis, as many techniques assume a flat membrane. Membrane curvature means that calculating membrane area or APL using system *xy* lengths will not work. New methods, such as that employed by MemSurfer take membrane curvature into account and characterise topological properties by using Delaunay triangulations and as such calculate membrane surface area with greater accuracy (207). Membrane area and APL for each membrane system were determined using the *fatslim* software, which calculates a Voronoi cell for each lipid within the membrane; therefore membrane curvature is taken into account during calculations.

Local membrane subdomains of lipids can lead to membrane curvature. The specific headgroup-to-acyl chain ratio of lipid species enables them to be classed as conical, inverted conical or cylindrical (208–210). Conical lipids, such as PE, DAG and phosphatic acid are able to impose positive curvature on a monolayer; conversely, inverted conical lipids, such as lysophosphatidylcholine or phosphatidylinositol phosphate species are able to impose negative curvature on a monolayer (211).

Cylindrical lipids, such as PS and phosphatidylcholine will form a monolayer with zero curvature (211).

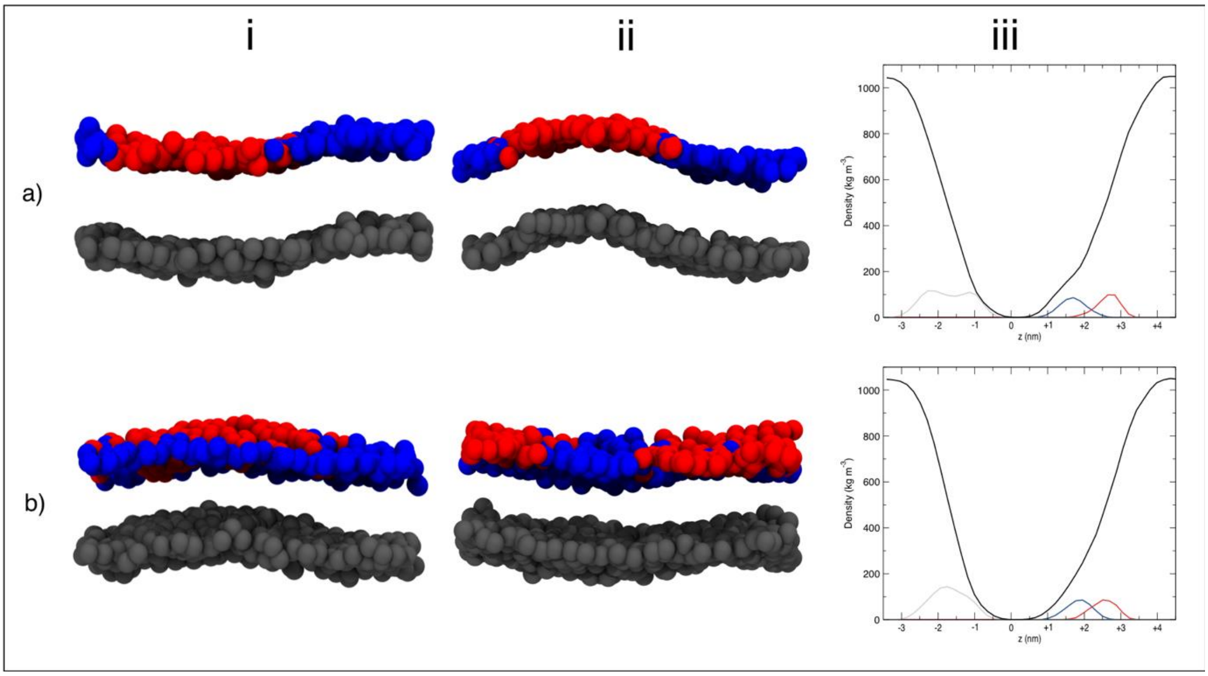

***Figure 52**. Effect of lipopolysaccharide deacylation on membrane curvature and system density. Images i and ii show lipid phosphate beads at 0 μs and 20 μs respectively. Image colouring is the same as **Figure 49**. **52a)** shows the results of the hDEMPa membrane condition and **52b)** the hDEMPb condition.*

On further inspection of these trajectories, it appeared that cardiolipin lipids in the inner leaflet were prone to clustering in areas of the inner leaflet that corresponded to the deacylated LPS lipid areas in the outer leaflet, as can be seen in **Figures 53** and **54** for the hDEMPa and hDEMPb conditions respectively. In panels **a)**, **b)** and **c)** of these figures, a comparison of the mass density across the *xy* plane can be seen for wildtype LPS, deacylated LPS and cardiolipin respectively. Panel **d)** is a cross-section view of the membrane, illustrating the extent of cardiolipin clustering. The significance of this cardiolipin clustering will be discussed later in this chapter.

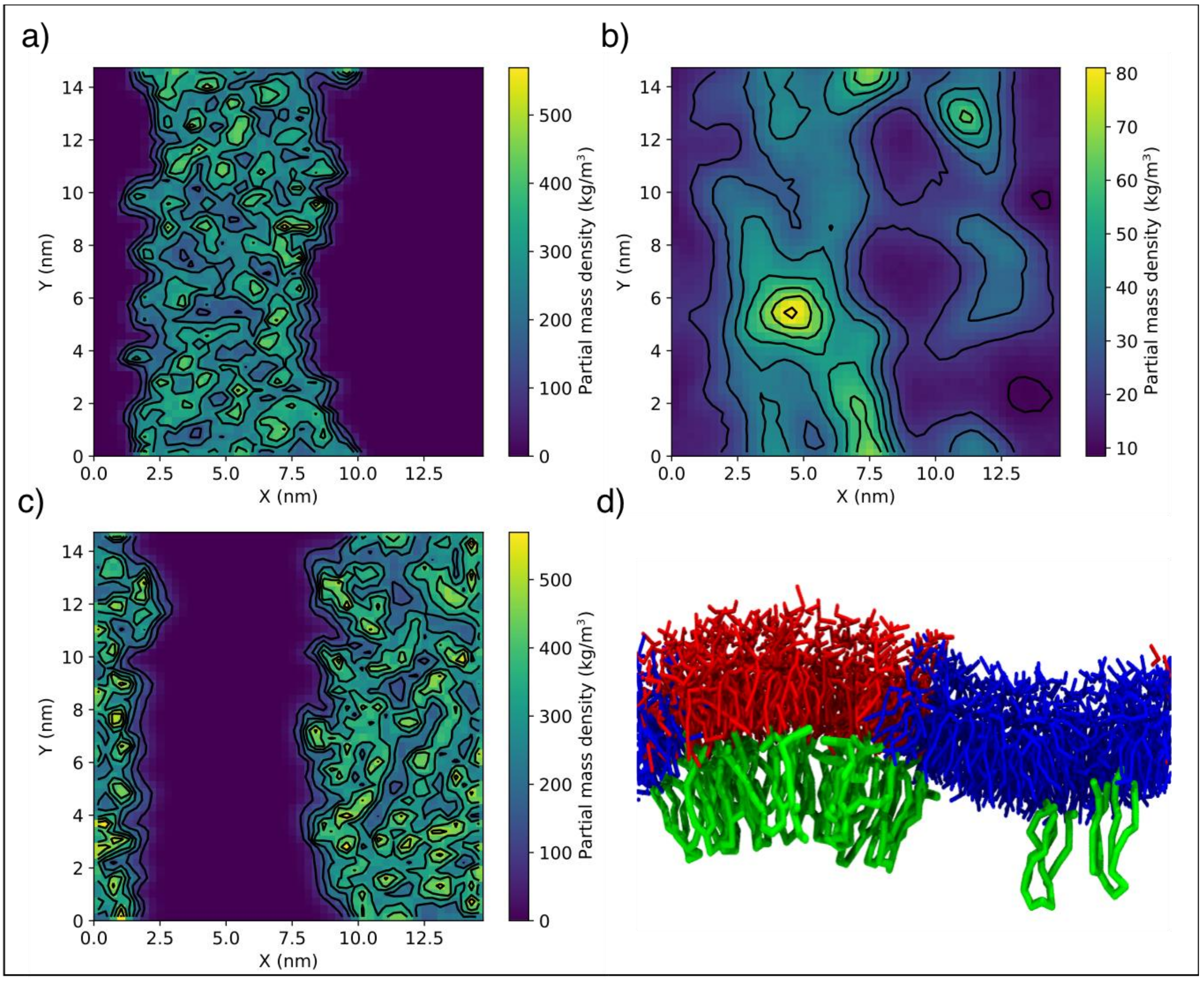

Figure 53. *Distribution of different lipid types in the xy plane from the hDEMPa membrane condition.* ***53a)*** *2D heat-map representation mass density of deacylated Re LPS,* ***53b)*** *mass density of cardiolipin,* ***53c)*** *mass density of wildtype Re LPS and* ***53d)*** *showing the clustering of cardiolipin in the inner leaflet corresponding to patches of deacylated Re LPS in the outer leaflet, with wildtype LPS, deacylated LPS and cardiolipin coloured blue, red and green respectively. Image generated from system coordinates resulting after 20 μs simulation at 310 K.*

It is again important to remember here that the inner leaflet of these membranes had not been modified, so it may be possible that both the membrane curvature of the systems and the cardiolipin clustering were due to the mismatch in hydrophobic bulk between the leaflets. That being said, the same curvature or cardiolipin clustering was not observed in the mixed membrane conditions, so this finding certainly necessitated further investigation.

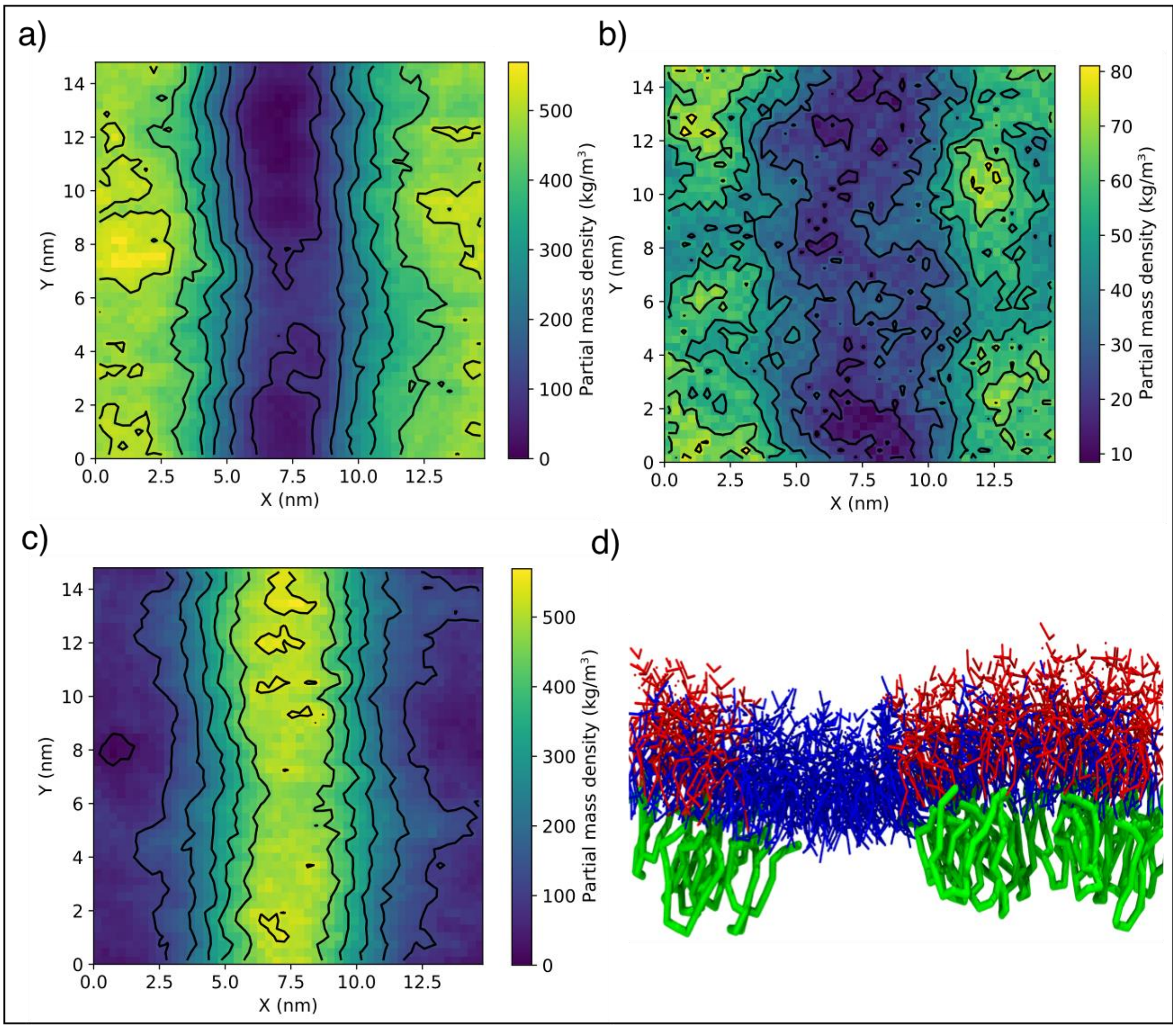

Figure 54. *Distribution of different lipid types in the xy plane from the hDEMPb membrane condition.* ***54a)*** *2D heat-map representation mass density of deacylated Re LPS,* ***54b)*** *mass density of cardiolipin,* ***54c)*** *mass density of wildtype Re LPS and* ***54d)*** *showing the clustering of cardiolipin in the inner leaflet corresponding to patches of deacylated Re LPS in the outer leaflet, with colours as in* ***Figure 53****. Image generated from system coordinates resulting after 20 μs simulation at 310 K.*

In order to test whether the membrane curvature was due to a mismatch in hydrophobic bulk, two further conditions were devised for the hDEMPa and hDEMPb membranes. Firstly, the resultant coordinate file from the 20 μs simulation was modified such that the same number of acyl tails were removed from the inner leaflet as were from the outer leaflet, as detailed in the ***Methods*** section of this chapter. Secondly, the initial wildtype Re LPS membrane condition was modified such that both inner and outer leaflets were altered at the same time. Both of these new conditions were subject to an additional 5 μs simulation after the appropriate equilibration. The former of these new conditions will be considered first.

The APL for outer leaflet lipids is decreased to 1.63 (±0.02) nm^2 for both the hDEMPa and hDEMPb conditions, compared with the 1.76 (±0.03) nm^2 for the wildtype membrane. The further modification resulted in APL values of 1.56 (±0.01) nm^2 and 1.57 (±0.03) nm^2 for the hDEMPa* and hDEMPb* conditions respectively. Again, the further inner leaflet modification does not have as significant an effect on the APL than the initial modifications to the outer leaflet.

The APL for inner leaflet phospholipids show a similar pattern to the hDEMPc and hDEMPc* conditions. The initial outer leaflet modification caused a decrease from the 0.66 (±0.01) nm^2 of the REMP condition to the 0.62 (±0.02) nm^2 of the hDEMPa and hDEMPb conditions. These values then increased to 0.73 (±0.02) for both conditions. As the whole membrane area still decreased with each modification, these data again underline the importance of LPS in maintaining membrane structural integrity and rigidity.

After 5 μs simulation, both hDEMPa* and hDEMPb* still showed the same level of curvature as was apparent before inner leaflet modification. Further to this, cardiolipin clustering was still observed to occur in the regions corresponding to the patches of deacylated LPS. The extent of cardiolipin clustering for both the hDEMPa* and hDEMPb* conditions is shown in **Figures 55** and **56** respectively. In panels **55a)**, **b)** and **c)**, a clear trend is shown, which hotspots of cardiolipin corresponding to hotspots of deacylated Re LPS.

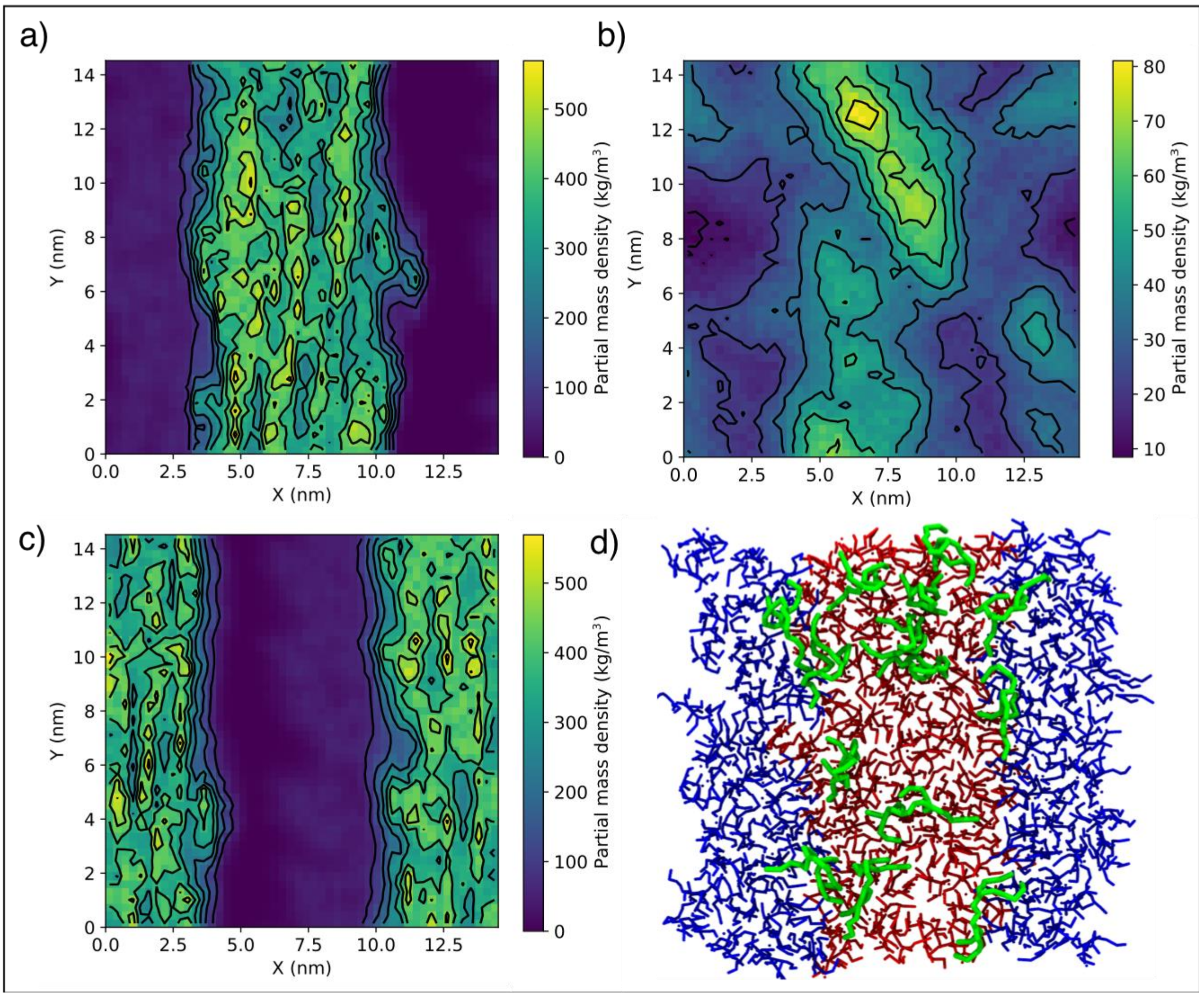

Figure 55. *Correlation of mass density of deacylated Re LPS and cardiolipin in the xy plane in the hDEMPa* system with inner leaflet modified.* ***55a)*** *2D heat-map representation mass density of deacylated Re LPS,* ***55b)*** *mass density of cardiolipin,* ***55c)*** *mass density of wildtype Re LPS.* ***55d)*** *periplasmic view of the membrane, showing cardiolipin clustering, with colours as in* ***Figure 53****. Image generated from system coordinates resulting after 5 μs simulation at 310 K.*

In agreement with the hDEMPa* simulations, **Figures 56a)**, **b)** and **c)** show a correlation of high cardiolipin density with high deacylated Re LPS density in the hDEMPb* simulations. Further to this, it seems as though this correlation is greater than in the initial hDEMPb simulations, when comparing panels **a)**, **b)** and **c)** of **Figures 54** and **56**.

The continued clustering of cardiolipin in these conditions is certainly intriguing, but a known drawback of molecular dynamics simulations of LPS is their frustratingly slow dynamics (31). In order to conclude that both the membrane curvature and cardiolipin clustering observed in these conditions, the membranes with simultaneous inner and outer leaflet modifications must be considered.

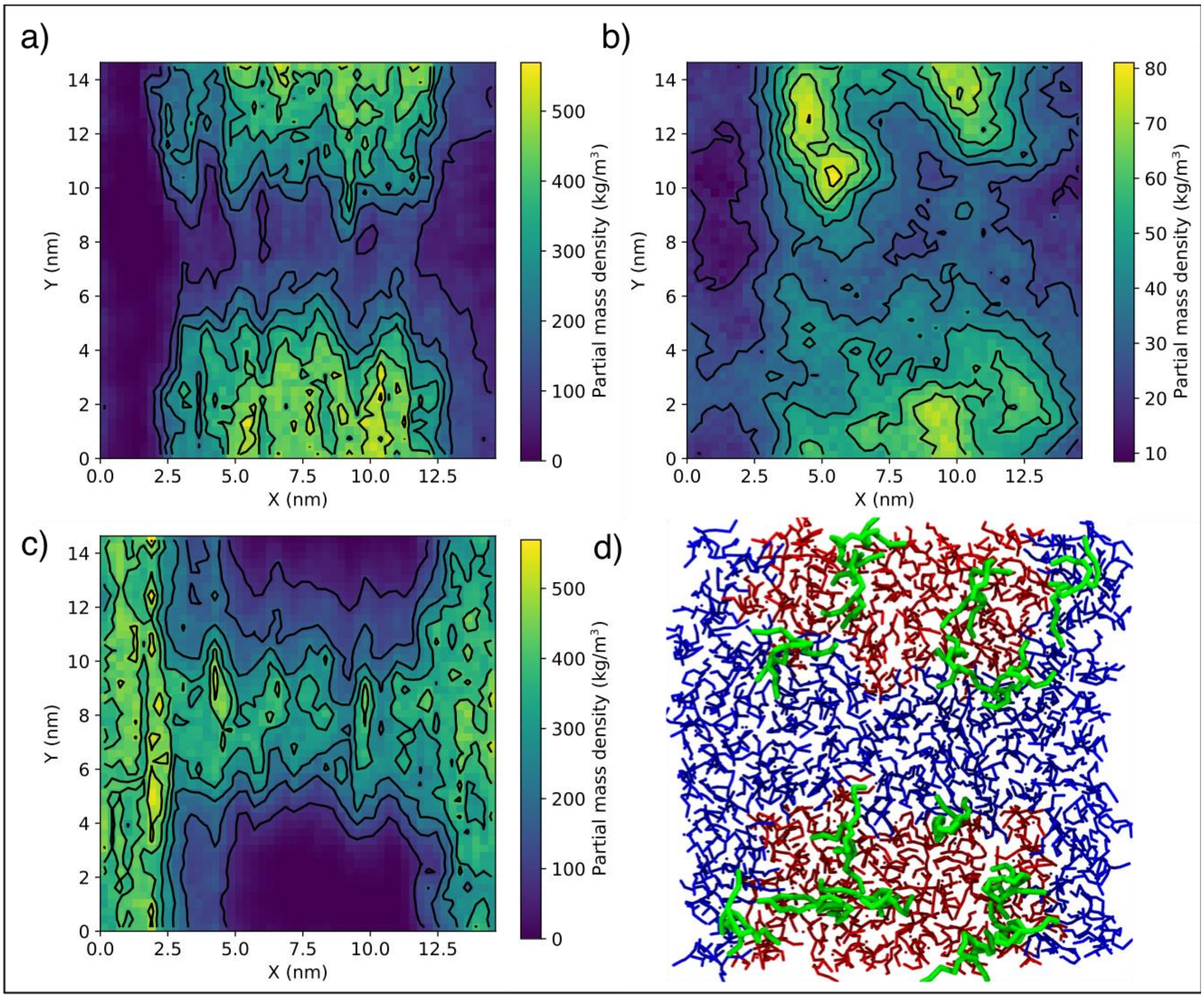

__Figure 56.__ Correlation of mass density of deacylated Re LPS and cardiolipin in the xy plane in the hDEMPb system with inner leaflet modified. __56a)__ 2D heat-map representation mass density of deacylated Re LPS, __56b)__ mass density of cardiolipin, __56c)__ mass density of wildtype Re LPS. __56d)__ periplasmic view of the membrane, showing cardiolipin clustering, with colours as in __Figure 53__. Image generated from system coordinates resulting after 5 μs simulation at 310 K.*

Two final conditions were devised as a test to ensure that the observed membrane curvature was due to the deacylated patch of Re LPS, and not an artefact of the simulation procedures. These conditions, hDEMPa** and hDEMPb**, were produced from the resultant coordinates of the 20 μs equilibrium molecular dynamics simulation performed on the wildtype Re LPS membrane. These differ from the initial hDEMPa and hDEMPb conditions as these membranes had both the inner and outer leaflets modified simultaneously in the methods previously described. The system composition of the hDEMPa* and hDEMPa** conditions, and the hDEMPb* and hDEMPb** conditions were identical, but their corresponding starting configurations were not.

After 5 μs of simulation, the familiar curvature and cardiolipin clustering phenomena were once again observed in the hDEMPa** and hDEMPb** membrane conditions. The clustering of cardiolipin molecules was more apparent in the hDEMPb** condition than in the hDEMPa** condition, as can be seen in **Figures 57** and **58**, respectively.

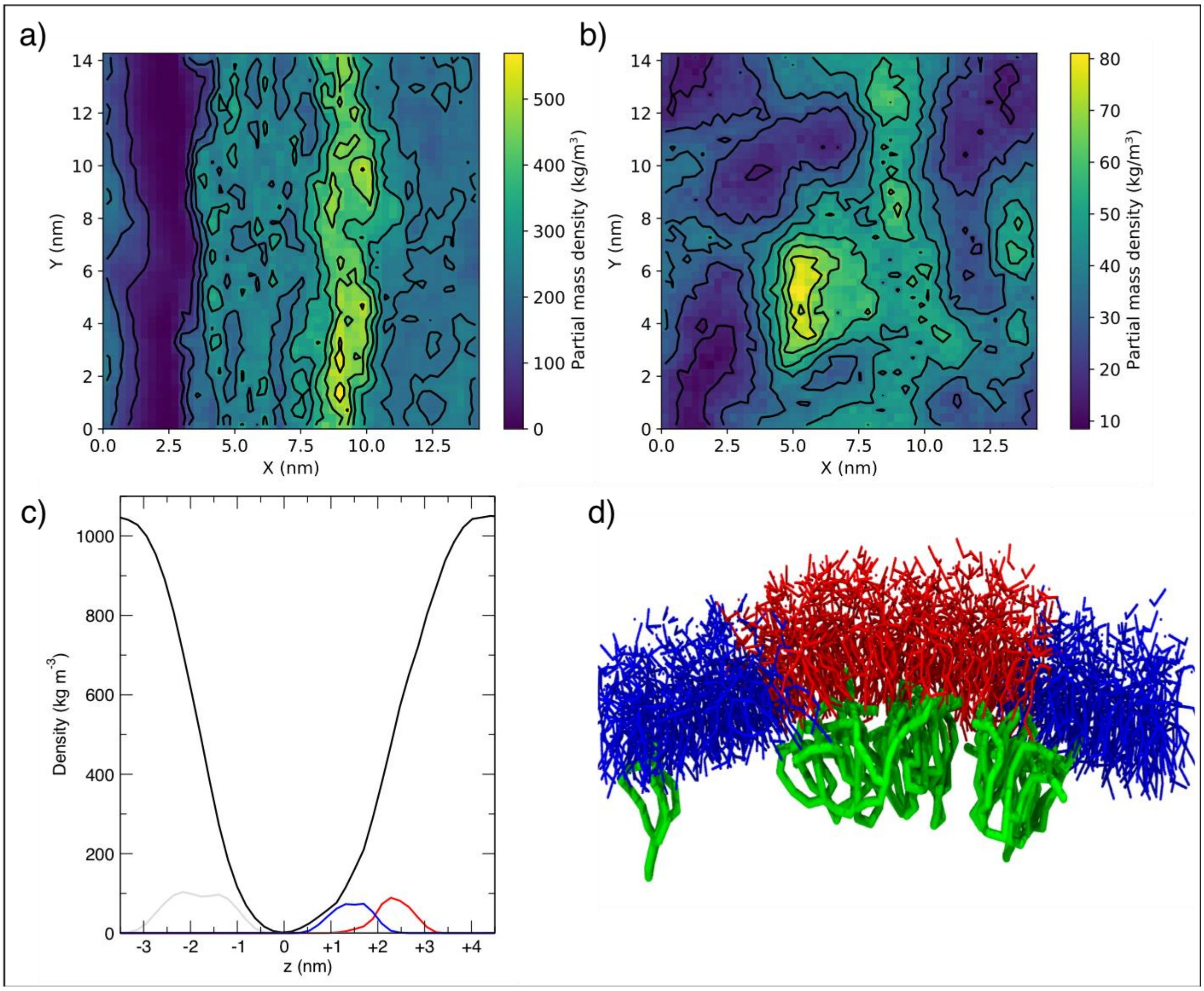

Figure 57. *Distribution of membrane lipids in hDEMPa** system.* ***57a)*** *2D heat-map representation mass density of deacylated Re LPS in the* xy *plane.* ***57b)*** *2D heat-map representation mass density of cardiolipin in the* xy *plane.* ***57c)*** *system density across the z plane. Polarisable water, deacylated Re LPS phosphates, wildtype Re LPS phosphates and inner leaflet phosphates are coloured black, red, blue and grey respectively.* ***57d)*** *showing the clustering of cardiolipin in the inner leaflet corresponding to patches of deacylated Re LPS in the outer leaflet, with colours as in* ***Figure 53****. Image generated from system coordinates resulting after 5 μs simulation at 310 K.*

The extent of the membrane curvature of both hDEMPa** and hDEMPb** conditions is further exemplified in the *z* axis system density plots of deacylated and wildtype LPS phosphates, as seen in **Figures 57c)** and **58c)**. The modification of both leaflets causes a decrease in membrane area, but does not appear to affect the hydrophobic integrity of the membranes, as both remain able to exclude water from their membrane core. In the case of hDEMPa**, there is a decrease in membrane area of 12.5 nm^2 as compared with the hDEMPa condition, and a decrease of 28.38 nm^2 compared with the wildtype membrane. Similarly, with the hDEMPb** membrane condition, there is a decrease in membrane area of 14.74 nm^2 compared with the hDEMPb condition and 30.07 nm^2 compared with the wildtype membrane.

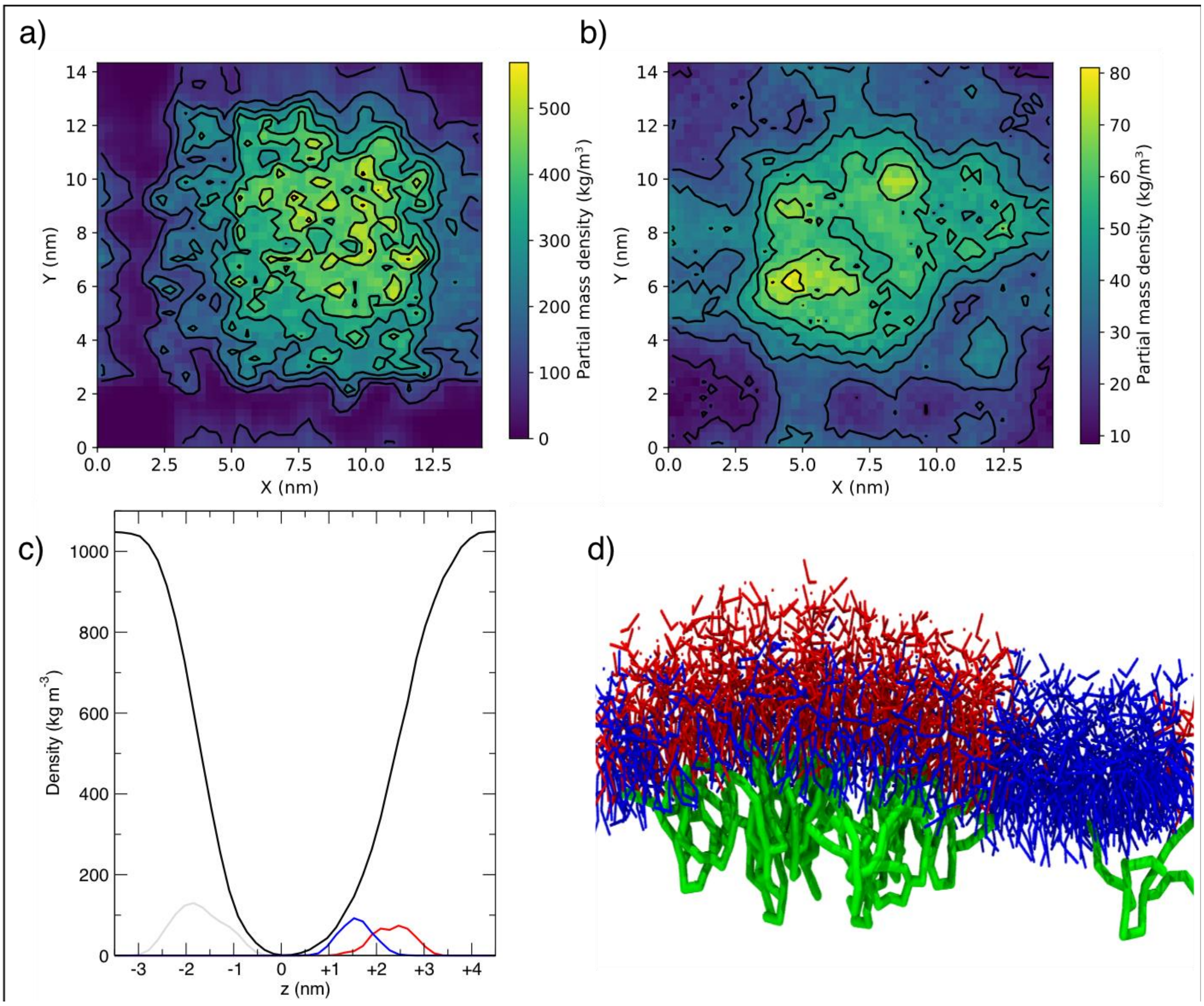

Figure 58. *Distribution of membrane lipids in hDEMPb** system.* ***58a).*** *2D heat-map representation mass density of deacylated Re LPS in the* xy *plane.* ***58b)*** *2D heat-map representation mass density of cardiolipin in the* xy *plane.* ***58c)*** *system density across the z plane. Polarisable water, deacylated Re LPS phosphates, wildtype Re LPS phosphates and inner leaflet phosphates are coloured black, red, blue and grey respectively.* ***58d)*** *showing the clustering of cardiolipin in the inner leaflet corresponding to patches of deacylated Re LPS in the outer leaflet, with colours as in* ***Figure 53****. Image generated from system coordinates resulting after 5 μs simulation at 310 K.*

The presented simulations lend credibility to the assertion that distinct patches of deacylation of Re LPS can cause localised membrane curvature, as well as triggering cardiolipin clustering. The phospholipid aggregation is particularly noteworthy due to its occurrence in certain signalling cascades involving cellular membranes. For example, the exposure of phosphatidylserine clusters on the outer leaflet of membranes in many eukaryotic species will trigger cellular apoptosis and leads to phagocytosis by a leukocyte (212,213). Phospholipid aggregation is also observed in *E. coli*, in which cardiolipin is preferentially localised at the poles and septal regions (214). This localisation of cardiolipin in areas of negative curvature supports the observations presented here. Further to this, research suggests that the OMPs FhuA and BtuB have specific PG binding locations in regions interacting with the periplasmic leaflet, and the cytoplasmic membrane protein AqpZ has a cardiolipin-binding site (186,215); if membrane curvature can drive lipid sorting, it may also be the case that seemingly minute modifications such as the lipid A 3' O-deacylation of Re LPS by LpxR can have wider implications for the organism's behaviour.

Membrane curvature is utilised in certain biological roles; mechanosensitive proteins can respond to membrane stress and carry out their cellular function. Membrane bending can cause a mismatch in the hydrophobic width of embedded proteins and the membrane, which may in turn lead to conformational change and therefore signal propagation (216). The mechanosensitive ion channels MscL and MscS are excellent examples of this, serving as valve-like structures and preventing cellular lysis by permitting ionic permeation in cases of extreme cellular turgor (217). MscS is typically localised at the cellular poles in *E. coli*, and this localisation has previously been shown to be cardiolipin-dependent (214).

4.3.4 Electroporation of Asymmetric Lipopolysaccharide-Containing Membranes Solvated with Polarisable MARTINI Water

Studies in the literature describe the formation of a membrane pore resulting from the application of an electric field as beginning with the a single-file transmembrane water channel developing, which is stabilised through interactions with lipid headgroups (139,218,219). This causes lipid headgroups to move into the membrane core, widening the channel and allowing larger molecules to traverse the membrane (195,220,221). In contrast to this, Piggot *et al.* presented the findings that poration of an asymmetric LPS-containing membrane will always be initiated by movement of phospholipids from the inner leaflet into the membrane core, regardless of electric field polarity (139). Following this, flip-flopping of inner leaflet phospholipids into the outer leaflet may be observed. After this has occurred, LPS molecules from the outer leaflet may begin to line the outer leaflet portion of the pore. Pore formation is preceded by inner leaflet phospholipid movement in asymmetric LPS-containing membranes due to the slow dynamics of LPS molecules. The crosslinking of phosphate moieties of neighbouring molecules by divalent cations, coupled with steric hindrance from the sheer complexity of the molecules prevents the same swift rearrangement observed from phospholipids. In molecular dynamics simulations, electroporation is frequently followed by membrane collapse.

Yesylevskyy *et al.* observed that electroporation can occur in coarse-grained systems solvated with polarisable MARTINI water, by the same mechanism observed in atomistic resolution simulations (119). The study involved two different methods of initiating electroporation: the application of an external electric field to an octane slab, and ionic permeation through a symmetric DPPC membrane caused by ionic charge imbalance. The ability of the polarisable MARTINI water model to reproduce the dielectric screening of bulk water to a level comparable with atomistic resolution simulations is crucial here, as it enables the researcher to reap the benefits of the coarse-grained resolution without forfeiting important physical behaviours.

While Piggot *et al.* performed electroporation of an asymmetric Rd_1 LPS (Re LPS with the first three heptose sugars of the outer core) membrane, there were no subsequent published studies investigating different chemotypes of LPS under an electric field. Further to this, there are no published studies exploring the behaviour of a full-complement O-antigen LPS-containing asymmetric membrane under an electric field. To this end, simulations were devised to investigate how the number of sugar moieties present in LPS influences the time taken for poration to occur under an electric field at the coarse-grained resolution. Simulations of Re and Ra LPS membrane with OmpA embedded were also run with an electric field applied; while there are published studies of membrane-embedded beta barrel proteins with an electric field applied, these are typically focused on protein-mediated translocation (222). What is lacking from the literature is the process of membrane electroporation adjacent to a membrane protein.

Initially, united-atom resolution simulations were run as a control for the electroporation mechanism. The Re and Ra LPS asymmetric membrane models were used here, due to their extensive use and validation in the literature. As can be seen in **Figures 59a-d)**, the electroporation of the united-atom Re LPS system occurs via the same mechanism as reported by Piggot *et al.*, commenced by a membrane defect which develops into a water channel (139). This behaviour is very closely matched in the coarse-grained resolution system, as seen in **Figures 59e-h)**.

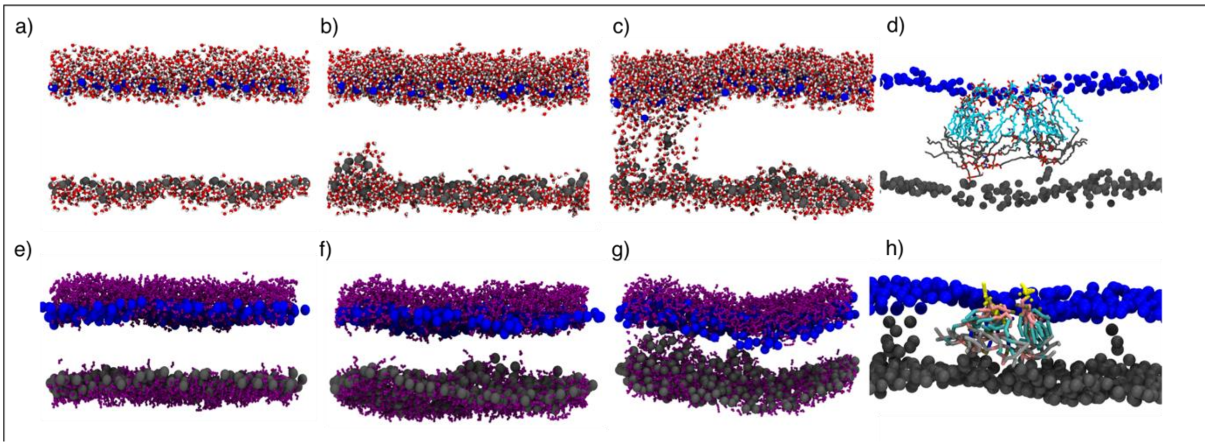

Figure 59. *Electroporation of the wildtype Re LPS asymmetric membrane at united-atom resolution (**a, b, c, d**) and coarse-grained resolution (**e, f, g, h**). **59a)** & **59e)** membrane at equilibrium, with water and phosphate beads shown. Re LPS phosphates in blue and inner leaflet phosphates in grey **59b)** & **59f)** movement of water into the hydrophobic core leads to a membrane defect **59c)** & **59g)** a water channel opens up and membrane lipids rearrange to line the pore, with greater movement seen from inner leaflet phosphates **59d)** & **59h)** image of headgroups lining the newly formed pore. Carbon atoms of LPS molecules coloured cyan and phospholipids grey. Water omitted for clarity.*

In contrast to the LPS sugar rearrangements into the pore shown by Piggot *et al.* in the united-atom Rd_1 LPS asymmetric membrane, membrane collapse occurs too quickly in the coarse-grained Re LPS model for this to be observed. This may be due to the LPS molecules lining the pore favouring interaction with neighbouring LPS molecules over the rearranged phospholipids from the inner leaflet.

The ionic conductance of the non-specific porin OmpA has been measured at ~60 pS experimentally and *in silico* (223,224). Up to 20 water molecules are able to fit within the barrel lumen in the open conformation (224). The coarse-grained model, however, does not allow water into its barrel segment due to steric bulk of the water molecule (each CG particle represents 4 water molecules). As it is unclear how and indeed if the electroporation process is effected by nonporous embedded membrane proteins, coarse-grained OmpA here is an excellent choice. The focus of this experiment was to understand whether the presence of OmpA would weaken intermolecular interactions between lipids and thus facilitate electroporation

Simulations suggest that the presence of OmpA facilitated the electroporation of Re LPS at a much lower field strength than the membrane-only system, as poration occurred under both a 0.1 V/nm and 0.15 V/nm electric field. In the membrane-only systems, an electric field strength of 0.3 V/nm was required to trigger poration, and no poration occurred under a field strength of 0.2 V/nm. The electroporation process in the OmpA-embedded Re LPS membrane system was largely similar to that of the membrane-only system, in that the pore was generated from the inner leaflet. The difference here was that in six independent simulations with either a 0.1 V/nm or 0.15 V/nm external electric field applied, the pore was consistently initiated by phospholipids directly interacting with the protein (annular phospholipids). The same was observed in systems to which an electric field with a reversed polarity was applied. The electroporation of the membrane adjacent to OmpA can be seen in **Figures 60a** to **60c**. Molecular dynamics simulations by Shearer *et al.* show localised membrane thinning around OmpA in native Re, Ra and O-antigen type LPS membranes(186); as membrane thinning is associated with lipid tail disorder, and therefore membrane disruption, this area is likely more susceptible to electroporation. The KDO sugars of Re LPS showed no significant rearrangement prior to pore formation under either polarity of electric field, further suggesting that the intermolecular interactions between the LPS molecules of the outer leaflet provide much greater stability to the membrane than the inner leaflet phosphates.

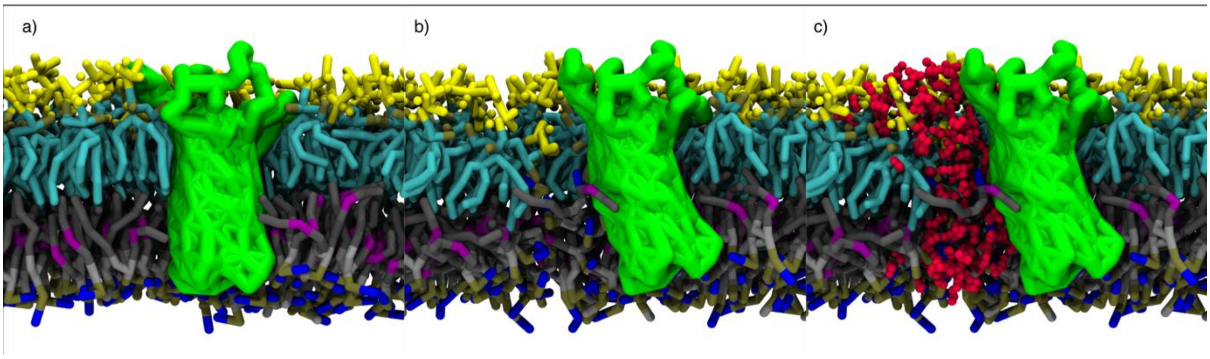

Figure 60. *Electroporation of the Re LPS membrane with an OmpA monomer embedded with a 0.15 V/nm external electric field applied.* ***60a)*** *System at equilibrium. OmpA is coloured green; Re LPS coloured with sugars yellow, phosphates tan and acyl tails cyan; phospholipids coloured with amines blue, phosphates tan, glycerols silver, acyl tails grey and unsaturated segments purple.* ***60b)*** *Inner leaflet annular phospholipids rearrange such that headgroups are in the membrane core.* ***60c)*** *water (red) is able to flow freely through the phospholipid-lined membrane pore.*

The mixed wildtype/deacylated membranes hDEMPa* and hDEMPb* were also simulated with an external electric field applied as a further test of membrane integrity. In the six independent simulations for both mixed membranes, poration occurred either within the deacylated patch or at the boundary between deacylated and wildtype LPS. The reasoning for this is most likely that the deacylated lipid has a decreased hydrophobic area as compared to the wildtype. It is therefore less energetically expensive for water and then phospholipids to move into the membrane core in the deacylated sections. No particular phospholipids appear to be favoured in the electroporation mechanism; this was investigated due to the earlier observation that deacylated LPS favoured interaction with cardiolipin, leading to the phospholipid clustering underneath patches of the deacylated lipid. The locations of pore formation in the hDEMPa* and hDEMPb* membranes can be seen in **Figures 61a)** and **61b)**.

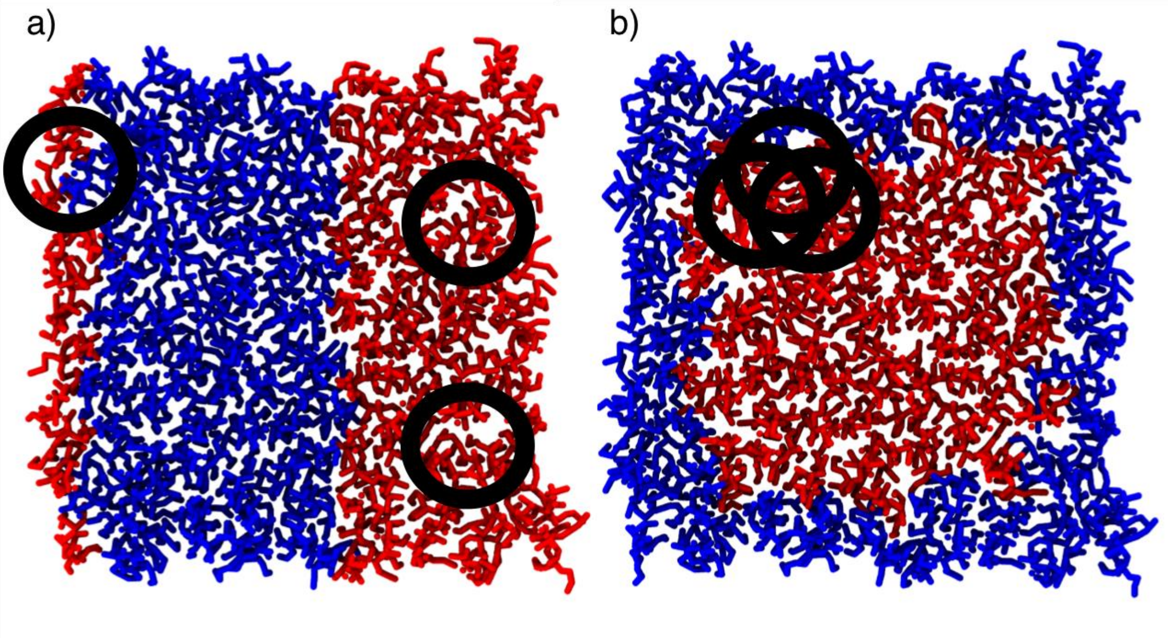

Figure 61. *The location of pore formation relative to patches of deacylated Re LPS lipids in membranes with an external electric field of 0.3 V/nm applied. Location of pore formation in each of three repeats denoted by a black circle.* ***61a)*** *Pore location in hDEMPa* membrane condition.* ***61b)*** *Pore location in hDEMPb* membrane condition.*

As can be seen from **Figures 61a)** and **61b)**, the location of pore formation was largely consistent across repeats for the hDEMPb* condition, but not in the hDEMPa* condition; it seems here that the local topography of the hDEMPb membrane condition triggers localised membrane weakness, facilitating poration. The consistent poration in the deacylated LPS regions of these modified membranes suggests a lack of structural integrity caused by the deacylated LPS lipids. The previous electroporation studies presented in this chapter have shown the importance of intermolecular interactions between LPS molecules in maintaining structural integrity in the membrane, and the deacylation of 50% of these molecules has clearly disrupted these interactions.

The Ra LPS system, at both resolutions, follows the same electroporation mechanism observed in the Re LPS system, with inner leaflet headgroups rearranging into the membrane core before any movement is observed in the outer leaflet. At both united-atom and coarse-grained resolutions, a single file water channel is seen to protrude through the inner leaflet to the outer leaflet; these can be seen in **Figures 62a** to **62c)** and **62d)** to **62f)** respectively.

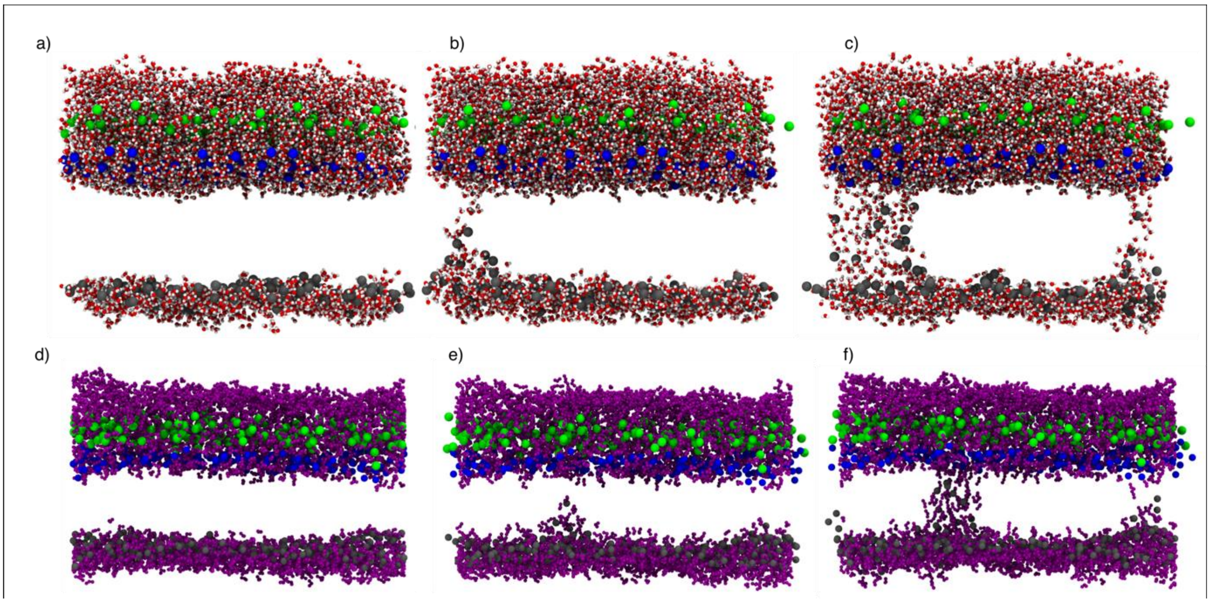

Figure 62. *Electroporation of the Ra LPS asymmetric membrane at united-atom resolution (**a, b, c**) and coarse-grained resolution (**d, e, f**). **62a)** & **62d)** membrane at equilibrium, with water and phosphate beads shown. Inner and outer core LPS phosphates are shown in blue and green respectively, and inner leaflet phosphates in grey **62b)** & **62e)** movement of water into the hydrophobic core leads to a membrane defect **62c)** & **62f)** a water channel opens up and membrane lipids rearrange to line the pore, with greater movement seen from inner leaflet phosphates**.***

The lipid A phosphates of Ra LPS make more movement towards the pore than the core sugars at the coarse-grained resolution. Core sugars favour interaction with the core sugars of neighbouring LPS molecules and show very little conformational rearrangement in the *z* axis during the poration process, even up until membrane collapse. Lateral rearrangements were observed, and these allowed water through the newly formed pore; these observations were replicated when the polarity of the electric field was switched. Simulations at the united-atom resolution yielded similar behaviour as, due to the strength of interaction between neighbouring LPS core sugar moieties, the inner and outer core segments did not move towards the membrane core. Lipid A phosphates did move closer to the membrane core, and were seen to interact with flip-flopped phospholipids from the inner leaflet lining the pore.

Embedding OmpA into the Ra LPS membrane had a similar effect to the Re LPS membrane. A lower electric field strength was required for poration in these membrane systems, possibly due to the disordering effect of the OMP; poration occurred in the membrane under a field strength 0.15 V/nm, but not under a field strength of 0.1 V/nm. The lack of poration due to the 0.1 V/nm field suggests that the additional sugar-sugar and sugar-protein interactions from the outer core sugars of LPS afford the membrane a greater level of structural integrity than the Re LPS membrane with OmpA embedded. Annular phospholipids were once again observed to initiate the poration process in the six independent simulations, with three repeats for each polarity. The core sugar regions of only two Ra LPS molecules were observed to move towards the membrane core during the poration event. These were two of the annular LPS molecules at the outer leaflet entrance to the pore. The core sugar regions of other annular LPS molecules were observed to laterally rearrange to allow the passage of water through the membrane. The electroporation process involving annular phospholipids can be seen in **Figures 63a)** to **63c)**.

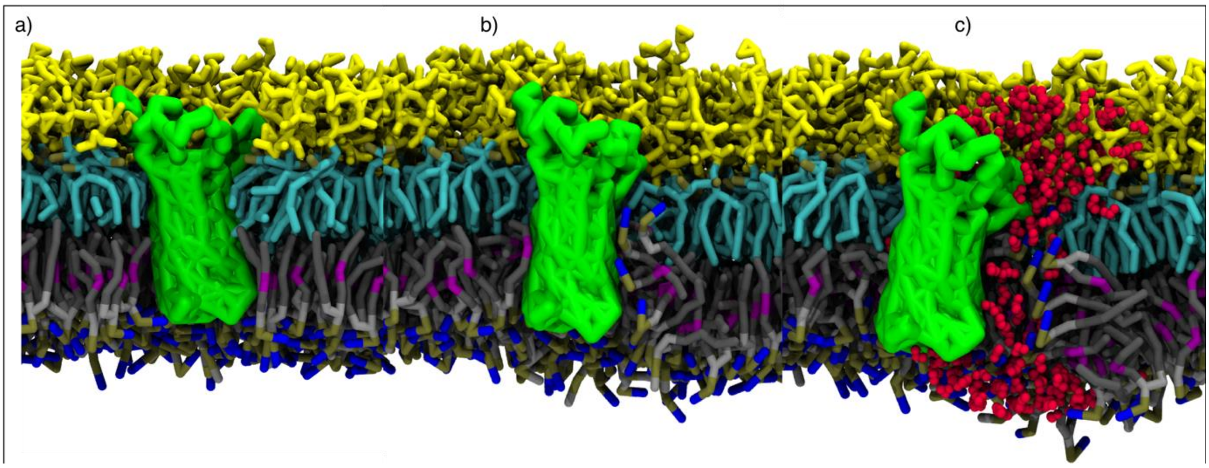

Figure 63. *Electroporation of the Ra LPS membrane with an OmpA monomer embedded with a 0.15 V/nm external electric field applied.* ***63a)*** *System at equilibrium. OmpA is coloured green; Ra LPS coloured with sugars yellow, phosphates tan and acyl tails cyan; phospholipids coloured with amines blue, phosphates tan, glycerols silver, acyl tails grey and unsaturated segments purple.* ***63b)*** *Inner leaflet annular*

phospholipids rearrange such that headgroups are in the membrane core. ***63c)*** *water (red) is able to flow freely through the phospholipid-lined membrane pore.*

The behaviour of smooth LPS at the coarse-grained resolution has previously been reported by the Khalid group, and at the atomistic resolution by the Im group (186,225,226). As *in vivo* electroporation protocols may involve disrupting the *E. coli* outer membrane with smooth LPS present, its inclusion here is highly appropriate. When analysing resultant trajectories, particular attention was paid to sugars of the O-antigen region of the molecules. In equilibrium molecular dynamics simulations, the O-antigen sugars of neighbouring LPS molecules have been observed to tilt towards each other (186). This tilting, or tenting, is particularly prominent around proteins and is more extreme as a greater number of O-antigen sugars are included.

The electroporation process of this membrane is largely similar to the processes of the Re and Ra type LPS membranes. Interestingly, while the lipid A region of the smooth LPS molecules at the outer leaflet entrance to the pore are seen to move further into the membrane centre, the core and O-antigen sugars of these molecules barely move in the *z* axis. Tenting of O-antigen sugars is observed, which results in areas of the outer leaflet at which the lipid A segments of LPS molecules are exposed; Poration consistently occurred at the site in the membrane which had the lipid A segment of LPS exposed due to O-antigen tenting, and it seems highly likely that this tenting decreased the energetic barrier to poration. Several pores formed simultaneously when a field strength of 0.3 V/nm or above was applied the membrane. In these scenarios, lateral rearrangement of core and O-antigen sugars was only observed in the region of the membrane with the lipid A segments observed due to O-antigen tilting. Membrane deterioration occurred too quickly to observe further rearrangements under these conditions. The electroporation process can be seen in **Figures 64a)** to **64d)**.

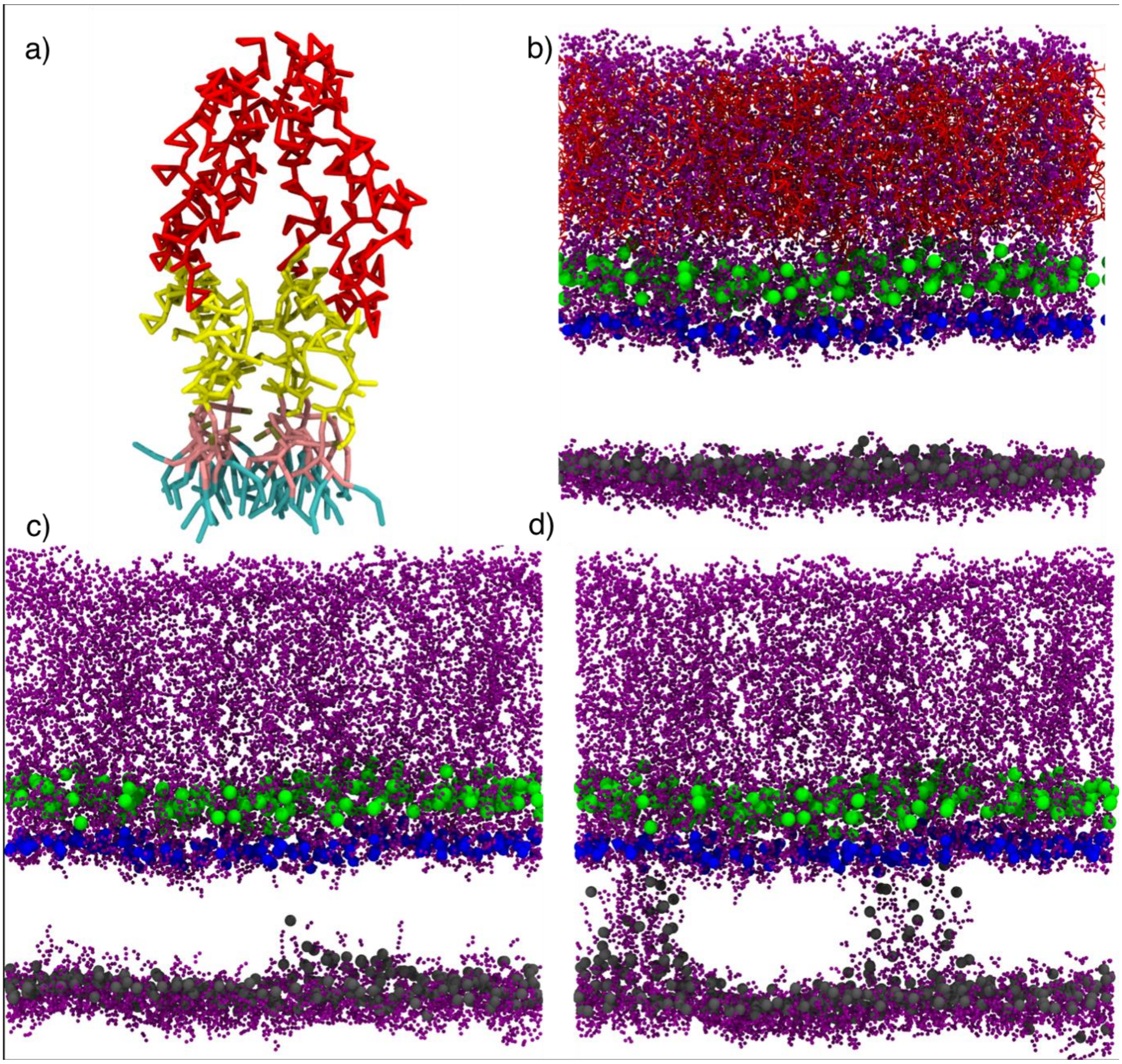

***Figure 64.** Electroporation of the full-complement LPS asymmetric membrane at coarse-grained resolution under an electric field strength of 0.2 V/nm, with beads coloured as in **Figure 62** with the addition of O-antigen sugar beads in red. **64a)** outer leaflet of membrane at equilibrium, showing tenting of O-antigen sugars. **64b)** membrane at equilibrium, with inner and outer leaflet phosphates beads shown along with O-antigen sugars and water within 0.6 nm. **64c)** movement of water into the hydrophobic core leads to a membrane defect. **64d)** a water channel opens up and membrane lipids rearrange to line the pore, with greater movement seen from inner leaflet phosphates.*

The time taken for poration to occur in each outer membrane model can be seen in **Table 6**, along with the voltage generated by each membrane. Pore formation was deemed complete when more than one polarisable water molecule was able to traverse the membrane simultaneously, and the simulation time was recorded at this point.

Table 6. *Time taken for pore formation in each membrane system with an external electric field applied.*

System	Electric Field (V/nm)	Voltage (V)	Poration Time
REMP	0.2	0.75	No poration after 1 µs
	-0.2	-0.75	
	0.3	1.13	19.92 ns
			21.24 ns
			30.64 ns
	-0.3	-1.13	16.02 ns
			20.44 ns
			17.56 ns
	0.4	1.50	1.98 ns
			2.22 ns
			1.64 ns
	-0.4	-1.50	1.22 ns
			1.60 ns
			1.54 ns
	0.5	1.88	0.82 ns
			0.98 ns
			1.02 ns
	-0.5	-1.88	0.60 ns
			0.52 ns
			0.42 ns
RAMP	0.2	0.77	958.12 ns
			No poration after 1 µs
			No poration after 1 µs

	-0.2	-0.77	No poration after 1 μs
			924.44 ns
			939.86 ns
	0.3	1.15	3.38 ns
			7.42 ns
			3.36 ns
	-0.3	-1.15	4.58 ns
			2.50 ns
			2.64 ns
	0.4	1.54	0.84 ns
			0.96 ns
			0.82 ns
	-0.4	-1.54	0.68 ns
			0.58 ns
			0.82 ns
	0.5	1.92	0.62 ns
			0.64 ns
			0.62 ns
	-0.5	-1.92	0.60 ns
			0.42 ns
			0.58 ns
OANT	0.2	0.81	30.10 ns
			9.68 ns
			103.44 ns
	-0.2	-0.81	5.46 ns
			15.62 ns
			52.82 ns
	0.3	1.21	1.74 ns
			2.32 ns
			1.88 ns
	-0.3	-1.21	2.34 ns
			1.34 ns

			1.56 ns
	0.4	1.61	0.64 ns
			0.56 ns
			0.62 ns
	-0.4	-1.61	0.54 ns
			0.52 ns
			0.48 ns
	0.5	2.02	0.28 ns
			0.24 ns
			0.18 ns
	-0.5	-2.02	0.24 ns
			0.18 ns
			0.20 ns
Inner	0.3	1.22	1.22 ns
			1.08 ns
			1.32 ns
	-0.3	-1.22	1.02 ns
			1.20 ns
			1.28 ns

In each of the Re and Ra LPS membrane systems, it was noted that the poration time was reduced when the polarity of the electric field was reversed. Under the positive electric field, positively charged atoms would move to the top, or extracellular side of the *z* axis and negatively charged atoms to the bottom, or periplasmic side; the opposite occurred under reversed polarity. The reason for the drop in poration time may have been due to the negatively charged PG (-1 *e*) and cardiolipin (-2 *e*) now being pulled towards the membrane core. However, while either PG or cardiolipin were consistently involved in each poration event under the reversed polarity electric field, it remained unclear whether their involvement was vital to the mechanism, particularly as the uncharged PE lipids were also involved.

It was observed that poration occurred at a quicker rate in the Ra LPS membrane systems compared with the Re LPS membrane systems subjected to the same strength of electric field. The voltages generated by the two membranes were within 0.03 (±0.01) V for each field strength applied, suggesting that increased number of sugars attached to the LPS molecules were somehow causing weakness in the structural integrity of the membrane. Poration in the O-antigen membrane consistently occurred at the previously mentioned sites where the lipid A segments of LPS molecules were exposed. Poration was still preceded by movement of inner leaflet phosphates, but the repeated occurrence over 30 independent simulations certainly suggests structural weakness in this area, possibly caused by O-antigen tilting. The data presented here suggest that the increased sugar-sugar interactions in the Ra and O-antigen LPS molecules may be the cause of the decreased poration times. Sugar-sugar interactions may cause localised tilting of LPS molecules, which in turn leads to the exposure of the lipid A segments of the surrounding lipids. This is further evidenced by the previously discussed SASA data. The lipid A segments of Ra and O-antigen type LPS molecules exhibited greater SASA than those of their Re LPS counterparts. The hypothesised localised tilting of LPS molecules due to increased sugar-sugar interactions may also increase the SASA, leading to regions of exposed lipid A. These regions may be exploited due to structural weakness. These potential structural weaknesses may of course be negated by the presence of embedded membrane proteins; while poration occurred under the lower electric field strength of 0.15 V/nm in both the CG_REMP_OmpA and CG_RAMP_OmpA systems, it only occurred in the Re LPS system at the field strength of 0.1 V/nm. Increased LPS sugar-protein interactions may in some way negate the disordering effect of membrane thinning proteins on annular lipids.

The electroporation protocol was also applied to the inner membrane model as simplistic membrane comparison. The thickness of the inner membrane was noted to be 4.06 (±0.11) nm. In contrast to all iterations of the outer membrane model, poration of the inner membrane model can be initiated from either inner or outer leaflet. The lack of the bulky sugar headgroups from LPS molecules expedites the poration process. The electroporation of the inner membrane model seen in **Figures 65a)** to **65d).**

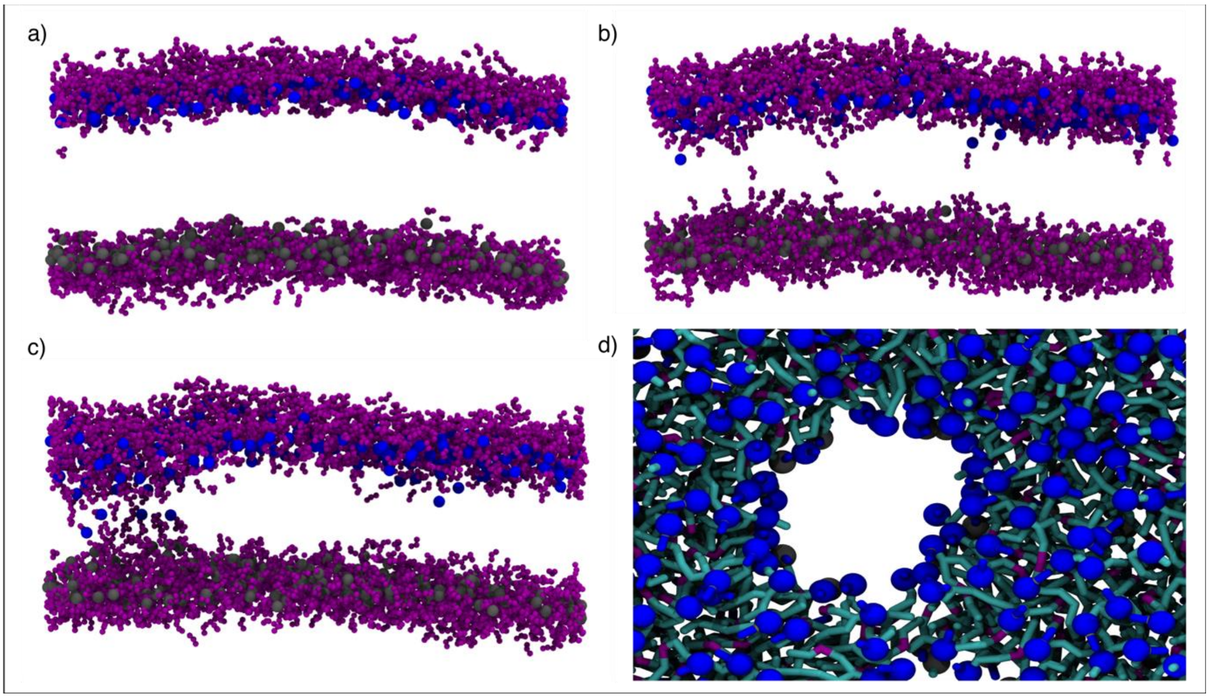

Figure 65. *Electroporation of the inner membrane model at coarse-grained resolution (**a, b, c, d**). **65a)** membrane at equilibrium, with water and phosphate beads shown. Outer leaflet phosphates are shown in green, and inner leaflet phosphates in grey. **65b)** movement of water into the hydrophobic core leads to a membrane defect. **65c)** a water channel opens up and membrane lipids rearrange to line the pore, with greater movement seen from inner leaflet phosphates. **65d)** image of headgroups lining the newly formed pore. Water omitted for clarity.*

It appeared that no particular phospholipid type was favoured in the electroporation process of the inner membrane model, and rearrangement of headgroups from both leaflets, leading to the formation of a symmetric pore was observed. The electroporation of inner and outer membranes will be revisiting in the following chapter, with the addition of the antimicrobial peptide polymyxin B1.

4.4 Conclusion

The polarisable MARTINI water model approximately replicates the membrane-water interface of LPS-containing membrane systems seen in united-atom systems solvated with SPC water with greater precision than the standard MARTINI water model. It also, as described in the literature, is more accurate in its description of density, freezing point and dielectric permittivity than the standard model (119). However, other metrics used to test for system convergence, such as area per lipid and membrane thickness, seem to be more closely replicated by the standard model than the polarisable model when it comes to comparison with SPC-solvated united-atom systems. The data presented here further underline how important it is to select the correct tools when designing a molecular dynamics study. While the polarisable model employed in this and the subsequent chapter in invaluable due to its ability to accurately recreate phenomena such as electroporation, it also has the drawback of increasing the computational load due to the requirement of the calculation of long-range electrostatic interactions.

Deacylation of Re LPS appears to have a paradoxical effect in terms of membrane topology. When mixed throughout the upper leaflet, membrane topology is unaffected, but when grouped in a distinct patch or strip, localised curvature is observed. Further to this curvature, clustering cardiolipin in the inner leaflet is detected in regions directly beneath the deacylated Re LPS. In the mixed systems, the deacylation of Re LPS is recognised in differences to the APL and membrane thickness.

In the investigation of the electroporation process of the Gram negative outer membrane with a β barrel embedded, it was discovered that the poration event is initiated by movement of annular phospholipids into the membrane core. As β barrel proteins are ubiquitous in the Gram negative outer membrane, their inclusion in studies such as these is essential.

The application of an external electric field to the O-antigen type LPS membrane, which had not been attempted previously, resulted in membrane poration at sites where the lipid A segment of LPS was exposed due to O-antigen tenting. Interactions between O-antigen segments of neighbouring LPS molecules leads to some areas of the outer leaflet having greater coverage by core and O-antigen sugars than other parts. These sites of reduced sugar coverage were consistently the site of poration when the external electric field was applied.

Future projects in relation to the work presented in this chapter would certainly include the application of an external electric field to an O-antigen type LPS membrane with OmpA embedded, to understand whether the trend of poration triggered by annular phospholipids is continued for each chemotype of LPS and whether the tenting behaviour of the O-antigen lipids influences the poration mechanism. Another avenue of investigation could be the application of an electric field to an LPS membrane system with a membrane-thickening protein. As discussed previously in this thesis, membrane thinning and thickening are associated with annular lipid tail disordering and ordering respectively. If it is indeed the case that localised membrane disorder facilitates poration, then it follows that localised membrane ordering could limit poration in that area.

The electroporation of the entire Gram negative cell envelope would also be an avenue of investigation. Electroporation is performed in order to transfect model organisms such as *E. coli* with plasmids, and therefore nucleic acids would have to pass through both inner and outer membranes, as well as the peptidoglycan mesh *in vivo* (192). Electroporation studies typically focus on single membrane systems, often without sufficient proteins. In order to fully understand the process of electroporation, the behaviours of each component of the full cell envelope must be considered. Finally, much larger versions of the mixed wildtype and deacylated Re LPS membranes would be simulated in order to gather data on how the deacylation effects leaflet tension and whole membrane compressibility.

Computational models of eukaryotic and prokaryotic membranes have come a considerable way in the past few decades, with the advent of advanced computational methods. However, while the level of detail included has certainly improved, many models still fall short of including molecules vital for the biochemical processes occurring within living cells. Biological membranes are known to include phospholipid mixtures with saturated and unsaturated acyl tails, as well as non-phosphorylated lipids such as ornithine lipids, sulfolipids, glycolipids and hopanoids. Hopanoid diplopterol shows noticeable ordering effect on bacterial membranes from molar concentrations as low as 5%, and as such their exclusion from many computational studies is certainly an oversight (81,82).

Biological membrane environments are typically crowded, and can contain surface densities of up to 30,000 proteins per μm^2 (227). Certain computational research groups have begun to include more complex membrane protein mixtures in their systems, which has led to the observation of previously unseen clustering behaviour. In order to understand the interplay between the major structures in the bacterial cellular envelope, an accurate environment must be described. Systems are also often limited to one or two types of ion. More complex ionic mixtures would be a closer representation of environments *in vivo*.

Another important note is that bacterial membrane compositions change with the organism's life cycle, as well as the temperature and of the local environment (228). For example, the inner membrane protein LpxP adds a monounsaturated palmitoleate tail to lipid IV_a as a response to temperatures below 12 °C (229). The inclusion of a more diverse range of lipids in computational research may lead to more accurate findings.

The deacylation of LPS by the OMP LpxR appears to cause weakness in the membrane at the interface with wildtype lipid. Further to this, the presence of membrane-thinning proteins such as OmpA also appears to weaken the ability of the membrane to withstand and electrical field. This poses the question as to whether these weaknesses could be exploited by environmental hazards such as antimicrobial peptides? To this end, the interaction of polymyxin B1 with the native OM and IM models will be discussed in the following chapter.

Chapter 5: Investigating the permeation of polymyxin B1 through the inner and outer membranes of Escherichia coli

5.1 Introduction

This chapter explores interactions between polymyxin B1 and the outer membrane models previously studied in this thesis. Through a series of equilibrium and non-equilibrium molecular dynamics techniques, polymyxin B1 was eventually observed to permeate the outer membrane model, following a similar poration mechanism to that observed and discussed in the previous chapter. Results here add further evidence to the hypothesised self-promoted uptake mechanism discussed in the literature.

Polymyxins are a class of cyclic lipopeptides produced by Gram-positive bacteria such as *Paenibacillus polymyxa* (230). The class consists of polymyxins A, B, C, D, E and M, although only polymyxins B and E (colistin) are used clinically to treat Gram-negative bacterial infections. Polymyxins are typically used as a last-resort treatment option due to their nephrotoxicity and neurotoxicity, but the increasing fears over multidrug resistant bacteria has led to renewed interest in the antimicrobial peptides (AMPs) (93,231). This chapter focuses on polymyxin B1 (PMB1), although the differences with the other clinically used polymyxin chemotypes will be discussed.

Polymyxins are synthesised by a non-ribosomal peptide synthetase system, which are a modular, multi-enzyme structures that do not utilise the translation of mRNA (88). These multi-enzyme structures contains three core domains, which perform adenylation, thiolation and condensation reactions. Similarly, these regions are referred to as A/T/C domains. The biosynthesis of polymyxins is co-ordinated proteins produced from the *pmx* gene cluster, which consists of five genes: *pmxA – pmxE.* The synthetase complex consists of protein subunits PmxA, PmxB and PmxE, and the other two proteins (PmxC and PmxD) are involved in membrane transport during secretion (230).

The synthesis of PMB1 begins with the construction of a pentapeptide chain by PmxE, consisting of the following residues: ʟ-α-γ-diaminobutyric acid (DAB), ʟ-threonine (Thr) and three more DAB residues. The pentapeptide chain is then moved to the PmxA subunit, where D-phenylalanine (phe), L-leucine (Leu) and two more DAB residues are added. The resultant nonapeptide is transferred to the PmxB subunit, where an additional Thr residue is added. The molecule undergoes a cyclisation reaction, during which a peptide bond is formed between the carboxylate moiety of the terminal Thr residue and the γ nitrogen of the fourth residue, DAB. In colistin, the D-Phe residue is replaced with D-leu (leu). Polymyxins are lipidated at the first residue; in PMB1, this is the addition of 6-methyloctanoic acid, but in polymyxins B2 and E2 it is 6-methylheptanoic acid (232). There is debate in the literature about precisely which of the synthetase subunits performs the lipidation of the first residue, although PmxE contains an N-terminal C domain, capable of performing the lipidation reaction (230). The chemical structure of PMB1, coloured coded with the synthetase subunits responsible for the addition of each residue, can be seen in **Figure 66**.

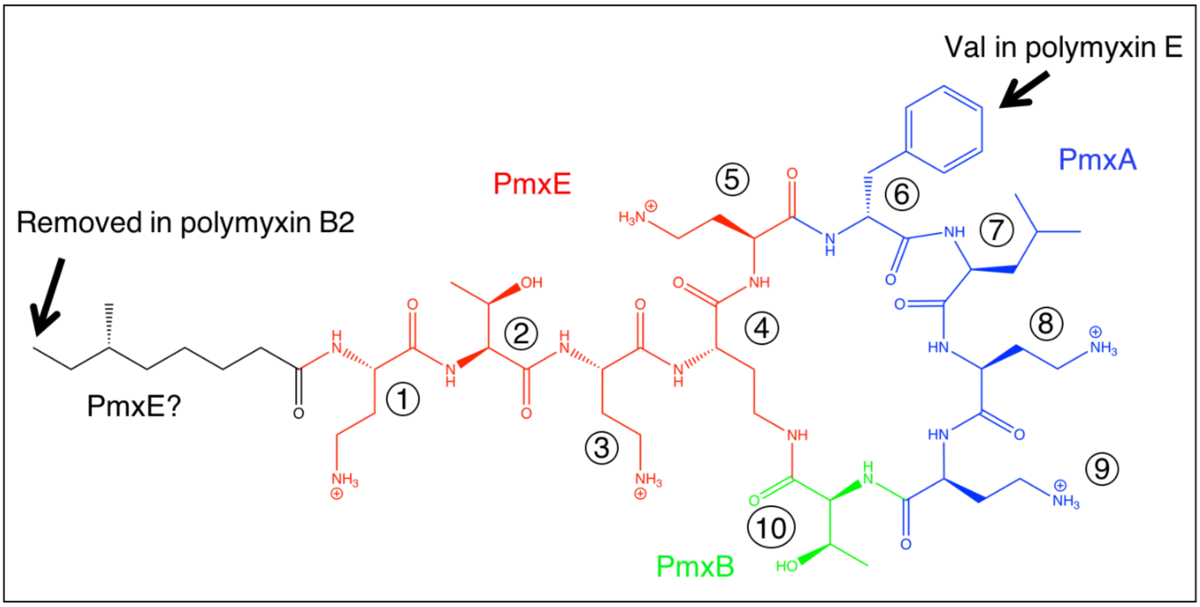

***Figure 66**. Chemical structure of polymyxin B1 colour coded with respect to non-ribosomal peptides involved in its biosynthesis. Numbers signify order of amino acid loading. Residues are as follows: DAB, Thr, DAB, DAB, DAB, D-Phe, Leu, DAB, DAB, Thr.*

Distinctive mechanisms of action have been proposed for other AMPs, such as the barrel-stave, toroidal, carpet and detergent models. While the barrel-stave and toroidal models involve the AMP adopting a transmembrane and result in membrane-spanning aqueous channels, the carpet and detergent models have AMPs causing membrane disruption without penetration into the membrane core (233–235). Both the carpet and detergent models rely on the AMPs disrupting interactions between neighbouring phospholipids (PLs), leading to denaturing of the bilayer structure and even the loss of PLs from the membrane in ejected micelles (236,237).

Five of the total six DAB residues are protonated at physiological pH, making PMB1 a polycation with a charge of +5. The incorporation of the lipid tail and hydrophobic D-Phe and Leu residues makes PMB1 an amphipathic molecule, which is thought to be vital to the antibacterial activity of the AMP (94,238). Polymyxins have been suggested to act through a self-promoted uptake mechanism, by which damage to the outer membrane (OM) increases its permeability and in turn enables more polymyxin molecules to cross the membrane (91). Once through the OM, polymyxins may cross the peptidoglycan cell wall and interact with the inner membrane (IM). It is possible that the disruption of cellular processes located at the IM adds to the cytotoxicity of polymyxins. Surface adsorption is likely aided by interactions between the positively charged DAB residues of PMB1 and negatively charged phosphate and carboxylate moieties of LPS in the OM. After surface adsorption, the cyclic region of PMB1 is understood to increase membrane permeability and disrupt LPS-LPS interactions (238,239); modified PMB1 species with the lipid tail removed have reduced antibacterial activity, but still increase membrane permeability to other antibiotics (240). An illustration of the PMB1 disrupting the *E. coli* cell envelope through the self-promoted uptake mechanism can be seen in **Figure 67.**

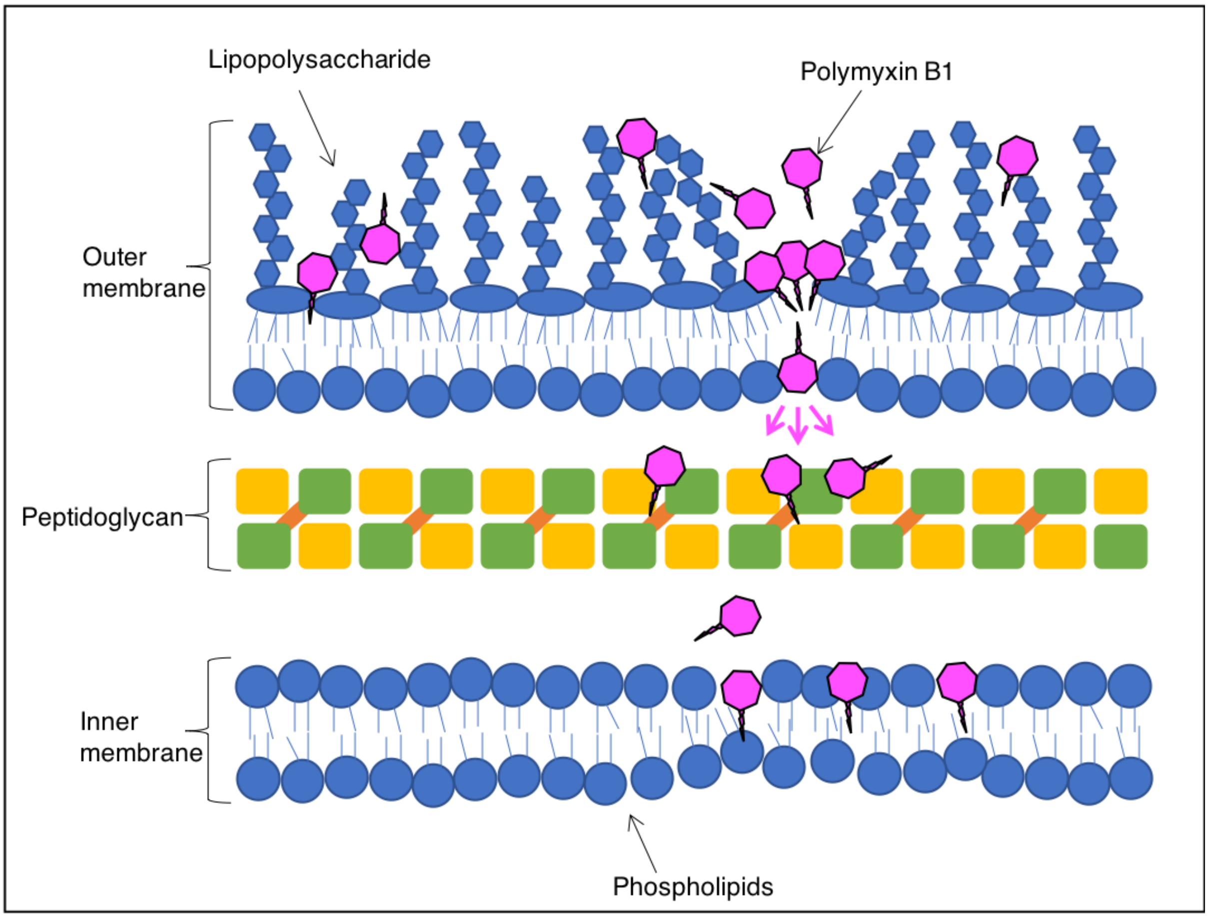

Figure 67. *A representation of the self-promoted uptake mechanism by polymyxin antimicrobial peptides.*

Molecular dynamics studies have shown that PMB1 can cause interdigitation of LPS and PL acyl tails, a phenomenon which has also been reported in X-ray diffraction and spin label studies (191,241,242). Further to this, PMB1 may also induce localised phase change in asymmetric Re LPS membranes; through an increase in order, PMB1 seemingly induced the formation of localised crystalline domains in the LPS leaflet of asymmetric Re LPS membranes (52). Previous united-atom and coarse-grained studies have highlighted the importance of interactions between PMB1 DAB residues and LPS phosphates in the initial adsorption into the membrane surface (52,191). However, these studies also report that penetration of the PMB1 lipid tail through LPS sugars into the membrane core is a very slow and rare event with the timescales available. In the coarse-grained study by Jefferies *et al.*, it was suggested that the interactions between PMB1 and the OM led to a decrease in entropy of the Re LPS lipids, which was related to the emergence of small crystalline domains, similar to those observed in LPS monolayers under high surface pressure (52,243,244). It remains unclear how the apparent ordering effect of PMB1 on the OM leads to its degradation and increased permeability.

The aim of this chapter is to investigate the permeation of PMB1 through the *E. coli* OM, using both equilibrium molecular dynamics and the application of an external electric field.

5.2 Methods

5.2.1 Atomistic Simulation Protocols

Antimicrobial Peptide System Setup

Ten PMB1 molecules were added into a 5 nm^3 box, which was then solvated and had Cl^- counterions added. Systems were energy minimised using the steepest descent algorithm to a maximum of 50,000 steps, then equilibrated for 5 ns at 310 K in the NPT ensemble with position restraints on the PMB1 molecules. Production runs of 500 ns at either 310 K or 323 K were then performed, and the resultant trajectories analysed.

Membrane with Antimicrobial Peptide System Setup

PMB1 in water systems after 500 ns at 323 K were used. Water was discarded, then PMB1 and ions were inserted into an equilibrated membrane system at a minimum distance of 1 nm from the outer leaflet. This was to prevent the PMB1 molecules from diffusing away from the outer leaflet, crossing the *z* axis periodic boundary and interacting with the inner leaflet. Systems were energy minimised using the steepest descent algorithm to a maximum of 50,000 steps, then equilibrated in the NPT ensemble for 1 ns then 5 ns with timesteps of 1 fs and 2 fs respectively. Position restraints (1000 kJ mol^{-1} nm^2) remained on PMB1 during equilibration. Production runs of either 500 ns or 1 μs at either 310 K or 323 K were then performed, and the resultant trajectories analysed.

Antimicrobial Peptide with Diacylglycerol System Setup

PMB1 systems after 500 ns at 323 K were used. Water was discarded, and DAG molecules added to AMP at a ratio of 5:1 in randomised conformations. The box size was increased to 9 nm^3 and system solvated. Systems were energy minimised using the steepest descent algorithm to a maximum of 50,000 steps, then equilibrated in the NPT ensemble for 1 ns then 5 ns with timesteps of 1 fs and 2 fs respectively. Position restraints (1000 kJ mol^{-1} nm^2) remained on PMB1 and DAG during equilibration.

Production runs of 500 ns at either 310 K or 323 K were then performed, and the resultant trajectories analysed.

Membrane with Antimicrobial Peptide in Diacylglycerol Micelle System Setup

PMB1 with DAG systems after 500 ns at 323 K were used. Water was discarded, then PMB1, DAG and ions were inserted into an equilibrated membrane system at a minimum distance of 1 nm from the outer leaflet. Systems were energy minimised using the steepest descent algorithm to a maximum of 50,000 steps, then equilibrated in the NPT ensemble for 1 ns then 5 ns with timesteps of 1 fs and 2 fs respectively. Position restraints (1000 kJ mol^{-1} nm^2) remained on PMB1 and DAG during equilibration. Production runs of 500 ns at either 310 K or 323 K were then performed, and the resultant trajectories analysed.

5.2.2 Coarse-Grained Simulation Protocols

Membrane with Antimicrobial Peptide System Setup

Molecular coordinates of LPS membrane systems solvated with polarisable water from the previous chapter were used. Ten antimicrobial peptide molecules were placed at a minimum distance of 1 nm from the outer leaflet.

All coarse-grained membrane systems were energy minimised using the steepest descent algorithm for a maximum of 50,000 steps. Systems were then subjected to three rounds of 100 ns in the NPT ensemble with a timestep of 5 fs, 10 fs and then 20 fs, before final equilibration in the NPT ensemble for 500 ns at 310 K. After equilibration, production runs of either 5, 10 or 20 μs were performed at 310 K and 323 K. During equilibration and production simulations, long-range electrostatic interactions were treated with the smooth particle mesh Ewald (PME) algorithm. The simulation details of all united-atom and coarse-grained systems with a single membrane, or PMB1 in solution, can be seen in **Table 7.**

Table 7. *All single membrane or solution simulations performed in this chapter under equilibrium molecular dynamics. Inner leaflet of all membrane systems consists of 90% PE, 5% PG and 5% cardiolipin mixture. All simulations performed at 310 K (x2) and 323 K (x1).*

System	**Notes**	**Length of Simulation**
PMB1_SOL	10x PMB1 molecules in water, neutralised with Cl- ions	500 ns (x3)
PMB1_PMBoD	10x PMB1 and 50x DAG molecules in water, neutralised with Cl- ions	500 ns (x3)
AT_REMP_PMB1	64x Re LPS lipids in outer leaflet, 10x PMB1 molecules added	1 μs (x3)
AT_RAMP_PMB1	64x Ra LPS lipids in outer leaflet, 10x PMB1 molecules added	500 ns (x3)
AT_REMP_PMBoD	Re LPS membrane with PMB1 and DAG micelle added	4 μs (x1), 500 ns (x2)
CG_REMP_PMB1	142x Re LPS lipids in outer leaflet, 10x PMB1 molecules added	10 μs (x3)
CG_RAMP_PMB1	112x Ra LPS lipids in outer leaflet, 10x PMB1 molecules added	10 μs (x3)
CG_OANT_PMB1	105x O-antigen LPS lipids in outer leaflet, 10x PMB1 molecules added	10 μs (x3)
CG_OmpA_PMB1	101x Re LPS lipids in outer leaflet with OmpA embedded, 10x PMB1 molecules added	10 μs (x3)

5.2.3 Electric Field System Set-Up

The coordinates of representative membrane systems NPT ensemble equilibration simulations, were used as a starting point for the application of electric fields of strength -0.1 – -0.25 V/nm. A negative external field was applied to encourage the positively charged PMB1 to diffused towards the outer leaflet of the membrane, rather than crossing the periodic boundary and interacting with the inner leaflet of the membrane. Systems were then simulated at 310 K for either 200 ns, or until the periodic box became unstable due to membrane deterioration due to electroporation. If no electroporation was observed, the simulation was extended to either 1 μs or 5 μs. Details of all simulations with an electric field applied can be found in **Table 8.**

Table 8. *All simulations performed in this chapter with an electric field applied. Inner leaflet of membranes is as previously described. All simulations performed at 310 K.*

System	**Notes**	**Field Strength (V/nm)**	**Length of Simulation**
CG_REMP_PMB1	142x Re LPS lipids in outer leaflet, 10x PMB1 molecules added	-0.1	1 μs (x3)
		-0.15	1 μs (x3)
		-0.2	200 ns (x3)
		-0.25	200 ns (x3)
CG_REMP_PMB1_shuffle	142x Re LPS lipids in outer leaflet, positions of 10x PMB1 molecules shuffled	-0.2	200 ns (x3)
CG_REMP_OmpA_PMB1	101x Re LPS lipids in outer leaflet with OmpA embedded, 10x PMB1 molecules added	-0.1	5 μs (x3)
		-0.15	1 μs (x3)

5.2.4 Double Membrane System Set-Up

Membrane systems with ten PMB1 molecules added were doubled and rotated 180° in the *z* axis using the GROMACS *genconf* utility (114). In some cases, additional PMB1 molecules were added so the resultant systems had a total of 20, 40 or 60 PMB1 molecules in the central compartment. The average distance between the phosphates of the innermost leaflet of each membrane was noted and used to calculate the compartment volume and thus the effective concentration of PMB1. Examples of system setups can be seen in **Figure 68.**

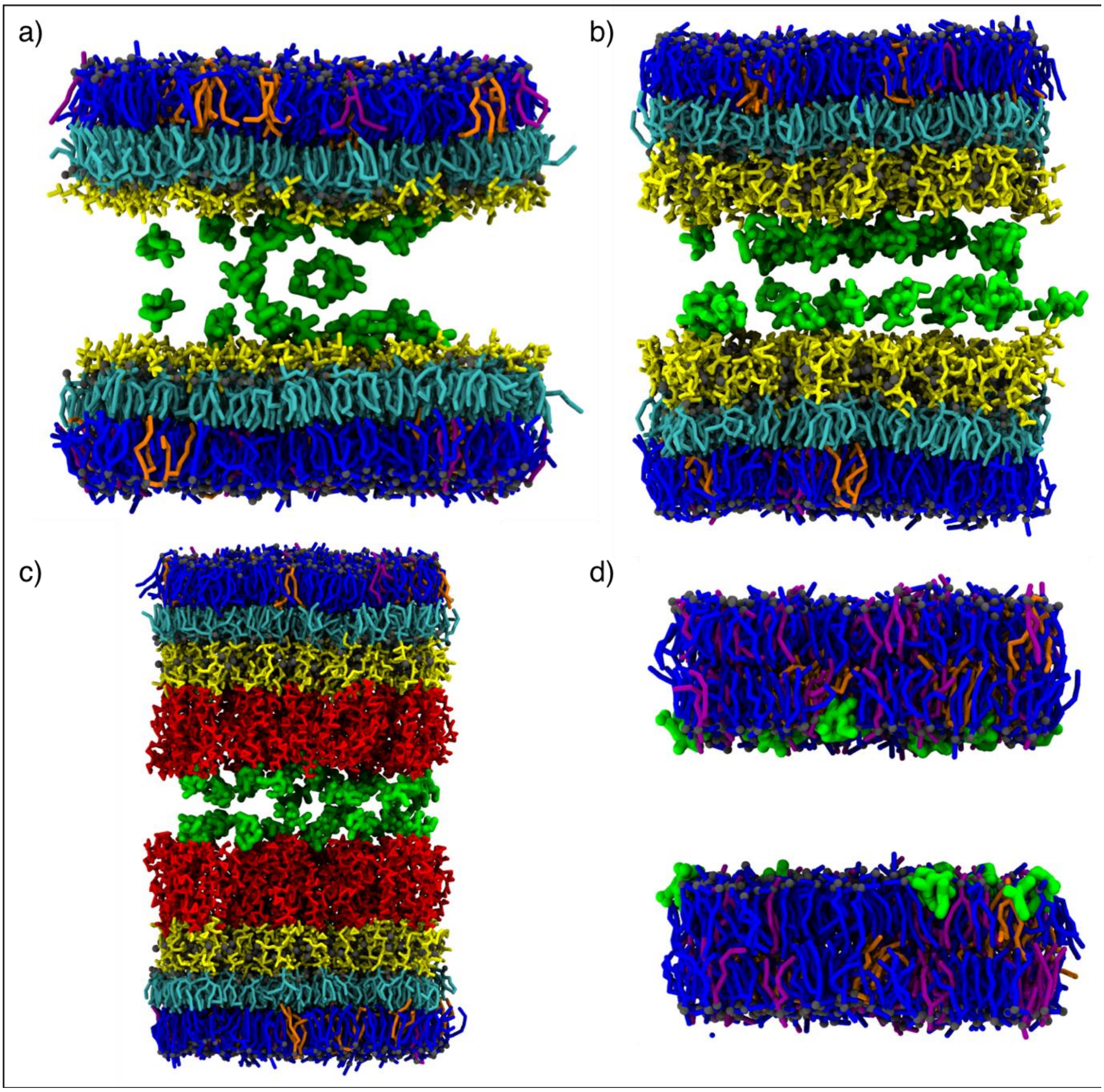

Figure 68. *Double membrane system setup for the wildtype outer and inner membrane models. Here PMB1 is coloured green, PE blue, PG purple, cardiolipin orange and LPS O-antigen, core and acyl tail segments red, yellow and cyan respectively.* ***68a)*** *the asymmetric Re LPS membrane.* ***68b)*** *the asymmetric Ra LPS membrane.* ***68c)*** *the asymmetric O-antigen LPS membrane.* ***68d)*** *the symmetric phospholipid inner membrane.*

The presence of two membranes created a central compartment, blocking off charged particles in the central compartment from bulk solvent. As such, a charge imbalance could be created between the inner and outer compartments. The charge imbalance was noted at the point of system setup and at the end of production simulations.

All coarse-grained double membrane systems were energy minimised using the steepest descent algorithm for a maximum of 50,000 steps. Systems were then subjected to three rounds of 100 ns in the NPT ensemble with a timestep of 5 fs, 10 fs and then 20 fs, during which all ions and PMB1 molecules were position restrained (1000 kJ mol^{-1} nm^{2}). After equilibration, production runs of either 1 or 5 μs were performed at 310 K and 323 K. During equilibration and production simulations, long-range electrostatic interactions were treated with the smooth particle mesh Ewald (PME) algorithm. The simulation details of coarse-grained double membrane systems can be seen in **Table 9.**

***Table 9**. All double membrane simulations performed in this chapter. Inner leaflets of membranes are as previously described, unless stated otherwise. All simulations performed at 310 K (x2) and 323 K (x1)*

System	**Notes**	**PMB1**	**Length of Simulation**
CG_REMP_Perm	142x Re LPS molecules in outer leaflet of each membrane	x40	5 μs (x3)
		x60	5 μs (x3)
CG_REMP_OmpA_Perm	101x Re LPS molecules in outer leaflet of each membrane, with OmpA embedded	x20	5 μs (x3)
		x40	5 μs (x3)
		x60	5 μs (x3)
CG_hDEMPa_Perm	71x wildtype Re LPS molecules and 71x Re LPS molecules deacylated at the 3' O position	x40	5 μs (x3)
		x60	5 μs (x3)
CG_RAMP_Perm	112x Ra LPS molecules in outer leaflet of each membrane	x40	5 μs (x3)
		x60	5 μs (x3)
CG_OANT_Perm	105x O-antigen LPS molecules in outer leaflet of each membrane	x40	5 μs (x3)
		x60	5 μs (x3)
CG_Inner_Perm	Two symmetric bilayers composed of 75% PE, 20% PG and 5% cardiolipin	x20	5 μs (x3)
		x40	5 μs (x3)
		x60	5 μs (x3)

5.3 Results and Discussion

5.3.1 Interactions Between Polymyxin B1 and the Outer Membrane Under Equilibrium Conditions

PMB1 was studied in solution at the united-atom resolution before its addition to the OM models. Due to its amphipathic nature, it was expected to form micelle-like structures in water, as reported by Berglund *et al.* (191). Aggregation of all ten PMB1 molecules was observed in three independent simulations within 500 ns. Total aggregation of all molecules took between 80 – 230 ns, depending on the molecular starting configurations. One clustered, PMB1 molecules typically remained within the resultant micelle. Hydrophobic residues D-Phe and Leu were buried within the micelle structures, whereas charged DAB residues and other polar moieties were exposed on the surface. Although transient interactions were observed between DAB residues and Cl^- ions, the Cl^- ions did not appear to be incorporated into the micelle aggregates. The aggregation of PMB1 molecules in solution can be seen in **Figure 69.**

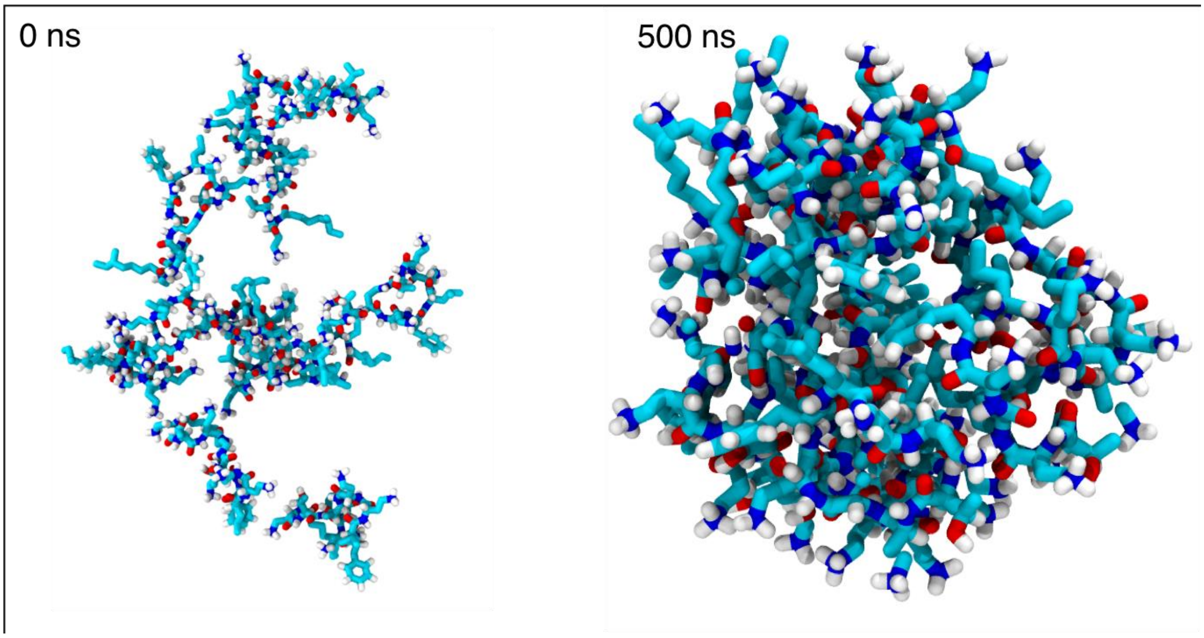

Figure 69. *Formation of PMB1 micelles in water.*

The radius of gyration (R_g) and RMSD were used as a measure of system convergence for PMB1 in solution simulations. As can be seen from the rolling average **Figures 70a** and **70b**, both the R_g and RMSD reached convergence within the first half of simulations. Interesting, the values of both the R_g and RMSD typically ranged between 2 – 3 nm, suggesting that the conformations adopted by the PMB1 molecules in solution were stable, and remained stable across the 500 ns simulations.

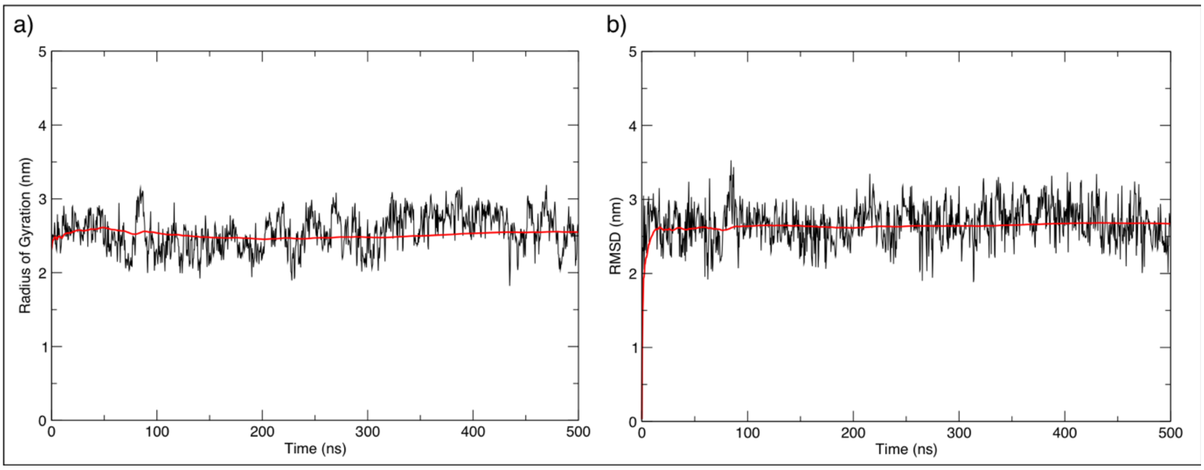

Figure 70. *Convergence of the dynamic properties of polymyxin B1 in solution. Data averaged across repeat simulations shown in black, with rolling average in red.* ***70a)*** *radius of gyration, averaged per residue.* ***70b)*** *RMSD, averaged per residue.*

The PMB1 micelles were then added to wildtype Re and Ra LPS membranes. It seems highly likely that PMB1 would form tight micelle clusters during its clinical application to pathogens, and as such the interactions of PMB1 micelles was studied here. The interactions between PMB1 and the wildtype Re LPS membrane will be discussed first.

Interestingly, PMB1 micelles usually denatured and partially dispersed upon contact with Re LPS KDO sugars. This may have been due to the PMB1 molecules favouring interaction with Re LPS over the other PMB1 molecules. Upon dispersion of the micelle structure, PMB1 molecules often diffused away from the membrane and crossed the *z* axis of the simulation box, and subsequently interacted with the inner leaflet of membrane. The PMB1 molecules which remained in contact with the outer leaflet were largely unable to penetrate through the KDO sugars of Re LPS towards the membrane core; however, close attention was paid to interactions between PMB1 and regions of Re LPS which are known to be modified in polymyxin-resistant species. Consistent ionic interactions were observed between DAB residues of PMB1 and carboxylate moieties of primary and secondary KDO sugars of Re LPS, as can be seen in **Figures 71a** and **71b**. The phosphoethanolamine (PEtN) transferase EptB is known to conjugate PEtN to the 6 C position of the secondary KDO residue of Re LPS in polymyxin-resistant *E. coli* (78). The introduction of PEtN also presents the possibility of salt bridge interactions with KDO carboxylate moieties of neighbouring Re LPS molecules, thereby excluding PMB1 from these potential adsorption sites.

Snorkelling behaviour of DAB residues, similar to that exhibited by lysine residues in proteins, was observed towards lipid A phosphates, as seen in **Figure 71c**. Snorkelling of lysine towards lipid A phosphates was also observed in LpxR, and has also been observed to occur in synthetic coiled-coil peptides E and K towards charged phospholipid headgroups (159,245). These lipid A phosphates are also targets of modification in cases of polymyxin resistance, through the addition of PEtN or 4-amino-4-deoxy-L-arabinose (Ara4N) by EptA or ArnT (77,78).

One PMB1 molecule was able to penetrate through the KDO sugars of Re LPS within the total 3 μs of simulation time at united-atom resolution. Polar regions of the AMP interacted with KDO sugars, causing structural rearrangements. This enabled the lipid tail of the PMB1 molecule to pass the KDO sugars and angle towards the membrane core. The penetration of the PMB1 lipid tail through Re LPS KDO sugars can be seen in **Figure 71d**. In addition, the minimum distance between PMB1 DAB residues and Re LPS phosphate moieties over time can be seen in **Figure 71e**; although DAB residues were observed to snorkel towards phosphate moieties, direct interaction between the residues were transient.

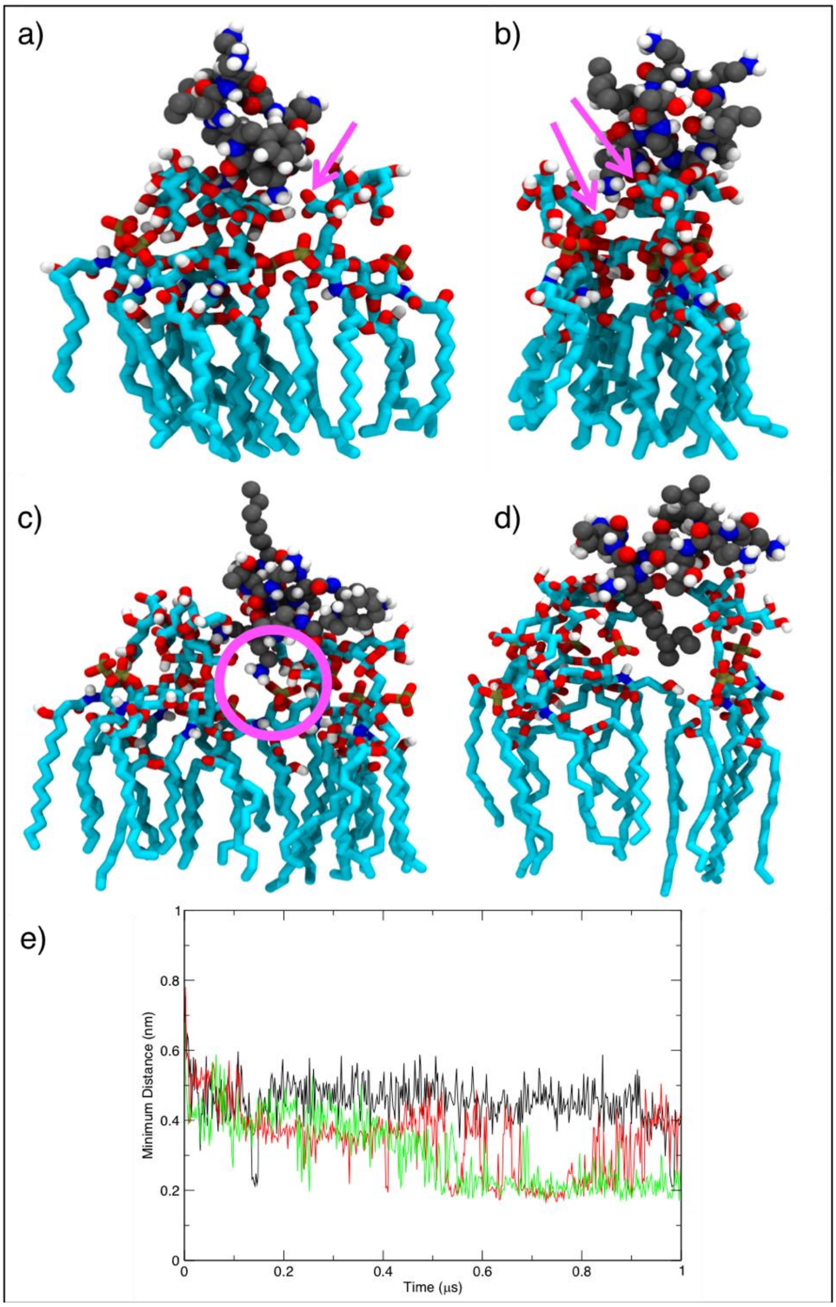

Figure 71. *Specific interactions between polymyxin B1 and Re LPS.* ***71a) & 71b)*** *PMB1 interacts with the inner core KDO sugars of Re LPS via carboxylate moieties. Pink arrows show carboxylate moieties interacting with PMB1.* ***71c)*** *snorkelling-like behaviour of PMB1 DAB residue towards phosphate moiety of Re LPS, highlighted by pink circle.* ***71d)*** *Furthest extent of PMB1 lipid tail through Re LPS core sugars towards membrane core.* ***71e)*** *The minimum distance between DAB residues and Re LPS phosphates. Black and red lines are data from simulations at 310 K and the green line data from the simulation at 323 K.*

The interactions of PMB1 molecules with the inner leaflet of the OM were also investigated, to see if the locations of PMB1 interactions with the membrane corresponded between leaflets. The self-promoted uptake model suggests that some PMB1 molecules remain interacting with the inner leaflet of the OM, and it may be these interactions which facilitate the permeation of further PMB1 molecules. While no correspondence was seen in the locations of PMB1 interactions with either leaflet of the membrane, full insertion of the D-Phe residues and the lipid tails into the membrane core through the inner leaflet was observed. Polar regions of PMB1 molecules remained associated with PL headgroups and were excluded from the membrane core. If PMB1 insertion into the inner leaflet does indeed facilitate further PMB1 permeation, there may be some phenomena missing from these simulations. It is possible that PMB1 permeation causes PL flip-flopping into the outer leaflet, thereby providing an easier route of access for PMB1 through the OM.

PMB1 micelles were also added to the wildtype Ra LPS membrane. Similarly, to the Re LPS membrane, PMB1 micelles denatured and partially dissipated upon contacts with LPS and a number of PMB1 molecules crossed the *z* dimension periodic boundary and interacted with the inner leaflet of the membrane. PMB1 molecules which remained in contact with Ra LPS molecules were unable to penetrate through the outer core sugars, as can be seen in **Figures 72a** and **72b**. Interestingly, DAB residues were once again observed to exhibit snorkelling-like behaviour towards LPS phosphate moieties, although these were conjugated to heptose sugars of the outer core. The snorkelling-like behaviour can be seen in **Figure 72c**. Salt bridge interactions were not observed between PMB1 and Ra LPS due to the lack of carboxylate moieties in the outer core sugars. However, hydrogen bonding was observed between the peptide bonds of PMB1 and hydroxyl moieties of galactose and glucose sugars.

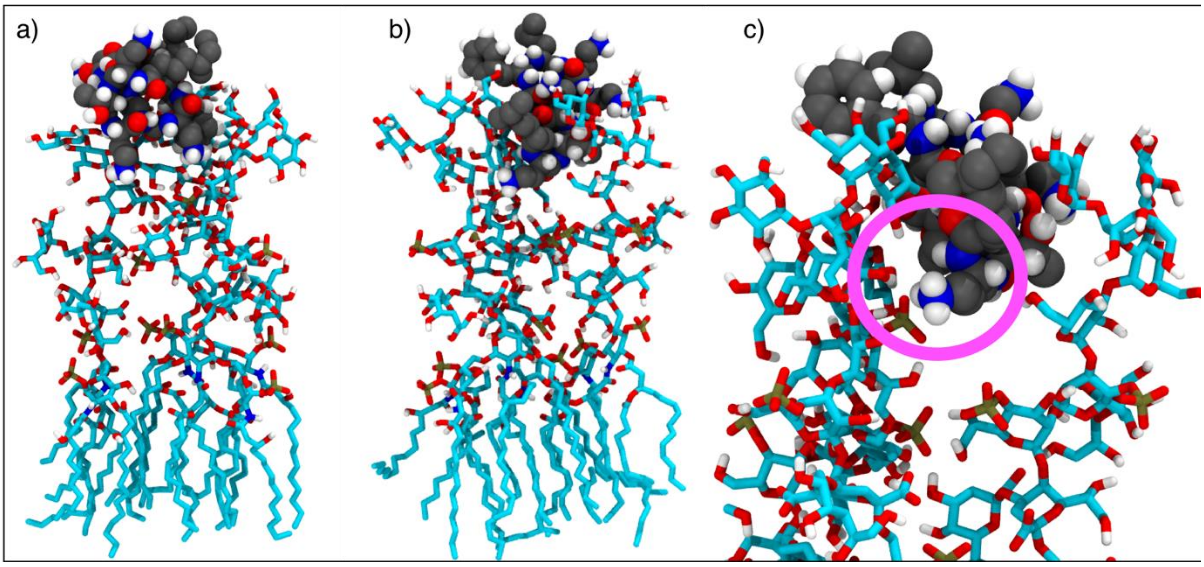

Figure 72. *Specific interactions between polymyxin B1 and Ra LPS.* ***72a) & 72b)*** *PMB1 interacts with the galactose and glucose sugars of the Ra LPS outer core, but is unable to interact with inner core or lipid A sugars.* ***72c)*** *snorkelling-like behaviour of a DAB residue of PMB1 is observed towards the phosphorylated secondary heptose sugar of an Ra LPS molecule.*

In order to quantify the extent of PMB1 penetration through LPS core sugar regions, the number of interactions between the AMP molecules and separate sugar groups were calculated. Interactions, or contacts, were defined as an intermolecular distance of ≤0.3 nm between PMB1 and LPS sugars. A higher number of interactions with inner core and lipid A sugars would signify a great level of penetration through LPS core sugars. As can be seen from **Figures 73a** and **73b**, a significantly greater number of contacts were recorded between PMB1 and KDO sugars of Re LPS, compared with the lipid A sugars or phosphates. Similar results were seen with the Ra LPS membrane, where contacts were only observed between PMB1 and the outermost galactose, α-glucose and β-glucose sugars, and 4’ phosphate of the secondary heptose sugar. The recorded number of contacts between PMB1 and Ra LPS outer core sugars or 4’ heptose phosphate can be seen in **Figures 73c** and **73d**.

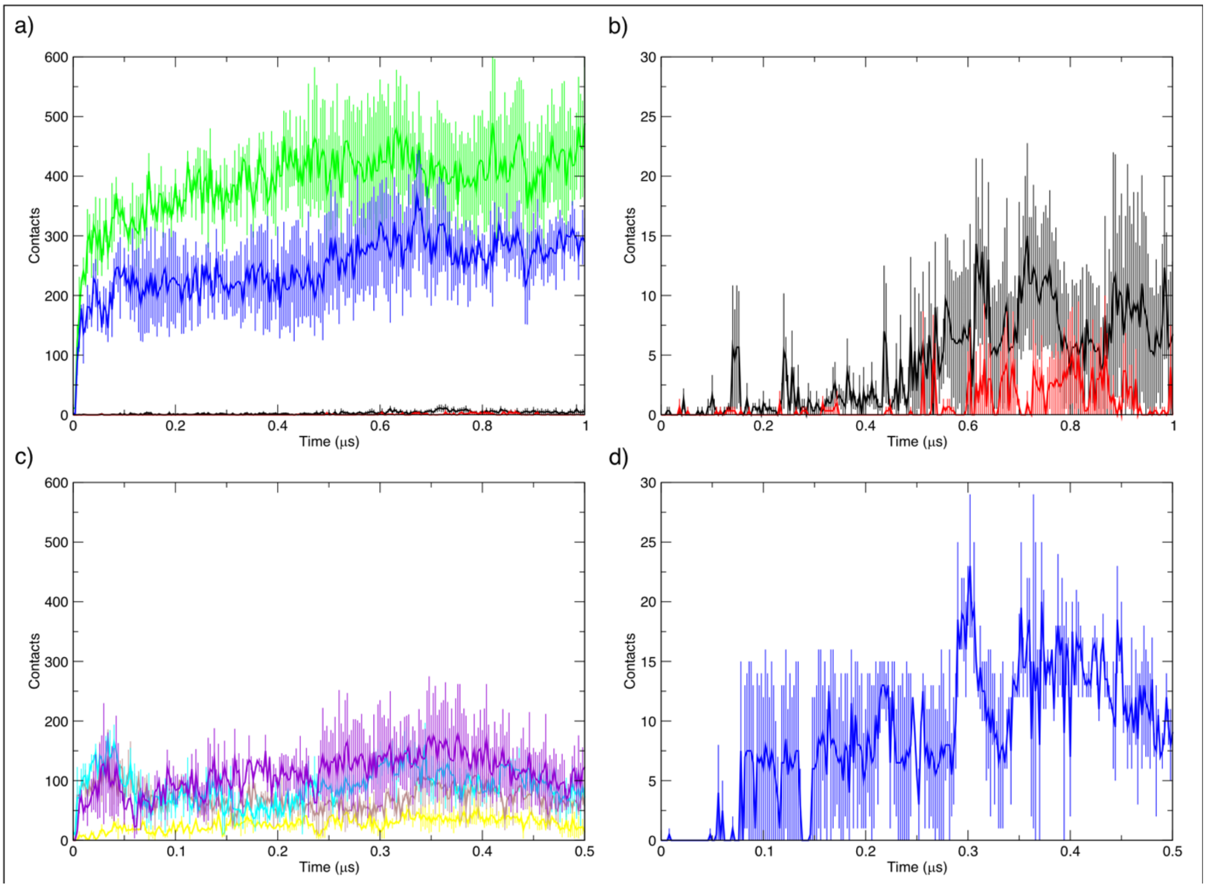

Figure 73. *Number of contacts between PMB1 and LPS moieties. Contact is defined as an intermolecular distance of ≤0.3 nm. Sugars are coloured as follows: first N-acetylglucosamine black, second red, first KDO green, second blue, second α glucose yellow, β glucose brown, first galactose cyan and second galactose violet. Contacts with phosphates are on separate plots and coloured as follows: 1 and 4' phosphates of lipid A coloured black and red, and the 4' phosphate the outer core coloured green.* ***73a)*** *PMB1 contacts with Re LPS sugars.* ***73b)*** *PMB1 contacts with Re LPS phosphates.* ***73c)*** *PMB1 contacts with Ra LPS outer core sugars.* ***73d)*** *PMB1 contacts with Ra LPS phosphate of second heptose.*

The coarse-grained resolution study by Jefferies *et al.* suggested that the presence of PMB1 increased the order and packing of LPS molecules in contact with the AMP (52). Therefore, the deuterium order parameter of each of the LPS acyl tails was calculated for both Re and Ra LPS membrane system with PMB1 and compared to membranes in the absence of PMB1. There was a slight increase in order across all six acyl tails of Re LPS molecules in the membrane system with PMB1 present, as can be seen in **Figure 74a**. Although the presence of PMB1 did appear to effect the order parameters of Ra LPS acyl tails (**Figure 74b**), the differences in values were less pronounced. It seems likely that the extent of PMB1 penetration may play a role in the ordering effect of PMB1 on LPS acyl tails.

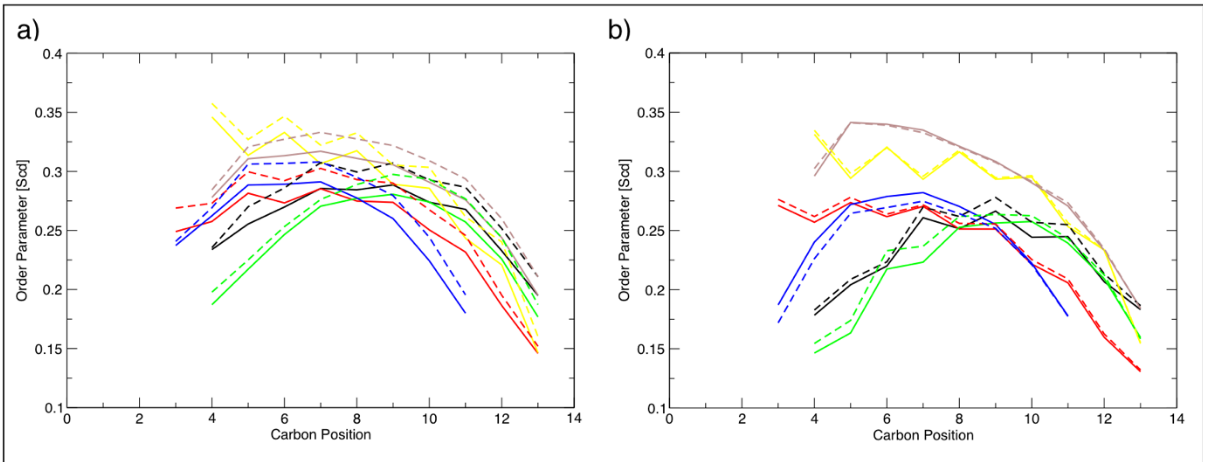

***Figure 74.** Deuterium order parameters for the six tails of Re and Ra LPS in the absence and presence of polymyxin B1. Data from membrane only systems shown with solid lines and from systems with PMB1 with dashed lines **74a)** Re LPS membrane system. **74b)** Ra LPS membrane system.*

PMB1, as previously mentioned, is suggested to cause bacterial cell death through membrane disruption, which makes the apparent ordering effect on LPS acyl tails seem unusual. However, as suggested by Jefferies *et al.*, the induction of localised phase changes in the membrane is highly likely to have destabilising effects on the membrane as a whole (52). If PMB1 permeation through the LPS membrane could be observed, more could be understood about the consequences of interactions between the AMP and the OM.

The addition of diacylglycerol (DAG) was considered as a means of encouraging PMB1 penetration through the LPS core regions. DAG is found in biological membranes, and often involved in biochemical signalling and metabolic processes such as lipid biosynthesis (246,247). It was anticipated that the presence of an amphipathic molecule such as DAG could encourage the dispersion of Re LPS inner core sugars, thereby facilitating PMB1 insertion into the membrane core. For the purpose of this experiment, 1, 3-dimyristin was used as a representative DAG molecule.

A closely packed DAG micelle was formed within 2 – 4 ns in three independent simulations. PMB1 molecules were not initially associated with the micelle structure, although all AMP molecules were recruited to the micelle within 12 – 22 ns, depending on starting coordinates. The micelle proved to be a stable conformation for the molecules, remaining in shape for 500 ns across all three simulations. Micelle formation can be seen in **Figure 75**.

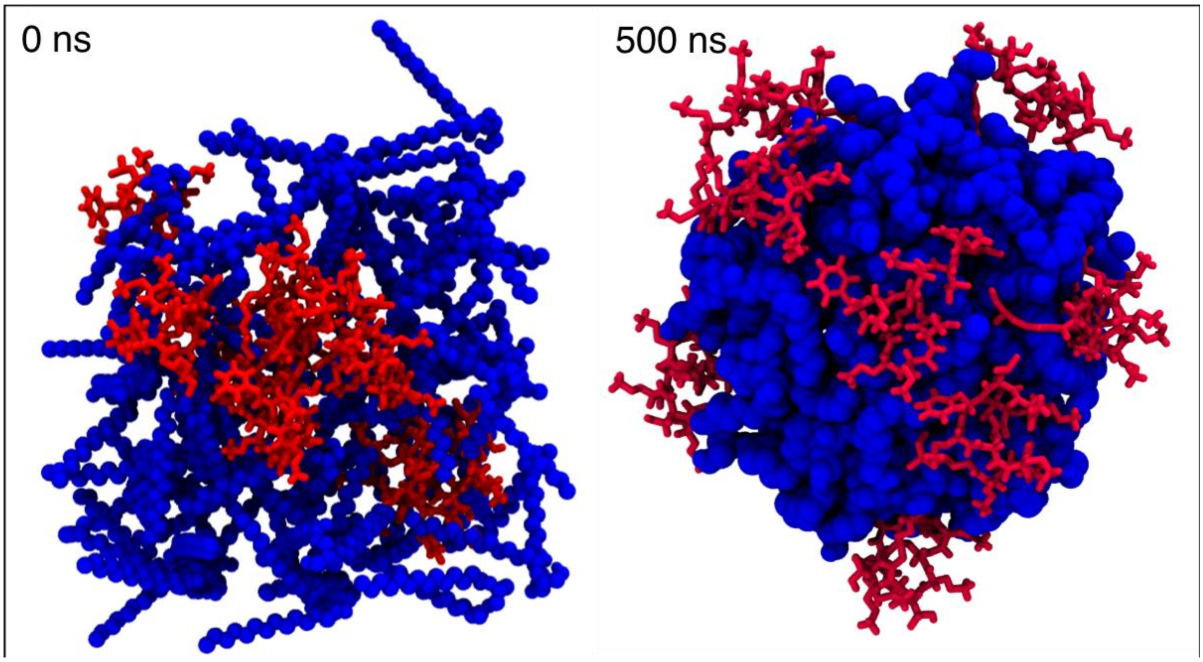

Figure 75. *Formation of PMB1 micelles with 1, 3-dimyristin in water.*

PMB1 coated the surface of the DAG micelle, with DAB residues angled into bulk solution and lipid tails dissolved into the hydrophobic micelle core. Limited insertion of D-Phe and Leu residues into the micelle, along with electrostatic interactions between polar PMB1 regions and glycerol headgroups of 1, 3-dimyristin. RMSD and R_g were calculated to assess convergence of the dynamic properties of PMB1. Similarly to the simulations without DAG, both RMSD and R_g converged at ~2.5 nm. The range of the R_g remained 2.45 – 2.5 nm for 60% of the simulations, although increased up to 3.3 nm. The R_g remained between 2.45 – 2.5 nm when all PMB1 molecules were associated with the DAG micelle, which appeared to constrict conformational change in the molecules. RSMD and R_g convergence can be seen in **Figures 76a** and **76b**.

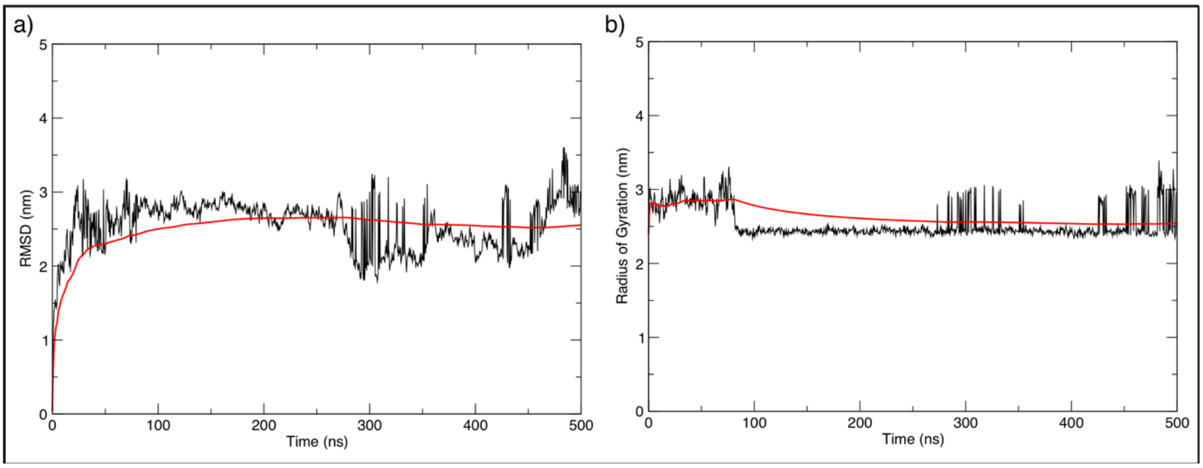

Figure 76. *Convergence of the dynamic properties of polymyxin B1 in solution with diacylglycerol. Data averaged across repeat simulations shown in black, with rolling average in red**. 76a)** radius of gyration, averaged per residue.* ***76b)*** *RMSD, averaged per residue.*

PMB1 and DAG micelles were added to the Re LPS membrane. No penetration of PMB1 past Re LPS KDO sugars was observed after 4 μs simulation at 323 K. The PMB1-DAG structure remained in a micelle conformation, with no molecules ejected from the micelle. Interactions between Re LPS and PMB1 were favoured over DAG, leading to conformational rearrangements in the micelle such that DAB residues of seven or eight PMB1 molecules were within hydrogen bonding distance of Re LPS KDO residues. The result of 4 μs simulation, along with PMB1 movement in the PMB1-DAG micelle can be seen in **Figure 77**. As the presence of DAG did not aid PMB1 penetration through Re LPS core sugars, the PMB1-DAG micelle was not added to the Ra LPS membrane.

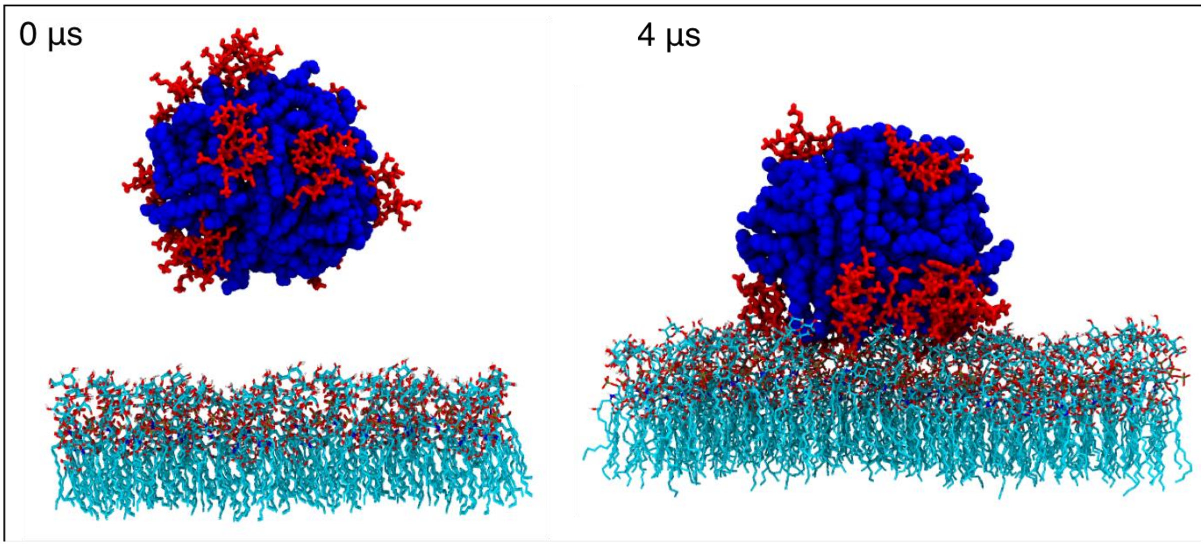

***Figure 77**. Addition of united-atom polymyxin B1 and diacylglycerol micelle to the Re LPS membrane, with water ion and inner leaflet removed for clarity. PMB1 molecules in red liquorice format, DAG in blue VDW and Re LPS coloured with carbon cyan, oxygen red, phosphorous tan, nitrogen blue and hydrogen white, all in liquorice format.*

The number of contacts between PMB1 and Re LPS sugars and phosphates were calculated in order to quantify the extent of PMB1 penetration through inner core sugars. The addition of DAG appeared to reduce the number of interactions between PMB1 and both Re LPS KDO sugars and phosphates. In the absence of DAG, PMB1 micelles dispersed upon contacts with LPS molecules, and it may be that the conformational freedom gained from this dispersion aided penetration. The presence of the DAG micelle may prevent PMB1 molecules from causing the structural rearrangements to KDO sugars necessary for lipid tail insertion. Contacts between PMB1 and Re LPS can be seen in **Figures 78a** and **78b**.

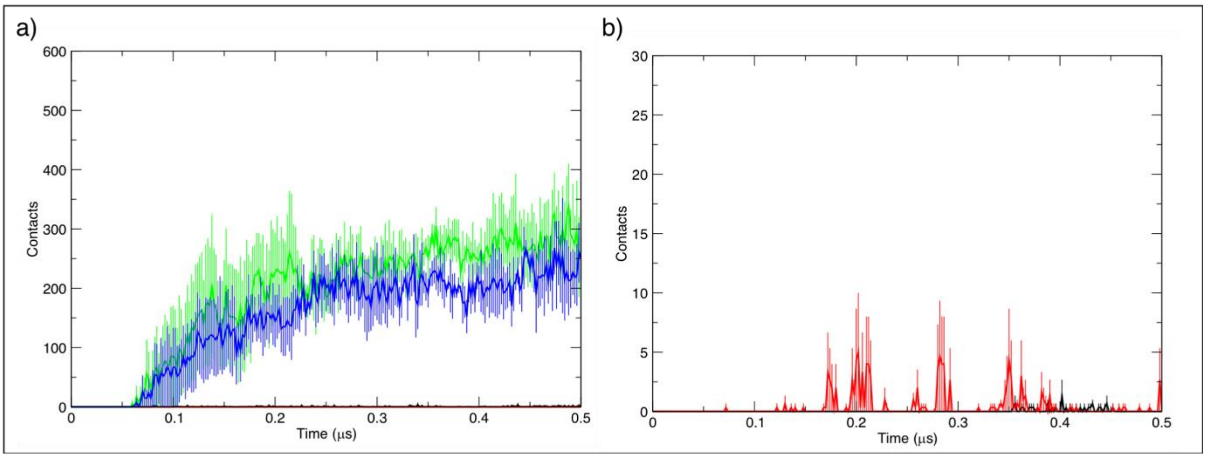

Figure 78. *Number of contacts between polymyxin B1 and LPS core sugars in Re LPS membrane system with PMB1 and DAG added. Contact is defined as an intermolecular distance of ≤0.3 nm. Sugars and phosphates are coloured as in* ***Figure 73. 78a)*** *PMB1 contacts with Re LPS sugars.* ***78b)*** *PMB1 contacts with Re LPS phosphates.*

The addition of DAG appeared to increase the ordering effect of PMB1 on the acyl tails of Re LPS, compared to simulations in the absence of the AMP, as can be seen from **Figure 79a**. The acyl tails of Re LPS molecules in contact with PMB1 seemed to undergo a transition into the gel phase, with significantly reduced movement perpendicular to the bilayer normal. The acyl tails of bulk Re LPS molecules, away from PMB1 molecules, were observed to splay outwards, as is characteristic of lipids in the liquid phase (**Figure 79b**). This apparent localised phase change was previously presented by Jefferies *et al.*, although their observation was that phase change was limited to Re LPS phosphates (52). It is important to note here that a reduced ability to reseal gaps and imperfections in the membrane is a characteristic of membranes in the gel phase. This supports the suggestion that the unusual ordering effect, and subsequent localised phase transition, of PMB1 on the Re LPS membrane is key to the antibacterial action of the AMP.

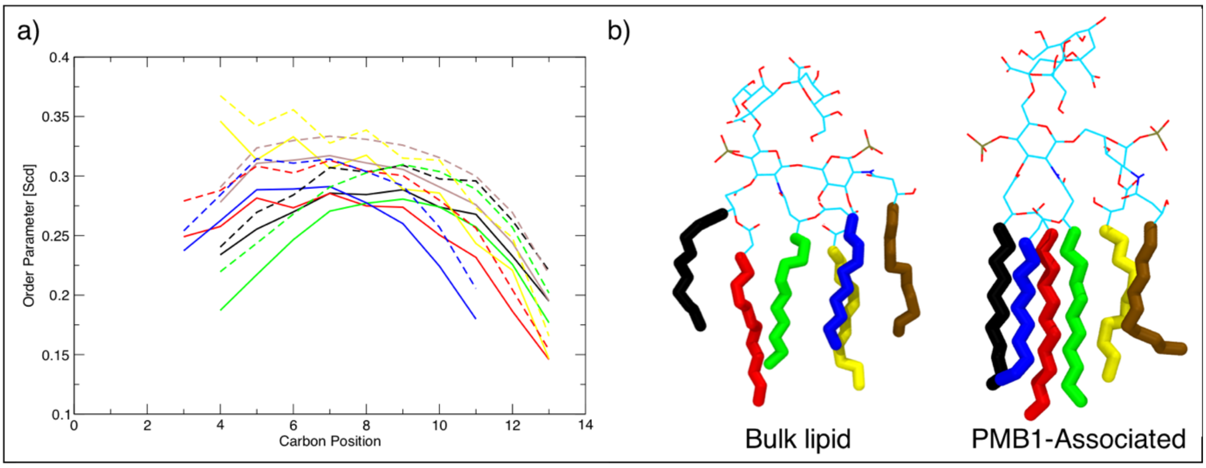

Figure 79. *PMB1 causes localised ordering of Re LPS acyl tails.* ***79a)*** *Deuterium order parameters for the six tails of Re LPS in the presence of PMB1 and DAG. Data from membrane only systems shown with solid lines and from systems with PMB1 and DAG with dashed lines.* ***79b)*** *Direction of acyl tails between Re LPS molecule interacting (≤0.3 nm) with a PMB1 molecule compared with Re LPS molecule from the bulk lipid. Images generated from co-ordinates resulting from 4 μs simulation at 323 K.*

Evidence from united-atom simulations appears to suggest that the rearrangement of LPS core sugars required for PMB1 insertion into the OM is a time-dependent process. In an effort to extend the timescale of observations, simulations of PMB1 with Re, Ra and O-antigen LPS membranes were performed at the coarse-grained resolution. Observations of interactions between PMB1 and O-antigen LPS have not been published previously, and were as such of particular interest.

The extent of PMB1 penetration through LPS core sugars was greater at the course-grained resolution across 30 μs total simulation time for each membrane. While complete insertion of the PMB1 lipid tail into the membrane core was not observed with any OM model, transient interactions between the PMB1 and Re LPS tails were seen. A comparison of the extent of PMB1 penetration through Re LPS core sugars at each resolution can be seen in **Figures 80a** and **80b**. PMB1 was able to induce structural rearrangements to the KDO and GlcNAc sugars of Re LPS, while maintaining charge-charge interactions with LPS phosphates.

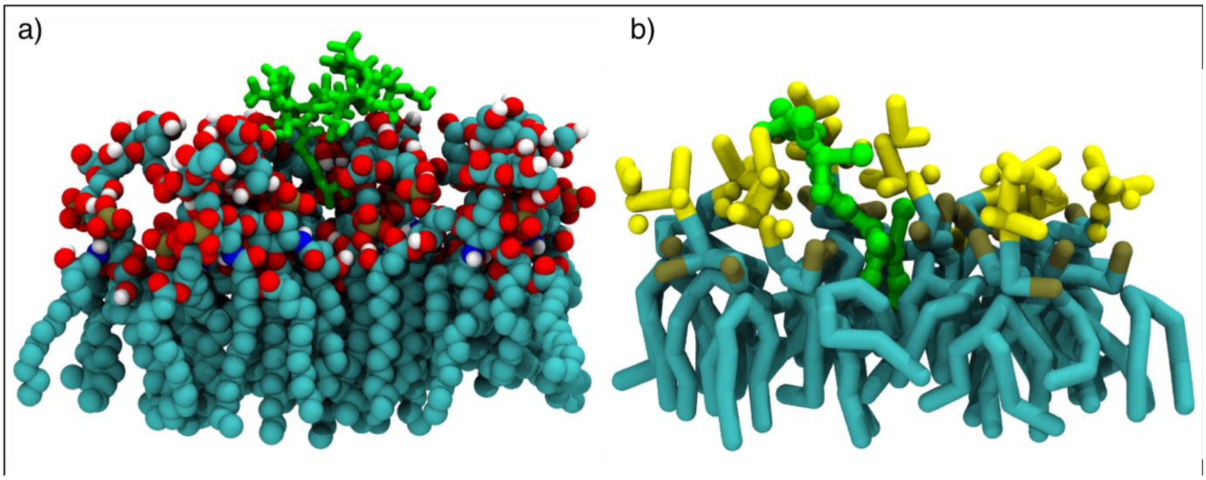

Figure 80. *Comparison of coarse-grained and united-atom resolution PMB1 penetration into Re LPS membrane core.* ***80a)*** *extent of penetration by a united-atom PMB1 molecule into the Re LPS membrane.* ***80b)*** *extent of penetration by a coarse-grained PMB1 molecule into the Re LPS membrane.* ***80c)*** *extent of penetration by a united-atom PMB1 molecule into the Ra LPS membrane.* ***80b)*** *extent of penetration by a coarse-grained PMB1 molecule into the Ra LPS membrane.*

Contacts were counted between PMB1 and segments of LPS, namely the O-antigen sugars, outer core sugars, inner core sugars, lipid A sugars and acyl tails. LPS segments were used rather than individual sugars due to the decrease in resolution from united-atom to coarse-grained.

An increase in the number of contacts between PMB1 and inner core and lipid A segments of LPS suggested greater penetration through the Re and Ra LPS membranes in coarse-grained simulations as compared with united-atom simulations. This increase in number of contacts, along with observations of PMB1 molecules penetrating further through the core sugars of LPS suggests that the coarse-grained resolution may indeed be the more appropriate tool for studying PMB1 permeation through the OM. An increased number of interactions were observed between PMB1 and Re LPS phosphates; interactions were also recorded between AMP molecules and the acyl tails of Re LPS molecules, giving further evidence of the partial PMB1 insertion into the membrane. Contacts between PMB1 and Re LPS segments or phosphates can be seen in **Figures 81a** and **81b**.

Similar levels of PMB1 penetration through the Ra LPS outer core sugars were observed in simulations at both resolutions, with PMB1 barely interacting with the inner core sugars at the coarse-grained resolution. Interactions were recorded with the phosphate of the primary heptose sugar, as well as an increased number of interactions with the phosphate of the secondary heptose sugar. Contacts between PMB1 and Ra LPS segments or phosphates can be seen in **Figures 81c** and **81d**.

Voids were observed due to the sugar packing of Ra and O-antigen LPS outer core sugars. These voids were discussed in the previous chapter and are amplified in the O-antigen LPS membrane by tilting of the O-antigens. This tilting was exploited by some PMB1 molecules, which were able to bypass the bulky O-antigen regions and interact with the outer and inner core segments of LPS (**Figure 81e**). Similarly, interactions were recorded between PMB1 and lipid A phosphates (**Figure 81f**).

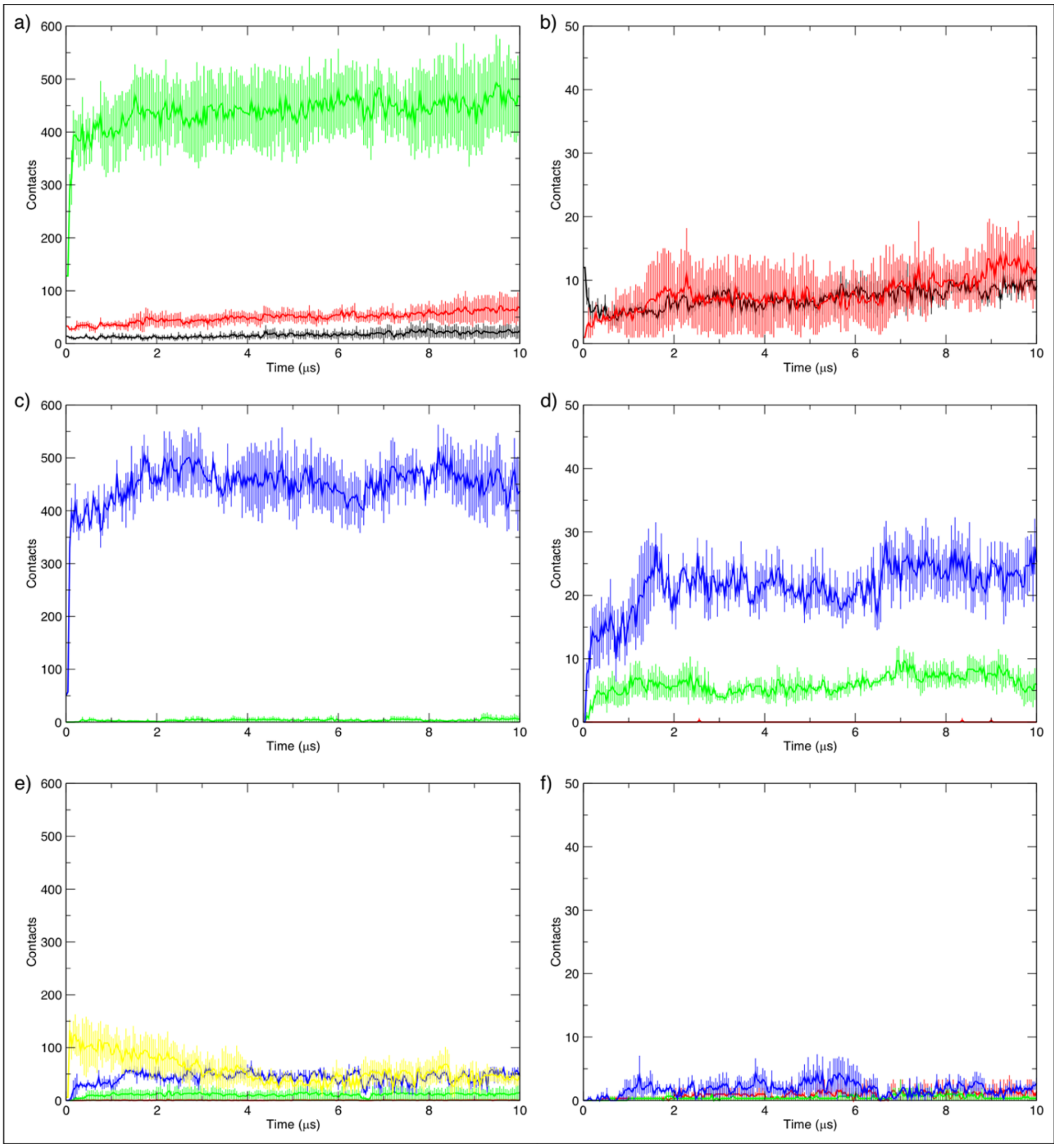

Figure 81. *Number of contacts between PMB1 and LPS segments at coarse-grained resolution. Contact is defined here as an intermolecular distance of ≤0.6 nm. Segments are coloured as follows: acyl tails black, lipid A red, inner core sugars green, outer core sugars blue, O-antigen sugars yellow. Contacts with LPS phosphates are on separate plots and coloured as follows: 1 and 4' phosphates of lipid A coloured black and red, and the 4 and 4' phosphates the outer core coloured green and blue.* ***81a)*** *PMB1 contacts with Re LPS segments.* ***81b)*** *PMB1 contacts with Re LPS phosphates.* ***81c)*** *PMB1 with Ra LPS segments membrane.* ***81d)*** *PMB1 contacts with Ra LPS phosphates.* ***81e)*** *PMB1 contacts with O-antigen LPS segments.* ***81f)*** *PMB1 contacts with O-antigen phosphates.*

A similar level of PMB1 penetration towards the membrane core was seen in each of the LPS membrane. In the Ra and O-antigen membranes, PMB1 exploited gaps in sugar-sugar packing between neighbouring LPS molecules. Representations of the extent of PMB1 penetration through LPS sugars can be seen in **Figures 82a** to **82c**.

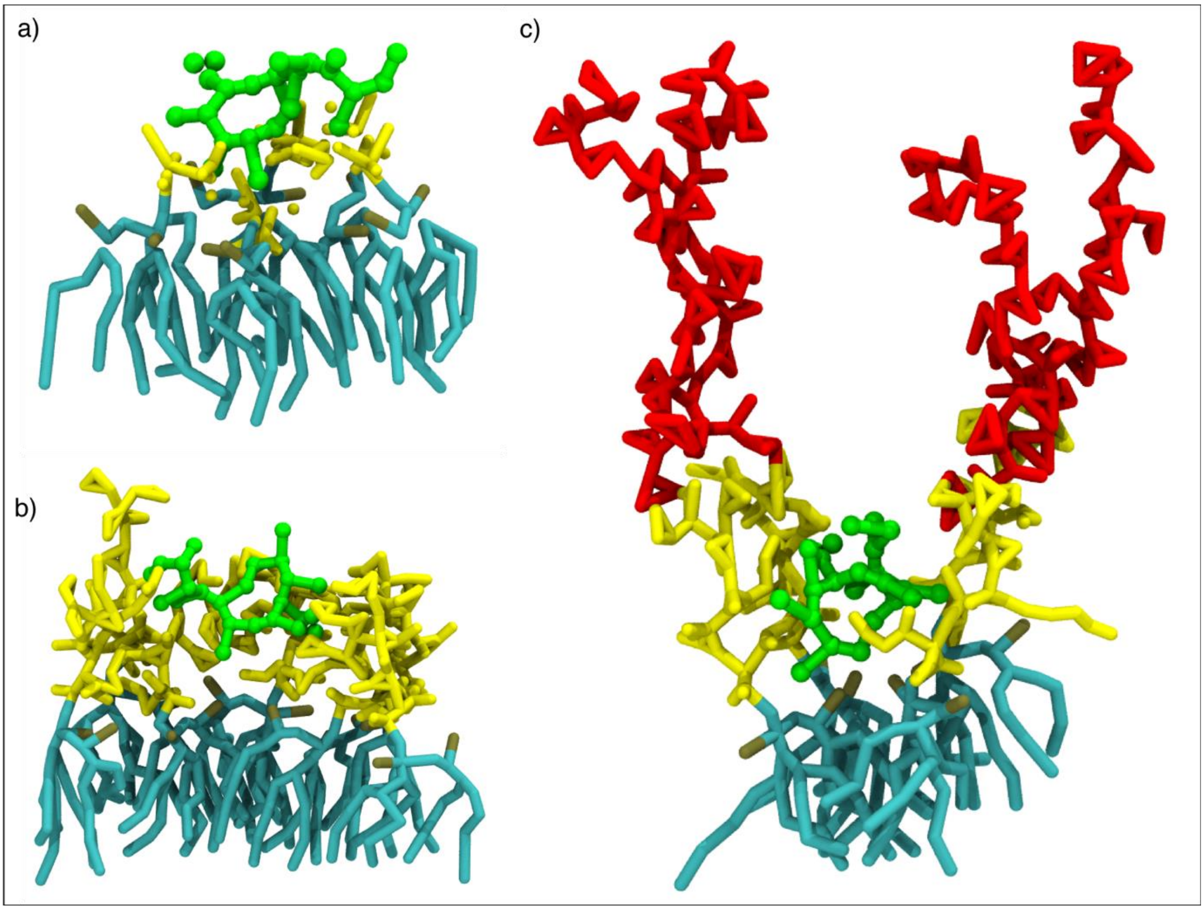

Figure 82. *Penetration of PMB1 through LPS core and O-antigen sugars.* ***82a)*** *PMB1 penetration through Re LPS inner core sugars.* ***82b)*** *PMB1 penetration through Ra LPS core sugars.* ***82c)*** *PMB1 penetration through LPS O-antigen sugars.*

LPS area per lipid (APL) and system density along the *z* axis were calculated as metric by which to assess the effect of PMB1 interactions with OM models. The greatest effect with regards to LPS APL was seen with the Re LPS membrane, which experienced an decrease of 0.1 (±0.01) nm^2 when exposed to PMB1. Conversely, PMB1 exposure to the Ra LPS membrane caused a slight increase in LPS APL. Interactions between PMB1 and the O-antigen membrane did not appear to have an impact on LPS APL. Comparisons of LPS APL in the presence and absence of PMB1 can be seen in **Figure 83a**.

Calculation of density of system constituents along the *z* axis further evidence the lack of penetration of PMB1 into the membrane core. The PMB1 molecules which did not cross the *z* dimension periodic boundary we unable to pass LPS phosphates. PMB1 molecules which did cross the *z* boundary typically inserted themselves into the inner leaflet and were observed to remain in the same plane as inner leaflet phosphates. The system densities for Re, Ra and O-antigen membrane systems with PMB1 can be seen in **Figures 83b** to **83d**.

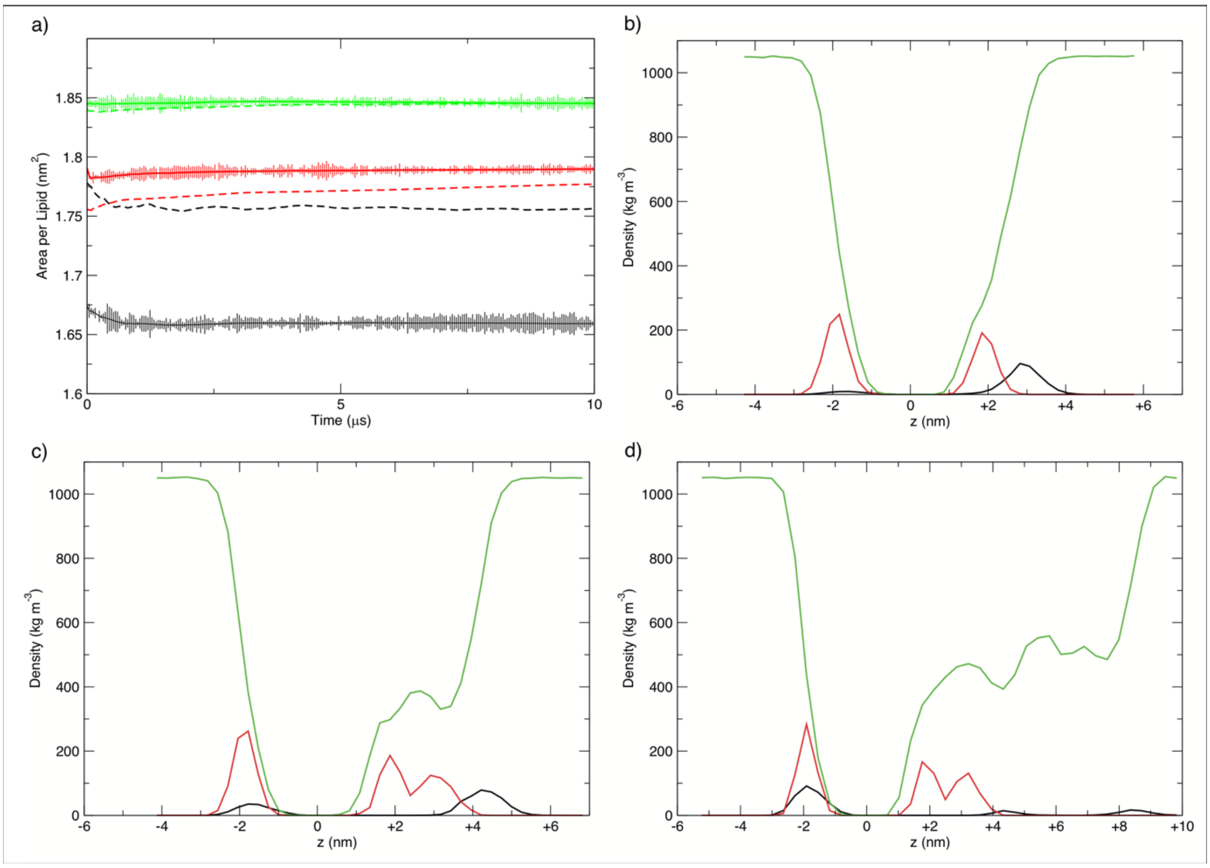

Figure 83. *Rolling average area per lipid with standard error fitted for coarse-grained resolution LPS membranes in the presence of PMB1, and z axis system densities showing membrane localisation of PMB1, with phosphates in black, PMB1 red and polarisable water green.* ***83a)*** *APL of Re (black), Ra (red) and O-antigen (green) LPS lipids in membrane. Data from systems with PMB1 present shown with solid lines and error bars, and data from membrane-only systems with dashed lines.* ***83b)*** *Re LPS*

with PMB1 system density. ***83c)*** *Ra LPS with PMB1 system density.* ***83d)*** *O-antigen LPS with PMB1 system density.*

It was shown in the previous chapter that an Re LPS with OmpA embedded consistently electroporated under a lower field strength, potentially due to disorder in the acyl tails of annular LPS molecules. It was therefore considered that the increased disorder in annular LPS molecules may also facilitate insertion of PMB1 into the OM. An increase in the number of interactions between PMB1 and lipid A sugars was observed (**Figure 84a**), along with complete insertion of the lipid tail of one PMB1 molecule into the membrane core (**Figure 84b**). Further to this insertion, lipid tails of three further PMB1 molecules were able to penetrate through Re LPS inner core sugars towards the membrane core.

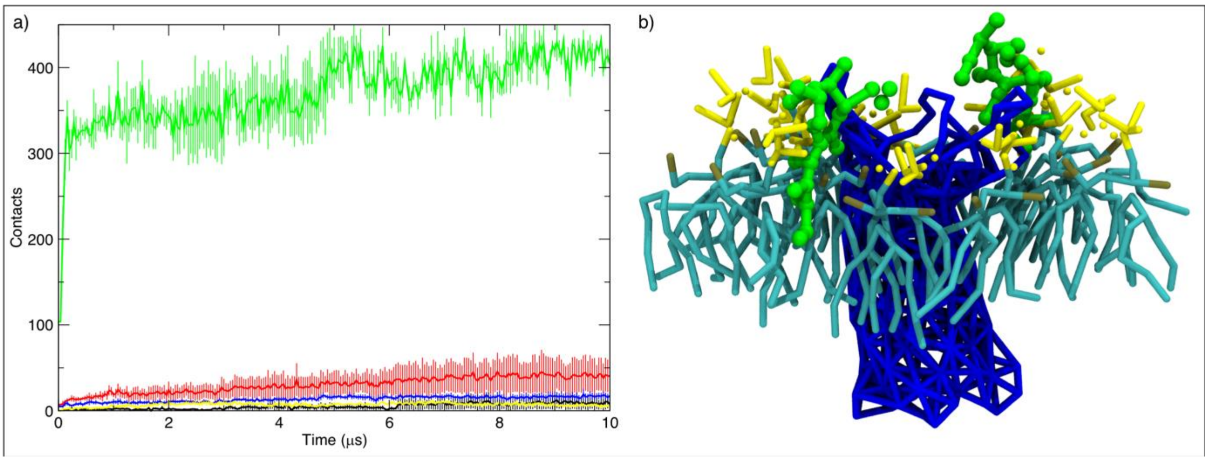

Figure 84. *The interaction of PMB1 with Re LPS.* ***84a)*** *number of contacts between PMB1 and Re LPS segments at coarse-grained resolution. Contact is defined here as an intermolecular distance of ≤0.6 nm. Segments are coloured as follows: acyl tails black, lipid A sugars red, inner core sugars green, 1 phosphate of primary GlcNAc blue and 4' of secondary GlcNAc yellow**.** **84b)** image of PMB1 penetration through inner core sugars of annular LPS lipids. PMB1 in green, OmpA in blue and Re LPS in yellow (core sugars), tan (phosphates) and cyan (acyl tails).*

The presence of OmpA in the Re LPS membrane appeared to aid PMB1 penetration through LPS sugars; PMB1 may indeed exploit localised disorder around membrane-thinning OMPs in order to gain access to bacterial cells. Although the methods used so far have allowed the observation of PMB1 insertion into the membrane core, they have been insufficient with regards to the observation of permeation through membrane. Equilibrium molecular dynamics did not provide the correct conditions for the PMB1-triggered membrane degradation described in the literature. In order to encourage penetration through LPS core sugars, an electric field was applied.

5.3.2 Applying an Electric Field to the Outer Membrane Models in the Presence of Polymyxin B1

The methods discussed in the previous chapter were successful in replicating the united-atom electroporation protocol performed by Piggot *et al.* at coarse-grained resolution (139). As such, a similar protocol was applied here. The resultant co-ordinates of Re LPS membranes, in the presence of PMB1, with and without OmpA, embedded simulated for 10 μs were used.

Initially, an electric fields of -0.2 or -0.25 V/nm was applied, as the voltage generated by a field of -0.2 V/nm was not sufficient to induce electroporation to the Re LPS membrane without OmpA embedded. In the presence of PMB1, however, a pore formed and the membrane subsequently deteriorated at both field strengths. Pore formation did not consistently involve Re LPS lipids interacting with PMB1, but did follow the same mechanism previously reported, with PLs moving into the membrane core preceded by movement of water. Once a pore had formed, PMB1 molecules were able to permeate the membrane **Figures 85a** and **85b**. The application of the -0.25 V/nm electric field typically caused total membrane degradation within 22 ns, which was too rapid to allow for collection of meaningful data regarding PMB1 interactions with Re LPS segments.

The external electric field was applied to the membranes after 10 μs of equilibrium molecular dynamics. As such, a number of interactions between the antimicrobial peptides and LPS molecules were already established. To ensure that these interactions were not biasing the electroporation process, the starting coordinate files were altered such that the minimum distance between LPS and PMB1 molecules was 1 nm. After the appropriate energy minimisation and equilibration simulations, the external electric field was applied once more, and again resulted in total membrane degradation within 62.5 (±4.10) ns. A lower field strength was therefore considered.

The application of an electric field at strengths of -0.1 or -0.15 V/nm did not result in electroporation or membrane degradation within 1 μs, and as such data could be collected on the interactions between PMB1 and Re LPS segments. The number of contacts between PMB1 and Re LPS inner core sugars marginally increased with the application of an electric field of -0.1 V/nm, compared with -0.15 V/nm or no field. However, the application of an electric field did not appear to affect the number of interactions between PMB1 and the lipid A sugars or acyl tails of Re LPS. The number of contacts between PMB1 and Re LPS segments with the application of an electric field of strengths -0.1 or -0.15 V/nm can be seen in **Figures 85c** and **85d** respectively.

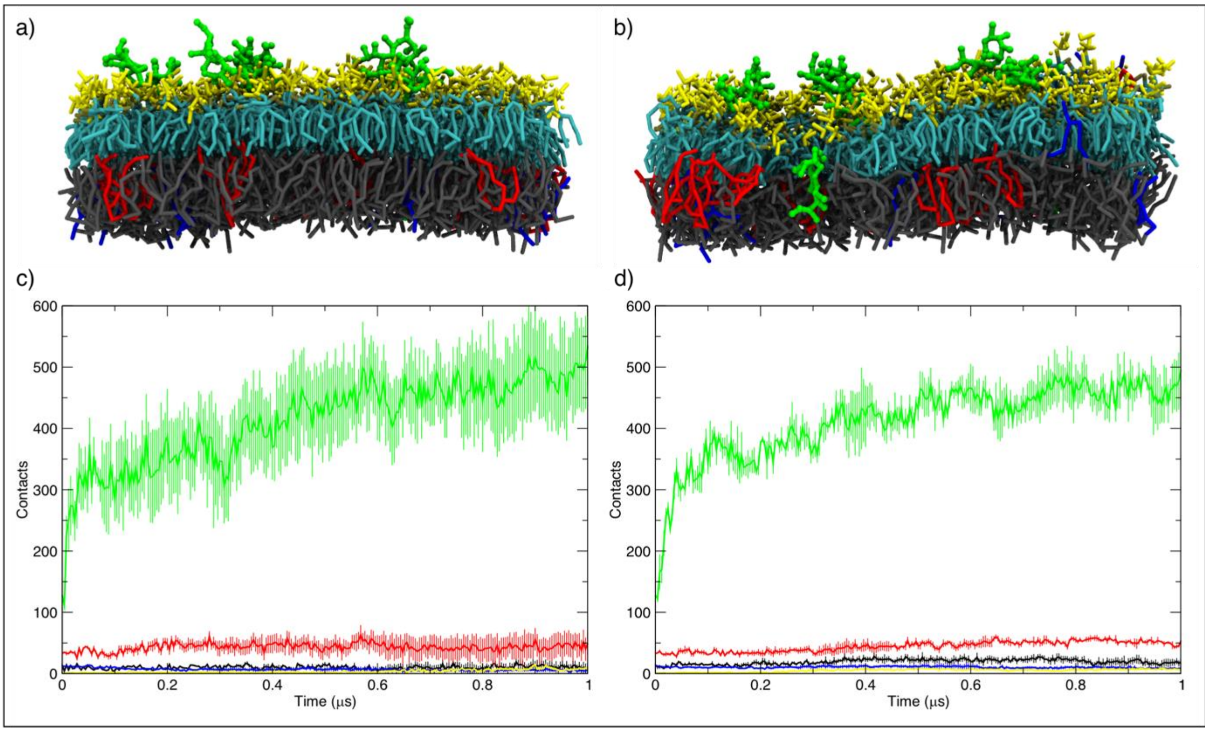

Figure 85. *The interaction of PMB1 and the Re LPS membrane under an external electric field.* ***85a) & 85b)*** *Re LPS membrane electroporating in the presence of PMB1 under and electric field of strength 0.2 V/nm. System coloured as follows: PMB1 in green, POPE in grey, POPG in blue, cardiolipin in red, and Re LPS core sugars, acyl tails and phosphates in yellow, cyan and tan respectively.* ***85c)*** *number of contacts*

between PMB1 and Re LPS segments with a -0.1 V/nm electric field applied. ***85d)*** *contacts between PMB1 and Re LPS segments with a -0.15 V/nm electric field applied.*

The electroporation of LPS-containing membranes often results in the flip-flopping of PLs into the outer leaflet, as shown by Piggot *et al.* and data presented in the previous chapter (139). If PMB1 permeates the OM through transient membrane pores, flip-flopping of PLs may also occur, which may facilitate the permeation of additional PMB1 molecules through the OM. In order to investigate the behaviour of the OM during and after the collapse of these pores, snapshots were obtained of systems with membrane pores with PMB1 in the lumen. The electric field was removed, and the systems were simulated for an additional 10 μs.

The membrane pore consistently collapsed within 5 ns, and all water was ejected from the membrane core. Between seven and ten PL molecules were observed to flip-flop into the outer leaflet, where they remained in a tight cluster and did not disperse amongst the Re LPS molecules. One and two Re LPS molecules were observed to flip-flop into the inner leaflet in two of the three independent simulations. In the simulation where two Re LPS molecules flip-flopped, they did not remain associated and diffused away from each other laterally to the bilayer normal. PMB1 molecules were still not observed to permeate the membrane, despite the starting conformations of the systems having the centre-of-mass of the AMPs passed the midpoint of the membrane core. Interactions between PMB1 and Re LPS proved stronger than those with inner leaflet PLs, and this resulted in the return of PMB1 molecules to the outer leaflet. Although a very slight increase in the number of interactions between PMB1 and the lipid A segments of Re LPS was recorded across the repeated simulation, no penetration of PMB1 lipid tails was observed into the membrane core. A typical starting configuration of these “post-pore” simulations, along with the recorded contacts between PMB1 molecules and Re LPS segments can be seen in **Figures 86a** and **86b**.

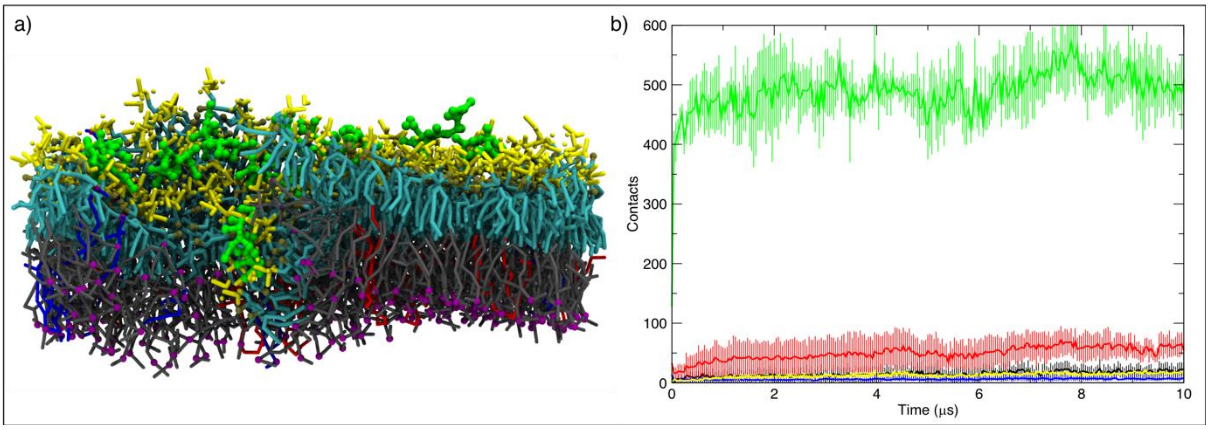

Figure 86. *System starting configuration before external electric field removed and subsequent number of contacts between PMB1 and Re LPS segments.* ***86a)*** *PMB1 in in the lumen of a Re LPS membrane pore. System coloured as follows: PMB1 in green, POPE in grey, POPG in blue, cardiolipin in red, phospholipid phosphates in purple and Re LPS core sugars, acyl tails and phosphates in yellow, cyan and tan respectively.* ***86b)*** *Contacts between PMB1 and Re LPS segments. Contact is defined as an intermolecular distance of ≤0.6 nm. Segments are coloured as in* ***Figure 85****.*

The presence of OmpA embedded within the Re LPS membrane appeared to facilitate the insertion of the PMB1 lipid tail into the membrane core under equilibrium conditions, due to the localised disorder in annular Re LPS acyl tails. This disorder also appeared to enable electroporation with the application of a -0.15 V/nm electric field. Annular PLs flip-flopped to the outer leaflet, enabling three to four PMB1 molecules to permeate the membrane per simulation, before membrane degradation. PMB1 molecules consistently diffused away from OmpA once embedded into the inner leaflet. The number of contacts between PMB1 and Re LPS segments, along with an image of two PMB1 permeating through a pore involving annular lipids, can be seen in **Figures 87a** and **87b**.

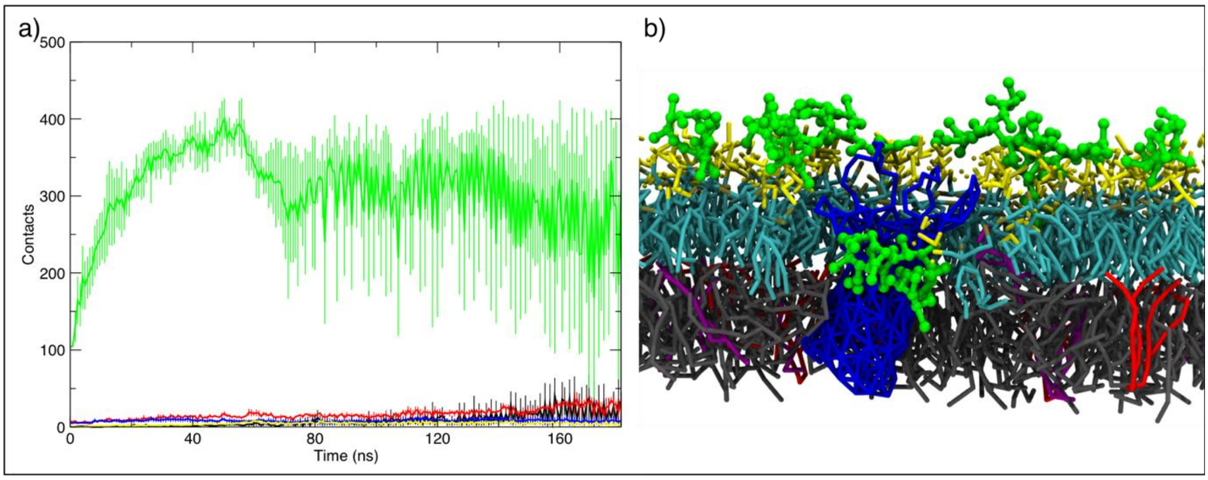

Figure 87a) Number of contacts between PMB1 and Re LPS segments in system with OmpA embedded and external electric field applied. Contact is defined as an intermolecular distance of ≤0.6 nm. Segments are coloured as in ***Figure 84****.* ***87b)*** *Two PMB1 molecules pass through a membrane pore formed by annular lipids. Image coloured as follows: OmpA in blue, PMB1 in green, POPE in grey, POPG in purple, cardiolipin in red and Re LPS core sugars, acyl tails and phosphates in yellow, cyan and tan respectively.*

Interestingly, the presence of both PMB1 and OmpA appear to lower the energy barrier required for Re LPS electroporation. PMB1 was not consistently involved in the electroporation process; the presence of the polycation molecules may have caused a localised increase in voltage across the membrane, assisting in electroporation. The time take for electroporation, including details of whether PMB1 molecules were interacting with lipids involved in pore formation, can be seen in **Table 10**.

Table 10. *Time taken for pore formation in Re LPS membrane systems with an external electric field applied in the presence of polymyxin B1*

System	**Electric Field (V/nm)**	**Time to Poration**	**PMB1 Involved?**
CG_REMP_PMB1	-0.2	23.12 ns	Yes
		26.80 ns	No
		31.34 ns	No
	-0.25	22.80 ns	No
		18.94 ns	Yes
		18.44 ns	Yes
CG_REMP_PMB1_shuffle	-0.2	44.00 ns	No
		33.34 ns	No
		51.42 ns	No
CG_REMP_OmpA_ PMB1	-0.15	68.22 ns	Yes
		141.64 ns	No
		83.64 ns	No

It is possible that the permeation of PMB1 through the OM requires a “tail first” configuration. If so, the application of an external electric field may not have aided the process at all, as neutral atoms would not be accelerated by the field. Electroporation through the application of an external electric field consistently had the result of total membrane degradation rather than recovery of the bilayer structure after permeation events. Computational electrophysiology studies, such as those performed by Trick *et al.*, Kutzner *et al.* and Melcr *et al.*, have presented double membrane systems, used to artificially imbalance ionic charge within a segregated membrane compartment (248–250). It was therefore considered that modified double membrane protocol might be suitable for the observation of PMB1 permeation under equilibrium molecular dynamics conditions.

5.3.3 Attempting Ionic Permeation of Polymyxin B1 Through the Gram Negative Outer Membrane

Permeation of sodium ions through a simplistic DPPC membrane was presented by Yesylevskyy *et al.* when validating the polarisable MARTINI water model (119). This method caused transient electroporation without membrane collapse, making it an intriguing option with regards to the work of this chapter. As previously mentioned, while applying an external electric field to the OM model in the presence of PMB1 did indeed result in membrane permeation, it also caused total membrane degradation. As detailed in the *Methods* section, membrane compartments were created, leading to a charge imbalance between the inner and outer compartments. PMB1 molecules were placed within the inner compartment with membrane leaflets containing LPS lining the compartment; this ensured that if permeation occurred, it would be through LPS molecules. This permeation protocol was tested with the Re, Ra and O-antigen type LPS membrane models, and later the inner membrane model. The Re LPS membrane was used with and without OmpA embedded. Either 40 or 60 PMB1 molecules were placed inside the compartments for Re, Ra and O-antigen LPS membrane. An additional scenario was tested for the double inner membrane system, as well as the Re LPS membrane with OmpA embedded, in which 20 PMB1 molecules were placed inside the central compartment. The placement of a greater number of PMB1 molecules in the central compartment resulted in a greater number of ionic and PMB1 permeations through both membranes. The number of flip-flopped phospholipids, along with the number of ions and PMB1 molecules which permeated the membrane were recorded. Details of all of the double membrane systems, including the effective PMB1 concentration in the central compartment as well as the initial and final charge imbalances, can be seen in **Table 11**.

Table 11. *Number of permeation events, as well as initial and final charge imbalance between central compartment and bulk solution. Red values denote a reverse in membrane polarisation due to permeation of charged molecules.*

System	**[PMB1]**	**Ionic Permeations**	**Phospholipid Flip-Flop**	**Charge Imbalance (Initial/Final)**
REMP_ x40	38.27 mM	N/A	N/A	72 *e* / 72 *e*
		N/A	N/A	72 *e* / 72 *e*
		N/A	N/A	72 *e* / 72 *e*
REMP_ x60	67.12 mM	Ca^{2+} x21, Cl^{-} x18, PMB1 x9	PE x26, PG x10, CDL x8	266 *e* / 10 *e*
		Ca^{2+} x25, Cl^{-} x13, PMB1 x4	PE x20, PG x9, CDL x15	266 *e* / 22 *e*
		Ca^{2+} x22, Cl^{-} x10, PMB1 x9	PE x17, PG x9, CDL x12	266 *e* / 12 *e*
REMP_ OmpA_x20	26.53 mM	Ca^{2+} x7, PMB1 x2	PE x6, PG x5, CDL x3	82 *e* / 12 *e*
		Ca^{2+} x1, PMB1 x2	PE x5, PG x9, CDL x10	82 *e* / 20 *e*
		Ca^{2+} x7	PE x1, PG x7, CDL x3	82 *e* / 28 *e*
REMP_ OmpA_x40	48.75 mM	Ca^{2+} x20, Cl^{-} x34, PMB1 x1	PE x7, PG x11, CDL x8	222 *e* / 10 *e*
		Ca^{2+} x21, Cl^{-} x23, PMB1 x4	PE x18, PG x8, CDL x7	222 *e* / 8 *e*
		Ca^{2+} x20, Cl^{-} x17, PMB1 x3	PE x17, PG x10, CDL x9	222 *e* / 22 *e*
REMP_ OmpA_x60	80.45 mM	Ca^{2+} x34, Cl^{-} x65, PMB1 x6	Re LPS x1, PE x30, PG x5, CDL x7	358 *e* / 6 *e*
		Ca^{2+} x44, Cl^{-} x57, PMB1 x2	PE x22, PG x9, CDL x8	358 *e* / 2 *e*

		Ca^{2+} x35, Cl^- x57, PMB1 x4	PE x23, PG x10, CDL x9	358 *e* / 8 *e*
RAMP_ x40	33.66 mM	Ca^{2+} x20, Cl^- x6, PMB1 x1	PE x25, PG x12, CDL x14	238 *e* / 56 *e*
		Ca^{2+} x20, Cl^- x10, PMB1 x1	PE x20, PG x17, CDL x14	238 *e* / 19 *e*
		Ca^{2+} x28, Cl^- x3	PE x23, PG x15, CDL x11	238 *e* / 23 *e*
RAMP_ x60	50.30 mM	Ca^{2+} x33, Cl^- x32, PMB1 x2	PE x19, PG x19, CDL x16	240 *e* / 22 *e*
		Ca^{2+} x28, Cl^- x27, PMB1 x3	PE x25, PG x18, CDL x14	240 *e* / 12 *e*
		Ca^{2+} x26, Cl^- x48, PMB1 x2	PE x24, PG x18, CDL x17	240 *e* / 16 *e*
OANT_ x40	20.01 mM	Ca^{2+} x36, Cl^- x5, PMB1 x1	PE x38, PG x17, CDL x15	296 *e* / 38 *e*
		Ca^{2+} x40, Cl^- x9, PMB1 x1	PE x32, PG x12, CDL x14	296 *e* / 24 *e*
		Ca^{2+} x39, Cl^- x8, PMB1 x1	PE x30, PG x10, CDL x12	296 *e* / 46 *e*
OANT_ x60	31.89 mM	Ca^{2+} x28, Cl- x43, PMB1 x7	PE x25, PG x15, CDL x16	340 *e* / 10 *e*
		Ca^{2+} x27, Cl^- x48, PMB1 x6	PE x30, PG x14, CDL x9	340 *e* / 12 *e*
		Ca^{2+} x28, Cl^- x41, PMB1 x5	PE x22, PG x17, CDL x11	340 *e* / 18 *e*
hDEMPa*_x40	52.13 mM	Ca^{2+} x16, PMB1 x4	PE x7, PG x6, CDL x4	156 *e* / 24 *e*
		Ca^{2+} x24, PMB1 x2	PE x6, PG x8, CDL x2	156 *e* / 16 *e*
		Ca^{2+} x16, PMB1 x3	PE x7, PG x8, CDL x8	156 *e* / 14 *e*

hDEMPa*_x60	77.53 mM	Ca^{2+} x28, Cl^- x21, PMB1 x5	PE x9, PG x3, CDL x8	226 *e* / 16 *e*
		Ca^{2+} x24, Cl^- x20, PMB1 x7	PE x11, PG x7, CDL x3	226 *e* / 6 *e*
		Ca^{2+} x26, Cl^- x10, PMB1 x5	PE x8, PG x5, CDL x8	226 *e* / 10 *e*
Inner_x20	44.69 mM	Na^+ x39, PMB1 x1	PE x14, PG x10, CDL x2	130 *e* / 14 *e*
		Na^+ x44	PE x17, PG x10, CDL x2	130 *e* / 14 *e*
		Na^+ x38, PMB1 x1	PE x19, PG x9, CDL x4	130 *e* / 10 *e*
Inner_x40	100.33 mM	Na^+ x20, PMB1 x9	PE x45, PG x23, CDL x4	200 *e* / 8 *e*
		Na^+ x20, PMB1 x11	PE x36, PG x8, CDL x7	200 *e* / 10 *e*
		Na^+ x18, PMB1 x11	PE x52, PG x12, CDL x5	200 *e* / 10 *e*

No permeation of ions or PMB1 molecules was observed in any simulations of the REMP_x40 condition. However, the lipid tails of between eight and twelve PMB1 molecules were inserted into the membrane core after 5 μs in three independent simulations. Transient membrane defects were observed, with water moving past PL headgroups into the membrane core, although no transmembrane water channel was established through either membrane.

Permeation of a total of 22 PMB1 molecules (**Figure 88a**), along with 109 ions (**Figure 88b**), was observed in REMP_x60 simulations. The permeation of ions was observed both into and out of the central compartment. Ionic permeation always occurred down the concentration gradient and towards the compartment with the opposing charge, i.e. Ca^{2+} ions moved out of the central compartment and Cl^- ions moved in. The central membrane compartment had an initial net positive charge in all systems, which resulted in cations leaving the central compartment and anions entering. Each of the PMB1 and ionic permeation events were accompanied by PL flip-flopping. No PL species was favoured in the permeation process. Permeations followed a similar mechanism to the electroporation of the LPS membranes discussed previously; water caused a membrane defect, which enabled PL headgroups to move into the membrane core, facilitating the formation of a single file transmembrane water channel. Ions and PMB1 molecules were able to diffuse through these transmembrane pores, which quickly healed after permeation. Once the transient membrane pores had dissipated, PLs were often observed to flip-flop into the Re LPS leaflet, where they remained (**Figure 88c**). This flip-flopping of PLs is particularly interesting, as it may result in disruption to the cross-linking of neighbouring Re LPS phosphates moieties by divalent cations *in vivo*. Further to this, the steric hindrance caused by these phospholipids may break up the intricate network of hydrogen bonds and other electrostatic interactions between LPS sugar groups. In these simulations, permeation events typically took up to 5 ns to occur, with the majority taking 1 – 2 ns. In some cases, a PMB1 molecule would linger in the membrane core, due to its electrostatic interactions with headgroups from both leaflets of the bilayer. The result of a representative system of the REMP_x60 condition after 5 μs can be seen in **Figure 88d**.

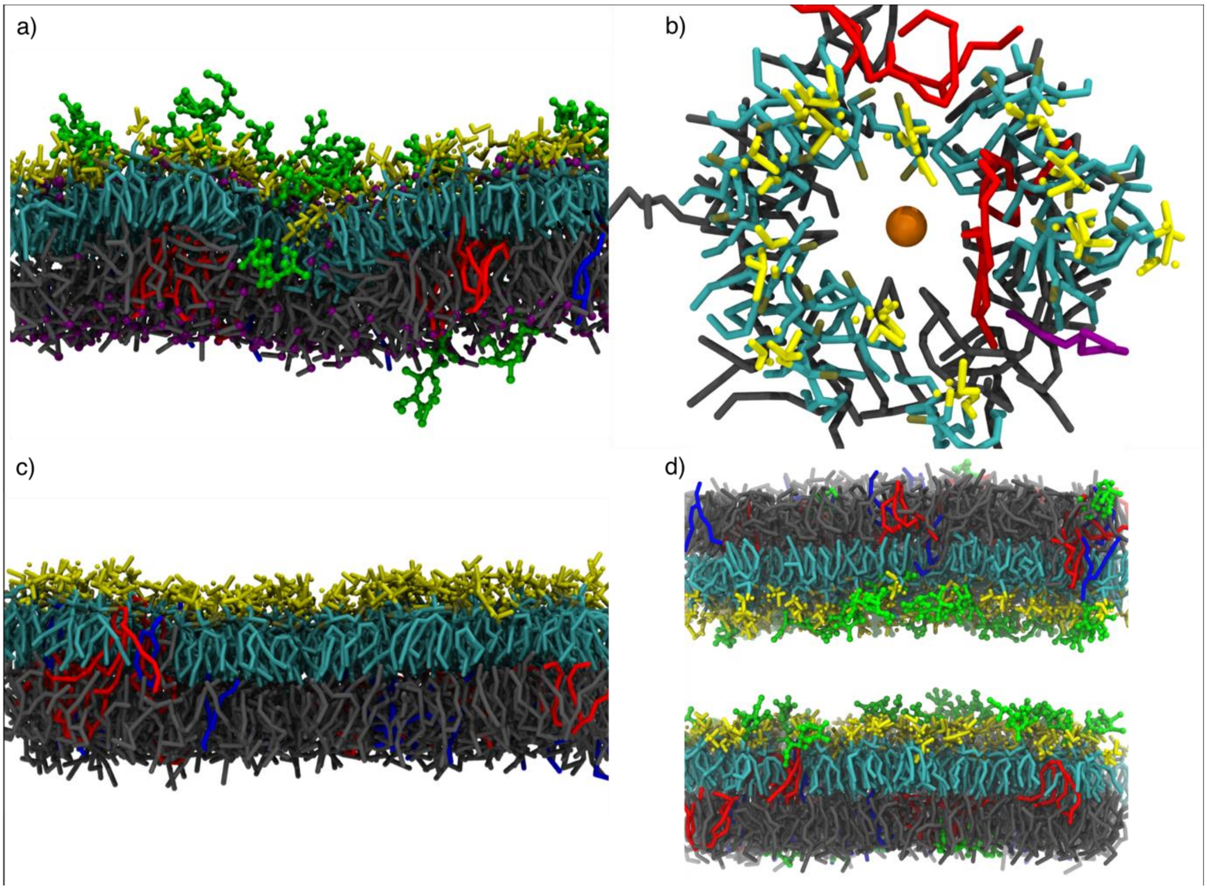

Figure 88. *Ionic permeation of PMB1 through the Re LPS membrane model compartment. System colours as follows: POPE grey, POPG blue, cardiolipin red, PMB1 green, all phosphates purple, chloride ion orange, and Re LPS sugars and acyl tails yellow and cyan.* ***88a)*** *PMB1 in a transmembrane conformation, interacting with lipids of both bilayer leaflets.* ***88b)*** *a chloride ion passing through a transient membrane pore into the central compartment.* ***88c)*** *view of outer leaflet after pore degradation with flip-flopped phospholipids visible.* ***88d)*** *Representative system configuration after 5 μs.*

Previous simulations showed that disorder in the acyl tails of annular PLs and Re LPS molecules facilitated electroporation. An additional condition with 20 PMB1 molecules was tested in an effort to understand whether this localised membrane disorder could be exploited by PMB1. A total of four PMB1 molecules and 15 Ca^{2+} ions permeated out of the central membrane compartment in the REMP_OmpA_x20 simulations. There was no permeation of molecules into the central compartment. Interestingly, all ionic and PMB1 permeation events occurred through transient membrane pores involving annular PLs. OmpA has been reported to have a membrane thinning effect on LPS-containing membranes *in silico* (186); the decrease in distance between opposing leaflet phosphates of annular lipids may have provided an energetically favourable route for pore formation, as opposed to bulk lipid. After displacing annular Re LPS molecules, flip-flopped PLs remained associated with OmpA up to the end of the 5 μs simulations.

A total of eight PMB1 permeations were recorded in the REMP_OmpA_x40 simulations, along with 145 ionic permeations. In these simulations, Ca^{2+} and Cl^{-} ions were observed to permeate out and into the central compartment respectively. Ionic permeation always occurred down the concentration gradient, as in the Re LPS double membrane system without OmpA embedded. Ionic and PMB1 permeations were not always observed to involve annular PLs in these systems, as up to 40% occurred in the bulk lipid region. PLs were still observed to flip-flop into the Re LPS leaflet, where they remained until the end of the simulations. Once inserted into the Re LPS leaflet, PL lateral diffusion became correlated with that of the Re LPS molecules.

In the REMP_OmpA_x60 systems, a total of twelve PMB1 molecules were observed to permeate into the “periplasmic” compartment, through pores involving both annular and bulk lipids. A total of 113 Ca^{2+} ions and 179 Cl^{-} ions permeated into and out of the central compartment respectively. A total of 124 lipid flip-flopping events were recorded over the repeated simulations, including one annular ReLPS molecule (**Figure 89a**). Flip-flopping of LPS molecules had not been observed in any previous simulations, including those with an electric field applied. At the end of one of the three simulations, the net charge of the membrane compartments was reversed due to the permeation of charged particles. While PMB1 molecules did permeate through annular lipids (**Figure 89b**), they were also able to cross the membrane in regions of bulk lipid. Once inserted into the phospholipid leaflet, PMB1 molecules diffused laterally through PL headgroups (**Figure 89c**). The result of a representative system of the REMP_OmpA_x60 condition after 5 μs can be seen in **Figure 89d**.

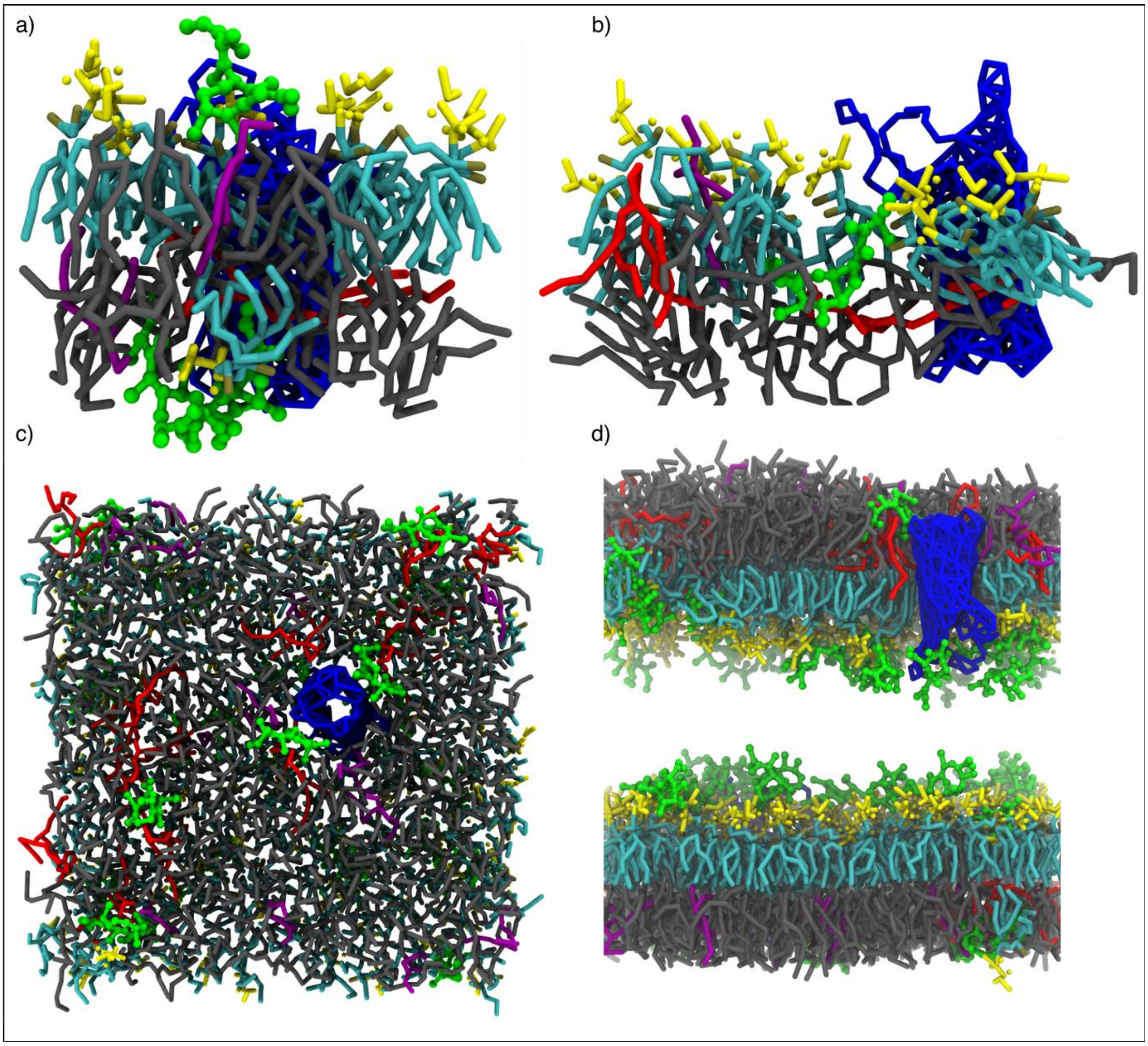

Figure 89. *Ionic permeation of PMB1 through the Re LPS membrane with OmpA embedded model compartment. System colours as follows: OmpA blue, POPE grey, POPG purple, cardiolipin red, PMB1 green, and Re LPS sugars and acyl tails yellow and cyan* ***89a)*** *Permeation of PMB1 causes Re LPS molecule to flip-flop to opposite leaflet.* ***89b)*** *PMB1 moving through pore consisting of annular lipids.* ***89c)*** *five PMB1 molecules interacting with inner leaflet of one membrane.* ***89d)*** *Representative system configuration after 5 μs.*

The permeation of both PMB1 molecules and ions, along with PL flip-flopping, was observed through the Ra LPS double membrane system. A total of just two PMB1 molecules permeated in the RAMP_x40 condition, along with 68 Ca^{2+} ions and 19 Cl^- ions. Similarly to the Re LPS double membrane systems, flip-flopped PLs remained in the Ra LPS leaflet for the remainder of the simulation, with their lateral diffusion correlated with that of their neighbouring Ra LPS molecules. The increase in PMB1 concentration in the RAMP_x60 condition resulted in a total of seven PMB1 molecules permeating through the membranes. There was also an increase to 87 Ca^{2+} ions and 107 Cl^{-} ions entering and exiting the central compartment respectively. Again, permeation of PMB1 molecules and ions occurred with the respective concentration gradient. PMB1 permeations did not occur as rapidly through the Ra LPS membrane compared with the Re LPS membrane. PMB1 molecules were often obstructed by LPS core sugars, and as such only one molecule permeated at a time. This can be seen in **Figure 90a**. Similarly to the Re LPS membrane condition, the PMB1 molecules which did not permeate the membrane were able to penetrate further through core sugars than in single membrane systems. A PMB1 molecule penetrating through Ra LPS core sugars can be seen in **Figure 90b**. Transient electrostatic interactions between polar and charged PMB1 beads and cardiolipin headgroups were observed. These associations lasted between 2 – 10 ns, and no further PL clustering was observed. PMB1 molecules interacting with cardiolipin in the PL leaflet can be seen in **Figure 90c**. Ra LPS molecules were not observed to flip-flop into the PL leaflet in any of the three independent simulations. The result of a representative system if the RAMP_x60 condition after 5 μs can be seen in **Figure 90d**.

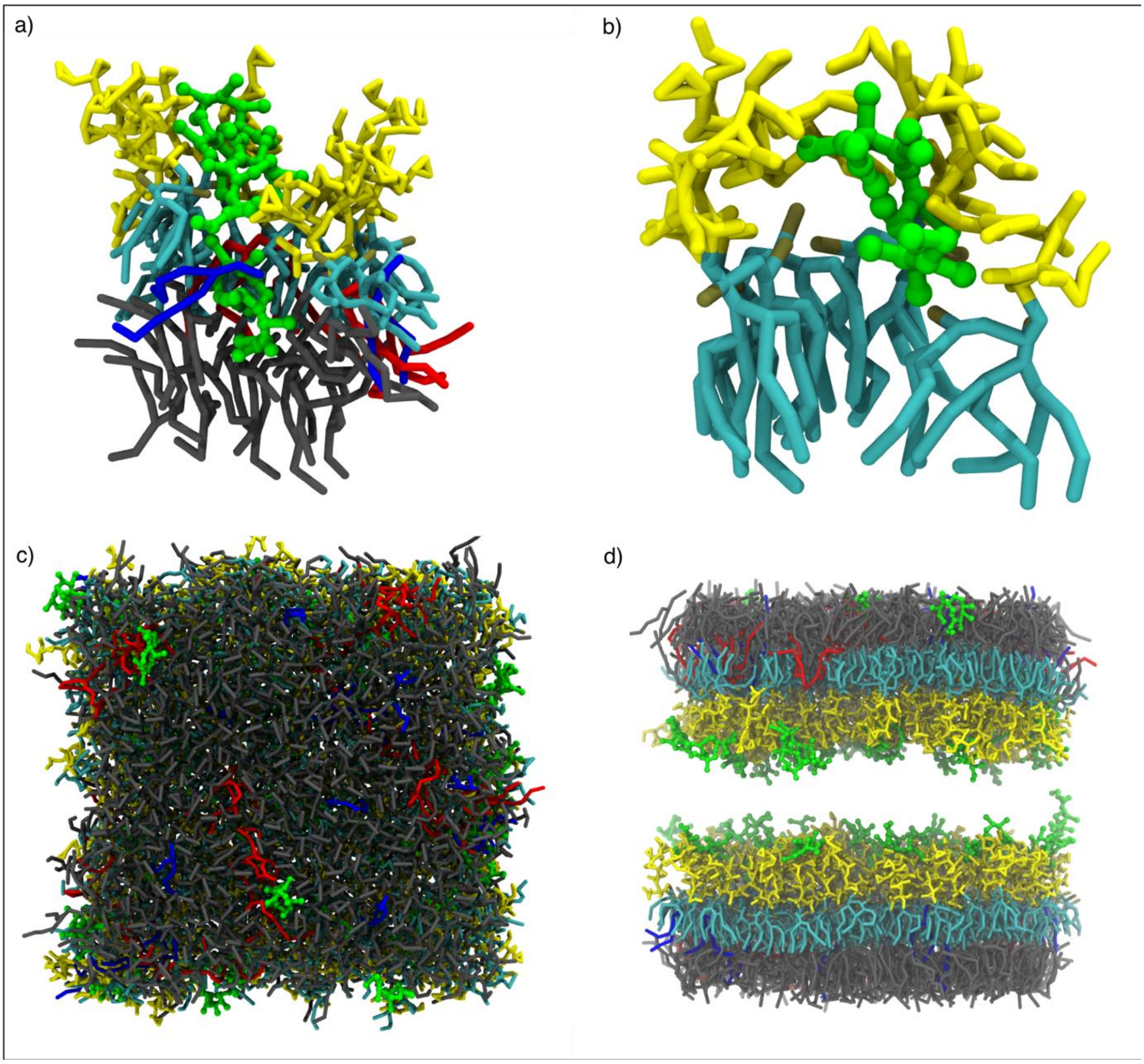

Figure 90. *Ionic permeation of PMB1 through the Ra LPS membrane model compartment. System colours as follows: PMB1 green, POPE grey, POPG blue, cardiolipin red, and Ra LPS sugars, acyl tails and lipid A phosphates yellow, cyan and tan respectively.* ***90a)*** *one PMB1 molecule permeates the membrane, with two PMB1 molecules hindered by Ra LPS core sugars.* ***90b)*** *increased concentration of PMB1 within membrane compartment encourages penetration through Ra LPS core sugars.* ***90c)*** *three PMB1 molecules interacting with the inner leaflet of one membrane.* ***90d)*** *Representative system configuration after 5 μs.*

PMB1 molecules were observed to permeate through the O-antigen membranes at both concentrations. A total of three PMB1 permeations were observed in the OANT_x40 condition, along with 22 Cl^- ions and 115 Ca^{2+} ions into and out of the central membrane compartment respectively. Permeations were again accompanied by PL flip-flopping into the LPS leaflet. While a number of PMB1 molecules were hindered by the O-antigen region of LPS and prevented from reaching the membrane, others exploited gaps in the O-antigen and caused structural rearrangements in the LPS core sugars; these PMB1 molecules were able to interact with flip-flopped PLs and occupy the space previously held by LPS core sugars (**Figure 91a**). In the OANT_x40 condition, one PMB1 permeation was observed in each of the three independent simulations. This permeation consistently occurred in the region of the membrane exposed due to O-antigen tilting, as can be seen in **Figure 91b**. O-antigen tilting also enabled the formation of a significantly larger pore, temporarily resulting in a large amount of water solvating the membrane core before membrane repair (**Figure 91c**).

The OANT_x60 condition resulted in a total of 18 PMB1 permeations, along with 132 Cl^- ions and 83 Ca^{2+} ions into and out of the central membrane compartment respectively. PMB1 molecules were observed to permeate through both the membrane area exposed by O-antigen tilting as well as unexposed areas. Flip-flopped PLs remained in the LPS leaflet and their lateral diffusion once again became completely correlated with that of LPS molecules. The result of a representative system of the OANT_x60 condition after 5 μs can be seen in **Figure 91d**.

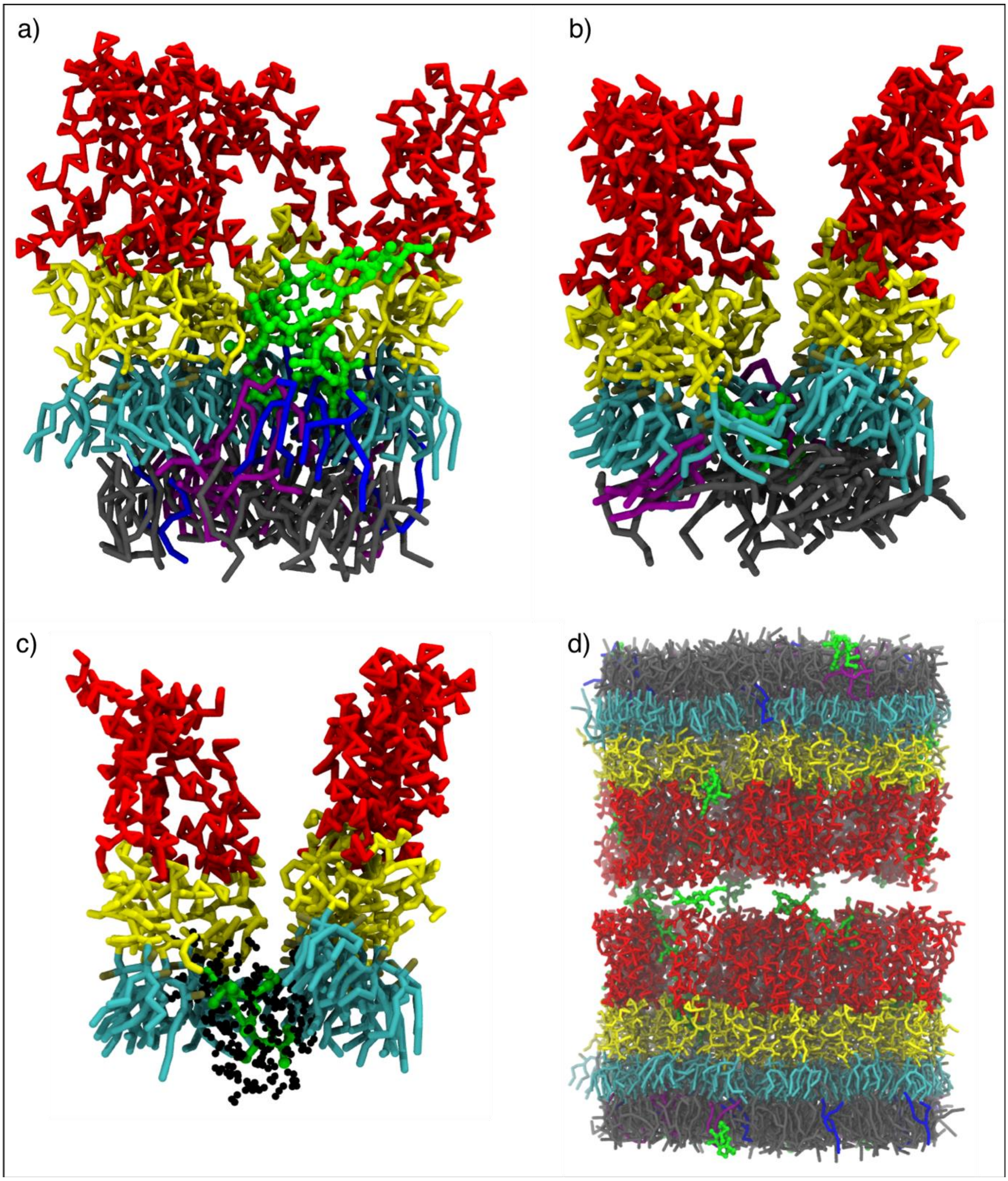

Figure 91. *Ionic permeation of PMB1 through the O-antigen LPS membrane model compartment. System colours as follows: PMB1 green, POPE grey, POPG blue, cardiolipin purple, PW black, and LPS O-antigen, core sugars, acyl tails and phosphates red, yellow, cyan and tan respectively.* ***91a)*** *PMB1 molecules occupy exposed areas due to O-antigen tenting.* ***91b)*** *PMB1 molecule permeating the membrane.* ***91c)*** *PW hydrates PMB1 molecule permeating the membrane.* ***91d)*** *Representative system configuration after 1 μs.*

The hDEMPa* membrane model from the previous chapter was used here to investigate how the presence of modified Re LPS might affect the permeation of PMB1 through the OM. While permeation of PMB1 molecules or ions was not observed in any simulations of the REMP_x40 condition, a total of nine PMB1 molecules and 56 Ca^{2+} ions were observed to cross the membranes to leave the central compartment across all simulations in the hDEMPa*_x40 condition. PMB1 molecules were observed to aggregate on the surface of the LPS leaflet in groups of two to five molecules before permeation. Interactions were observed between apolar beads lipid tail beads of neighbouring PMB1 molecules. The electrostatic interactions between PMB1 molecules and core and lipid A sugars of wildtype Re LPS molecules during permeation can be seen in **Figure 92a**.

In contrast to previous membrane conditions, PLs returned to the PL leaflet more frequently than flip-flopping into the LPS leaflet after the degradation of transient membrane pores. Only 62 PL flip-flopping events were observed in the hDEMPa*_x60 simulations, compared with the 126, 170 and 159 PL flip-flopping events in the REMP_x60, RAMP_x60 and OANT_x60 conditions respectively. The reason for this reduced rate of flip-flopping is unclear, although the positive curvature inflicted on the hDEMPa* membrane by the distinct patches of deacylated Re LPS was the major structural difference between these membrane conditions. It may be that the positive curvature modified LPS sugar-sugar packing such that PL flip-flopping became less energetically favourable. PMB1 molecules were frequently observed to localise in areas of the PLs leaflet corresponding to patches of deacylated Re LPS in the opposing leaflet; PMB1 aggregation in this region also resulted in both electrostatic and van der Waals interactions with co-localised cardiolipin molecules. DAB residues were observed to interact with cardiolipin headgroups, and PMB1 lipid tail beads were observed to interact with cardiolipin acyl tails. PMB1 molecules were also observed to occupy corresponding regions in opposing leaflets after degradation of transient membrane pores, as seen in **Figure 92b**.

A total of 17 PMB1 molecules permeated through the double membrane system the in hDEMPa*_x60 simulations. There was also an increase in the number of ions permeating the membranes, with a total of 78 Ca^{2+} ions leaving the central membrane compartment and 51 Cl^- ions entering. The net movement of ions resulted in reversed membrane polarity in two of the three repeated simulations, as was observed in the REMP_OmpA_x60 condition. A reduced number of PL flip-flopping events were observed again in the hDEMPa*_x60 simulation, compared to wildtype membranes with the same number of PMB1 molecules inserted. Co-localisation of PMB1 molecules with cardiolipin was observed again, and 80% of the permeated AMPs were in regions of the PL leaflet corresponding to deacylated Re LPS in the opposing leaflet at the end of the 5 μs simulations. Co-localisation of PMB1 and cardiolipin can be seen in **Figure 92c**. It was unclear whether this localisation was due to membrane curvature, the higher concentration of cardiolipin in these regions, or the presence of deacylated Re LPS in the opposing leaflet. As PMB1 molecules were not observed to aggregate with cardiolipin in the single membrane systems, the increased membrane curvature in the hDEMPa* condition may be the most likely explanation for co-localisation here. The result of a representative system of the hDEMPa*_x60 condition after 5 μs can be seen in **Figure 92d**.

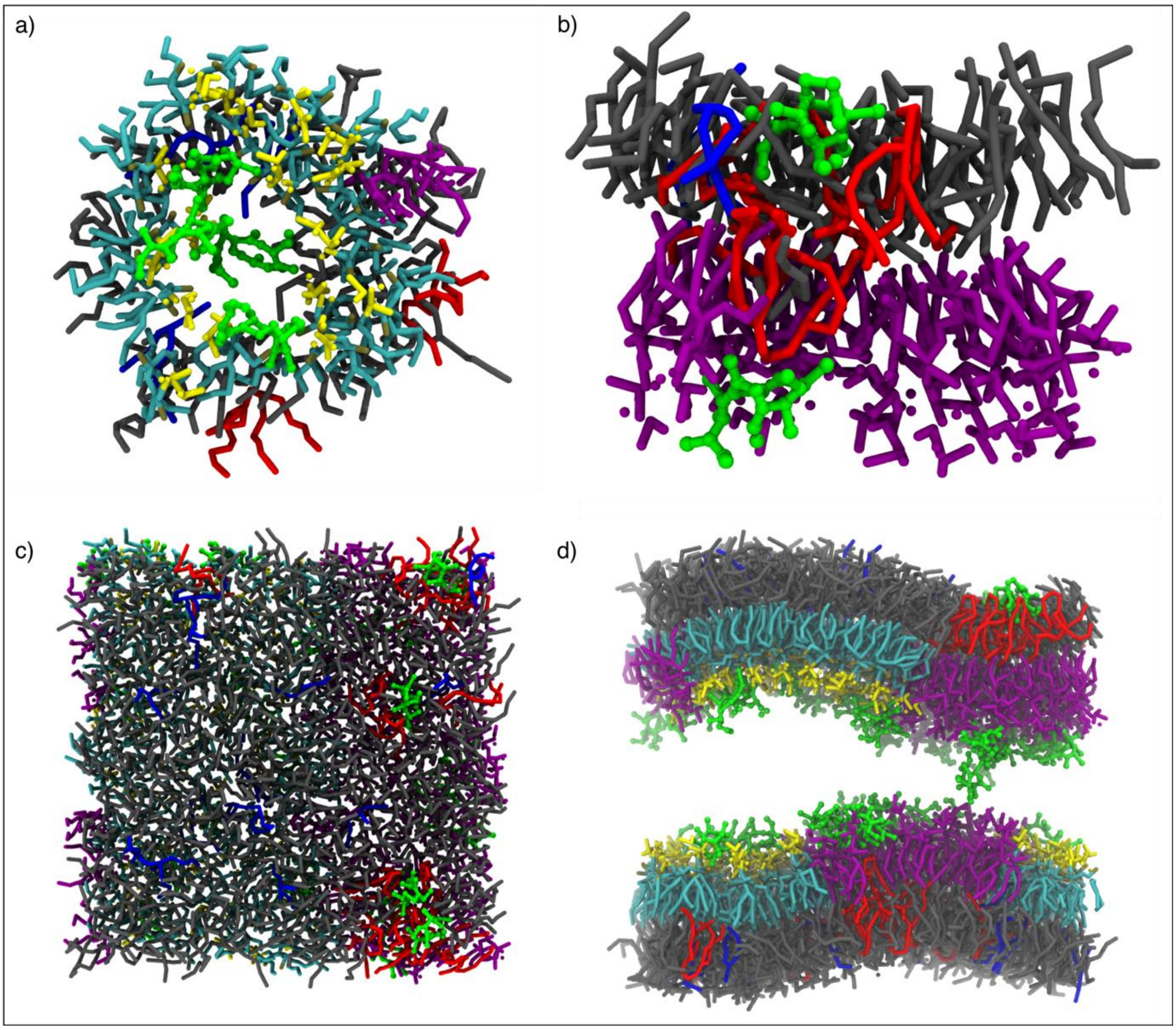

__Figure 92.__ Ionic permeation of PMB1 through the hDEMPa membrane model compartment. System colours are as follows: PMB1 green, deacylated Re LPS purple, POPE grey, POPG blue, cardiolipin red, and wildtype Re LPS sugars, acyl tails and phosphates yellow, cyan and tan respectively.* ***92a)*** *one PMB1 molecule permeating through the wildtype LPS section of membrane, with three additional molecules interacting with LPS lipids lining the pore.* ***92b)*** *two PMB1 molecules interacting with lipids of opposing leaflets after degradation of membrane pore.* ***92c)*** *view of inner leaflet of one membrane with four PMB1 molecules located in the area corresponding to deacylated Re LPS lipids in the opposing leaflet.* ***92d)*** *Representative system configuration after 5 μs.*

Finally, permeation of PMB1 through the inner membrane model was investigated, as part of the bactericidal activity of PMB1 is thought to come from disruption of the inner membrane (89,90). The inner membrane model electroporated in a shorter time than LPS-containing membranes under a field strength of 0.3 V/nm. For this reason, a system with only 20 PMB1 molecules was also trialled.

A total of only two PMB1 permeations were observed in the Inner_x20 condition, along with 121 Na^+ ions out of the central membrane compartment. Unlike in the LPS-containing membranes, poration was initiated from either leaflet, or both simultaneously. An established pore in one membrane can be seen in **Figure 93a**. PL flip-flopping was observed at a similar rate to that of the REMP_OmpA_x20 condition, although the inner membrane model had PL flip-flopping in both directions.

There was an increase to 31 total PMB1 permeations in the Inner_x40 condition, and an increase to 58 Na^+ ionic permeations out of the central membrane compartment. There was also an increase in the rate of PL flip-flopping in each repeated simulation; the rate of PL flip-flopping was greater in this condition than any LPS-containing membrane condition, even with a greater number of PMB1 molecules present. This increased rate of flip-flopping could be representative of large-scale membrane disturbance, and could lead to disruption of membrane-bound processes within Gram-negative bacteria.

PMB1 molecules typically remained associated to the membrane after permeation, although one molecule was observed to temporarily diffuse away from the membrane (**Figure 93b**). This molecule returned and inserted into the membrane after ~20 ns. Consistent electrostatic interactions were observed between PMB1 molecules and PG and cardiolipin PLs. Interactions were more pronounced in inner membrane model conditions compared with OM conditions, although this may have been simply due to the increased number of the negatively charged lipids. The association of permeated PMB1 molecules with the “inner” leaflet of the inner membrane model can be seen in **Figure 93c**, and a representative system configuration after 5 μs can be seen in **Figure 93d**.

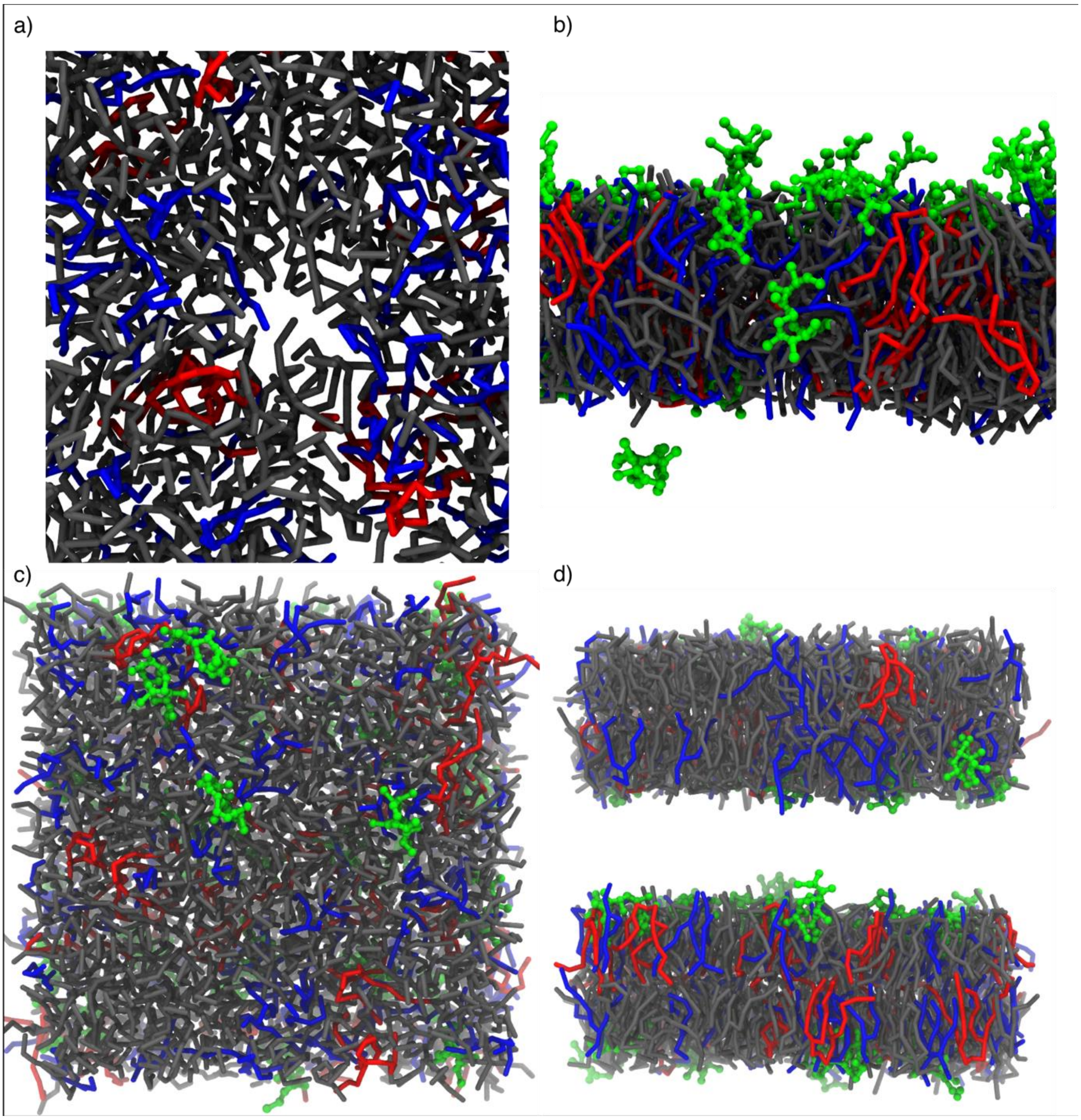

Figure 93. Ionic permeation of PMB1 through the inner membrane model compartment. System colours as follows: PMB1 green, POPE grey, POPG blue, cardiolipin red. ***93a)*** *open membrane pore.* ***93b)*** *PMB1 permeating membrane.* ***93c)*** *PMB1 molecules embedded in inner leaflet after pore degradation, showing transient association with PG and cardiolipin.* ***93d)*** *representative system configuration after 5 μs.*

A greater number of PMB1 in the central compartment resulted in a greater number of both PMB1 and ionic permeations across all membrane conditions. While it remains unclear whether this increase in PMB1 permeation was due to the increase in PMB1 concentration or due to the increased charge imbalance between membrane compartments, the behaviour of these systems give valuable clues as to the mechanism by which PMB1 infiltrates cells and implements its bactericidal activity.

Permeation of both ions and PMB1 molecules caused PL flip-flopping in all membrane conditions. In some cases, this also resulted in distinct patches of PL amongst LPS molecules. This evidence feeds directly into the self-promoted uptake mechanism, which suggests that initial PMB1 contact with the OM facilitates the uptake of further PMB1 molecules (91); these distinct patches of surface-exposed PLs may provide an easier route through the OM than through the bulk LPS.

The asymmetry of the OM is maintained by a number of processes. The maintenance of lipid asymmetry (Mla) system regulates the retrograde flip-flopping of surface-exposed PLs back into the inner leaflet (251). Other proteins, such as OmpLA and PagP, metabolise PLs in the outer leaflet; OmpLA hydrolyses PLs in a Ca^{2+}-dependent mechanism, whereas PagP transfers an acyl tail from the PL to the 2-N acyl tail of the lipid A segment of LPS (85,252). The activity of OmpLA (PldA) has been reported to be upregulated in perturbed membranes, and it may also be involved in the degradation of PLs flip-flopped by PMB1 permeation (253); further to this, Nhu *et al.* identified a mutantation in the *pldA* gene which caused the upregulation of OmpLA activity in colistin-resistant *A. baumannii* (254). OmpLA is known to be activated by dimerisation, which could certainly be facilitated by the introduction of PLs into the outer leaflet of the OM (71,130). The transcription of PagP is controlled by the PhoP/PhoQ signal transduction pathway, which is also known to be activated in cases of PMB1 resistance (126,252,255,256). The implication of these PL-metabolising OMPs in polymyxin-resistant bacteria certainly lends credit to the model of PMB1 OM disruption causing PL flip-flopping during permeation.

A recent molecular dynamics study suggested that the O-antigens of LPS may tilt away from PLs in the outer leaflet (186). PL flip-flopping caused by PMB1 permeation may lead to areas of the OM being exposed through intensified O-antigen tilting, which may in turn facilitate PMB1 permeations. In the previous chapter, it was presented that an increase in the number of LPS sugars, from Re to Ra to O-antigen type LPS resulted in an increase in lipid A solvent accessible surface area; the strengthened sugar-sugar interactions between core and O-antigen sugars of neighbouring LPS molecules led to regions of the membrane with the lipid A segment of LPS molecules partially exposed, and it is possible that PMB1 exploits these gaps to increase proximity to the membrane core. The additions of Ara4N and PEtN, associated with polymyxin resistance, may also act to reduce the exposure of lipid A due to O-antigen tilting (78,128). While the addition of these moieties will modulate the charge of LPS in the OM, the increased steric hindrance may also play a role in preventing PMB1 access to the membrane core.

The reduction of PL flip-flopping in the case of PMB1 permeations through the hDEMPa* double membrane systems is certainly interesting in the context of LPS modifications reducing PMB1 efficacy. A reduced rate of PL flip-flopping would likely hinder the self-promoted uptake mechanism proposed for PMB1 activity. The downregulation of lipid A 1-diphosphate synthase LpxT is also implicated in polymyxin resistance (76,77); as snorkelling-like behaviour of PMB1 DAB residues towards both Re and Ra LPS phosphates was observed, a reduction in the number of LPS phosphates and net OM anionic charge likely reduces the ability of polymyxins to adsorb onto the cell envelope.

Ionic permeation was also frequently observed alongside PMB1 permeation in all of the investigated membrane conditions. This could lead to the depolarisation of the inner membrane *in vivo*, or otherwise disrupt ion uptake and other cellular processes which may rely on membrane polarisation and ionic gradients. As a proton gradient, and thus membrane polarisation, is required for ATP synthesis in bacteria such as *E. coli*, the presence of PMB1 likely disrupts this and a number of other membrane-bound processes (257).

Attenuated polymyxin chemotypes with the lipid tail removed have been presented to cause membrane permeablisation without bactericidal activity (91,240,258). However, larger concentrations of the attenuated polymyxins were required to have the same permeabilising effect, underlining the importance of the lipid tail. With regards to data presented here, it is possible that the apparent ordering effect of PMB1 on LPS acyl tails is a result of electrostatic interactions with LPS core and lipid A sugars, possibly resulting in localised phase change. Berglund *et al.* suggested that this phase change could be another mechanism by which PMB1 increases permeability of the OM and leads to the formation of membrane pores (191).

5.4 Conclusion

Presented in this chapter is an expanded mechanism of the self-promoted uptake of PMB1 through the *E. coli* OM. Although PMB1 access to the OM core is hindered by LPS O-antigen and core sugars, the AMPs likely exploit gaps caused by O-antigen tilting to increase membrane proximity. Once directly interacting with the lipid A segment of LPS, PMB1 causes an increase in acyl tail order, possibly indicating a liquid-to-gel phase transition. This phase transition, as well as a local concentration and charge gradient, enables PMB1 to permeate the membrane. PMB1 was observed to move through transient membrane pores. These membrane pores form by the same mechanism as the electroporation presented in the previous chapter of this thesis. Water entered into the membrane core, leading to the headgroups of inner leaflet phospholipids moving towards the membrane core. Minimal rearrangements of LPS lipid A headgroups are seen, but phospholipid headgroups line a transient pore as PMB1 diffuses through. After permeation, phospholipids often remain flip-flopped into the outer leaflet, and other phospholipids involved in poration return to the inner leaflet as the pore dissipates. While the peptidoglycan cell wall was not included in these simulations, data presented here suggests that PMB1 will disrupt the inner membrane through permeation and potential depolarisation.

The biggest challenge in the experiments presented in this chapter was encouraging PMB1 penetration through LPS core sugars. The slow dynamics of LPS made united-atom resolution simulations impractical for observing PMB1 permeation, and as such coarse-grained simulations with non-equilibrium conditions had to be implemented. The membrane conditions investigated here give valuable clues as to how PMB1 permeates the Gram-negative cell envelope, and evidence here paves the way for future investigations with even more complex membrane compositions and potential novel antimicrobials.

Chapter 6: Conclusions and Future Work

The data presented in this thesis underline the importance of a thorough understanding of the Gram-negative bacterial cell envelope. Membrane proteins such as LpxR may have a membrane thinning effect, causing localised disorder, and can modify membrane constituents. The molecular dynamics simulations used here assisted in the prediction of the putative closed conformation of LpxR, as well as identifying a second cation binding site for the protein.

Modifications to LPS are known to impact immune responses to bacteria, as well as increasing resistance to antimicrobial attack (16,125,128,259). Further to this, modifications to membrane constituents affect the structural integrity of the membrane and can induce localised membrane curvature as well as lipid clustering. This clustering may in turn have implications for organism behaviour (183,246,247,260). Simulations showed the clustering of cardiolipin lipids in the inner leaflet of the outer membrane in areas associated with deacylated Re LPS in the outer leaflet. It remains unclear whether the phospholipid clustering was due to membrane curvature or the presence of deacylated LPS. Application of an external electric field suggested that weaknesses within the membrane, caused either by lipid modification or presence of a protein, can be exploited in pore formation.

Also presented in this thesis is an updated self-promoted uptake mechanism for polymyxins such as the B1 chemotype. PMB1 induces transient membrane poration in order to permeate the membrane. Inner leaflet PLs must rearrange into the membrane core, preceded by water movement, and line a pore which PMB1 moves through. After permeation, PLs are observed to flip-flop into the outer leaflet, facilitating the permeation of further PMB1 molecules due to the weakened interactions between neighbouring LPS molecules. Simulations of membranes with modified LPS or embedded protein again highlight that these features can weaken the membrane; these weaknesses may be exploited by antimicrobials in order to gain access to cells.

The vast number of LPS modifications discussed in this thesis provide a large bank of potential simulations when it comes to further understanding how they confer resistance to antimicrobial peptides. While some modified LPS species have been validated, all of the potential LPS chemotypes must be tested (134,261). In particular, the interactions between the polymyxins and L-Ara4N-modified, or PEtN-modified LPS would be of interest due to the association with resistance (51,128).

The protocol involving PMB1 molecules inserted into the central compartment of a double membrane system is certainly promising in terms of observing the permeation of antimicrobial peptides. While the permeation of PMB1 through Re, Ra and O-antigen type LPS asymmetric membranes was observed here, the Ra and O-antigen type LPS simulations must be repeated with membrane proteins embedded. The introduction of embedded OmpA into the Re LPS facilitated PMB1 permeation through the membrane at a lower concentration compared with the Re LPS membrane with no protein embedded. It may be that the localised disorder of annular LPS lipids and phospholipids present an energetically favourable route through the membrane than through the bulk lipid. Additionally, other chemotypes of polymyxin could be applied to the central compartment, to understand whether the differences them result in different mechanisms of permeation through the outer membrane. Periplasmic crowding by soluble proteins and other molecules such as autoinducers must also be considered, as these could possibly perturb the diffusion of polymyxins through the cellular envelope. Further to this, polymyxin molecules could be added to a membrane compartment with the LPS molecules modified with either L-Ara4N or PEtN moieties, to understand their part in bestowing resistance.

The entire cell envelope could be duplicated to fit into this protocol, which would enable the observation of polymyxin permeation through the outer membrane, peptidoglycan mesh and finally to and through the inner membrane. This would provide additional evidence to the self-promoted uptake mechanism widely discussed in the literature. To further understand the specific interactions at play during these permeation events, this protocol could also be replicated at the all-atom resolution.

Bibliography

1. Yelin I, Kishony R. Antibiotic Resistance. Cell. 2018.
2. Blair JMA, Webber MA, Baylay AJ, Ogbolu DO, Piddock LJ V. Molecular mechanisms of antibiotic resistance. Nature Reviews Microbiology. 2015.
3. Silhavy TJ, Kahne D, Walker S. The bacterial cell envelope. Cold Spring Harbor perspectives in biology. 2010.
4. Dmitriev B, Toukach F, Ehlers S. Towards a comprehensive view of the bacterial cell wall. Trends in Microbiology. 2005.
5. Sauvage E, Kerff F, Terrak M, Ayala JA, Charlier P. The penicillin-binding proteins: Structure and role in peptidoglycan biosynthesis. FEMS Microbiology Reviews. 2008.
6. Zapun A, Contreras-Martel C, Vernet T. Penicillin-binding proteins and β-lactam resistance. FEMS Microbiology Reviews. 2008.
7. Claus D. A standardized Gram staining procedure. World J Microbiol Biotechnol. 1992;
8. Beveridge TJ. Use of the Gram stain in microbiology. Biotech Histochem. 2001;
9. Malanovic N, Lohner K. Gram-positive bacterial cell envelopes: The impact on the activity of antimicrobial peptides. Biochim Biophys Acta - Biomembr. 2016;
10. Percy MG, Gründling A. Lipoteichoic Acid Synthesis and Function in Gram-Positive Bacteria. Annu Rev Microbiol. 2014;
11. Vollmer W, Blanot D, De Pedro MA. Peptidoglycan structure and architecture. FEMS Microbiology Reviews. 2008.
12. Gan L, Chen S, Jensen GJ. Molecular organization of Gram-negative peptidoglycan. Proc Natl Acad Sci U S A. 2008;
13. Rilfors L, Lindblom G. Regulation of lipid composition in biological membranes - Biophysical studies of lipids and lipid synthesizing enzymes. In: Colloids and Surfaces B: Biointerfaces. 2002.
14. Raetz CRH, Whitfield C. Lipopolysaccharide Endotoxins. Annu Rev Biochem. 2002;
15. Needham BD, Trent MS. Fortifying the barrier: The impact of lipid A remodelling on bacterial pathogenesis. Nature Reviews Microbiology. 2013.
16. Wang X, Quinn PJ. Lipopolysaccharide: Biosynthetic pathway and structure

modification. Progress in Lipid Research. 2010.

17. Vellai T, Vida G. The origin of eukaryotes: The difference between prokaryotic and eukaryotic cells. Proceedings of the Royal Society B: Biological Sciences. 1999.
18. Kerfeld CA, Aussignargues C, Zarzycki J, Cai F, Sutter M. Bacterial microcompartments. Nat Rev Microbiol. 2018;
19. Cornejo E, Abreu N, Komeili A. Compartmentalization and organelle formation in bacteria. Current Opinion in Cell Biology. 2014.
20. Nakayama H, Kurokawa K, Lee BL. Lipoproteins in bacteria: Structures and biosynthetic pathways. FEBS Journal. 2012.
21. Whitfield C, Trent MS. Biosynthesis and Export of Bacterial Lipopolysaccharides. Annu Rev Biochem. 2014;
22. Poetsch A, Wolters D. Bacterial membrane proteomics. Proteomics. 2008.
23. Zaritsky A, Parola AH, Abdah M, Masalha H. Homeoviscous adaptation, growth rate, and morphogenesis in bacteria. Biophys J. 1985;
24. Ernst R, Ejsing CS, Antonny B. Homeoviscous Adaptation and the Regulation of Membrane Lipids. Journal of Molecular Biology. 2016.
25. Royce LA, Liu P, Stebbins MJ, Hanson BC, Jarboe LR. The damaging effects of short chain fatty acids on Escherichia coli membranes. Appl Microbiol Biotechnol. 2013;
26. Zhang YM, Rock CO. Membrane lipid homeostasis in bacteria. Nature Reviews Microbiology. 2008.
27. Zimmer J, Doyle DA, Günter Grossmann J. Structural characterization and pH-induced conformational transition of full-length KcsA. Biophys J. 2006;
28. Bernèche S, Roux B. Molecular dynamics of the KcsA K+ channel in a bilayer membrane. Biophys J. 2000;
29. Papanastasiou M, Orfanoudaki G, Koukaki M, Kountourakis N, Sardis MF, Aivaliotis M, et al. The escherichia coli peripheral inner membrane proteome. Mol Cell Proteomics. 2013;
30. Tikhonova EB, Zgurskaya HI. AcrA, AcrB, and TolC of Escherichia coli form a stable intermembrane multidrug efflux complex. J Biol Chem. 2004;
31. Hsu PC, Samsudin F, Shearer J, Khalid S. It Is Complicated: Curvature, Diffusion, and Lipid Sorting within the Two Membranes of Escherichia coli. J Phys Chem Lett. 2017;8(22):5513–8.

32. Du D, Wang Z, James NR, Voss JE, Klimont E, Ohene-Agyei T, et al. Structure of the AcrAB-TolC multidrug efflux pump. Nature. 2014;
33. Deckers-Hebestreit G, Altendorf K. THE F $_0$ F $_1$ -TYPE ATP SYNTHASES OF BACTERIA: Structure and Function of the F $_0$ Complex. Annu Rev Microbiol. 1996;
34. Zavascki AP, Goldani LZ, Li J, Nation RL. Polymyxin B for the treatment of multidrug-resistant pathogens: A critical review. Journal of Antimicrobial Chemotherapy. 2007.
35. Vollmer W. Peptidoglycan. In: Molecular Medical Microbiology: Second Edition. 2014.
36. Vollmer W, Seligman SJ. Architecture of peptidoglycan: more data and more models. Trends Microbiol. 2010;
37. Glauner B, Holtje J V., Schwarz U. The composition of the murein of Escherichia coli. J Biol Chem. 1988;
38. Carballido-Lopez R. The Bacterial Actin-Like Cytoskeleton. Microbiol Mol Biol Rev. 2006;
39. Ouzounov N, Nguyen JP, Bratton BP, Jacobowitz D, Gitai Z, Shaevitz JW. MreB Orientation Correlates with Cell Diameter in Escherichia coli. Biophys J. 2016;
40. Ursell TS, Nguyen J, Monds RD, Colavin A, Billings G, Ouzounov N, et al. Rod-like bacterial shape is maintained by feedback between cell curvature and cytoskeletal localization. Proc Natl Acad Sci. 2014;
41. van Teeffelen S, Wang S, Furchtgott L, Huang KC, Wingreen NS, Shaevitz JW, et al. The bacterial actin MreB rotates, and rotation depends on cell-wall assembly. Proc Natl Acad Sci. 2011;
42. Braun V, Rehn K, Wolff H. Supramolecular Structure of the Rigid Layer of the Cell Wall of Salmonella, Serratia, Proteus, and Pseudomonas fluorescens. Number of Lipoprotein Molecules in a Membrane Layer. Biochemistry. 1970;
43. Samsudin F, Boags A, Piggot TJ, Khalid S. Braun's Lipoprotein Facilitates OmpA Interaction with the Escherichia coli Cell Wall. Biophys J. 2017;
44. Cowles CE, Li Y, Semmelhack MF, Cristea IM, Silhavy TJ. The free and bound forms of Lpp occupy distinct subcellular locations in Escherichia coli. Mol Microbiol. 2011;
45. Park JS, Lee WC, Yeo KJ, Ryu K-S, Kumarasiri M, Hesek D, et al. Mechanism

of anchoring of OmpA protein to the cell wall peptidoglycan of the gram-negative bacterial outer membrane. FASEB J. 2011;

46. Ortiz-Suarez ML, Samsudin F, Piggot TJ, Bond PJ, Khalid S. Full-Length OmpA: Structure, Function, and Membrane Interactions Predicted by Molecular Dynamics Simulations. Biophys J. 2016;111(8):1692–702.
47. Samsudin F, Ortiz-Suarez ML, Piggot TJ, Bond PJ, Khalid S. OmpA: A Flexible Clamp for Bacterial Cell Wall Attachment. Structure. 2016;24(12):2227–35.
48. Boags AT, Samsudin F, Khalid S. Binding from Both Sides: TolR and Full-Length OmpA Bind and Maintain the Local Structure of the E. coli Cell Wall. Structure. 2019;
49. Herrmann M, Schneck E, Gutsmann T, Brandenburg K, Tanaka M. Bacterial lipopolysaccharides form physically cross-linked, two-dimensional gels in the presence of divalent cations. Soft Matter. 2015;
50. Clifton LA, Skoda MWA, Le Brun AP, Ciesielski F, Kuzmenko I, Holt SA, et al. Effect of divalent cation removal on the structure of gram-negative bacterial outer membrane models. Langmuir. 2015;
51. Trimble MJ, Mlynárčik P, Kolář M, Hancock REW. Polymyxin: Alternative mechanisms of action and resistance. Cold Spring Harb Perspect Med. 2016;
52. Jefferies D, Hsu PC, Khalid S. Through the Lipopolysaccharide Glass: A Potent Antimicrobial Peptide Induces Phase Changes in Membranes. Biochemistry. 2017;56(11):1672–9.
53. Lu YC, Yeh WC, Ohashi PS. LPS/TLR4 signal transduction pathway. Cytokine. 2008.
54. Tomas JM, Ciurana B, Benedi VJ, Juarez A. Role of Lipopolysaccharide and Complement in Susceptibility of Escherichia coli and Salmonella typhimurium to Non-immune Serum. Microbiology. 2009;
55. Murray GL, Attridge SR, Morona R. Regulation of Salmonella typhimurium lipopolysaccharide O antigen chain length is required for virulence; identification of FepE as a second Wzz. Mol Microbiol. 2003;
56. Murray GL, Attridge SR, Morona R. Altering the length of the lipopolysaccharide O antigen has an impact on the interaction of Salmonella enterica serovar typhimurium with macrophages and complement. J Bacteriol. 2006;
57. Okuda S, Sherman DJ, Silhavy TJ, Ruiz N, Kahne D. Lipopolysaccharide

transport and assembly at the outer membrane: The PEZ model. Nature Reviews Microbiology. 2016.

58. Cunliffe D, Smart CA, Alexander C, Vulfson EN. Bacterial adhesion at synthetic surfaces. Appl Environ Microbiol. 1999;

59. Tourney J, Ngwenya BT. The role of bacterial extracellular polymeric substances in geomicrobiology. Chemical Geology. 2014.

60. Manning AJ, Kuehn MJ. Contribution of bacterial outer membrane vesicles to innate bacterial defense. BMC Microbiol. 2011;

61. Solano C, Echeverz M, Lasa I. Biofilm dispersion and quorum sensing. Current Opinion in Microbiology. 2014.

62. Prindle A, Liu J, Asally M, Ly S, Garcia-Ojalvo J, Süel GM. Ion channels enable electrical communication in bacterial communities. Nature. 2015;

63. Overington JP, Al-Lazikani B, Hopkins AL. How many drug targets are there? Nat Rev Drug Discov. 2006;

64. Yin H, Flynn AD. Drugging Membrane Protein Interactions. Annu Rev Biomed Eng. 2016;

65. Gong J, Chen Y, Pu F, Sun P, He F, Zhang L, et al. Understanding Membrane Protein Drug Targets in Computational Perspective. Curr Drug Targets. 2018;

66. Dong C, Beis K, Nesper J, Brunkan-LaMontagne AL, Clarke BR, Whitfield C, et al. Wza the translocon for E. coli capsular polysaccharides defines a new class of membrane protein. Nature. 2006;

67. Ford RC, Brunkan-LaMontagne AL, Collins RF, Clarke BR, Harris R, Naismith JH, et al. Structure-function relationships of the outer membrane translocon Wza investigated by cryo-electron microscopy and mutagenesis. J Struct Biol. 2009;

68. Low HH, Gubellini F, Rivera-Calzada A, Braun N, Connery S, Dujeancourt A, et al. Structure of a type IV secretion system. Nature. 2014;

69. Wallden K, Rivera-Calzada A, Waksman G. Type IV secretion systems: Versatility and diversity in function. Cellular Microbiology. 2010.

70. Neiditch MB, Federle MJ, Pompeani AJ, Kelly RC, Swem DL, Jeffrey PD, et al. Ligand-Induced Asymmetry in Histidine Sensor Kinase Complex Regulates Quorum Sensing. Cell. 2006;

71. Wu EL, Fleming PJ, Yeom MS, Widmalm G, Klauda JB, Fleming KG, et al. E. coli outer membrane and interactions with OmpLA. Biophys J. 2014;

72. Stanley AM, Chuawong P, Hendrickson TL, Fleming KG. Energetics of outer membrane phospholipase A (OMPLA) dimerization. J Mol Biol. 2006;358(1):120–31.
73. Ulmschneider MB, Sansom MSP. Amino acid distributions in integral membrane protein structures. Biochim Biophys Acta - Biomembr. 2001;
74. Makwana KM, Mahalakshmi R. Implications of aromatic-aromatic interactions: From protein structures to peptide models. Protein Sci. 2015;
75. Gessmann D, Chung YH, Danoff EJ, Plummer AM, Sandlin CW, Zaccai NR, et al. Outer membrane -barrel protein folding is physically controlled by periplasmic lipid head groups and BamA. Proc Natl Acad Sci. 2014;
76. Touzé T, Tran AX, Hankins J V., Mengin-Lecreulx D, Trent MS. Periplasmic phosphorylation of lipid A is linked to the synthesis of undecaprenyl phosphate. Mol Microbiol. 2008;
77. Herrera CM, Hankins J V., Trent MS. Activation of PmrA inhibits LpxT-dependent phosphorylation of lipid A promoting resistance to antimicrobial peptides. Mol Microbiol. 2010;
78. Reynolds CM, Kalb SR, Cotter RJ, Raetz CRH. A phosphoethanolamine transferase specific for the outer 3-deoxy-D-manno-octulosonic acid residue of Escherichia coli lipopolysaccharide: Identification of the eptB gene and Ca2+ hypersensitivity of an eptB deletion mutant. J Biol Chem. 2005;
79. Yang ST, Kreutzberger AJB, Lee J, Kiessling V, Tamm LK. The role of cholesterol in membrane fusion. Chem Phys Lipids. 2016;
80. Mouritsen OG, Zuckermann MJ. What’s so special about cholesterol? In: Lipids. 2004.
81. Sáenz JP, Grosser D, Bradley AS, Lagny TJ, Lavrynenko O, Broda M, et al. Hopanoids as functional analogues of cholesterol in bacterial membranes. Proc Natl Acad Sci. 2015;
82. Saenz JP, Sezgin E, Schwille P, Simons K. Functional convergence of hopanoids and sterols in membrane ordering. Proc Natl Acad Sci. 2012;
83. Gibbons HS, Reynolds CM, Guan Z, Raetz CRH. An inner membrane dioxygenase that generates the 2-hydroxymyristate moiety of Salmonella lipid A. Biochemistry. 2008;
84. Vorachek-Warren MK, Carty SM, Lin S, Cotter RJ, Raetz CRH. An Escherichia coli mutant lacking the cold shock-induced palmitoleoyltransferase of lipid A

biosynthesis. Absence of unsaturated acyl chains and antibiotic hypersensitivity at 12 °C. J Biol Chem. 2002;

85. Bishop RE. Structural biology of membrane-intrinsic β-barrel enzymes: Sentinels of the bacterial outer membrane. Vol. 1778, Biochimica et Biophysica Acta - Biomembranes. 2008. p. 1881–96.
86. Rutten L, Geurtsen J, Lambert W, Smolenaers JJM, Bonvin AM, de Haan A, et al. Crystal structure and catalytic mechanism of the LPS 3-O-deacylase PagL from Pseudomonas aeruginosa. Proc Natl Acad Sci [Internet]. 2006;103(18):7071–6. Available from: http://www.pnas.org/cgi/doi/10.1073/pnas.0509392103
87. Reynolds CM, Ribeiro AA, McGrath SC, Cotter RJ, Raetz CRH, Trent MS. An outer membrane enzyme encoded by Salmonella typhimurium lpxR that removes the 3???-acyloxyacyl moiety of lipid A. J Biol Chem. 2006;281(31):21974–87.
88. Yu Z, Qin W, Lin J, Fang S, Qiu J. Antibacterial mechanisms of polymyxin and bacterial resistance. BioMed Research International. 2015.
89. Clausell A, Garcia-Subirats M, Pujol M, Busquets MA, Rabanal F, Cajal Y. Gram-negative outer and inner membrane models: Insertion of cyclic cationic lipopeptides. J Phys Chem B. 2007;
90. Deris ZZ, Akter J, Sivanesan S, Roberts KD, Thompson PE, Nation RL, et al. A secondary mode of action of polymyxins against Gram-negative bacteria involves the inhibition of NADH-quinone oxidoreductase activity. J Antibiot (Tokyo). 2014;
91. Zhang L, Dhillon P, Yan H, Farmer S, Hancock REW. Interactions of bacterial cationic peptide antibiotics with outer and cytoplasmic membranes of Pseudomonas aeruginosa. Antimicrob Agents Chemother. 2000;
92. Poirel L, Jayol A, Nordmanna P. Polymyxins: Antibacterial activity, susceptibility testing, and resistance mechanisms encoded by plasmids or chromosomes. Clinical Microbiology Reviews. 2017.
93. Falagas ME, Kasiakou SK. Toxicity of polymyxins: A systematic review of the evidence from old and recent studies. Critical Care. 2006.
94. Baron S, Hadjadj L, Rolain JM, Olaitan AO. Molecular mechanisms of polymyxin resistance: knowns and unknowns. Int J Antimicrob Agents. 2016;
95. Zhao H, Caflisch A. Molecular dynamics in drug design. European Journal of

Medicinal Chemistry. 2015.

96. Liu X, Shi D, Zhou S, Liu H, Liu H, Yao X. Molecular dynamics simulations and novel drug discovery. Expert Opinion on Drug Discovery. 2018.

97. Hess B, Bekker H, Berendsen HJC, Fraaije JGEM. LINCS: A Linear Constraint Solver for molecular simulations. J Comput Chem. 1997;

98. Marrink SJ, Risselada HJ, Yefimov S, Tieleman DP, De Vries AH. The MARTINI force field: Coarse grained model for biomolecular simulations. J Phys Chem B. 2007;

99. Wu C, Shea JE. Coarse-grained models for protein aggregation. Current Opinion in Structural Biology. 2011.

100. Bond PJ, Holyoake J, Ivetac A, Khalid S, Sansom MSP. Coarse-grained molecular dynamics simulations of membrane proteins and peptides. J Struct Biol. 2007;

101. Kmiecik S, Gront D, Kolinski M, Wieteska L, Dawid AE, Kolinski A. Coarse-Grained Protein Models and Their Applications. Chemical Reviews. 2016.

102. Vanommeslaeghe K, Hatcher E, Acharya C, Kundu S, Zhong S, Shim J, et al. CHARMM general force field: A force field for drug-like molecules compatible with the CHARMM all-atom additive biological force fields. J Comput Chem. 2010;

103. Case DA, Cheatham TE, Darden T, Gohlke H, Luo R, Merz KM, et al. The Amber biomolecular simulation programs. Vol. 26, Journal of Computational Chemistry. 2005. p. 1668–88.

104. Schmid N, Eichenberger AP, Choutko A, Riniker S, Winger M, Mark AE, et al. Definition and testing of the GROMOS force-field versions 54A7 and 54B7. Eur Biophys J. 2011;40(7):843–56.

105. Pluhackova K, Kirsch SA, Han J, Sun L, Jiang Z, Unruh T, et al. A Critical Comparison of Biomembrane Force Fields: Structure and Dynamics of Model DMPC, POPC, and POPE Bilayers. J Phys Chem B. 2016;120(16):3888–903.

106. Sandoval-Perez A, Pluhackova K, Böckmann RA. Critical Comparison of Biomembrane Force Fields: Protein-Lipid Interactions at the Membrane Interface. J Chem Theory Comput. 2017;13(5):2310–21.

107. Cheatham TE, Miller JL, Fox T, Darden TA, Kollman PA. Molecular Dynamics Simulations on Solvated Biomolecular Systems: The Particle Mesh Ewald Method Leads to Stable Trajectories of DNA, RNA, and Proteins. Journal of

the American Chemical Society. 1995;

108. Nosé S. A molecular dynamics method for simulations in the canonical ensemble. Mol Phys. 1984;52(2):255–68.

109. Hoover WG. Canonical dynamics: Equilibrium phase-space distributions. Phys Rev A. 1985;31(3):1695–7.

110. Lemak AS, Balabaev NK. On the berendsen thermostat. Mol Simul. 1994;

111. Dong Q-Q, Hu H-B, Chen S-Q, He Q, Bao L-Y. Molecular dynamics simulation of freezing process of water droplets impinging on cold surface. Wuli Xuebao/Acta Phys Sin. 2018;

112. Shearer J, Khalid S. Communication between the leaflets of asymmetric membranes revealed from coarse-grain molecular dynamics simulations. Sci Rep. 2018;

113. Van Der Spoel D, Lindahl E, Hess B, Groenhof G, Mark AE, Berendsen HJC. GROMACS: Fast, flexible, and free. Vol. 26, Journal of Computational Chemistry. 2005. p. 1701–18.

114. Abraham M, Hess B, Spoel D van der, Lindahl E. Gromacs - User Manual 2016. SpringerReference. 2015;

115. Woodall CA. Electroporation of E. coli. Methods Mol Biol. 2003;

116. Lessard JC. Transformation of E. coli via electroporation. In: Methods in Enzymology. 2013.

117. Tieleman DP, Berendsen HJC. Molecular dynamics simulations of a fully hydrated dipalmitoylphosphatidylcholine bilayer with different macroscopic boundary conditions and parameters. J Chem Phys. 1996;105(11):4871–80.

118. Marrink SJ, Mark AE. The mechanism of vesicle fusion as revealed by molecular dynamics simulations. J Am Chem Soc. 2003;

119. Yesylevskyy SO, Schäfer L V., Sengupta D, Marrink SJ. Polarizable water model for the coarse-grained MARTINI force field. PLoS Comput Biol. 2010;

120. Domański J, Stansfeld PJ, Sansom MSP, Beckstein O. Lipidbook: A public repository for force-field parameters used in membrane simulations. J Membr Biol. 2010;

121. Schüttelkopf AW, Van Aalten DMF. PRODRG: A tool for high-throughput crystallography of protein-ligand complexes. Acta Crystallogr Sect D Biol Crystallogr. 2004;

122. Stroet M, Caron B, Visscher KM, Geerke DP, Malde AK, Mark AE. Automated

Topology Builder Version 3.0: Prediction of Solvation Free Enthalpies in Water and Hexane. J Chem Theory Comput. 2018;

123. Silvestrov P, Müller TA, Clark KN, Hausinger RP, Cisneros GA. Homology modeling, molecular dynamics, and site-directed mutagenesis study of AlkB human homolog 1 (ALKBH1). J Mol Graph Model. 2014;
124. DeLano WL. The PyMOL Molecular Graphics System, Version 1.8. Schrödinger LLC [Internet]. 2014;http://www.pymol.org. Available from: http://www.pymol.org
125. Maldonado RF, Sá-Correia I, Valvano MA. Lipopolysaccharide modification in gram-negative bacteria during chronic infection. FEMS Microbiology Reviews. 2016.
126. Rice A, Wereszczynski J. Atomistic Scale Effects of Lipopolysaccharide Modifications on Bacterial Outer Membrane Defenses. Biophys J [Internet]. 2018;114(6):1389–99. Available from: https://doi.org/10.1016/j.bpj.2018.02.006
127. Kawasaki K, Teramoto M, Tatsui R, Amamoto S. Lipid A 3’-O-deacylation by Salmonella outer membrane enzyme LpxR modulates the ability of lipid A to stimulate Toll-like receptor 4. Biochem Biophys Res Commun. 2012;428(3):343–7.
128. Olaitan AO, Morand S, Rolain JM. Mechanisms of polymyxin resistance: Acquired and intrinsic resistance in bacteria. Frontiers in Microbiology. 2014.
129. Rutten L, Mannie J-PBA, Stead CM, Raetz CRH, Reynolds CM, Bonvin AMJJ, et al. Active-site architecture and catalytic mechanism of the lipid A deacylase LpxR of *Salmonella typhimurium*. Proc Natl Acad Sci U S A [Internet]. 2009;106(6):1960–4. Available from: http://www.ncbi.nlm.nih.gov/pubmed/19174515%5Cnhttp://www.pubmedcentral.nih.gov/articlerender.fcgi?artid=PMC2644146
130. Baaden M, Meier C, Sansom MSP. A molecular dynamics investigation of mono and dimeric states of the outer membrane enzyme OMPLA. J Mol Biol. 2003;331(1):177–89.
131. Dominguez C, Boelens R, Bonvin AMJJ. HADDOCK: A protein-protein docking approach based on biochemical or biophysical information. J Am Chem Soc. 2003;
132. De Vries SJ, Van Dijk ADJ, Krzeminski M, Van Dijk M, Thureau A, Hsu V, et al. HADDOCK versus HADDOCK: New features and performance of

HADDOCK2.0 on the CAPRI targets. In: Proteins: Structure, Function and Genetics. 2007.

133. Hsu P-C, Jefferies D, Khalid S. Molecular Dynamics Simulations Predict the Pathways via Which Pristine Fullerenes Penetrate Bacterial Membranes. J Phys Chem B [Internet]. 2016;120(43):11170–9. Available from: http://pubs.acs.org/doi/abs/10.1021/acs.jpcb.6b06615

134. Jo S, Cheng X, Lee J, Kim S, Park SJ, Patel DS, et al. CHARMM-GUI 10 years for biomolecular modeling and simulation. Vol. 38, Journal of Computational Chemistry. 2017. p. 1114–24.

135. Parrinello M. Polymorphic transitions in single crystals: A new molecular dynamics method. J Appl Phys [Internet]. 1981;52(12):7182. Available from: http://scitation.aip.org/content/aip/journal/jap/52/12/10.1063/1.328693

136. Parrinello M, Rahman A. Crystal structure and pair potentials: A molecular-dynamics study. Phys Rev Lett. 1980;45(14):1196–9.

137. Woodcock L V. Isothermal molecular dynamics calculations for liquid salts. Chem Phys Lett. 1971;

138. Martins-Costa MTC, Ruiz-López MF. Gromacs 5.1 manual. J Comput Chem. 2017;38(10):659–68.

139. Piggot TJ, Holdbrook D a, Khalid S. Electroporation of the E. coli and S. Aureus membranes: molecular dynamics simulations of complex bacterial membranes. J Phys Chem B [Internet]. 2011;115(45):13381–8. Available from: http://www.ncbi.nlm.nih.gov/pubmed/21970408

140. Zhang L, DeHaven RN, Goodman M. NMR and modeling studies of a synthetic extracellular loop II of the κ opioid receptor in a DPC micelle. Biochemistry. 2002;41(1):61–8.

141. Marrink SJ, Tieleman DP, Mark AE. Molecular Dynamics Simulation of the Kinetics of Spontaneous Micelle Formation. J Phys Chem B [Internet]. 2000;104(51):12165–73. Available from: http://pubs.acs.org/doi/abs/10.1021/jp001898h

142. Bond PJ, Sansom MSP. Membrane protein dynamics versus environment: Simulations of OmpA in a micelle and in a bilayer. J Mol Biol. 2003;329(5):1035–53.

143. Abel S, Dupradeau FY, Marchi M. Molecular dynamics simulations of a characteristic DPC micelle in water. J Chem Theory Comput.

2012;8(11):4610–23.

144. Schiffrin B, Calabrese AN, Higgins AJ, Humes JR, Ashcroft AE, Kalli AC, et al. Effects of Periplasmic Chaperones and Membrane Thickness on BamA-Catalyzed Outer-Membrane Protein Folding. J Mol Biol. 2017;429(23):3776–92.
145. Castillo N, Monticelli L, Barnoud J, Tieleman DP. Free energy of WALP23 dimer association in DMPC, DPPC, and DOPC bilayers. Chem Phys Lipids. 2013;
146. Lagüe P, Zuckermann MJ, Roux B. Lipid-mediated interactions between intrinsic membrane proteins: Dependence on protein size and lipid composition. Biophys J. 2001;
147. Rollauer SE, Sooreshjani MA, Noinaj N, Buchanan SK. Outer membrane protein biogenesis in Gram-negative bacteria. Philos Trans B. 2015;370(20150023):1–10.
148. Khalid S, Bond PJ, Carpenter T, Sansom MSP. OmpA: gating and dynamics via molecular dynamics simulations. Biochim Biophys Acta. 2008;1778(9):1871–80.
149. Cox K, Bond PJ, Grottesi A, Baaden M, Sansom MSP. Outer membrane proteins: Comparing X-ray and NMR structures by MD simulations in lipid bilayers. Eur Biophys J. 2008;37(2):131–41.
150. Bond PJ, Faraldo-Gomez JD, Deol SS, Sansom MSP. Membrane protein dynamics and detergent interactions within a crystal: A simulation study of OmpA. Proc Natl Acad Sci [Internet]. 2006;103(25):9518–23. Available from: http://www.pnas.org/cgi/doi/10.1073/pnas.0600398103
151. Tamm LK, Abildgaard F, Arora A, Blad H, Bushweller JH. Structure, dynamics and function of the outer membrane protein A (OmpA) and influenza hemagglutinin fusion domain in detergent micelles by solution NMR. In: FEBS Letters. 2003. p. 139–43.
152. Piggot TJ, Piñeiro Á, Khalid S. Molecular dynamics simulations of phosphatidylcholine membranes: A comparative force field study. J Chem Theory Comput. 2012;8(11):4593–609.
153. Stansfeld PJ, Goose JE, Caffrey M, Carpenter EP, Parker JL, Newstead S, et al. MemProtMD: Automated Insertion of Membrane Protein Structures into Explicit Lipid Membranes. Structure. 2015;23(7):1350–61.

154. Lomize MA, Lomize AL, Pogozheva ID, Mosberg HI. OPM: Orientations of proteins in membranes database. Bioinformatics. 2006;

155. Lomize MA, Pogozheva ID, Joo H, Mosberg HI, Lomize AL. OPM database and PPM web server: Resources for positioning of proteins in membranes. Nucleic Acids Res. 2012;40(D1).

156. Deol SS, Bond PJ, Domene C, Sansom MSP. Lipid-protein interactions of integral membrane proteins: A comparative simulation study. Biophys J. 2004;

157. Sanchez KM, Kang G, Wu B, Kim JE. Tryptophan-lipid interactions in membrane protein folding probed by ultraviolet resonance Raman and fluorescence spectroscopy. Biophys J. 2011;

158. Tieleman DP, van der Spoel D, Berendsen HJC. Molecular Dynamics Simulations of Dodecylphosphocholine Micelles at Three Different Aggregate Sizes: Micellar Structure and Chain Relaxation. J Phys Chem B. 2000;

159. Saunders GM, Bruce Macdonald HE, Essex JW, Khalid S. Prediction of the Closed Conformation and Insights into the Mechanism of the Membrane Enzyme LpxR. Biophys J. 2018;115(8):1445–56.

160. Clifton LA, Skoda MWA, Daulton EL, Hughes A V., Le Brun AP, Lakey JH, et al. Asymmetric phospholipid: Lipopolysaccharide bilayers; a gram-negative bacterial outer membrane mimic. J R Soc Interface. 2013;

161. Yeow J, Tan KW, Holdbrook DA, Chong ZS, Marzinek JK, Bond PJ, et al. The architecture of the OmpC–MlaA complex sheds light on the maintenance of outer membrane lipid asymmetry in Escherichia coli. J Biol Chem. 2018;

162. Powers MJ, Trent MS. Phospholipid retention in the absence of asymmetry strengthens the outer membrane permeability barrier to last-resort antibiotics. Proc Natl Acad Sci. 2018;

163. Li W, Cowley A, Uludag M, Gur T, McWilliam H, Squizzato S, et al. The EMBL-EBI bioinformatics web and programmatic tools framework. Nucleic Acids Res. 2015;

164. Richens JL, Lane JS, Bramble JP, O’Shea P. The electrical interplay between proteins and lipids in membranes. Biochimica et Biophysica Acta - Biomembranes. 2015.

165. Sharma VK, Mamontov E, Tyagi M, Qian S, Rai DK, Urban VS. Dynamical and Phase Behavior of a Phospholipid Membrane Altered by an Antimicrobial Peptide at Low Concentration. J Phys Chem Lett. 2016;

166. Zeno WF, Hilt S, Aravagiri KK, Risbud SH, Voss JC, Parikh AN, et al. Analysis of lipid phase behavior and protein conformational changes in nanolipoprotein particles upon entrapment in sol-gel-derived silica. Langmuir. 2014;

167. Galvagnion C, Brown JWP, Ouberai MM, Flagmeier P, Vendruscolo M, Buell AK, et al. Chemical properties of lipids strongly affect the kinetics of the membrane-induced aggregation of α-synuclein. Proc Natl Acad Sci. 2016;

168. Javanainen M, Martinez-Seara H, Vattulainen I. Excessive aggregation of membrane proteins in the Martini model. PLoS One. 2017;

169. McGaughey GB, Gagné M, Rappé AK. π-Stacking interactions. Alive and well in proteins. J Biol Chem. 1998;

170. Domon B, Aebersold R. Mass spectrometry and protein analysis. Science. 2006.

171. Di Falco MR. Mass spectrometry-based proteomics. In: Methods in Molecular Biology. 2018.

172. Lever G, Cole DJ, Lonsdale R, Ranaghan KE, Wales DJ, Mulholland AJ, et al. Large-scale density functional theory transition state searching in enzymes. J Phys Chem Lett. 2014;

173. Huang W, Lin Z, Van Gunsteren WF. Validation of the GROMOS 54A7 force field with respect to β-peptide folding. J Chem Theory Comput. 2011;7(5):1237–43.

174. Hofer TS, Van Gunsteren WF. Exploring the properties of small molecule protein binding via molecular simulations: The TRSH-p53 core domain complex. Mol Biosyst. 2012;8(11):2891–900.

175. Merrill AH, Vu MN. Glycolipids. In: Encyclopedia of Cell Biology. 2015.

176. Volkman JK. Sterols in microorganisms. Applied Microbiology and Biotechnology. 2003.

177. Kannenberg EL, Poralla K. Hopanoid biosynthesis and function in bacteria. Naturwissenschaften. 1999.

178. Träuble H, Eibl H. Electrostatic effects on lipid phase transitions: membrane structure and ionic environment. Proc Natl Acad Sci U S A. 1974;

179. Brown DA, London E. Structure and Function of Sphingolipid- and Cholesterol-rich Membrane Rafts. J Biol Chem. 2000;

180. Boeynaems S, Alberti S, Fawzi NL, Mittag T, Polymenidou M, Rousseau F, et al. Protein Phase Separation: A New Phase in Cell Biology. Trends in Cell

Biology. 2018.

181. Mitrea DM, Kriwacki RW. Phase separation in biology; functional organization of a higher order. Cell Commun Signal. 2016;

182. Heberle FA, Feigenson GW. Phase separation in lipid membranes. Cold Spring Harb Perspect Biol. 2011;

183. López D, Kolter R. Functional microdomains in bacterial membranes. Genes Dev. 2010;

184. Simons K, Ikonen E. Functional rafts in cell membranes. Nature. 1997.

185. Callan-Jones A, Sorre B, Bassereau P. Curvature-driven lipid sorting in biomembranes. Cold Spring Harbor Perspectives in Biology. 2011.

186. Shearer J, Jefferies D, Khalid S. Outer Membrane Proteins OmpA, FhuA, OmpF, EstA, BtuB, and OmpX Have Unique Lipopolysaccharide Fingerprints. J Chem Theory Comput. 2019;

187. Czech MP. PIP2 and PIP3: Complex roles at the cell surface. Cell. 2000.

188. Kirschner KN, Lins RD, Maass A, Soares TA. A glycam-based force field for simulations of lipopolysaccharide membranes: Parametrization and validation. J Chem Theory Comput. 2012;

189. Pavlova A, Hwang H, Lundquist K, Balusek C, Gumbart JC. Living on the edge: Simulations of bacterial outer-membrane proteins. Biochim Biophys Acta - Biomembr. 2016;1858(7):1753–9.

190. Soares TA, Straatsma TP. Assessment of the convergence of molecular dynamics simulations of lipopolysaccharide membranes. Mol Simul. 2008;34(3):295–307.

191. Berglund NA, Piggot TJ, Jefferies D, Sessions RB, Bond PJ, Khalid S. Interaction of the Antimicrobial Peptide Polymyxin B1 with Both Membranes of E. coli: A Molecular Dynamics Study. PLoS Comput Biol. 2015;

192. Gonzales MF, Brooks T, Pukatzki SU, Provenzano D. Rapid Protocol for Preparation of Electrocompetent Escherichia coli and Vibrio cholerae. J Vis Exp. 2013;

193. Poger D, Van Gunsteren WF, Mark AE. A new force field for simulating phosphatidylcholine bilayers. J Comput Chem. 2010;

194. Kotulska M, Kubica K, Koronkiewicz S, Kalinowski S. Modeling the induction of lipid membrane electropermeabilization. Bioelectrochemistry. 2007;

195. Tieleman DP. The molecular basis of electroporation. BMC Biochem. 2004;

196. Qi Y, Ingólfsson HI, Cheng X, Lee J, Marrink SJ, Im W. CHARMM-GUI Martini Maker for Coarse-Grained Simulations with the Martini Force Field. J Chem Theory Comput. 2015;
197. Essmann U, Perera L, Berkowitz ML, Darden T, Lee H, Pedersen LG. A smooth particle mesh Ewald method. J Chem Phys. 1995;
198. Piggot TJ, Holdbrook DA, Khalid S. Electroporation of the E. coli and S. aureus membranes: Molecular dynamics simulations of complex bacterial membranes. J Phys Chem B. 2011;
199. Humphrey W, Dalke A, Schulten K. VMD: Visual molecular dynamics. J Mol Graph. 1996;14(1):33–8.
200. Buchoux S. FATSLiM: A fast and robust software to analyze MD simulations of membranes. Bioinformatics. 2017;
201. Sára M, Sleytr UB. S-layer proteins. Journal of Bacteriology. 2000.
202. Piggot TJ, Holdbrook DA, Khalid S. Conformational dynamics and membrane interactions of the E. coli outer membrane protein FecA: A molecular dynamics simulation study. Biochim Biophys Acta - Biomembr [Internet]. 2013;1828(2):284–93. Available from: http://linkinghub.elsevier.com/retrieve/pii/S0005273612003021
203. Carpenter TS, Parkin J, Khalid S. The Free Energy of Small Solute Permeation through the Escherichia coli Outer Membrane Has a Distinctly Asymmetric Profile. J Phys Chem Lett. 2016;7(17):3446–51.
204. Park S, Beaven AH, Klauda JB, Im W. How Tolerant are Membrane Simulations with Mismatch in Area per Lipid between Leaflets? J Chem Theory Comput. 2015;
205. Jo S, Wu EL, Stuhlsatz D, Klauda JB, Mackerell AD, Widmalm G, et al. Lipopolysaccharide membrane building and simulation. Methods Mol Biol. 2015;
206. Snyder S, Kim D, McIntosh TJ. Lipopolysaccharide bilayer structure: Effect of chemotype, core mutations, divalent cations, and temperature. Biochemistry. 1999;38(33):10758–67.
207. Bhatia H, Ingólfsson HI, Carpenter TS, Lightstone FC, Bremer PT. MemSurfer: A Tool for Robust Computation and Characterization of Curved Membranes. J Chem Theory Comput. 2019;
208. Chernomordik L V., Kozlov MM. Protein-Lipid Interplay in Fusion and Fission

of Biological Membranes. Annu Rev Biochem. 2003;

209. Di Paolo G, De Camilli P. Phosphoinositides in cell regulation and membrane dynamics. Nature. 2006.
210. Zimmerberg J, Kozlov MM. How proteins produce cellular membrane curvature. Nature Reviews Molecular Cell Biology. 2006.
211. McMahon HT, Boucrot E. Membrane curvature at a glance. J Cell Sci. 2015;
212. Lakshmanan I, Batra SK. Protocol for Apoptosis Assay by Flow Cytometry Using Annexin V Staining Method. Bio-protocol. 2013;
213. Fadok VA, Voelker DR, Campbell PA, Cohen JJ, Bratton DL, Henson PM. Exposure of phosphatidylserine on the surface of apoptotic lymphocytes triggers specific recognition and removal by macrophages. J Immunol. 1992;
214. Romantsov T, Battle AR, Hendel JL, Martinac B, Wood JM. Protein localization in Escherichia coli cells: Comparison of the cytoplasmic membrane proteins ProP, LacY, ProW, AqpZ, MscS, and MscL. J Bacteriol. 2010;
215. Schmidt V, Sidore M, Bechara C, Duneau JP, Sturgis JN. The lipid environment of Escherichia coli Aquaporin Z. Biochim Biophys Acta - Biomembr. 2019;
216. Gianoli F, Risler T, Kozlov AS. Lipid bilayer mediates ion-channel cooperativity in a model of hair-cell mechanotransduction. Proc Natl Acad Sci. 2017;
217. Levina N. Protection of Escherichia coli cells against extreme turgor by activation of MscS and MscL mechanosensitive channels: identification of genes required for MscS activity. EMBO J. 1999;
218. Tarek M. Membrane electroporation: A molecular dynamics simulation. Biophys J. 2005;
219. Böckmann RA, De Groot BL, Kakorin S, Neumann E, Grubmüller H. Kinetics, statistics, and energetics of lipid membrane electroporation studied by molecular dynamics simulations. Biophys J. 2008;
220. Ziegler MJ, Thomas Vernier P. Interface water dynamics and porating electric fields for phospholipid bilayers. J Phys Chem B. 2008;
221. Sun S, Yin G, Lee YK, Wong JTY, Zhang TY. Effects of deformability and thermal motion of lipid membrane on electroporation: By molecular dynamics simulations. Biochem Biophys Res Commun. 2011;
222. Haynes T, Smith IPS, Wallace EJ, Trick JL, Sansom MSP, Khalid S. Electric-field-driven translocation of ssDNA through hydrophobic nanopores. ACS

Nano. 2018;

223. Arora A, Rinehart D, Szabo G, Tamm LK. Refolded outer membrane protein A of Escherichia coli forms ion channels with two conductance states in planar lipid bilayers. J Biol Chem. 2000;
224. Bond PJ, Faraldo-Gömez JD, Sansom MSP. OmpA: A pore or not a pore? Simulation and modeling studies. Biophys J. 2002;
225. Jefferies D, Shearer J, Khalid S. Role of O-Antigen in Response to Mechanical Stress of the E. coli Outer Membrane: Insights from Coarse-Grained MD Simulations. J Phys Chem B. 2019;
226. Patel DS, Re S, Wu EL, Qi Y, Klebba PE, Widmalm G, et al. Dynamics and Interactions of OmpF and LPS: Influence on Pore Accessibility and Ion Permeability. Biophys J. 2016;
227. Guigas G, Weiss M. Effects of protein crowding on membrane systems. Biochim Biophys Acta - Biomembr. 2016;
228. Furse S, Scott DJ. Three-Dimensional Distribution of Phospholipids in Gram Negative Bacteria. Biochemistry. 2016;
229. Carty SM, Sreekumar KR, Raetz CRH. Effect of cold shock on lipid a biosynthesis in Escherichia coli: Induction at 12 °C of an acyltransferase specific for palmitoleoyl-acyl carrier protein. J Biol Chem. 1999;
230. Choi SK, Park SY, Kim R, Kim S Bin, Lee CH, Kim JF, et al. Identification of a polymyxin synthetase gene cluster of Paenibacillus polymyxa and heterologous expression of the gene in Bacillus subtilis. J Bacteriol. 2009;
231. Bassetti M, Falagas ME, Kollef M. Ten old antibiotics that will never disappear. Intensive Care Med. 2015;
232. De Visser PC, Kriek NMAJ, Van Hooft PA V, Van Schepdael A, Filippov D V., Van Der Marel GA, et al. Solid-phase synthesis of polymyxin B1 and analogues via a safety-catch approach. J Pept Res. 2003;
233. Baumann G, Mueller P. A molecular model of membrane excitability. J Supramol Cell Biochem. 1974;
234. Yang L, Harroun TA, Weiss TM, Ding L, Huang HW. Barrel-stave model or toroidal model? A case study on melittin pores. Biophys J. 2001;
235. Brogden KA. Antimicrobial peptides: Pore formers or metabolic inhibitors in bacteria? Nature Reviews Microbiology. 2005.
236. Bechinger B, Lohner K. Detergent-like actions of linear amphipathic cationic

antimicrobial peptides. Biochimica et Biophysica Acta - Biomembranes. 2006.

237. Huang HW. Action of antimicrobial peptides: Two-state model. Biochemistry. 2000;

238. Storm DR, Rosenthal KS, Swanson PE. Polymyxin and Related Peptide Antibiotics. Annu Rev Biochem. 2003;

239. Tsubery I. Ofek, S. Cohen, M. Eisenstein, M. Fridkin H. Modulation of the Hydrophobic Domain of Polymyxin B Nonapeptide: Effect on Outer-Membrane Permeabilization and Lipopolysaccharide Neutralization. Mol Pharmacol. 2002;

240. Lu S, Walters G, Parg R, Dutcher JR. Nanomechanical response of bacterial cells to cationic antimicrobial peptides. Soft Matter. 2014;

241. Theretz A, Ranck JL, Tocanne JF. Polymyxin B-induced phase separation and acyl chain interdigitation in phosphatidylcholine/phosphatidylglycerol mixtures. BBA - Biomembr. 1983;

242. Boggs JM, Wang HY, Rangaraj G, Tümmler B. Interdigitation of phosphatidylcholine and phosphatidylethanolamine mixed with complexes of acidic lipids and polymyxin B or polymyxin B nonapeptide. BBA - Biomembr. 1989;

243. Le Brun AP, Clifton LA, Halbert CE, Lin B, Meron M, Holden PJ, et al. Structural characterization of a model gram-negative bacterial surface using lipopolysaccharides from rough strains of Escherichia coli. Biomacromolecules. 2013;

244. Jeworrek C, Evers F, Howe J, Brandenburg K, Tolan M, Winter R. Effects of specific versus nonspecific ionic interactions on the structure and lateral organization of lipopolysaccharides. Biophys J. 2011;

245. Woo SY, Lee H. All-atom simulations and free-energy calculations of coiled-coil peptides with lipid bilayers: Binding strength, structural transition, and effect on lipid dynamics. Sci Rep. 2016;

246. Carrasco S, Mérida I. Diacylglycerol, when simplicity becomes complex. Trends in Biochemical Sciences. 2007.

247. Topham MK, Prescott SM. Diacylglycerol kinases. In: Handbook of Cell Signaling, 2/e. 2010.

248. Trick JL, Chelvaniththilan S, Klesse G, Aryal P, Wallace EJ, Tucker SJ, et al. Functional Annotation of Ion Channel Structures by Molecular Simulation. Structure. 2016;

249. Kutzner C, Grubmüller H, De Groot BL, Zachariae U. Computational electrophysiology: The molecular dynamics of ion channel permeation and selectivity in atomistic detail. Biophys J. 2011;
250. Melcr J, Bonhenry D, Timr Š, Jungwirth P. Transmembrane Potential Modeling: Comparison between Methods of Constant Electric Field and Ion Imbalance. J Chem Theory Comput. 2016;
251. Malinverni JC, Silhavy TJ. An ABC transport system that maintains lipid asymmetry in the Gram-negative outer membrane. Proc Natl Acad Sci U S A. 2009;
252. Hwang PM, Kay LE. Solution structure and dynamics of integral membrane proteins by NMR: a case study involving the enzyme PagP. Methods Enzym [Internet]. 2005;394:335–50. Available from: http://www.ncbi.nlm.nih.gov/entrez/query.fcgi?cmd=Retrieve&db=PubMed&dopt=Citation&list_uids=15808227%5Cnhttp://ac.els-cdn.com/S0076687905940135/1-s2.0-S0076687905940135-main.pdf?_tid=454c7b7c-22d9-11e2-bb20-00000aab0f02&acdnat=1351632914_8c30a3fe5b299947
253. Audet A, Nantel G, Proulx P. Phospholipase a activity in growing Eacherichia coli cells. Biochim Biophys Acta (BBA)/Lipids Lipid Metab. 1974;
254. Nhu NTK, Riordan DW, Nhu TDH, Thanh DP, Thwaites G, Lan NPH, et al. The induction and identification of novel Colistin resistance mutations in Acinetobacter baumannii and their implications. Sci Rep. 2016;
255. Groisman EA. The pleiotropic two-component regulatory system PhoP-PhoQ. Journal of Bacteriology. 2001.
256. Miller SI, Kukral AM, Mekalanos JJ. A two-component regulatory system (phoP phoQ) controls Salmonella typhimurium virulence. Proc Natl Acad Sci U S A. 1989;
257. Nakanishi-Matsui M, Sekiya M, Futai M. ATP synthase from Escherichia coli: Mechanism of rotational catalysis, and inhibition with the ε subunit and phytopolyphenols. Biochimica et Biophysica Acta - Bioenergetics. 2016.
258. Daugelavicius R, Bakiene E, Bamford DH. Stages of polymyxin B interaction with the Escherichia coli cell envelope. Antimicrob Agents Chemother. 2000;
259. Dias RP, Da Hora GCA, Ramstedt M, Soares TA. Outer membrane remodeling: The structural dynamics and electrostatics of rough

lipopolysaccharide chemotypes. J Chem Theory Comput. 2014;10(6):2488–97.

260. Fujita Y, Matsuoka H, Hirooka K. Regulation of fatty acid metabolism in bacteria. Molecular Microbiology. 2007.

261. Hsu PC, Bruininks BMH, Jefferies D, Cesar Telles de Souza P, Lee J, Patel DS, et al. CHARMM-GUI Martini Maker for modeling and simulation of complex bacterial membranes with lipopolysaccharides. Journal of Computational Chemistry. 2017;

Appendix

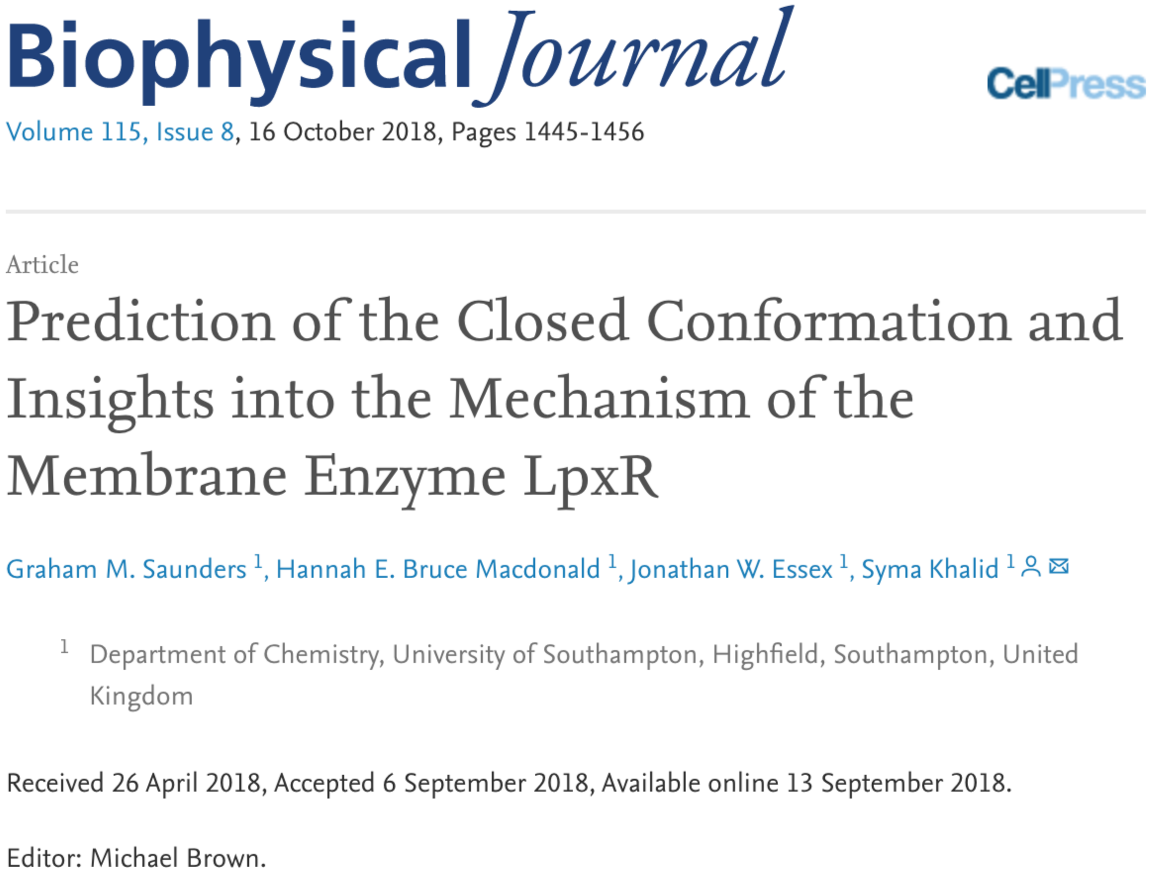

Biophysical Journal
CellPress
Volume 115, Issue 8, 16 October 2018, Pages 1445-1456

Article

Prediction of the Closed Conformation and Insights into the Mechanism of the Membrane Enzyme LpxR

Graham M. Saunders [1], Hannah E. Bruce Macdonald [1], Jonathan W. Essex [1], Syma Khalid [1] 👤 ✉

[1] Department of Chemistry, University of Southampton, Highfield, Southampton, United Kingdom

Received 26 April 2018, Accepted 6 September 2018, Available online 13 September 2018.

Editor: Michael Brown.